PERFORMANCE OF HIGH-STRENGTH REINFORCED CONCRETE COLUMNS UNDER SHOCK-TUBE INDUCED BLAST LOADING

By

Amer Hammoud

Thesis submitted in partial fulfillment of the requirements for the
Master of Applied Science degree in Civil Engineering

Under the auspices of the Ottawa-Carleton Institute for Civil Engineering

uOttawa

University of Ottawa
July 2017

ABSTRACT

Accounting for blast hazards has become one of the major concerns for civil engineers when analysing and designing structures. Recent terrorist attacks and accidental explosions have demonstrated the importance of mitigating blast effects on buildings to ensure safety, preserve life and ensure structural integrity. Innovative materials such as high-strength concrete, steel fibers, and high-strength steel offer a potential solution to increase resistance against extreme dynamic loading and improve the blast resilience of buildings. This thesis presents the results of an experimental and analytical study examining the effect of high-strength concrete, high-strength reinforcement and steel fibers on the blast behaviour of reinforced concrete columns.

As part of the study, a total of seventeen reinforced concrete columns with different design combinations of concrete, steel fibers, and steel reinforcement were designed, constructed, and tested under gradually increasing blast loads using the University of Ottawa shock-tube facility. Criteria used to assess the blast performance of the columns and the effect of the test variables included overall blast capacity, mid-span displacements, cracking patterns, secondary fragmentation, and failure modes. The effect of concrete strength was found to only have a moderate effect on the blast performance of the columns. However, the results showed that benefits are associated with the combined use of high-strength concrete with steel fibers and high-strength reinforcement in columns tested under blast loads. In addition to the experimental program, a dynamic inelastic single-degree-of-freedom analysis was performed to predict the displacement response of the test columns. A sensitivity analysis was also conducted to examine the effect of various modelling parameters such as materials models, DIFs, and accumulated damage on the analytical predictions.

ACKNOWLEDGMENTS

I would like to take this opportunity to express my deep gratitude to all whom supported me through this project.

I would like to thank my thesis supervisor, Dr. Hassan Aoude, for offering his continuous support and immense knowledge while guiding me through my research.

I would also like to thank Dr. Gamal Elnabelsya and Dr. Muslim Majeed for sharing their expertise with me and providing me with help in the structural lab.

For their help with the process of preparing and testing my specimens, I would like to thank my fellow colleagues: Yang Li, Corey Guertin-Normoyle, Omar Algassem, Ahmed Sulaiman, in addition to the group of undergraduate volunteers who helped as well: Dany Loua, Cheick Oumar Dembele, and Abdullah Sani.

Finally, I would like to thank my family for their endless love and unconditional support throughout the previous years. Their continuous encouragement inspired me to achieve my goals. This thesis is dedicated to them.

NOTATIONS

Symbol	**Definition**
A	Area impacted by the blast pressure
A_g	Gross cross-sectional area of column
A_s	Area of longitudinal reinforcement steel
A_{shy}/A_{shx}	Cross sectional area of transverse reinforcement in the x/y direction
C_x/C_y	Width of concrete core parallel to x/y direction
d_b	Steel reinforcement bar diameter
d_f	Fibre diameter
D_{anls}	Analytical displacement
D_{exp}	Experimental displacement
D_{max}	Maximum mid-height column displacement
D_{res}	Residual mid-height column displacement
E_c	Modulus of elasticity, concrete
E_{fp}	Modulus of elasticity of fibers
E_s	Modulus of elasticity, steel
$f_c^{'}$	Compressive concrete strength
f_{cc}	Confined concrete stress
f_{ctf}	Tensile stress of steel fiber reinforced concrete
f_{cu}	Unconfined concrete stress
$f_{cu}^{'}$	Unconfined compressive concrete strength
f_{cuf}	Unconfined fiber reinforced concrete stress
$f_{cuf}^{'}$	Unconfined compressive fiber reinforced concrete strength
f_{dy}	Dynamic yield stress of reinforcement steel
f_{le}'	Effective confinement pressure
f_{lf}	Confining pressure of fibers
f_r	Rupture stress of reinforcement steel
f_s	Stress of reinforcement steel
$f_{s/Du}$	Limiting value of stress when considering compression reinforcement buckling
f_u	Ultimate stress of reinforcement steel
f_y	Static yield stress of reinforcement steel
F(t)	External forcing function in dynamic equation of motion
I_E'	Effective confinement index
I_r	Reflected impulse
k	Stiffness in dynamic equation of motion
K_{LM}	Load mass transformation factor
k_{rot}	Rotational spring stiffness
l_f	Fiber length

L	Column length
L_d	Driver length
L_{pl}	Plastic hinge length
m	Total mass of the system
n	Ratio of steel modulus of elasticity to concrete modulus of elasticity
N_f	Effective number of fiber per unit area
P	Axial load
P_d	Driver pressure
P_r	Reflected pressure
s	Spacing of transverse steel ties
t_d	Positive phase duration
u	Deflection at mid-height
$\ddot{u}$	Acceleration at mid-height
V_f	Fibre volume ratio
$\dot{\varepsilon}$	Strain rate
$\dot{\varepsilon}_o$	Peak strain
ε_{50cu}	Unconfined concrete strain at 50% of peak stress
ε_{cc}	Confined concrete strain
ε_{cc50}	Confined concrete strain at 50% of peak stress
ε_{cu}	Unconfined concrete strain
$\varepsilon_{cu}^{'}$	Unconfined concrete strain at peak stress
ε_r	Rupture strain of reinforcement steel
ε_s	Strain of reinforcement steel
$\dot{\varepsilon}_s$	Static strain rate
$\varepsilon_{s/Du}$	Limiting value of strain when considering compression reinforcement steel buckling
ε_{sh}	Strain hardening strain of reinforcement steel
ε_u	Ultimate strain of reinforcement steel
ε_y	Yield strain of reinforcement steel
ρ_c	Ratio of area longitudinal reinforcement in the core area of the column
ρ_{sex}	Effective sectional ratio of confinement reinforcement in the x direction
ρ_{sey}	Effective sectional ratio of confinement reinforcement in the y direction
θ	Support rotation
θ_{max}	Maximum support rotation
τ_{bond}	Matrix bond strength

ACRONYMS

ACI	American Concrete Institute
ASTM	American Society of Testing and Materials
CEB	Comité Euro-International du |Béton (Euro-international Concrete Committee)
CRC	Compact Reinforced Composite
CSA A23.3	Canadian Standard Association- Design of Concrete Structures
DIF	Dynamic Increase Factor
FRC	Fiber Reinforced Concrete
FRP	Fiber Reinforced Polymer
HSC	High Strength Concrete
HSFRC	High Strength Fibre Reinforced Concrete
HSS	Hollow Steel Section
LTD	Load Transfer Device
LVDT	Linear Variable Displacement Transducer
MMFX	Microcomposite Multistructural Formable Steel
NEHRP	National Earthquake Hazards Reduction Program
NRC	Normal Reinforced Concrete
NSC	Normal Strength Concrete
NSS	Normal Strength Steel
RPC	Reactive Powder Concrete
SCC	Self Consolidating Concrete
SDOF	Single Degree of Freedom
SFRC	Steel Fiber Reinforced Concrete
SHPB	Split Hopkinson Pressure Bar
UDL	Uniformly Distributed Load
UHPC	Ultra High Performance Concrete
UHPFRC	Ultra High Performance Fiber Reinforced Concrete

TABLE OF CONTENTS

LIST OF FIGURES

LIST OF TABLES

CHAPTER 1. INTRODUCTION

1.1 Chapter Overview

Recently, civil engineering structures have become more susceptible to blast loads due to increased threats. Despite the rarity of blast incidents, they can result in catastrophic outcomes. Examples such as the Oklahoma City bombing (USA, 1995) and Khobar Towers Bombing (Saudi Arabia, 1996) put into evidence the severe consequences that can result from blast-induced failures in buildings. Structures are also susceptible to blast loading caused by accidental explosions. Examples of events in this category include: the Toronto Sunrise propane explosion (Canada, 2008) and the Toulouse ammonium nitrate plant explosion (France, 2001), among others. Thus, engineers must develop approaches to ensure the blast resilience of structures to mitigate against the consequences of blast failures.

The overall blast resistance of a structure relies on the performance of key load-carrying elements in the structural system. In the case of reinforced concrete buildings, failure of ground-story columns under blast loading can lead to progressive collapse as they are the primary carriers of gravity loads in the structure. Ground-storey columns must therefore be designed to have sufficient strength and ductility to prevent failure under blast loading.

High-strength concrete (HSC) is now commonly used in structures. In high-rise buildings, the use of HSC in columns allows for reduced cross-section sizes to meet architectural requirements, while also allowing for the capacities required to accommodate high axial loads. On the other hand, HSC is a more brittle material when compared to normal-strength concrete which can raise questions about the ductility of HSC columns. While important research exists on the seismic performance of HSC columns, blast research is limited and further research is required.

The use of high-performance materials is a possible solution to enhance the blast resistance of columns. Combined use of high-strength concrete and steel fibers can remedy the brittleness of HSC, which can lead to increased ductility of HSC columns under blast loads. Similarly, the combined use of high-strength concrete and high-strength reinforcement can possibly allow for increased column blast resistance. This research program investigates the blast performance of high-strength reinforced concrete columns. The effect of the combined use of HSC with high-strength reinforcement and steel fibers on blast behaviour is also investigated.

1.2 Research Objectives

The objective of this research is to investigate the behaviour of reinforced concrete columns built with high-strength concrete under simulated blast loads. The study focusses on high-strength concrete as it is a common concrete type in modern structures, such as high-rise buildings. In addition, the research program investigates the blast performance of columns built with high-strength concrete in combination with high-performance materials (high-strength steel and steel fibers). The objectives of the research are achieved through testing of half-scale columns under simulated blast loads using a high-capacity shock-tube. The research also examines the suitability of using dynamic inelastic single-degree-of-freedom (SDOF) analysis to predict the displacement response of the HSC columns tested in the experimental research program.

1.3 Scope of Work

A total of seventeen half-scale reinforced concrete columns were designed, constructed, and tested under simulated blast loads using the shock-tube facility at the University of Ottawa. The design parameters examined in this study include:

- Effect of concrete strength; high-strength concrete (HSC) vs. normal-strength concrete (NSC)
- Effect of longitudinal steel reinforcement type; normal-strength steel reinforcement (NSS) vs. high-strength steel reinforcement (MMFX)
- Effect of steel fibers in high-strength fiber-reinforced concrete (HSFRC) and fiber content
- Effect of longitudinal steel reinforcement ratio in HSC and HSFRC columns with normal-strength steel (NSS) and high-strength steel (MMFX)
- Effect of transverse reinforcement ratio; non-seismic detailing vs. seismic detailing in HSC columns

The specimens in this experimental study are divided into five series as shown in Table 1-1:

Table 1-1 Series matrix

Series	Concrete type	Steel type	Number of specimens
NSC	Normal-strength concrete (NSC)	Normal strength steel (NSS)	2
HSC-NSS	High-strength concrete (HSC)	Normal strength steel (NSS)	4
HSFRC-NSS	High-strength fiber-reinforced concrete (HSFRC)	Normal strength steel (NSS)	4
HSC-MMFX	High-strength concrete (HSC)	High-strength steel (MMFX)	4
HSFRC-MMFX	High-strength fiber-reinforced concrete (HSFRC)	High-strength steel (MMFX)	3

The columns are tested against repeated and gradually increasing blast pressures until failure. The criteria adopted to evaluate the effect of the test parameters on blast performance includes: magnitude of failure blasts, mid-span displacements at equivalent blasts, failure mode, crack control, and secondary fragmentation. Results and observations will be used to study the effect of high-strength concrete on blast performance and examine the advantages of using high-performance materials in columns subjected to blast loads. The study will also aim to predict the response of the test columns analytically using a SDOF analysis approach.

1.4 Thesis Organization

This thesis includes seven chapters divided as listed below:

Chapter 1 – Introduction:

- Introduces the significance of this research
- Provides a brief description of the objectives and scope of work

Chapter 2 – Literature Review:

- Summarizes previous research on the blast performance of reinforced concrete columns and previous research on the effect of fibers and high-strength steel on blast performance

Chapter 3 – Experimental Program:

- Describes specimens and materials used in construction
- Describes the shock-tube and the test procedure followed

Chapter 4 – Experimental Results:

- Summarizes the data obtained from the experimental program
- Presents the experimental results in detail for each specimen

Chapter 5 – Discussion of Experimental Results:

- Compares the performance of the columns and examines the effects of the various design parameters on the blast performance of companion columns

Chapter 6 – Dynamic Analysis:

- Describes the SDOF analysis approach and the materials models used in the analysis
- Summarizes the results of the SDOF analysis and compares it to the experimental results
- Presents a sensitivity analysis examining the effect of various modelling parameters

Chapter 7 – Conclusion:

- Presents concluding remarks for this research program
- Proposes recommendations for further research

CHAPTER 2. LITERATURE REVIEW

2.1 Chapter Overview

This chapter provides a summary of previous research related to the subject of this thesis. A brief review of materials used is presented, and studies are then sorted into major sections. The first section addresses research conducted to study the impact and blast behaviour of reinforced concrete columns. Studies are listed in Table 2-2, followed by a summary of their major findings. The second part of chapter 2 focuses on impact and blast studies concerning steel fiber reinforced concrete. These studies are listed in Table 2-3 and then summarized to present their major findings. Finally, previous studies examining the blast performance of components built with high-strength steel are listed in Table 2-4 and discussed.

2.2 Materials Review

High-strength concrete (HSC)

High-strength concrete (HSC) is defined as concrete with a 28-day compressive strength exceeding 8000 psi (55 MPa) (ACI CT-13, 2013). However, concrete with strengths ranging from 70 MPa to 125 MPa are now available for use in cast-in-place and precast applications (Wight & Macgregor, 2009). The high-compressive capacity of HSC allows for smaller cross-sections in structural members, which makes it well-suited for use in heavily-loaded structural elements, such as in the columns of high-rise buildings. The high-compressive strength is achieved by utilizing a low water-to-cementitious-materials ratio, and the addition of supplementary cementitious materials such as silica fume. To ensure adequate workability and improve setting time, chemical admixtures such as superplasticizers and set retarders are typically added to HSC mix designs. Due to its increased strength, HSC is characterized by a more brittle failure, particularly in compression, with reduced strain capacity when compared to normal-strength concrete (NSC). Its stress-strain relationship is characterized by a more linear ascending branch compared to that of NSC, with abrupt failure soon after peak stress is reached (Figure 2-1 (a)). Over the years several researchers have proposed compression models for HSC; one of the most common stress-strain relationship for unconfined HSC in compression is the model proposed by Popovics (1973).

High-strength fiber-reinforced concrete (HSFRC)

Plain concrete has very limited tensile capacity. Adding steel fibers is a solution to this problem and provides concrete with additional tensile resistance, post-cracking capacity and toughness due to the ability of fibers to arrest and redistribute cracking. The addition of fibers can also improve the compressive behaviour of high-strength concrete. High-strength fiber-reinforced concrete (HSFRC) is defined as a composite material that combines the HSC concrete matrix with randomly oriented short discrete steel fibers, which are added at volumetric ratios ranging from 0.5% to 2% of the total volume of concrete cast (40-160 kg/m^3). Steel fiber contents of 0.5% to 1% are typically used for structural applications to maintain workable concrete. Steel fibers provide an effective solution for overcoming the brittleness of HSC by providing it with increased ductility. In addition to the enhancement in tensile resistance, steel fibers slightly increase the elastic modulus and strength of concrete in compression. However, the more important effect is the post-peak range, where the steel fibers allow for the development of much higher ultimate strains and toughness as shown in Figure 2-1 (b). The model proposed by Mansur et al. (1999) can be used to account for the contribution of steel fibers in the stress-strain relationship of high-strength steel fiber-reinforced concrete.

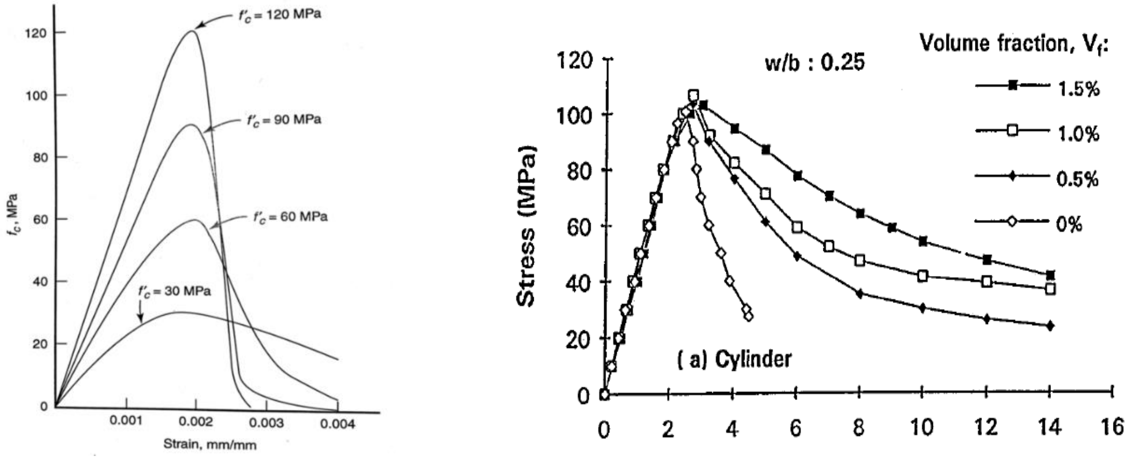

a) Stress-strain responses for concrete with different compressive strengths based on Popovics model (1973)

b) Stress-strain response of HSFRC with different fiber contents (Mansur et al. 1999)

Figure 2-1 Stress-strain curves for HSC and HSFRC

High-strength steel reinforcement (MMFX)

High-strength reinforcement can be defined as steel reinforcement with a yield strength of 72 ksi (500 MPa) or greater (NEHRP, 2014). In the past few decades, significant research has been conducted on the structural use of high-strength steel since this type of reinforcement is becoming more commonly used in construction. In reinforced concrete structures the high tensile capacity of high-strength reinforcement can allow for reduced reinforcement congestion and savings in labor and construction time. Microcomposite Multistructural Formable Steel (MMFX) are low-carbon, chromium alloy high-strength reinforcing bars which are referenced in the ASTM A1035 “Standard specification for deformed and plain, low-carbon chromium, steel bars for concrete reinforcement”. The typical chemical composition of MMFX bars is shown in Table 2-1. These high-strength bars are produced using a controlled rolling and manufacturing process where steel is rolled within specified temperature ranges and cooled at specific rates (MMFX, 2014). In addition to high-strength, these bars show very high corrosion-resistance, making them well suited for use in aggressive environments. The stress-strain relationship for this type of steel is characterized by a round-house type response without a well-defined yield plateau. Due the increased strength properties this steel shows a relatively reduced strain capacity when compared to conventional steel reinforcement. This steel is available in two grades; Grade 100 (690 MPa) and Grade 120 (830 MPa). Typical stress-strain curves for MMFX reinforcing bars are shown in Figure 2-2.

Table 2-1 MMFX chemical properties (ASTM A1035/A1035M-16)

Element	MMFX
Carbon	0.15%
Chromium	8-10.9%
Manganese	1.50%
Silicon	0.50%
Phosphorus	0.035%
Sulfur	0.045%
Nitrogene	0.5%

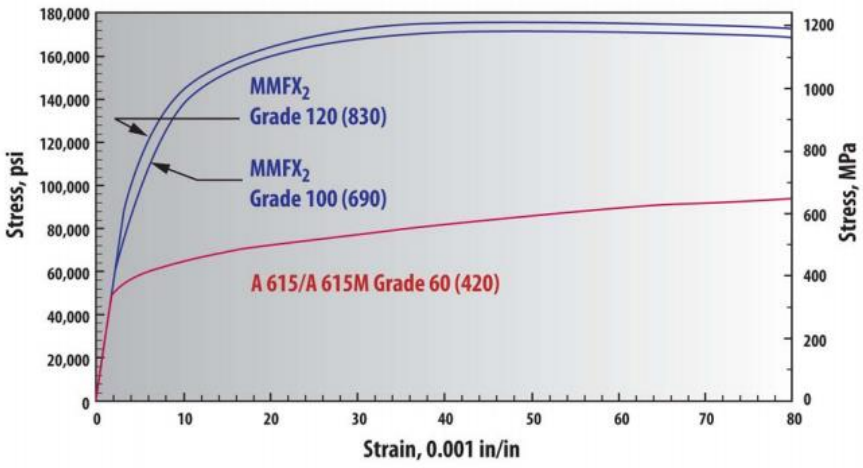

Figure 2-2 Typical stress-strain curves for MMFX reinforcing bars (www.mmfx.com)

2.3 Previous Research on Impact & Blast Performance of RC Columns

Previous research has been conducted on the impact and blast behaviour of reinforced concrete columns. Table 2-2 provides an overview of this research, with a summary of testing methods and parameters investigated. Further details are provided in the sub-sections that follow. A review of previous research reveals only two studies have focused on columns having concrete strengths greater than 60 MPa (one impact study and one analytical study).

Previous research on RC columns tested under impact loads

Louw et al. (1992) studied the response of cantilever beam-columns under combined axial and impulsive flexural loading. The parameters investigated included loading rate, concrete strength (f'_c = 19-37 MPa), longitudinal reinforcement ratio, and shear reinforcement ratio. Concrete strength and shear reinforcement were found to more greatly influence the shear resistance of the columns, while the longitudinal reinforcement was found to govern flexural strength. For shear-critical columns, doubling the concrete strength from 19 to 37 MPa was found to increase the impact strength by 33% (compared to an increase of 17% for static strength).

Remennikov and Kaewunruen (2006) tested a series of quarter-scale reinforced concrete columns (f'_c = 32 MPa) under the impact of a free-falling mass (160 kg) using a drop hammer test rig. The purpose of the study was to observe the performance of the concrete columns through failing patterns and mid-span deflections and compare them to other specimens tested statically. The impact-tested columns were shear dominant, with diagonal cracks developing at the point of load application and extending towards the adjacent supports in a more severe manner when compared to static specimens due to the high-velocity impact amplification. The study also found that the amplified shear forces occurring near the middle of the columns resulted in severe cracking before any significant bending could take place.

Hyunh et al. (2015) investigated the impact response of a series of high-strength concrete and reactive powder concrete (f'_c = 100-160 MPa) beams-columns under low and medium-velocity impact loading. The effects of axial force, load eccentricity, and reactive powder concrete (RPC) as a replacement for HSC were investigated. The results showed that both axial load and load eccentricity had an important effect on impact resistance and failure mode, while fiber-reinforced RPC was found to improve the impact performance of the columns when compared to HSC.

Previous research on RC columns tested under blast loads

Carriere et al. (2007) tested 10 reinforced concrete members (f'_c = 39 MPa) transversely wrapped with steel reinforced polymer (SRP) under blast loads. The specimens had square cross-sections and symmetrical reinforcement (top and bottom) in addition to fully fixed supports with the application of axial load to some of the specimens. The objective of this research was to examine the effect of the SRP wraps in improving the resistance of the lightly reinforced members against blast loadings. The transversely applied SRP wraps were found to reduce concrete crushing and prevent spalling on the tensile side. The use of SRP was found to increase the ductility of flexural-dominant specimens. However, it did not increase resistance in beam specimens where tensile failure of the reinforcement was the governing mode of failure

Fujikura and Bruneau (2008) tested a series of quarter-scale seismically resistant bridge pier-bents under close-in live explosives. Each bent consisted of three bridge piers with an integral cap beam. The study examined the blast performance of seismically detailed “ductile” RC columns with closely spaced stirrups, as well as “non-ductile” RC columns retrofitted with steel jackets (f'_c = 42 MPa). The seismically-detailed RC columns and the steel-jacketed RC columns were found to fail in direct shear at the base. The columns experienced breaching and spalling of concrete without flexural yielding. The study concluded that seismic detailing and steel jacketing in reinforced concrete columns are ineffective in the case of close-in blast conditions.

Fujikura et al. (2008) studied the close-in blast behaviour of two quarter-scale multicolumn pier-bents with concrete filled steel tube (CFST) columns (f'_c = 42 MPa). This experiment evaluated the potential of using CFST columns as multi-hazard piers which are capable of withstanding seismic and blast loads. After blast testing and the removal of the steel tube, cracks were noticed to develop on the tension side at mid-height of the column and on the tension sides at the top and bottom of the column (at the top due to some torsional rigidity provided by the cap beam). However, larger explosive charges led to buckling of the steel tube, and even larger blasts led to blow out failures and to the fracture of the column at the top support. Despite the mentioned failures at high blast pressures, the CFST columns were found to be effective in resisting blast loads due to the high ductility provided by the steel tube. CFST columns also managed to prevent breaching and spalling of concrete that had previously occurred with blast testing of seismic and steel-jacketed bridge piers (Fujikura and Bruneau, 2008).

Bao and Li (2010) studied the dynamic response and the residual axial capacities of a series of 12 reinforced concrete columns (f'_c = 30-70 MPa) tested under the impact of short standoff distance blast conditions. This parametric study was carried out using the finite element software LS-DYNA. It examined the effects of transverse reinforcement ratio, axial load ratio, longitudinal reinforcement ratio, and column aspect ratio. Seismic detailing of the transverse reinforcement was found to contribute to a reduction of blast damage and to a decrease in recorded displacements. As for the residual axial capacity, it increased as the longitudinal reinforcement ratio increased or as the aspect ratio of the columns decreased. The axial load ratio was also found to be more critical in columns having low reinforcement ratios.

Lloyd (2010) conducted an experimental program to study the response of 14 reinforced concrete columns (f'_c = 46-58 MPa) under shock wave loading using the shock-tube facility at the University of Ottawa. The effects of transverse reinforcement, longitudinal reinforcement, and axial load were examined in the study. In addition, the experiment results were compared to those predicted with numerical modeling through a SDOF analysis. The difference in performance between non-seismic and seismic columns under blast loadings was insignificant (although seismic columns performed slightly better). The limited improvements were justified by the limited confinement effect resulting from loss of axial load and slenderness of the columns. A higher reinforcement ratio led to better control of lateral displacements, and the drop of axial load due to horizontal deformation was found to have a major effect on the analysis results later. Finally, a single degree of freedom analysis was performed and resulted in accurate predictions in the cases of moderate levels of blast intensity, as well as effectively predicting displacements under severe damage if a proper collapse mechanism is considered.

Wu et al. (2011) tested two RC columns ($f'_c = 40$ MPa) using near-field explosive charges. In addition to the experiments, a parametric study was conducted using the software LS-DYNA to further examine the effects of different parameters on the blast behaviour of the columns. The results of the numerical models for the two columns were in good agreement with the experimental results obtained, particularly in terms of cracking profiles and the location of failures. As for the numerical study, the parameters investigated included the cross-section properties, longitudinal and transverse reinforcement ratios, height, stand-off distance, and residual axial capacities of the columns. The columns were found to exhibit less damage and perform better when designed with larger effective depths and larger reinforcement ratios. Residual axial capacities of the columns were significantly affected by higher longitudinal reinforcement ratios, where an increased area of rebar led to an increase in residual axial load capacity. The capacities were also affected by the transverse reinforcement ratio where higher ratios led to more confinement and thus more axial capacity. Two empirical equations were developed to predict residual axial capacities of columns.

Williamson et al. (2011) conducted an experimental program including 10 reinforced concrete columns ($f'_c = 28$ MPa) with the purpose of better understanding the behaviour of blast-loading on concrete bridge columns. The columns in this study were tested under close-in live blast loads. Parameters included the cross-sectional shape (circular or square), longitudinal reinforcement ratio, and transverse steel configuration (typical, seismic, and blast). Post-damage assessment of the columns showed that the columns with blast and seismic design performed better than columns with typical details. However, failure of the columns was associated with direct shear at the base. This study also led to the observation of a phenomenon not previously seen in similar experiments: the spalling of side-cover concrete. The side-cover spalling was found to be a result of Poisson's ratio; as the concrete core contracts in the direction of the loading, it leads to an expansion perpendicular to the direction of the loading. The phenomenon was also found to be a localized response and not dependent on the formation of a plastic hinge.

Li et al. (2012) used numerical modelling through LS-DYNA to examine the residual axial capacity of four columns ($f'_c = 25$ MPa) subjected to quasi-static loadings. The numerical study was accompanied by an experimental study where the columns were tested using three hydraulic actuators to examine their lateral displacement response and residual axial capacity. The study also aimed to examine the effects of axial loading and the transverse reinforcement ratio. A higher axial load was found to increase stiffness and result in a smaller deflected profile. However, as the impulse and corresponding displacement exceeded critical values, it was found that the high axial load would lead to an increased lateral displacement due to the P- δ effect. As for transverse reinforcement, an increase in the reinforcement ratio from 0.19% to a 0.58% provided more confinement to the concrete core, increased shear capacity, and limited the lateral deflection profile.

Table 2-2 Summary of previous studies on RC columns

Study	Test method	No. of specimens	Specimen type	Cross-section shape	Cross-section dimensions b x c or d (mm)	Height (mm)	Axial load?	Axial load level (kN)	Boundary conditions	Concrete strength (MPa)	Longitudinal steel rein.		Transverse reinf. ratio (%)
											yield strength (MPa)	Ratio (%)	
Louw et al. (1992)	Impact: FM	36	RC column	Square	300 x 300	4000	Yes	201 / 245	Simply supported	16-40	518	1.5-3	0.85
Remennikov & Kaewunruen (2006)	Impact: FM	7	RC column	Square	100 x 100	1000	Yes	60	Fully fixed	32	500	3.1-4.5	0.55
Huynh et al. (2015)	Impact: FM	16	RC /RPC column	Square	250 x 250	2000	Yes	440	Simply supported	100-160	574	1.6	0.33
Carriere et al. (2007)	Blast: Live	10	RC column wrapped with SRP	Square	150 x 150	2100	Yes	0-300	Fully fixed	39	500	0.56	0.55
Fujikura & Bruneau (2008)	Blast: Live	4 (Bridge bents)	RC column	Circular	203	1500	Yes	4098	Fixed bottom / Pinned Top	42	420	0.9	0.35-1
Fujikura et al. (2011)	Blast: Live	2 (Bridge bents)	CFST column	Circular	102-152	1500	No	(only weight of cap beam)	Fixed bottom / Pinned top	42	254-419	4.3-6.6	NA
Bao & Li (2010)	Blast: Live	12[1]	RC column	Square	355 x 355	2130 / 3480	Yes	378 / 3529	Fixed bottom / Pinned top	30-70	460	1.8-3.2	0.12-0.46
Lloyd (2010)	Shock-tube	14	RC column	Rectangular / Square	100 x 150 / 150 x150	2438	Yes	350	Partially fixed	46-58	483	1.79-2.67	1.1-2.1
Wu et al. (2011)	Blast: Live	2 (11[1])	RC column	Square	400 x 400 / 600 x 600	2400 / 4400	Yes	1280 / 5760	Fully fixed	40	420	1.57-2.52	0.21-1.0
Williamson et al. (2011)	Blast: Live	10	RC column	Circular / Square	460 / 760 / 760 x 760	3430	No	-	Fixed bottom / Pinned top	28	475	1.04-1.18	NA[2]
Li et al. (2012)	Blast: Live	4	RC column	Square	260 x 260	2400	Yes	338-676	Fixed Bottom / Pinned top	25	460	2.3	0.19-0.58

---

[1] Specimens tested analytically

[2] typical, seismic, and blast transverse reinf. arrangement

2.4 Previous Research on Impact & Blast Performance of SFRC members

Limited research has been conducted on the impact and blast behaviour of reinforced concrete structures incorporating steel fibers. Previous studies in this area (with a focus on structural members: beams and columns) are summarized in Table 2-3. Further details are provided in the sub-sections that follow.

Impact studies on SFRC

Banthia (1987) studied the effects of concrete strength (f'_c = 42-82 MPa) and steel fiber reinforcement on the impact response of plain and conventionally reinforced concrete beams using an instrumented drop-weight impact machine. In the case of the plain specimens, HSC was found to have higher peak bending strength under dynamic loading compared to NSC, although fracture energy was reduced, indicating increased brittleness. Moreover, HSC specimens with conventional reinforcement showed reduced fracture energy under impact vs. static loading and as drop-height increased, an indicator of more brittle behaviour with an increased stress-rate. Adding fibers was found to be effective in remedying the brittleness of HSC, leading to increased ductility and energy absorption capacity. The effect of fibers on increasing the energy absorption capacity was found to be greater for HSC compared to NSC, particularly at higher drop-heights.

Miyamoto et al. (1989) tested a series of RC and SFRC beams (f'_c = 29 MPa) against gradually increased static loads and against impact loads using a falling mass of 100 kg. This study examined the effects of high strain rates on the behaviour of the different specimens. Impact loads led to an increase of load capacity, drop in deflection capability, increase in local failure, and decrease in failure region. Steel fibers were found to improve the impact resistance of the beams to the improvement in tensile capacity. Steel fibers also better controlled cracking and deformation capability, thus providing additional ductility to the beams. A drop of impact resistance was also observed with an increase in beam depth. Finally, higher concrete strength was found to decrease dynamic resistance, with the authors noting that it can be improved with the addition of steel fibers.

Other impact studies: Many studies have also been conducted to examine the impact behaviour of SFRC at the material level using drop-weight, pendulum or Split-Hopkinson Pressure Bar (SHPB) tests (Naaman and Gopalaratnam 1983, Gopalaratnam and Shah 1986, Banthia et al. 1996, Wang et al. 1996, Bindiganavile at al. 2002, Xu et al. 2006, Lok and Zhao 2004, Wang et al. 2007 and others). These studies have shown that the addition of steel fibers leads to improved cracking control and fragmentation resistance against impact loads. Moreover, the studies confirm the strain-rate sensitivity of SFRC. However, some researchers such as Bindiganavile et al. (2007) and Lok & Zhao (2004), reported that the ductility of SFRC which is observed under static loads, reduces under dynamic impact loads, and can even become absent at large stress-rates.

Blast studies on SFRC structural members

As shown in Table 2-3, several researchers have investigated the blast performance of fiber reinforced concrete (FRC), mostly from tests conducted on panels under close-in live explosive testing. In general, these researchers have confirmed the improved resistance of FRC to fragmentation when compared to conventional concrete. A fewer number of studies have been conducted on beams and columns. This section looks at the major findings of some of the studies presented in Table 2-3.

Lok and Xiao (1999) investigated the blast response of SFRC (f'_c = 29-44 MPa) by testing 42 one-way and two-way panels under live blast loads. Variation in the type and content of steel fibers in the specimens allowed for an investigation into the effect of fiber properties on blast performance. Other parameters such as the effect of mesh reinforcement, panel cross section dimensions, and boundary conditions were also studied. Experiment results were also validated through a SDOF analysis. SFRC panels were found to have better resistance with lower displacements and less damage over plain concrete panels, contributing significantly to the integrity of the panels under blast effects. Increased fiber content was found to have positive effect in terms of narrower cracks and less breaching, but not necessarily fewer cracks. However, a steel fiber content of 1.5% was found to have minimal improvement when compared to 0.5% and 1%. Predicted results using the SDOF analysis were in good agreement with the experimental results of the simply supported panels having steel fiber ratio between 0.5% and 1%. Fully fixed conditions and increased fiber content, however, resulted in some over-predictions of the results.

Yusof et al. (2010) tested eight doubly-reinforced SFRC panels (f'_c = 35 MPa) against close-in live explosives. The steel fiber content of the specimens varied from 0.5% to 1.5%; a specimen with plain concrete was also included. The plain and 0.5% specimens were found to show poor blast resistance, whereas increasing the fiber content to 1% and 1.5% led to better results. The specimen containing 1.5% fiber content delivered the best overall performance.

Li et al. (2016) performed close-in live blasts on four fiber-reinforced concrete slabs (f'_c = 45 MPa) in which two slabs included high-performance polyethylene fibers and the other two included hybrid fibers (steel fibers + high-performance polyethylene fibers). The study examined the effect of fibers on the blast behaviour of the slabs when compared to a fifth slab cast with plain concrete, in addition to studying the advantages of using hybrid fibers. The fiber-reinforced specimens were superior to the plain concrete specimen in terms of damage and deformation control. As for the hybrid specimens, the combination of additional strength and stiffness of the steel fibers plus the additional ductility and flexibility supplied by the polyethylene fibers was reflected by improvements in the overall performance of the slabs.

Magnusson et al. (2010) studied the behaviour of a large set of normal-strength and high-strength reinforced concrete beams under air-blast loading using a shock-tube. Blast loads were applied by the detonation of a spherical plastic explosive placed within the center of the shock-tube. The test program included beams of varying concrete strengths (f'_c = 40, 100, 140, 150, and 200 MPa) and reinforcement ratios (ρ = 1.1-2.5%), and included specimens with and without steel fibers. The tests demonstrated that the load capacity of the beams increased under dynamic loading, with dynamic-static load ratios ranging from 1.04 to 1.81. In some cases, the failure mode changed from ductile flexure under static loads to brittle shear under dynamic loading. Plain HSC beams with larger reinforcement ratios were found to be particularly susceptible to shear failure under blast loads. Steel fibers were found to be effective in preventing shear failure and improving the blast performance and ductility of the HSC beams.

Burrell (2012) tested a series of SFRC columns against blast loads simulated using a shock-tube. The columns had varied steel fiber types and contents. The study also looked at the effect of seismic detailing and the effect of concrete strength between self-consolidating concrete (SCC) and compact reinforced composite (CRC), a type of ultra-high performance concrete that could reach up to 160 MPa in compressive strength. Steel fibers were found to have a major effect in limiting mid-span maximum and residual displacements, in addition to significantly reducing damage and secondary fragments. Increasing the fiber content had the effect of proportionally increasing the overall resistance of the members, but at the cost of reduced concrete workability which can increase placement difficulties. The type of steel fiber had a limited effect on mid-span displacements and crack control, although performance of the members improved slightly with steel fibers having higher strength and aspect ratios. Finally, seismically detailed columns experienced lower displacements than the non-seismic ones due to the developed ductility in the concrete core. Higher concrete strength (in the form of fiber-reinforced CRC) contributed to better results, especially when combined with higher steel fiber content.

Table 2-3 Summary of previous research on SFRC studies

Study	Test method	Specimen type	Cross-section shape	Specimen dimensions L x b x h (mm)	No. of specimens	Boundary conditions	Concrete strength (MPa)	Longitudinal reinforcement		Fiber properties		
								Yield strength (MPa)	Ratio (%)	Content (%)	Type	Aspect ratio
Banthia (1984)	Impact: FM	Beam	Rectangular	1400 x 100 x 125	27	Simply supported	42-82	-	-	0.5-1.5	Hooked ends / Polypropylene	83.3-61.6
Miyamoto et al. (1989)	Impact: FM	Beam	Rectangular	1300 x 150 x 160	20	Simply supported	29	420	1.64	NA	NA	NA
Bindiganavile et al. (2002)	Impact: FM	Beam	Square	350 x 100 x 100	12	Simply supported	40 - 192	-	-	0.75-6	Flat end / Crimped / Polypropylene	42.8-33.3
Yoo et al. (2015)	Impact: FM	Beam	Rectangular	2900 x 200 x 270	4	Simply supported	150	523	0 – 1.71	2	Smooth, straight	65
Lok & Xiao (1999)	Blast: Live close-in	Panel	Rectangular / Square	810 x 810 x 50	42	Simply supported / Fully fixed	29-44	460	0-0.28 / glass fiber mat on tension side	0.5-1.5	Uniform Slightly crimped ends / Hooked ends	33.4-75
Yusof et al. (2010)	Blast: Live close-in	Panel	Rectangular	600 x 600 x 100	8	Fully fixed	35	420	0.57	0.5-1.5	Hooked ends	80
Li et al. (2016)	Blast: Live close-in	Slab	Rectangular	2000 x 800 x 120	5	Fully fixed	45	270	2.12	2.5	High performance polyethylene / Hybrid (polyethylene + smooth straight steel)	83.3-100
Magnusson et al. (2010)	Blast: shock-tube	Beam	Rectangular	1720 x 300 x 160	49	Simply supported	40-200	544-604	1.1-2.5	0-1-2.4	Smooth, straight	31.3
Burrell (2012)	Blast: Shock-tube	Column	Square	2468 x 152 x 152	13	Partially fixed	50-165	480	1.72	0-0.5-4	Hooked ends (low and high-strength)	30-79

2.5 Previous Research on Blast Performance of High-Strength Steel

A limited number of research projects have investigated the behaviour of high-strength steel in structural members under blast loads. A few of these studies are summarized in Table 2-4, followed by explanations of their major findings. Note that two of these studies also examined the effect of fibers in their testing.

Thiagarajan et al. (2014) tested four doubly reinforced concrete slabs under blast loads using a shock-tube. The specimens included different combinations of concrete (HSC: 107 MPa vs. NSC: 28 MPa) and steel reinforcement (high-strength vandium reinforcement vs. normal-strength reinforcement, designated as VR and NR respectively). In comparison to the control slab with normal-strength concrete and normal reinforcement (NSC-NR), the use of either HSC or high-strength VR bars resulted in improved blast performance, with better control of maximum displacements. Optimal results were obtained for the slab containing both high-strength concrete and high-strength reinforcement (HSC-VR).

Melançon (2015) conducted an experimental program to examine the response of reinforced concrete one-way slabs (f'_c = 40-150 MPa) under shock-tube blast loads. Among the 14 specimens tested, 3 were constructed using high-strength steel reinforcement to investigate their contribution to the overall blast performance. Other parameters investigated included concrete type, steel fibers type, and steel fibers content. The slabs built with high-strength reinforcement showed significant improvement compared to the slabs with normal-strength reinforcement. The performance of the high-strength steel slabs was characterized by lower maximum and residual mid-span displacements as well as increased resistance (ability to sustain higher blast loads). The specimen with stainless steel showed similar improvements with the addition of supplying the member with high ductility features that are not present in the high-strength steel. Response to blast loads also improved when higher strength steel was combined with ultra-high performance concrete (UHPC).

De Carufel (2016) studied the behaviour of a series of ultra-high performance concrete (UHPC) columns built with high-strength reinforcement using a shock-tube. The main objective was to examine the effects of steel reinforcement type, concrete type (f'_c = 40-150 MPa), and steel fibers. Out of the 17 columns, 5 were built with high-strength steel. The use of high-strength reinforcement in UHPC columns was found to critically reduce mid-span displacements and increase blast capacities. The high capacity of tension steel equilibrated the high compressive capacity of the UHPC concrete and prevented steel bar rupture that occurred with conventional steel. Although the high-strength reinforcement specimens allowed for greater blast resistance and absorbed the shock-wave energy, brittle bar rupture was inhibited when capacity was exceeded due to the low rupture strain of the high-strength bars.

Table 2-4 Summary of previous research on high-strength steel studies

Study	Test method	Specimen type	Cross-section shape	Specimen dimensions L x b x h (mm)	No. of specimens	Boundary conditions	Concrete strength (MPa)	Longitudinal reinforcement		Fiber properties		
								Yield strength (MPa)	Ratio (%)	Fiber content (%)	Fiber type	Aspect ratio
Thiagrajan (2014)	Blast: Shock-tube	Slab	Rectangular	1652 x 857 x 102	10	Simply supported	28 - 107	414-572	0.92	-	-	-
Melançon (2015)	Blast: Shock-tube	Slab	Rectangular	2438 x 440 x 80 / 2440 x 440 x 100	14	Partially fixed	40 - 150	435-1000	0.72-1.29	0-2	Hooked end / smooth, straight	43-79
De Carufel (2016)	Blast: Shock-tube	Column	Square	2438 x 152 x 152	17	Partially fixed	40 – 150	424-950	1.23-4.93	0-3	Smooth, straight	43-62

2.6 Summary of Literature Review

This chapter provided a review of literature related to the materials used in this research as well as a review of previous studies on the blast and impact performance of RC columns, and structures built with SFRC and high-strength reinforcement. The following conclusions can be drawn from this chapter:

- High-strength concrete shows increased brittleness when compared to normal-strength concrete. The addition of steel fibers is effective in increasing the ductility of HSC, while also allowing for increased tensile capacity. High-strength reinforcement shows higher strength but unique stress-strain characteristics when compared to conventional steel.
- Several researchers have investigated the blast behaviour of reinforced concrete columns. Conclusions are conflicting on the benefit of seismic detailing on blast performance. A review of the literature reveals a need for further blast studies, particularly in the case of columns built with HSC having strengths greater than 60 MPa.
- Several studies have focused on the dynamic response of SFRC structures under impact and blast loads. In general, the research demonstrates benefits associated with the use of fibers in structures subjected to impact or blast. However, limited studies have been conducted on columns and there is a need for further data, particularly in the case of structural members built with high-strength fiber-reinforced concrete.
- A limited number of studies have examined the effect of high-strength steel in structural members subjected to blast loads, with results from slab testing indicating the ability of high-strength bars to increase blast resistance. The review of the literature reveals a need for additional experiments, with no existing studies on use of high-strength bars in high-strength concrete columns. The characteristics of these materials in terms of high ultimate capacity but limited ductility should be further examined against the effects of blast loads.
- Research on the combined use of high-performance materials such as high-strength steel and high-performance concrete shows the great potential of these materials for improving blast performance. The high-strength properties of HSC and MMFX reinforcement are well suited as their properties can be balanced potentially allowing for increased blast resistance, while the use of steel fibers can potentially allow for greater ductility – further research is needed, particularly in the case of columns.

CHAPTER 3. EXPERIMENTAL PROGRAM

3.1 Chapter Overview

This research study examines the blast performance of high-strength concrete columns tested using the shock-tube facility at the University of Ottawa. Seventeen columns were designed, constructed, and tested in this experimental program. Different column configurations were designed to examine the effects of different parameters on blast behaviour. The parameters investigated included the effect of concrete strength, longitudinal steel reinforcement ratio, steel reinforcement type (normal vs. high-strength), steel fibers, steel fiber content and seismic detailing.

This chapter provides a detailed description of the experimental program, including: specimen specifications, materials used, specimen construction, experimental setup, and test procedure.

3.2 Specimen Specifications

A total of seventeen columns were constructed and tested under blast loads in this experimental program. Three different concrete types and two grades of longitudinal steel reinforcement were considered. The specimens included two columns with normal-strength concrete (NSC), eight with high-strength concrete (HSC) and seven with high-strength fiber-reinforced concrete (HSFRC). Among the specimens, ten were constructed with normal-strength steel (NSS) bars, with seven columns designed with high-strength steel (MMFX) bars. For the HSFRC series, two steel fiber contents of 0.5% and 1.0% by volume of concrete (39 and 78 kg/m^3) were considered.

All columns had the same dimensions; the cross-section was equal to 152.4 mm x 152.4 mm (6 in. x 6 in.) with a total height of 2438 mm (8 ft.). The size of the columns was dictated by the capacity of the shock-tube. The longitudinal reinforcement included four identical steel bars to produce symmetrically reinforced columns. Varied bar sizes were used in the columns to examine the effect of normal-strength and high-strength reinforcement ratio (Canadian size 10M and 15M bars; American size #3, #4 and #5 bars). To ensure the full development of the reinforcement into the support regions, the four longitudinal bars were equipped with 90° hooks extending 75 mm into each extremity. Steel cages were assembled so that a clear concrete cover of 5 mm was provided to the columns all around. Transverse reinforcement consisted of closed square hoops made of 6.3 mm smooth steel wires. The tie spacing (s) followed the provisions of CSA-A23.3-14 Standard, with either “non-seismic” detailing with s = 75 mm (moderately ductile columns), or “seismic” detailing with s = 38 mm (ductile columns).

The specimens can be divided into five categories depending on the types of concrete and steel used for their construction. The normal-strength concrete series (NSC), the high-strength concrete (HSC) series with normal-strength steel (NSS), the high-strength fiber-reinforced concrete (HSFRC) series with normal-strength steel (NSS), the high-strength concrete (HSC) series with high-strength steel (MMFX), and finally the high-strength fiber-reinforced concrete (HSFRC) series with high-strength steel (MMFX). Table 3-1 shows a summary of the specimens' configurations for each series. The nomenclature of the specimens was based on the following logic:

CONCRETE TYPE – FIBER CONTENT (%) – STEEL TYPE – RIENFORCING BAR SIZE - SEISMIC

For example, HSC-0%-NSS-10M is the ID for the column cast with high-strength concrete, 0% fibers (i.e. plain HSC), and constructed with normal-strength steel (NSS) longitudinal reinforcement consisting of 4 - 10M bars. It should be noted that a letter "S" was added to the nomenclature of the columns with seismic detailing (spacing of hoops, s = 38 mm), where in this research only two columns were given that type of detailing.

Table 3-1 Specimen matrix

Series	Specimen ID	Concrete type	Fiber content (%)	Steel type	Bar size	Reinf. ratio (%)	Transverse reinf.
NSC	NSC-0%-NSS-#4	Normal-strength	0	Normal-strength	#4	2.22	Non-seismic (s = 75 mm)
	NSC-0%-NSS-15M				15M	3.44	
HSC-NSS	HSC-0%-NSS-10M	High-strength			10M	1.72	
	HSC-0%-NSS-10M-S						Seismic (s =38 mm)
	HSC-0%-NSS-#4				#4	2.22	Non-seismic (s = 75 mm)
	HSC-0%-NSS-15M				15M	3.44	
HSFRC-NSS	HSC-0.5%-NSS-10M		0.5		10M	1.72	
	HSC-1%-10M-NSS		1				
	HSC-1%-NSS-#4				#4	2.22	
	HSC-1%-NSS-15M				15M	3.44	
HSC-MMFX	HSC-0%-MMFX-#3		0	High-strength	#3	1.22	
	HSC-0%-MMFX-#4				#4	2.22	
	HSC-0%-MMFX-#4-S						Seismic (s = 38 mm)
	HSC-0%-MMFX-#5				#5	3.44	Non-seismic (s = 75 mm)
HSFRC-MMFX	HSC-1%-MMFX-#3		1		#3	1.22	
	HSC-1%-MMFX-#4				#4	2.22	
	HSC-1%-MMFX-#5				#5	3.44	

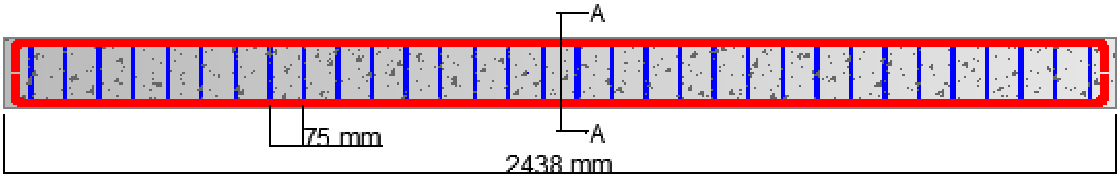

Column with non-seismic detailing

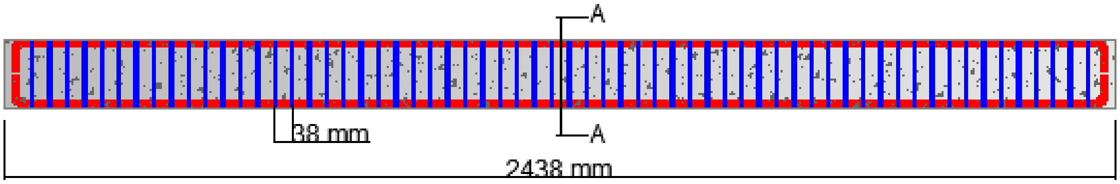

Column with seismic detailing

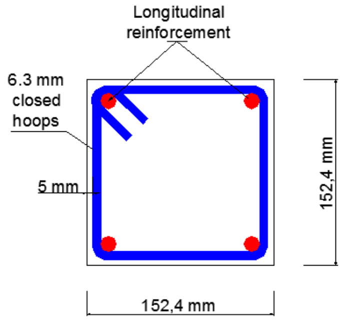

Section A-A

Figure 3-1 Specimen dimensions

3.2.1 NSC Series

The specimens in this series are also referred to as the control specimens. Conventional materials were used to build these specimens. The two specimens were: NSC-0%-NSS-#4 and NSC-0%-NSS-15M. They were both built with conventional normal-strength concrete and conventional normal-strength steel with varied bar sizes (#4 and 15M).

3.2.2 HSC-NSS Series

This series included four specimens cast with plain high-strength concrete (no fibers). Steel bars were of normal-strength and varied bar sizes (10M, #4 and 15M). Only one specimen was assembled with seismic details while the other three had non-seismic details. Specimens included were: HSC-0%-NSS-10M, HSC-0%-NSS-10M-S, HSC-0%-NSS-#4, and HSC-0%-NSS-15M.

3.2.3 HSFRC-NSS Series

This series consisted of four specimens built with high-strength fiber-reinforced concrete (HSFRC). Three of the specimens in this series contained a steel fiber content of 1% of the total concrete volume, while only one specimen contained a steel fiber ratio of 0.5% of the total concrete volume. As for steel, they were all constructed using normal-strength steel with varied bar sizes

(10M, #4 and 15M). The specimens were as follows: HSC-0.5%-NSS-10M, HSC-1%-NSS-10M, HSC-1%-NSS-#4, and HSC-1%-NSS-15M.

3.2.4 HSC-MMFX Series

This series consisted of four specimens. Plain high-strength concrete was used again to cast these specimens; however, the specimens were designed with high-strength steel bars (MMFX) with varied bars sizes (#4 or #5). Seismic detailing was also provided to one of the specimens, while the other three were given non-seismic details. Specimens in this series included: HSC-0%-MMFX-#3, HSC-0%-MMFX-#4, HSC-0%-MMFX-#4-S, and HSC-0%-MMFX-#5.

3.2.5 HSFRC-MMFX Series

The final series included three specimens. Concrete used was of high-strength with a steel fiber volumetric ratio of 1% (HSFRC). MMFX high-strength steel bars were used for the longitudinal reinforcement with varied bar sizes (#4 or #5). Specimens of this series included: HSC-1%-MMFX-#3, HSC-1%-MMFX-#4, HSC-1%-MMFX-#5.

3.3 Materials

This section describes the materials used for the construction of the specimens. Materials discussed include: Concrete type, steel reinforcement, and steel fibers.

3.3.1 Concrete

Three different types of concrete were used for the casting of the specimens in this research: Normal-strength concrete (NSC), high-strength concrete (HSC), and high-strength fiber-reinforced concrete (HSFRC). All concrete was cast at the University of Ottawa.

The normal-strength concrete (NSC) mix was used to cast two columns in this study. The concrete used was of a simple mix design, with a target compressive strength of 35 MPa. The mix components included: Portland cement, course aggregates (19 mm), sand, and water. Table 3-2 shows the mix design quantities used per cubic meter of concrete volume. Actual compressive strength developed using this mix was approximately 40 MPa.

Table 3-2 Mix design for NSC

Component	Content (kg/m^3)
Cement	300
Course aggregate	1200
Sand	600
Water	180

The two other types of concrete used were high-strength concrete (HSC) and high-strength fiber-reinforced concrete (HSFRC). The only difference between the two types is the addition of steel fibers to the concrete mix in the case of HSFRC. The mix design implemented was developed at the structural lab of the University of Ottawa to achieve a target compressive strength of 90-100 MPa. The components for the HSC mix included: cementitious materials (Portland cement, slag, silica fume), course aggregate (9.53 mm), sand, water and liquid admixtures. For the HSFRC columns, the same mix design is used except for the addition of the assigned steel fibers ratio to the mix (0.5% or 1.0%, by volume of concrete). To ensure adequate workability and setting time, liquid admixtures consisting of a super-plasticizer (MasterGlenium 7500) and set-retarder (MasterSet R 100) were added to the mixes (Both admixtures are a product of BASF). The addition of steel fibers reduces workability and results in more difficult concrete placement. Therefore, in some cases, the quantities of these admixtures were increased at low increments as needed to overcome difficulties faced while casting. Table 3-3 shows the mix properties for the HSC and HSFRC types used in this research.

Table 3-3 Mix design for HSC and HSFRC

Component	Content (kg/m^3)
Cement	373
Slag	164
Silica Fume	48
Course aggregate	1120
Sand	740
Water (w/c = 0.3)	175.5
Super-plasticizer	5.85
Set-retarder	1.93
Steel Fibers (1% or 0.5%)	78 or 39

3.3.2 Steel Reinforcement

Three types of steel reinforcement were used in this experimental program. These types included: normal-strength steel (NSS), high-strength steel (MMFX) and non-deformed steel wires. Three coupons for each steel type and bar size were tested using a GALDABINI Universal Testing Machine to determine their tensile stress-strain relationships (Figure 3-2). Stress-Strain relationships obtained for all the samples tested are shown in Figure 3-3. Additionally, Table 3-4 displays the designations, diameters, cross-sections and average strains and stresses at yield, ultimate and rupture for each bar type. Finally, Figure 3-4 shows typical stress-strain relationships for each size of each type tested.

The non-deformed smooth wires were exclusively used in the fabrication of the transverse ties and had a diameter of 6.3 mm with a cross-sectional area of 31 mm^2.

The normal-strength steel bars were used as longitudinal reinforcement for ten columns in this study. Three different bar sizes were employed in the specimens: 10M, #4, and 15M. The American #4 bars have an intermediate size when compared to the Canadian 10M and 15M bars.

The high-strength steel used in this research is referred to as MMFX, which stands for "Microcomposite Multistructural Formable Steel". This proprietary high-strength steel is produced by MMFX Technologies Corporation. It is described as an uncoated, corrosion-resistant, low-carbon chromium-steel alloy conforming to the requirements of ASTM A1035 (ASTM A1035/A1035M-11 ,2011). It has high tensile strength but with reduced ductility. Three bar sizes from this type of steel were used: #3, #4, and #5 American size bars. The stress-strain relationships derived for this bar type do not show a well-defined yield point and exhibits more of a roundhouse curve, therefore the 0.2% offset method was used to determine the yield strains and stresses for this steel type.

Table 3-4 Steel reinforcement mechanical properties

Bar	Type	Diameter (mm)	Area (mm^2)	Yield		Ultimate		Rupture
				Strain ε_y	Stress f_y (MPa)	strain ε_u	stress f_u (MPa)	strain ε_r
6.3 wire	Non-deformed NSS	6.4	32	0.0028	542	0.0844	594	0.0885
10M	NSS	11.3	100	0.0026	474	0.1602	582	0.2232
#4	NSS	12.7	129	0.0027	464	0.1152	695	0.1226
15M	NSS	16.0	200	0.0026	449	0.1386	596	0.2167
#3	MMFX	9.5	71	0.0070	987	0.0516	1276	0.0715
#4	MMFX	12.7	129	0.0065	889	0.0554	1195	0.0652
#5	MMFX	15.9	200	0.0061	821	0.0567	1132	0.0749

Figure 3-2 GALDABINI Universal Floor Standing Testing Machine used for steel coupons

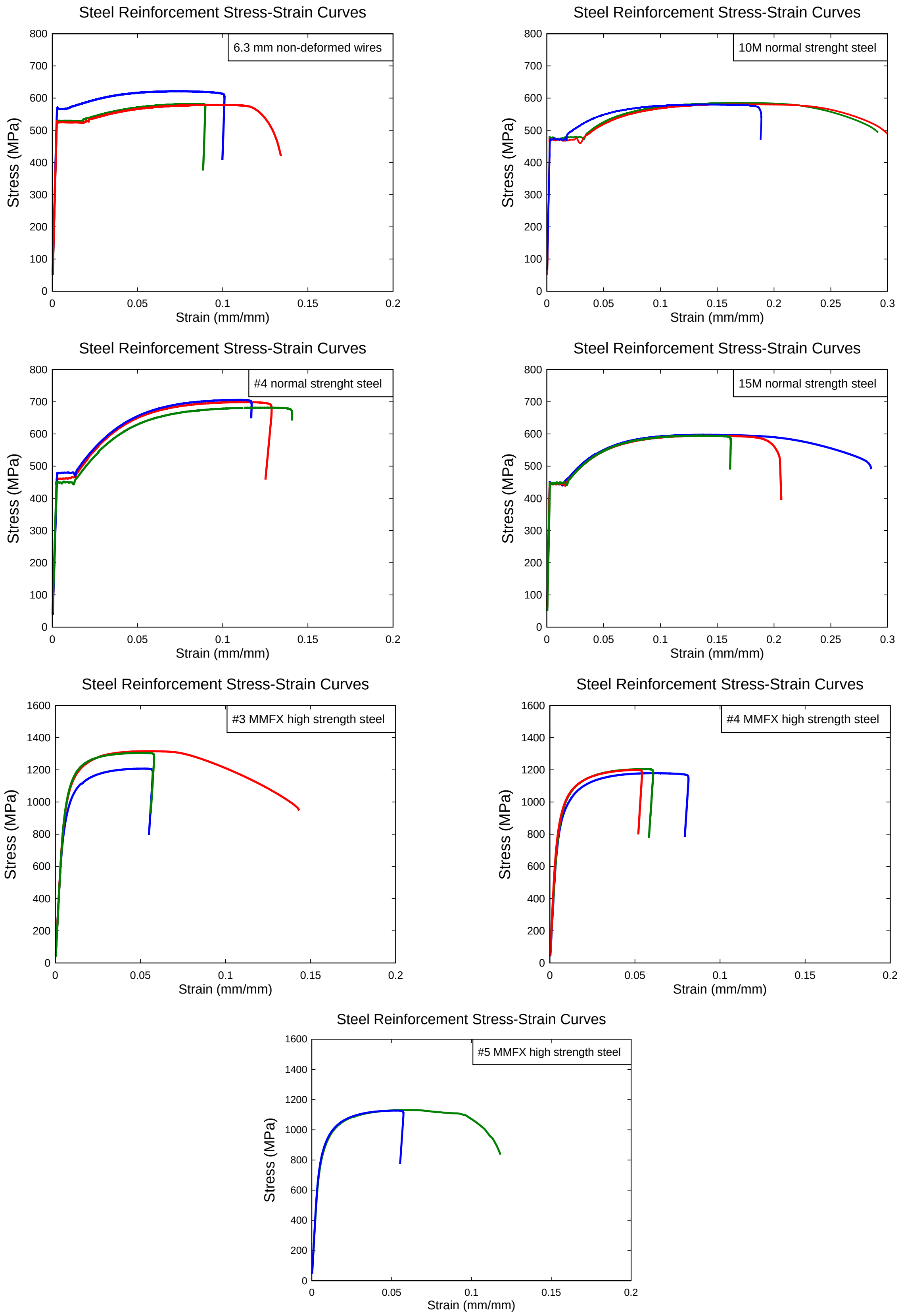

Figure 3-3 Steel reinforcement stress-strain relationships (3 coupons/bar size)

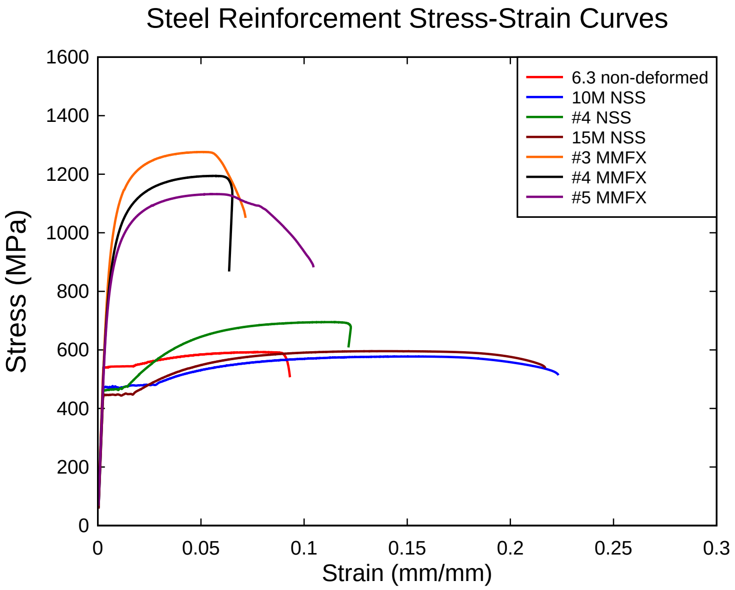

Figure 3-4 Average steel reinforcement stress-strain relationships

3.3.3 Steel Fibers

Only one type of steel fiber was used in this experimental program. The ZP fibers are hook-end steel fibers manufactured by BEKAERT under the Dramix ZP305 (3D) brand (Figure 3-5). The properties of the steel fibers used are listed in Table 3-5. Among the seven HSFRC specimens, only one had a steel fibers ratio of 0.5% to the total concrete volume (39 kg/m^3), whereas the rest had a steel fibers ratio of 1% (78 kg/m^3).

Table 3-5 Steel fibers properties

Fiber ID	ZP
Fiber name	ZP 305
Length l_f (mm)	30
Diameter d_f (mm)	0.55
Aspect ratio (mm/mm)	55
Tensile strength (MPa)	1350

Figure 3-5 ZP 305 steel fibers

3.4 Construction of Test Specimens

The test specimens were constructed at the University of Ottawa structural lab. Completion of the process included: Construction of the formwork, fabrication of transverse hoops, bending of the longitudinal reinforcement extremities, assembly of the steel cages, applying strain gauges, casting and curing of the specimens. Fresh state properties and hardened state properties were also examined during the process.

3.4.1 Preparation and Casting

The formwork used were constructed using 1219 x 2238 mm (4 x 8 ft.) plywood sheets with a thickness of 19 mm (3/4 in.). Pieces were cut and assembled accordingly to produce the designated shape shown in Figure 3-6 (f). Form oil was applied on the bottom and sides of the formwork to allow the easy removal of the columns when hardened, and to help preserve the formwork with a relatively good condition for it to be reused as needed.

Transverse hoops were made of 6.3 mm non-deformed steel wires. Wires were cut to pieces of 770 mm in length, and then three 90° and two 135° bents were applied on the cut pieces using a hand bending jig designed to produce the hoops shown in Figure 3-6 (a). The hoops specifications and the formwork dimensions allow for obtaining the 5-mm clear concrete cover required for the columns. As for the longitudinal steel reinforcement, bars were cut to the desired lengths and then bent at 90° angles at each extremity to ensure the full development of hooks within the supports. Next, transverse hoops were tied to the longitudinal reinforcement using quick tie wires and the steel cages shown in Figure 3-6 (d-e) were assembled. The spacing of hoops was set at 75 mm in the case of columns with non-seismic detailing, while columns with seismic detailing followed a spacing of 38 mm (Figure 3-6 (c)). Finally, strain gauges were installed at mid-span after having their locations smoothed using a hand-held belt-grinder (Figure 3-6 (b)).

After getting steel cages ready within the formwork, preparation for casting began. Materials needed for mixes were pre-weighted and emptied into the pan mixer. The pan mixer used is a 420-volt electric multi-flow pan mixer with a 225L (8 cu. ft.) mix capacity available at the University of Ottawa structural lab (Figure 3-6 (g)). After being properly mixed, concrete was poured into the formwork containing the steel cages. To ensure a uniform placement of concrete, a 1-in. diameter vibrator was used during casting. After casting, the column surfaces were levelled and finished. Finally, the specimens were covered with wet burlap and plastic sheets and were cured for a seven-day period. After the seventh day, curing sheets were removed and the specimens were air-cured until testing date.

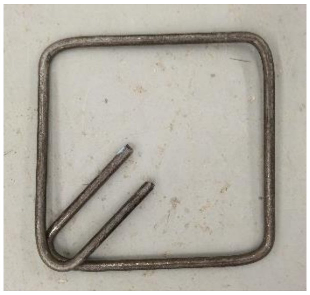

a) Transverse hoop

b) Strian gauges at the middle of the bars

c) Seismic detailing vs. non-seismic detailing

d) NSS cages

e) MMFX cages

f) Prior to casting

g) Concrete during mixing

Figure 3-6 Preparation of test specimens

3.4.2 Fresh State Properties

Slump tests were performed according to the ASTM C143 “Standard Test Method for Slump of Hydraulic-cement Concrete”. The slump cone mold was filled with fresh concrete in three layers, where each layer was compacted 25 times using a circular metal rod. After filling the cone, the cone mold is lifted, reversed upside down with the metal rod placed on top of it, and then the slump is measured as the vertical distance between the top of the mold and the top of the consolidated concrete as the standard requires.

Table 3-6 provides the summary of slump test results for each batch of concrete mixed. Figure 3-7 also shows typical slumps for each type of concrete used in this research. Normally, slump should be lower for fiber-reinforced concrete when compared to plain concrete due to the stiffness of the fibers which render the FRC mix less workable. However, in this study, increased increments of super-plasticizer were added as needed to allow for more flowable and workable fiber-reinforced concrete. Therefore, the slump results do not always follow a clear trend when comparing the HSC and HSFRC batches. In general, regardless of slump, additional vibration was required to ensure uniform placement of HSFRC in the confined formwork space.

Table 3-6 Summary of slump results

Specimen ID	Concrete type	Fiber content (%)	Slump (mm)
NSC-0%-NSS-#4	NSC	0	130
NSC-0%-NSS-15M	NSC	0	130
HSC-0%-NSS-10M	HSC	0	150
HSC-0%-NSS-10M-S	HSC	0	150
HSC-0%-NSS-#4	HSC	0	130
HSC-0%-NSS-15M	HSC	0	130
HSC-0.5%-NSS-10M	HSFRC	0.5	180
HSC-1%-10M-NSS	HSFRC	1	60
HSC-1%-NSS-#4	HSFRC	1	150
HSC-1%-NSS-15M	HSFRC	1	190
HSC-0%-MMFX-#3	HSC	0	100
HSC-0%-MMFX-#4	HSC	0	N/A
HSC-0%-MMFX-#4-S	HSC	0	200
HSC-0%-MMFX-#5	HSC	0	210
HSC-1%-MMFX-#3	HSFRC	1	N/A
HSC-1%-MMFX-#4	HSFRC	1	200
HSC-1%-MMFX-#5	HSFRC	1	160

NSC *HSC* *HSFRC*

Figure 3-7 Typical slumps for each concrete type

3.4.3 Hardened State Properties

Hardened concrete properties (compressive strength and flexural strength) were examined using concrete cylinders and flexural beams obtained from each batch of concrete (samples followed the same curing conditions as the specimens).

3.4.3.1 Cylinders Tests

A minimum of three cylinders with a diameter of 100 mm and a height of 200 mm were cast from each batch of concrete. The cylinders were tested to determine their 28th day average compressive strength (f'_c) using a 1000 kN PILOT Control System cylinder testing machine in accordance with ASTM C39 "Standard Test Method for Compressive Strength of Cylindrical Concrete Specimens". Summary of cylinders' compressive strengths are shown in Table 3-7. Figure 3-8 also shows photographs at failure for each type of concrete. Cylinders were also examined to determine the compressive stress-strain relationships for each type of concrete. Instrumentation to record the curves shown in Figure 3-9 included an extensometer with 140 mm gage length attached to the cylinders to capture axial strains. Cylinders made of plain HSC showed brittle and more explosive failures once maximum stresses was exceeded. In contrast, for the HSFRC cylinders, the provision of fibers prevented brittle failure and provided a post-peak phase in the stress-strain curve, resulting in increased ductility. These behaviours can be seen in Figure 3-9.

Table 3-7 Concrete compressive strength summary

Specimen ID	Concrete type	Fiber content (%)	Cylinders compressive strength (MPa)			
			#1	#2	#3	Avg.
NSC-0%-NSS-#4	NSC	0	38.72	42.40	-	40.56
NSC-0%-NSS-15M	NSC	0	38.72	42.40	-	40.56
HSC-0%-NSS-10M	HSC	0	93.54	99.05	89.24	93.94
HSC-0%-NSS-10M-S	HSC	0	93.54	99.05	89.24	93.94
HSC-0%-NSS-#4	HSC	0	80.42	80.01	93.62	84.68
HSC-0%-NSS-15M	HSC	0	80.42	80.01	93.62	84.68
HSC-0.5%-NSS-10M	HSFRC	0.5	96.57	95.43	88.68	93.56
HSC-1%-10M-NSS	HSFRC	1	89.95	96.75	-	93.35
HSC-1%-NSS-#4	HSFRC	1	101.42	91.57	95.17	96.05
HSC-1%-NSS-15M	HSFRC	1	99.40	106.88	95.07	100.45
HSC-0%-MMFX-#3	HSC	0	111.05	103.80	95.91	103.59
HSC-0%-MMFX-#4	HSC	0	64.63	76.56	67.11	69.43
HSC-0%-MMFX-#4-S	HSC	0	87.55	87.36	98.93	91.28
HSC-0%-MMFX-#5	HSC	0	85.79	82.07	96.26	88.04
HSC-1%-MMFX-#3	HSFRC	1	89.48	85.79	89.22	88.16
HSC-1%-MMFX-#4	HSFRC	1	77.65	82.38	76.19	78.74
HSC-1%-MMFX-#5	HSFRC	1	86.35	88.35	94.63	89.78

NSC *HSC* *HSFRC 0.5%* *HSFRC 1%*

Figure 3-8 Typical concrete cylinder failure for each type

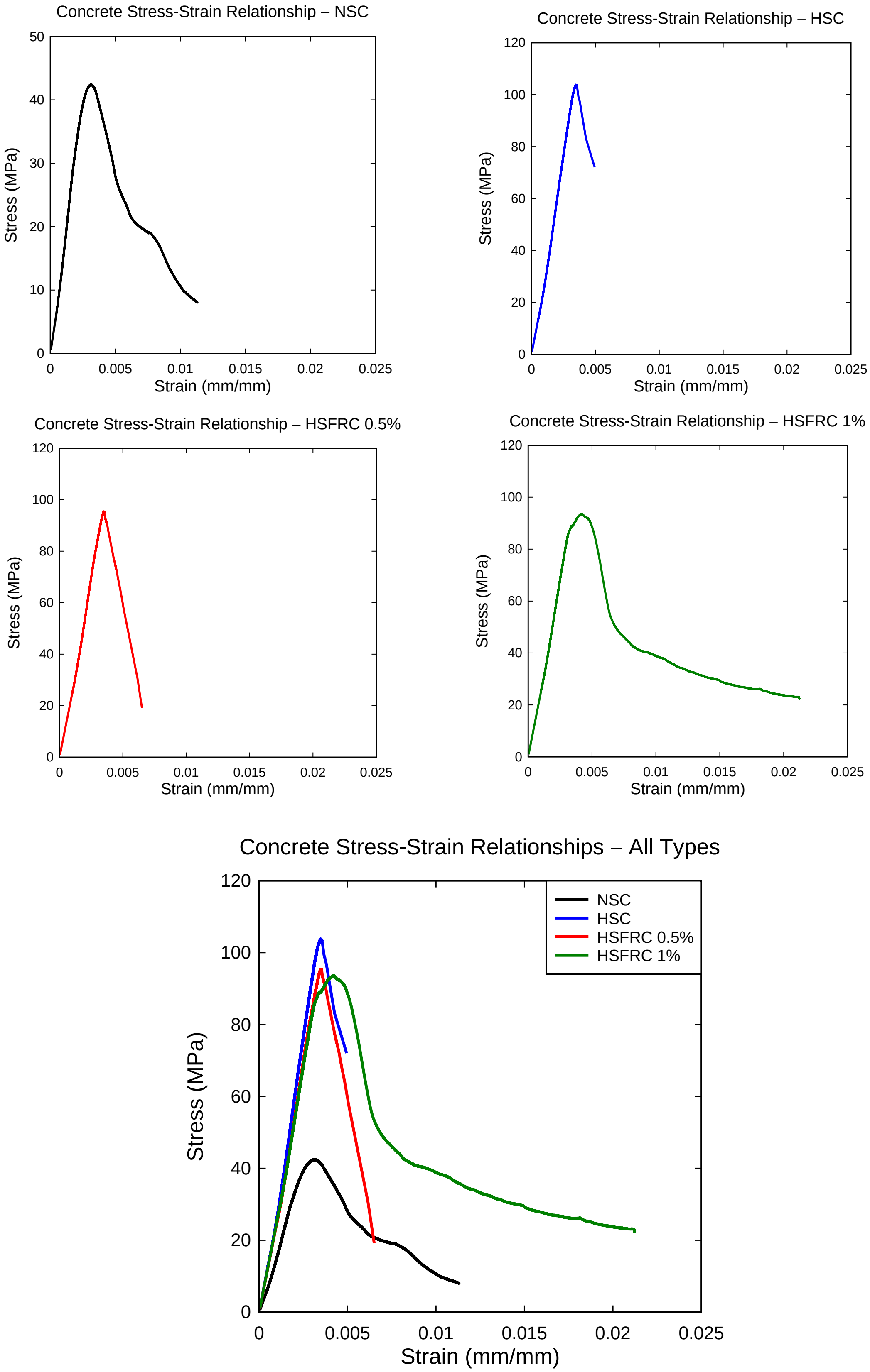

Figure 3-9 Typical compressive stress-strain relationships for each type of concrete

3.4.3.2 Flexural Beams

Flexural beams (prisms) were also cast from each batch of concrete to be tested under four-point bending according to ASTM C1609 “Standard Test for Flexural Performance of Fiber-Reinforced Concrete (Using Beam with Third-Point Loading)” to determine their flexural toughness. Flexural beams dimensions were 100 mm x 100 mm x 400 mm as required by the standard. The testing was conducted over a span of 300 mm, under a constant loading rate of 0.075 mm/min. A “yoke” and a LVDT were used to measure the deflection at mid-span as required by ASTM C1609. The test setup is shown in Figure 3-10. Results of the flexural toughness tests for each type of concrete are also summarized in Table 3-8, and typical load-deformation curves obtained are provided in Figure 3-11. Typical behaviour of the prisms showed a brittle failure for the NSC and HSC types at the instance of first cracking. As for the HSFRC beams, the presence of fibers allowed for tensile capacity beyond first-cracking, resulting in post-cracking ductility and enhanced flexural toughness when compared to the plain HSC. The use of 1% fibers allowed for strain-hardening response, where peak strength exceeds the first cracking strength.

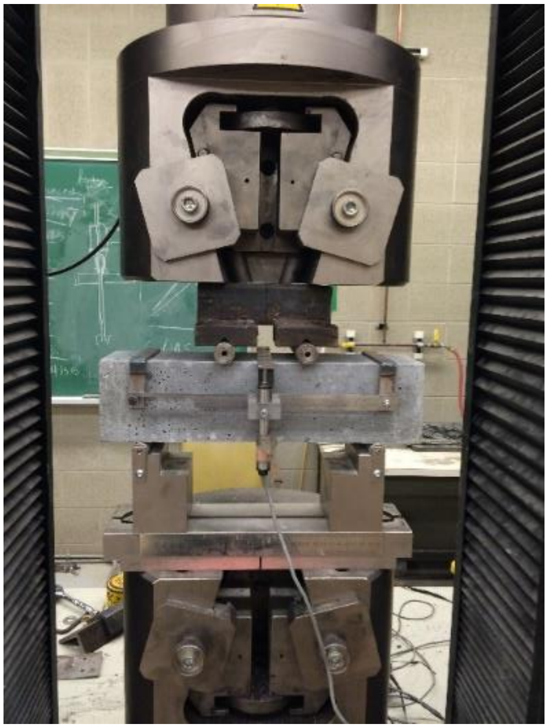

Figure 3-10 Flexural beam testing setup

Table 3-8 ASTM C1609 flexural toughness tests summary

Concrete type	ASTM C1609										
	P_1	δ_1	P_p	δ_p	f_1	f_p	P_{600}	f_{600}	P_{150}	f_{150}	T_{150}
NSC	16.88	0.04	16.88	0.04	5.06	5.06	-	-	-	-	-
HSC	27.07	0.04	27.07	0.04	8.12	8.12	-	-	-	-	-
HSFRC 0.5%	25.51	0.05	25.51	0.05	7.65	7.65	21.53	6.46	5.19	1.56	22.48
HSFRC 1%	27.88	0.05	33.30	0.30	8.36	9.99	28.33	8.50	9.31	2.79	39.18

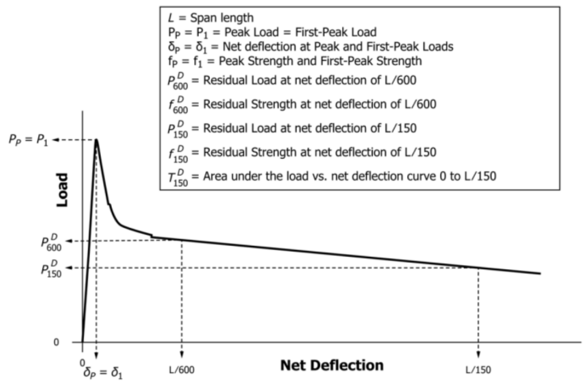

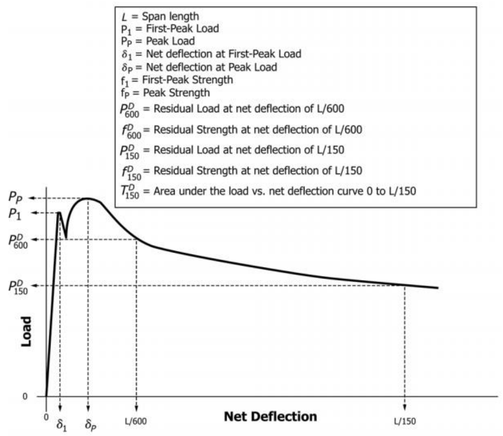

Where:
L = Span Length (300 mm), (L/600 = 0.5, L/150 =2)
P_1= First-Peak Load (kN)
δ_1= Net Deflection at First-Peak Load (mm)
P_p= Peak Load (kN)
δ_p= Net Deflection at Peak Load (mm)
f_1= First-Peak Strength (MPa)
f_p= Peak Strength (MPa)
P_{600}= Residual Load at net deflection of L/600 (kN)
f_{600}= Residual Strength at net deflection of L/600 (MPa)
P_{150}= Residual Load at net deflection of L/150 (kN)
F_{150}= Residual Strength at net deflection of L/150 (MPa)
T_{150}= Area under load vs. net deflection curve (0 to L/150), (kN*mm)
FT = Flexural Toughness Factor = $(T_{150}*L)/(L/150 *b*d^2)$

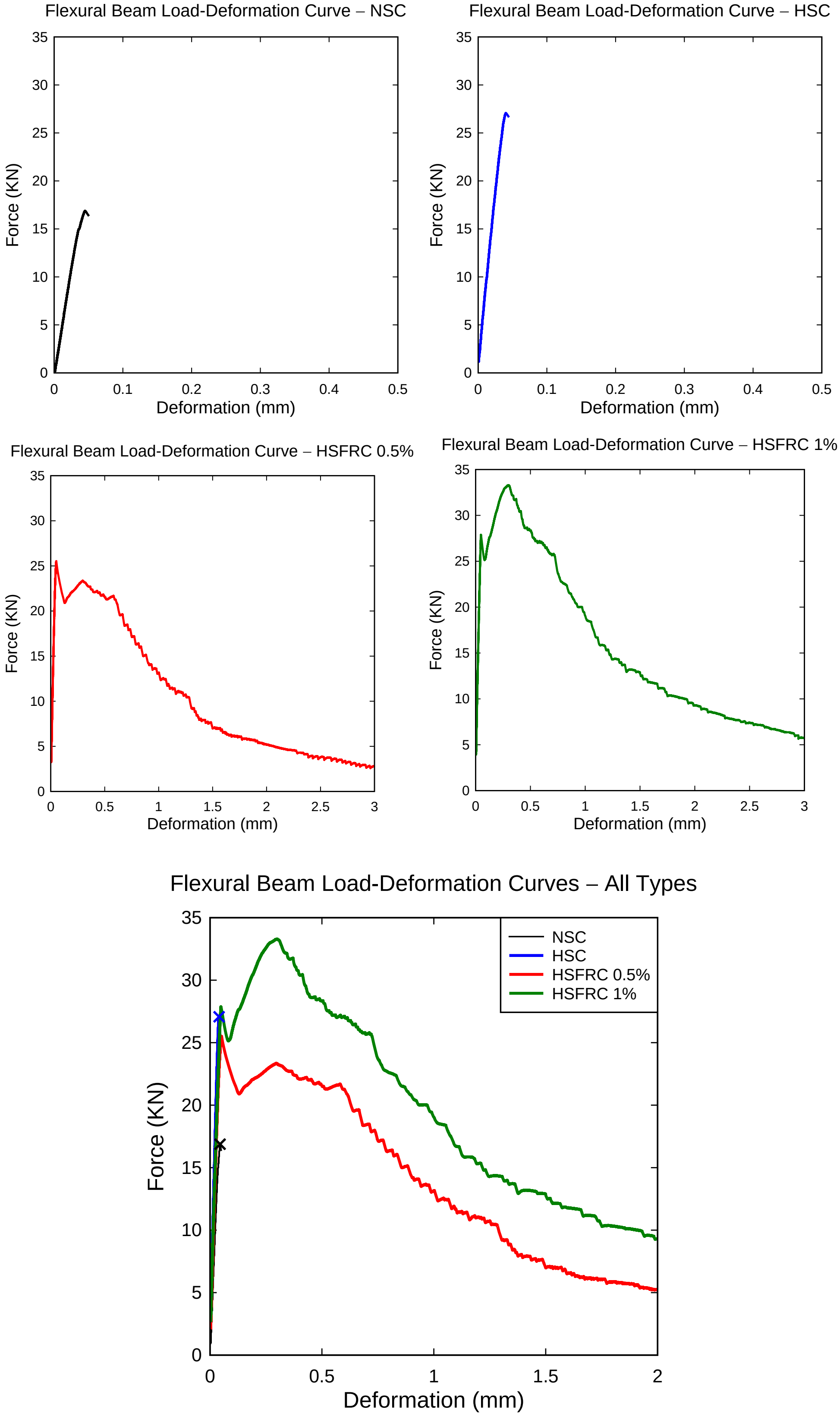

Figure 3-11 Typical flexural beam load-deflection curves

3.5 Experimental Setup

The following section describes the details of the experimental setup. All columns were tested using the shock-tube, under a combined effect of axial loads and transverse simulated blast loads. The elements of the test setup include: Description of the shock-tube, the load transfer device (LTD), specimen setup (supports and axial load), and the instrumentation used.

3.5.1 Shock-Tube

The shock-tube facility available in the structural lab at the University of Ottawa is capable of simulating far-range hemispherical shock waves. It consists of four main components: the variable length driver, the spool section, the expansion chamber, and the rigid-end test frame (Figure 3-12).

The rear portion of the shock-tube is responsible for the pressure waves generated. It has a 597-mm diameter circular cross-section and divided into two parts that are used to build up the pressures needed; the variable length driver and the spool section. The driver length varies from 305 mm (1 ft.) to 5158 mm (17 ft.) and controls the positive phase duration of the shock wave. In this research, the driver length was set to 2743 mm (9 ft.) throughout all the tests. The second part which is the spool is used to build up pressure inside the shock-tube and can be controlled to generate the pressure differential required to trigger the blast wave. A double-diaphragm firing system composed of two sets of aluminum sheets with specified gauge lengths is used to contain the air being pumped. One set is placed between the driver and the spool, and the second one is placed between the spool and the expansion chamber.

Air is pumped into both sides (the driver and the spool) simultaneously and kept within the resistance limit of the aluminum sheets installed. Once the desired pressure is reached, the air in the spool section is drained. This process will lead to a differential pressure higher than the resistance capacity of the aluminum sheets and thus their rupture. The rapid release of compressed air travels through the expansion chamber to reach the end test frame, where the specimen is attached. The expansion chamber starts with a circular cross-section of 597 mm and increases over a length of 6096 mm (20 ft.) to a 2032 mm square opening at the end frame. The square opening is covered with a load transfer device (LTD) to transfer the loads to the tested specimen and (LTD used is described in the next section).

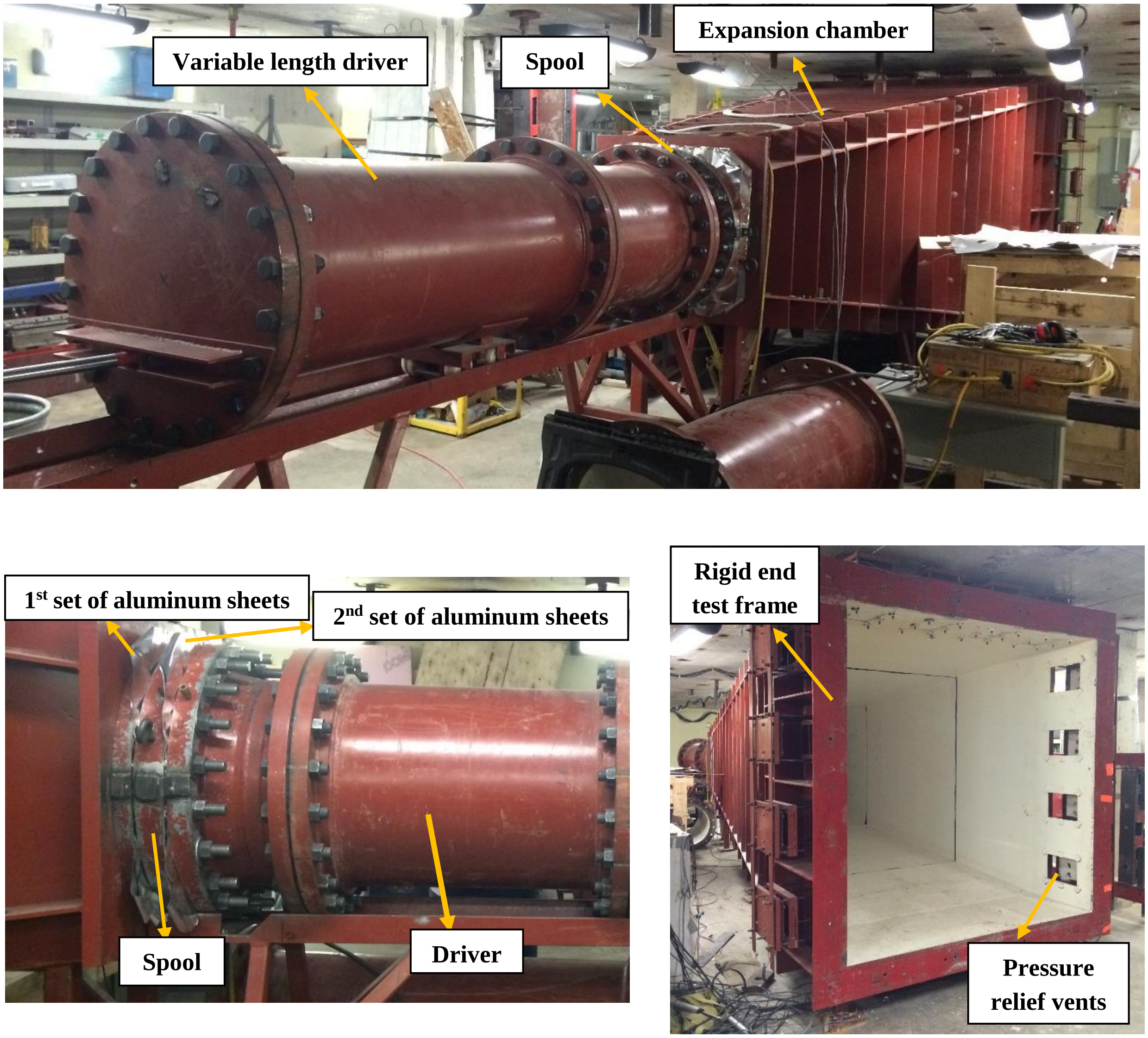

Figure 3-12 University of Ottawa shock-tube's components

3.5.2 Load Transfer Device (LTD)

As mentioned previously, the end test frame consists of a square opening of 2032 x 2032 mm. In the case of the non-planar structural specimens which can't cover the entire opening, a load transfer device (LTD) is required to redirect the blast wave to the tested specimen. This was the case for the columns of this experimental program. The LTD was built to cover the shock-tube's opening and uniformly distribute the load on the face of the columns.

The LTD was built with two light gauge metal sheets connected to eight hollow-section steel (HSS) beams through sets of small pieces of threaded rods and nuts. The dimensions of the metal sheets were enough to cover the shock-tube's opening. As for the HSS pieces, they were 76 x 76 x 6.35 mm spanning a length of 2438 mm along the width of the shock-tube opening and perpendicular to the specimens. Each HSS had another two short HSSs of the same cross-section welded on the top and bottom at mid-span. The short HSSs were 229 mm long and are added to ensure full contact with the tested columns (152.4 mm side length for the columns). The eight HSS sections were connected to the 0.71 mm thick metal sheets and uniformly spaced along the height of the opening. The LTD assembly had a total mass of 210 kg after construction. The LTD was connected to the shock-tube through two pins designed to go through the top HSS and into the top support that is connected to the top end frame of the shock-tube. The LTD was free to rotate through these pins as the blast wave hits. Figure 3-13 shows a picture of the finished LTD and a schematic of the blast response of the LTD used in this research.

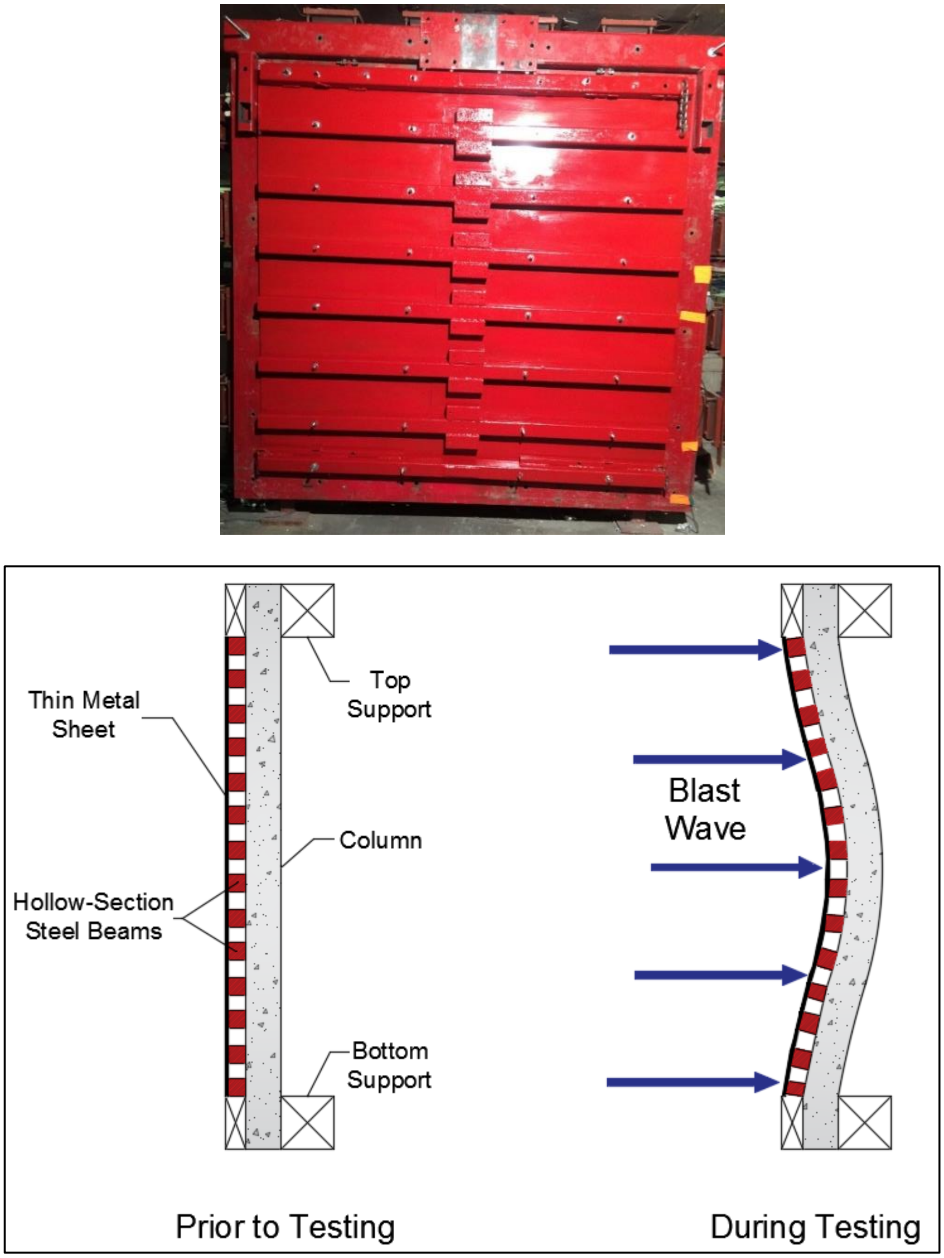

Figure 3-13 Load transfer device (LTD)

3.5.3 Specimen Setup and Instrumentation

Setting up each column required clamping the column at the top and bottom supports and applying the static axial load. Instrumentation to record the data after each shot included a data acquisition system, pressure sensors, linear variable displacement transducers (LVDT), and a high-speed video camera. Figure 3-14 shows the typical setup for a specimen prior to testing.

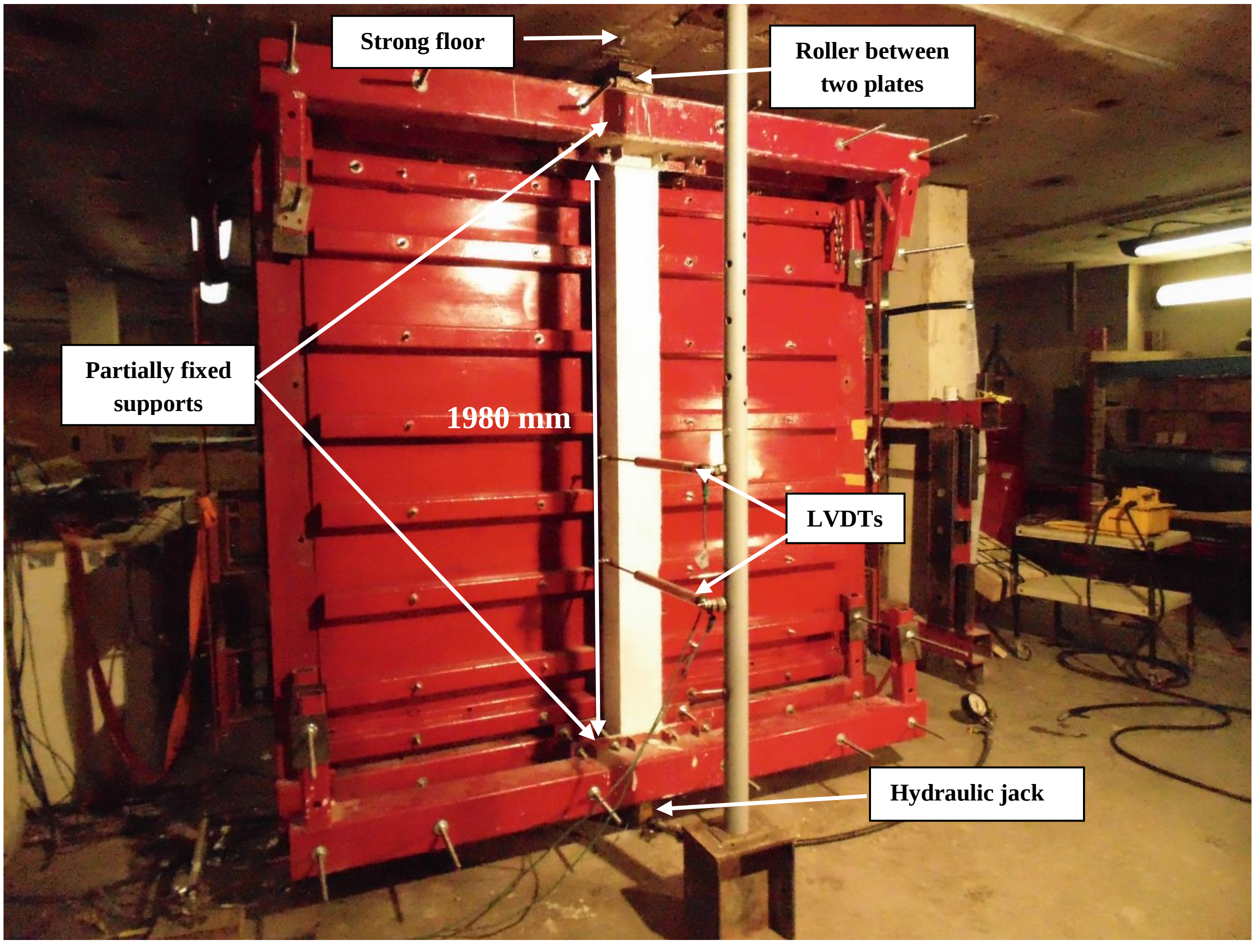

Figure 3-14 Typical test setup

3.5.4 Supports

The columns were fixed to the shock-tube using partially-fixed supports at the top and bottom. The use of these supports intended to test the columns under more realistic fixed-fixed boundary conditions similar to those of columns in actual building construction. However, based on previous experimental work, this assembly provides partial fixity (rather than full fixity), with a measured rotational stiffness of 903000 N.m/rad (Lloyd 2010). Each support (top and bottom) consists of inner and outer support pieces. Each assembly consists of a long HSS section spanning the width of the end frame, along with steel end-plates welded halfway to properly tighten the columns from both sides. The outer support beams are connected to the end-frame using twelve 15.9 mm long threaded rods (6 at each end), and then shorter rods are used to span around the columns into the end-plates to help tighten and ensure the required fixity is achieved. The dimensions of the steel plates at the supports leave the 2438 mm long columns with a clear test span of 1980 mm.

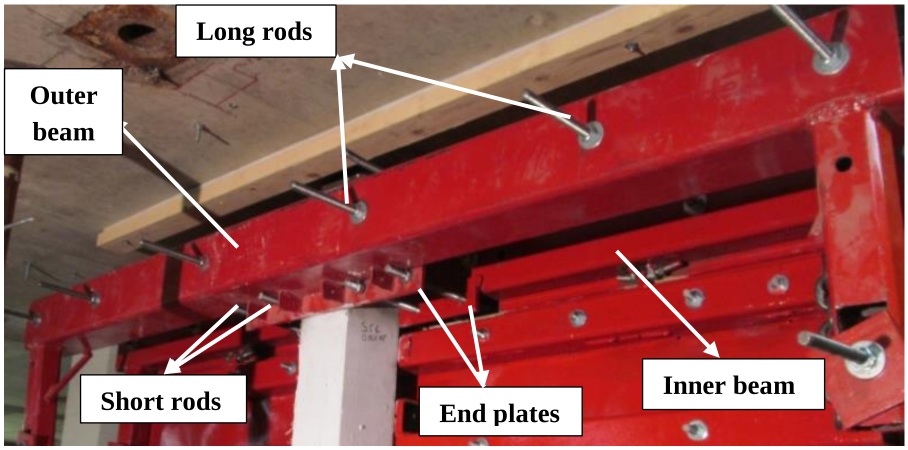

Figure-3-15 Top support

3.5.5 Axial Load Mechanism

As mentioned before, the columns were tested under the combined effect of axial and lateral loading. Application of the axial load was through a 3871 mm^2 (6 in^2) hydraulic jack positioned beneath the specimens. The column was seated on top of two steel plates with a steel roller in between, which are in turn placed on top of the hydraulic jack. Another two steel plates and a roller were placed on top of the column and shimmed to the 914-mm thick concrete strong floor above to allow for the transfer of axial load in the columns. The axial load applied at the start of testing was equal to 294 KN, which is near the maximum capacity of the pump-jack assembly and equal to around 30% of the nominal capacity of the NSC columns.

3.5.6 Data Acquisition System

A Yokogawa SL 1000 High Speed Data Acquisition Unit was used to record the data. The data recorded includes measured pressures, displacements, and strains. The machine is capable of recording 100000 samples of data per second. When set to recording, the data acquisition system continues to loop, record and constantly overwrite data until the blast occurs. At that instance, the unit is triggered and then starts saving the data over a period of 3 seconds. The data is later imported to a ".csv" file which can be examined to extract pressure and displacement data.

3.5.7 Pressure Sensors

Accurate reflected pressures are measured through two PCB Piezotronics Model #112A22 piezoelectric pressure sensors installed on the side and the bottom of the shock-tube's end frame and connected to the data acquisition unit. The sensors' readings allow the measurement of the complete pressure time-history for each blast. It is also responsible of sending the trigger signal to the unit once the blast initiates.

3.5.8 Linear Variable Displacement Transducers (LVDT)

Displacements of the columns were measured through two Celesco CLWG-300 linear variable displacement transducers (LVDT) with a stroke length of 300 mm installed at mid-span and 1/3 of the height of the columns. The displacements recorded are sent to the data acquisition system in which complete displacement time-histories could be obtained.

3.5.9 High-Speed Video Camera

An AOS Technology X-PRI high-speed camera was used to record the columns' responses during testing. The camera was positioned to capture the side-view footage of the blast tests. The camera is capable of recording full color images with an 800 x 600-pixel resolution and was set to record at 500 frames per second. The camera is launched by the same trigger that initiate the pressure sensors.

3.5.10 Strain Gauges

Two FLA-6-350-11 strain gauges were installed on the longitudinal steel bars at mid-span (on the tension face of the columns). The gauges had a length of 6 mm and a resistance of 350 ohms.

3.6 Experimental Procedure

Each specimen was tested under repeated blast loads until failure. All columns in this program were flexural-dominant; shear had no major contribution in specimens' failure. Typical failures occurred through excessive deformations, concrete damage or bar rupture. The repeated blasts for each column were gradually increased with the same increments for all columns. The driver length was kept constant (9ft), while the driver pressures for the different blast intensities were as follows: 17 psi, 35 psi, 80 psi, 100 psi, and 110 psi. Five specimens failed at 80 psi, ten failed at 100 psi, while only two survived up to the 110-psi shot. Table 3-9 lists the resulting average blast wave parameters for each blast (reflected pressure, reflected impulse and positive phase duration). Figure 3-16 also shows a typical pressure time history plot for each blast intensity.

Table 3-9 Blast test properties

Test #	Driver Pressure kPa (psi)	Driver length mm (ft.)	Avg. reflected pressure (P_r) kPa	Avg. reflected Impulse (I_r) kPa.msec	Avg. positive phase duration (t_d) msec
Blast 1	117 (17)	2743 (9)	21.78	220.0	22.12
Blast 2	241 (35)	2743 (9)	38.08	419.1	23.64
Blast 3	552 (80)	2743 (9)	70.77	802.7	26.86
Blast 4	689 (100)	2743(9)	84.41	1028.4	29.07
Blast 5	758 (110)	2743 (9)	81.81	1017.1	25.41

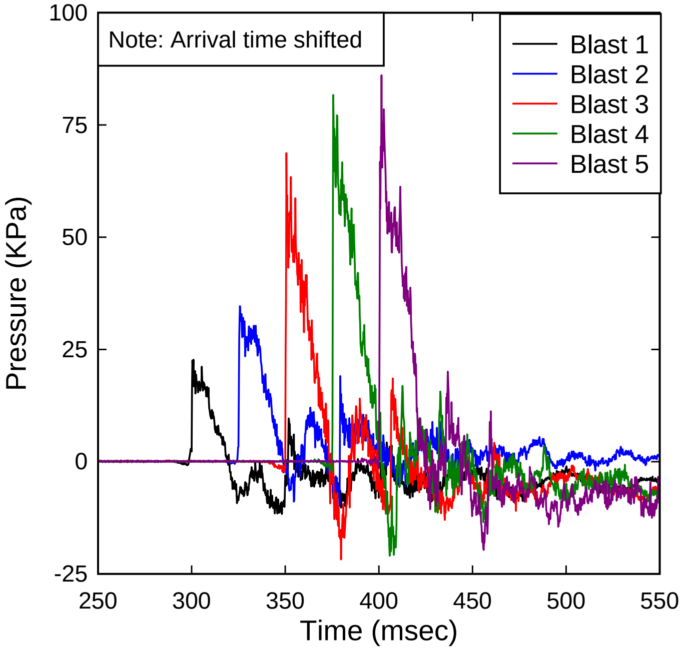

Figure 3-16 Typical pressure-time histories for blasts 1-5

CHAPTER 4. EXPERIMENTAL RESULTS

4.1 Chapter Overview

This chapter presents the detailed results of the experimental program. A full overview of the acquired data for each of the seventeen specimens tested in this research is presented. To start, a summary of results for all specimens is presented in a tabular form in section 4.2. A close look at the response of each specimen is provided in section 4.3. Elaboration of experimental results includes: providing reflected pressure and impulse properties for each test step, listing of displacement data in terms of maximum and residual, summary of strain gage data if available, discussion of damage and failure mechanisms, and finally visual demonstration of damage through selected photographs of specimens after tests.

4.2 Summary of Results

An overall summary of results is provided in Tables 4-1 to 4-5. The specimens are listed and grouped based on their series classification. The order in which specimens are discussed in the sections that follow is by series: Control NSC specimens first, then the HSC and HSFRC specimens that utilized conventional normal-strength steel, and finally the HSC and HSFRC specimens that included MMFX high-strength steel reinforcement.

The tables summarize the shockwave properties for each test, including: driver pressure (P_d), peak reflected pressure (P_r), positive phase duration (t_d), and the positive reflected impulse (I_r). Tables also list the maximum and residual mid-span displacements measured by the LVDTs (D_{max} and D_{res} respectively) and the corresponding maximum support rotations (θ_{max}). It is worth mentioning that the residual displacements in the tables are not cumulative, but the cumulative values are mentioned in section 4.3.

Reflected pressure-time histories and peak reflected pressures (P_r) were measured through a pair of pressure transducers that were installed on the end test frame of the shock-tube. They measure the approximate pressure being transferred by the LTD to the tested specimen. As for the positive reflected impulse (I_r), it is calculated through integration of the pressure-time history over the positive phase, corresponding to the first peak of the impulse time-history.

A minimum of three blasts were conducted for each specimen. Most specimens were tested under the impact of four blasts, and only two specimens were tested under five blasts. Blasts 1 and 2 were intended to test the specimens within the elastic and post-yield ranges, respectively. Blast 3, 4 and 5 were applied to cause failure in the specimens.

Table 4-1 Blast data summary: NSC series

Specimen ID	Shockwave properties					Mid-span displacements (mm)		Support rotation (Degrees)
	Blast #	P_d (kPa)	P_r (kPa)	t_d (msec)	I_r (kPa.msec)	D_{max}	D_{res}	θ_{max}
NSC-0%-NSS-#4	1	117	22.12	23.60	242.02	10.70	-	0.62
	2	241	40.34	24.40	464.30	20.47	5.50	1.18
	3	552	65.10	26.81	853.57	87.38	51.31	5.04
NSC-0%-NSS-15M	1	117	22.16	22.60	193.18	7.41	1.25	0.43
	2	241	38.90	23.02	427.61	20.01	6.71	1.16
	3	552	71.85	26.60	845.56	83.96	54.78	4.85
	4	689	83.22	32.21	1097.66	162.77	136.60	9.34

Table 4-2 Blast data summary: HSC- NSS series

Specimen ID	Shockwave properties					Mid-span displacements (mm)		Support rotation (Degrees)
	Blast #	P_d (kPa)	P_r (kPa)	t_d (msec)	I_r (kPa.msec)	D_{max}	D_{res}	θ_{max}
HSC-0%-NSS-10M	1	117	22.98	23.21	233.17	8.38	1.31	0.48
	2	241	45.11	26.40	429.13	33.64	14.69	1.95
	3	552	75.43	25.01	779.06	132.57	118.68	7.63
HSC-0%-NSS-10M-S	1	117	19.82	21.60	211.29	9.49	2.41	0.55
	2	241	41.16	24.60	377.95	20.81	4.60	1.20
	3	552	74.10	26.40	731.31	106.13	87.14	6.12
HSC-0%-NSS-#4	1	117	24.44	21.00	181.20	7.21	1.96	0.42
	2	241	39.55	23.30	462.05	20.07	7.84	1.16
	3	552	78.34	31.80	874.51	82.35	44.29	4.76
	4	689	92.28	27.81	1112.21	210.58	173.50	12.01
HSC-0%-NSS-15M	1	117	21.29	22.41	226.31	7.57	1.72	0.44
	2	241	39.01	23.01	371.78	16.02	3.41	0.93
	3	552	72.83	24.60	695.89	77.70	54.45	4.49
	4	689	87.81	33.01	997.92	141.09	117.56	8.11

Table 4-3 Blast data summary: HSFRC- NSS series

Specimen ID	Shockwave properties					Mid-span displacements (mm)		Support rotation (Degrees)
	Blast #	P_d (kPa)	P_r (kPa)	t_d (msec)	I_r (kPa.msec)	D_{max}	D_{res}	θ_{max}
HSC-0.5%-NSS-10M	1	117	24.35	25.61	227.46	9.08	1.25	0.53
	2	241	42.78	23.62	421.99	22.85	2.78	1.32
	3	552	75.43	26.81	812.73	91.41	62.13	5.28
HSC-1%-10M-NSS	1	117	23.30	22.81	216.20	7.07	0.52	0.41
	2	241	31.31	25.60	453.54	19.41	6.70	1.12
	3	552	74.45	24.66	733.85	83.78	52.85	4.84
HSC-1%-NSS-#4	1	117	21.71	21.60	222.68	7.62	2.50	0.44
	2	241	34.48	25.60	452.74	15.37	4.14	0.89
	3	552	68.33	29.84	868.87	62.73	29.11	3.63
	4	689	86.07	27.83	1010.18	153.13	130.30	8.79
HSC-1%-NSS-15M	1	117	19.22	22.40	217.40	8.07	0.41	0.47
	2	241	32.25	22.40	416.27	17.52	4.01	1.01
	3	552	63.91	25.61	752.28	54.62	34.09	3.16
	4	689	86.72	31.41	933.62	120.52	92.24	6.94

Table 4-4 Blast data summary: HSC- MMFX series

Specimen ID	Shockwave properties					Mid-span displacements (mm)		Support rotation (Degrees)
	Blast #	P_d (kPa)	P_r (kPa)	t_d (msec)	I_r (kPa.msec)	D_{max}	D_{res}	θ_{max}
HSC-0%-MMFX-#3	1	117	20.89	21.60	228.04	9.15	2.49	0.53
	2	241	37.17	22.21	420.45	18.35	3.84	1.06
	3	552	63.06	25.20	798.87	67.28	25.74	3.89
	4	689	79.97	23.83	924.40	-	-	-
HSC-0%-MMFX-#4	1	117	19.59	20.60	196.53	9.65	3.16	0.56
	2	241	35.01	22.00	442.62	16.76	3.33	0.97
	3	552	76.67	26.61	865.57	46.17	10.97	2.67
	4	689	101.14	30.41	1101.47	94.24	44.11	5.44
HSC-0%-MMFX-#4-S	1	117	23.91	21.41	219.61	6.82	2.01	0.39
	2	241	34.71	22.20	404.47	13.28	2.16	0.77
	3	552	72.20	29.97	898.82	39.95	8.88	2.31
	4	689	75.41	32.63	1086.89	84.30	19.70	4.87
HSC-0%-MMFX-#5	1	117	22.71	20.40	241.01	8.74	4.09	0.51
	2	241	34.64	25.40	476.10	17.18	2.42	0.99
	3	552	68.72	27.18	745.98	37.06	11.15	2.14
	4	689	81.69	29.34	1003.52	62.68	24.85	3.62
	5	758	86.07	25.21	984.98	182.59	147.77	10.45

Table 4-5 Blast data summary: HSFRC- MMFX series

Specimen ID	Shockwave properties					Mid-span displacements (mm)		Support rotation (Degrees)
	Blast #	P_d (kPa)	P_r (kPa)	t_d (msec)	I_r (kPa.msec)	D_{max}	D_{res}	θ_{max}
HSC-1%-MMFX-#3	1	117	23.40	21.20	254.86	12.37	2.16	0.72
	2	241	40.58	21.80	403.02	25.18	5.84	1.46
	3	552	73.98	27.60	741.43	98.92	26.02	5.71
	4	689	75.57	25.52	1003.68	516.77	516.77	27.56
HSC-1%-MMFX-#4	1	117	19.25	21.40	193.93	6.07	2.17	0.35
	2	241	38.33	24.21	417.44	13.26	3.58	0.77
	3	552	68.17	27.07	793.93	40.65	14.64	2.35
	4	689	82.32	30.42	934.35	99.02	33.80	5.71
HSC-1%-MMFX-#5	1	117	19.13	22.60	235.61	9.23	3.48	0.53
	2	241	33.43	21.63	440.86	15.59	4.36	0.90
	3	552	60.52	24.87	853.34	33.20	10.04	1.92
	4	689	78.59	25.81	1040.39	55.39	21.54	3.20
	5	758	77.55	25.60	1049.14	87.89	42.44	5.07

4.3 Discussion of Experimental Results

4.3.1 NSC Series

4.3.1.1 NSC-0%-NSS-#4

This is the first of two control columns cast with plain normal-strength concrete. This column was constructed with #4 normal-strength steel bars (ρ= 2.22%). Hoops were assembled at a spacing s= 75 mm; thus, non-seismic detailing was provided to the column. This specimen was tested under the impact of three blasts. The shockwave and displacement data are listed in Table 4-1. Reflected pressure and impulse time histories as well as reflected pressure and displacement time histories are provided in Figure 4-1. It should be noted that displacement data was lost for the first blast for this column. Selected photographs for various stages of testing are also included in Figure 4-2.

The first blast (17 psi) was meant to test the specimen within the elastic range (i.e. for the longitudinal steel). As mentioned before, a complete pressure and displacement time history could not be recovered due to a technical issue, but processing the available files obtained allowed to recover a maximum displacement value equal to 10.70 mm. Several cracks appeared on the tension face of the middle third of the section, but all were too thin to be considered major. The strain gauge recorded a maximum strain equal to 0.0045 mm/mm which indicates the bars were pushed slightly past yield.

Blast 2 (35 psi) resulted in a maximum mid-span displacement equal to 20.47 mm, while the residual displacement was equal to 5.50 mm. Cracks from blast 1 became wider after blast 2, and extended half-way through the column’s cross section. The maximum strain recorded was equal to 0.0105 mm/mm, which confirms that the tension steel bars were now in the post-yield range.

Blast 3 (80 psi) was the last blast for this specimen. Though the damage was not considered a complete failure of the column, the decision was made to not proceed with further testing due to the expectation failure would be severe if testing had continued. During the test, the mid-span LVDT recorded a maximum displacement of 87.38 mm. The residual displacement at the end of testing was equal to 51.31 mm, which left the column with a cumulative residual displacement of 56.81 mm. Cracks widened even more and stretched in length after this shot, with others forming along the full length of the column (Figure 4-2 (e)). Transverse cracks followed a typical spacing of 75 mm which corresponds to the spacing of the hoops (s= 75 mm). The major crack width measured was equal to 5.7 mm. The compression zone also experienced concrete crushing after this blast (Figure 4-2). The high-speed video showed concrete fragments breaking apart as the column deformed. As for the top and bottom supports, hinging was visible with cracking on the tension sides due to the negative moments generated at the column ends.

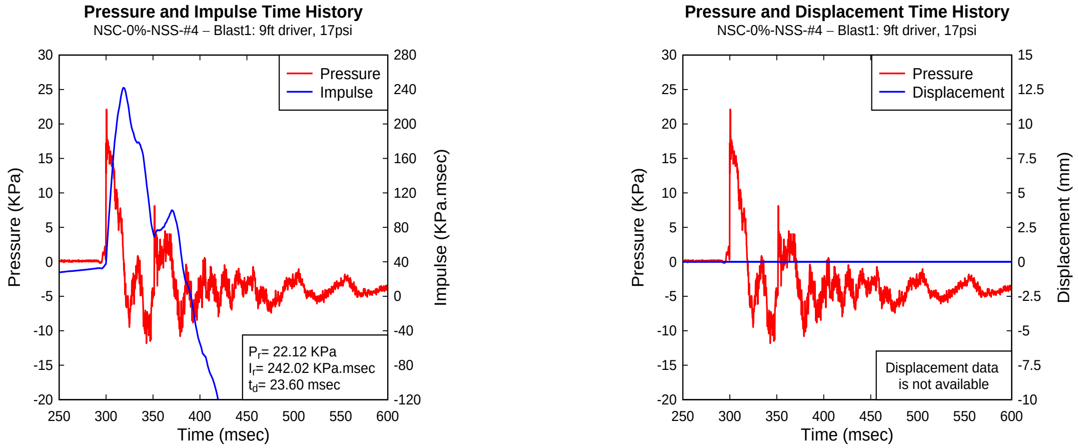

a) Blast 1: Reflected pressure, impulse, and displacement time histories

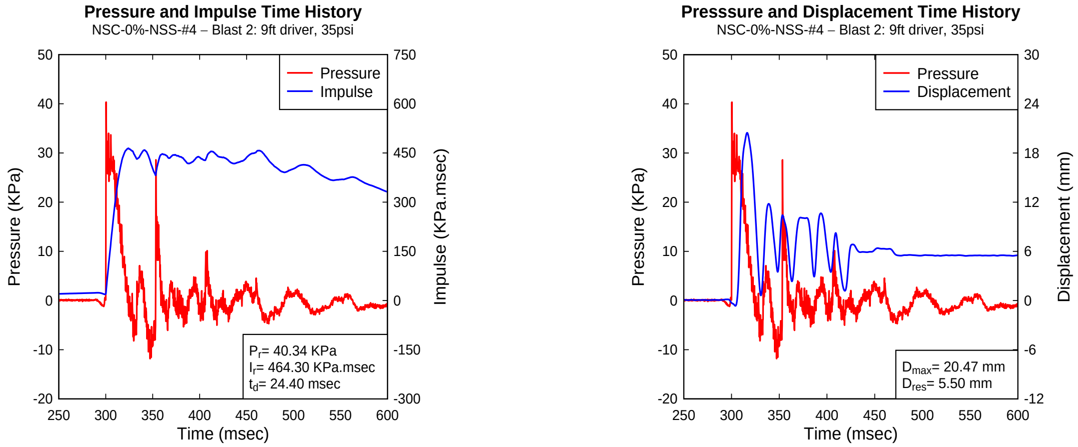

b) Blast 2: Reflected pressure, impulse, and displacement time histories

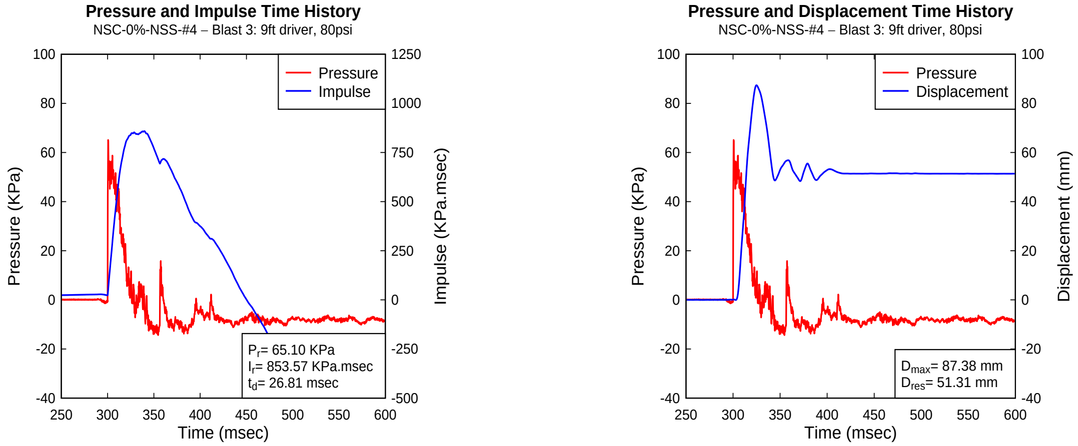

c) Blast 3: Reflected pressure, impulse, and displacement time histories

Figure 4-1 NSC-0%-NSS-#4: Recorded reflected pressure, impulse, and displacement for blasts 1-3

a) Blast 1 (17 psi) b) Blast 2 (35 psi) c) Blast 3 (80 psi)

d) Mid-span at blast 3 e) Mid-span at blast 4 f) Compression zone at blast 4

Figure 4-2 NSC-0%-NSS-#4: Photographs at the end of blasts 1-3

4.3.1.2 NSC-0%-NSS-15M

The second specimen that was cast with plain normal-strength concrete was designed with 15M normal-strength steel bars (ρ= 3.44 %). Spacing of hoops was equal to 75 mm. A total of four blasts were conducted on this column. The shockwave data and displacement data are included in Table 4-1. Complete reflected pressure and impulse time histories along with reflected pressure and displacement time histories are available in Figure 4-3. Selected photographs of the column after each blast are also available in Figure 4-4.

The first blast (17 psi) tested the specimen within its elastic range. The displacements obtained after this shot were 7.41 mm for maximum and 1.25 mm for residual. A few cracks were noticed on the tension face of the column, but they were too thin to be considered as major. The strain gauge data showed a maximum strain at the time of maximum displacement equal to 0.0012 mm/mm, which indicates the 15M bars were not pushed beyond their elastic capacity.

Blast 2 (35 psi) resulted in a maximum mid-span displacement of 20.01 mm. The residual mid-span displacement was equal to 6.71 mm (cumulative= 7.96 mm). More cracks surfaced along the middle third of the column, and extended from the tension face and traveled along the section's depth. The strains recorded showed a maximum value of 0.0074 mm/mm, which indicates that the 15M bars had been taken into their plastic range.

Blast 3 (80) psi resulted in some damage (concrete crushing) occurring to the compression side at mid-span as shown in Figure 4-4. The maximum and residual displacements were 83.96 mm and 54.78 mm respectively, and the cumulative residual displacement summed up to 62.74 mm. Cracks from the previous shots spread on the tension face and increased in width, with a maximum measured crack width of 12.7 mm. Also, a piece of concrete, approximately 60 mm in length, spalled off the edge of the column's tension face at mid-span as shown in Figure 4-4 (e).

Blast 4 (100 psi) was the final blast for this specimen. Extreme deformation and severe fragmentation took place. The column displaced a maximum value equal to 162.77 mm and could not recover much of it, resulting in a residual displacement of 136.60 mm. The specimen was left with a total cumulative residual displacement equal to 199.34 mm. Several openings in the concrete defined the failure zone in the mid-span region and their locations matched that of the cracks that formed in the previous blast (Figure 4-4 (f)). Cracks also intensified and spread in all directions. The compression zone was totally damaged, concrete spalled in that region, and the compression bars could be seen over a span of around 400 mm. Hinging was clearly visible at both supports with the formation of large diagonal cracks (Figure 4-4 (g)). The inclined cracks could be due to the combination of both shear stresses and flexural stresses at the supports, which subsequently translates to a combination of cracks' orientation between inclined (shear stresses) and horizontal (flexural stresses).

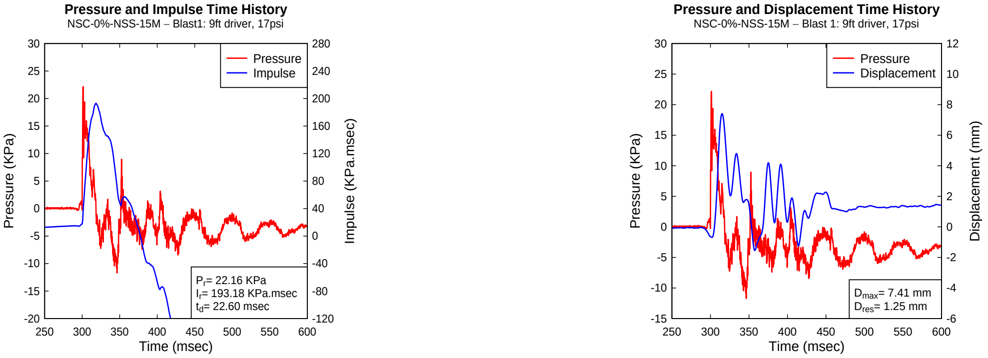

a) Blast 1: Reflected pressure, impulse, and displacement time histories

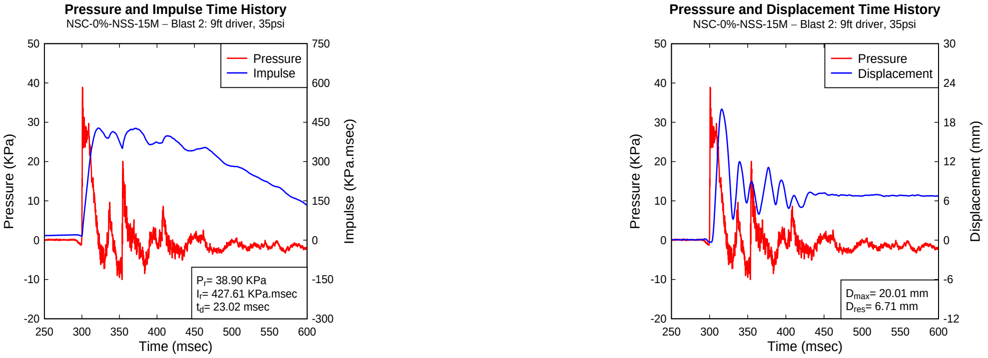

b) Blast 2: Reflected pressure, impulse, and displacement time histories

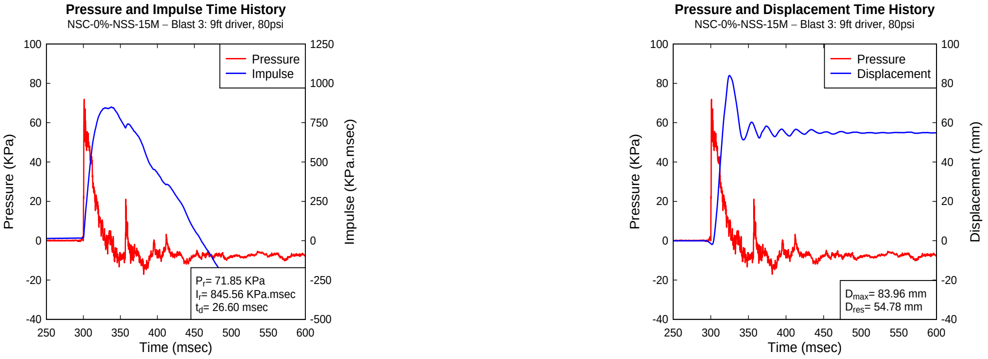

c) Blast 3: Reflected pressure, impulse, and displacement time histories

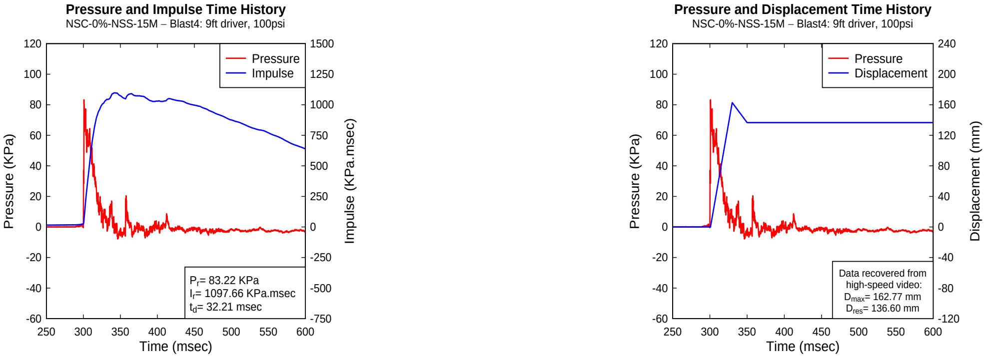

d) Blast 4: Reflected pressure, impulse, and displacement time histories

Figure 4-3 NSC-0%-NSS-15M: Recorded reflected pressure, impulse, and displacement for blasts 1-4

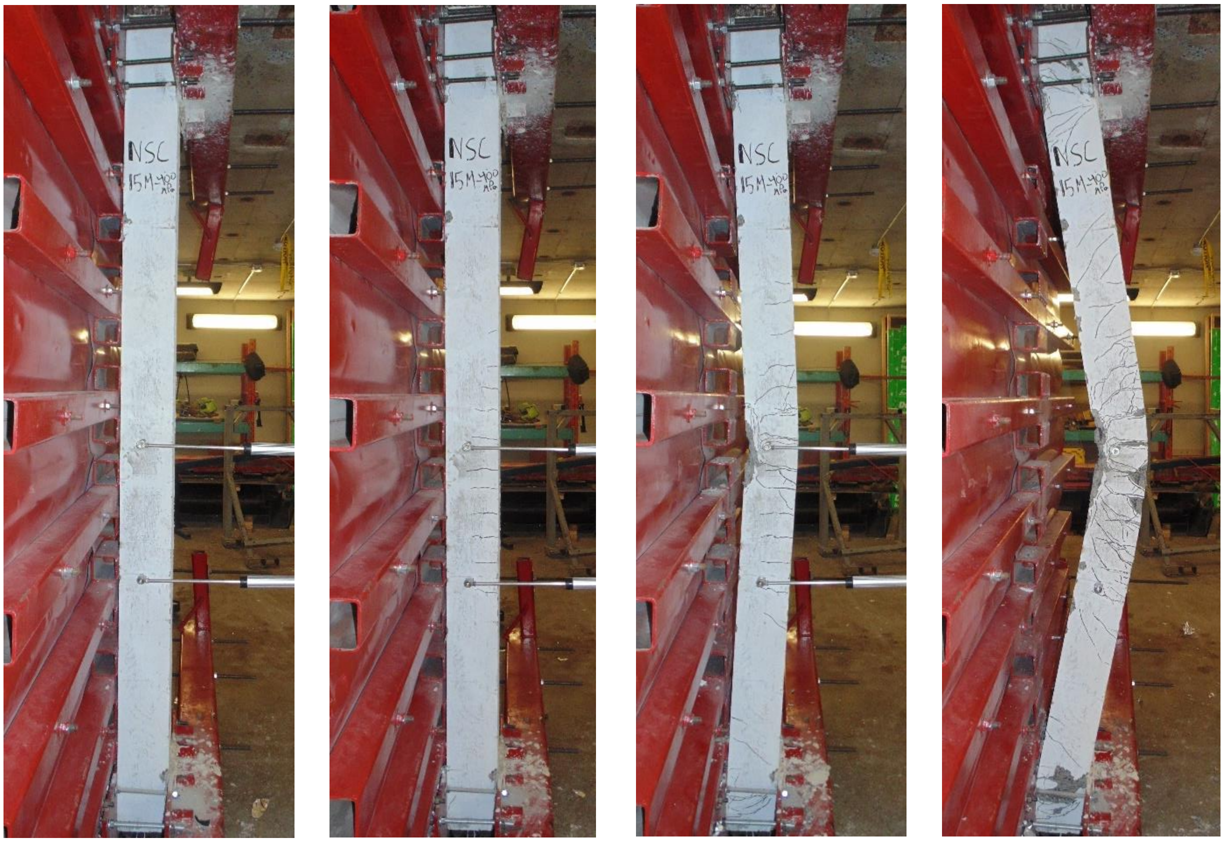

a) Blast 1 (17 psi) b) Blast 2 (35 psi) c) Blast 3 (80 psi) d) Blast 4 (100 psi)

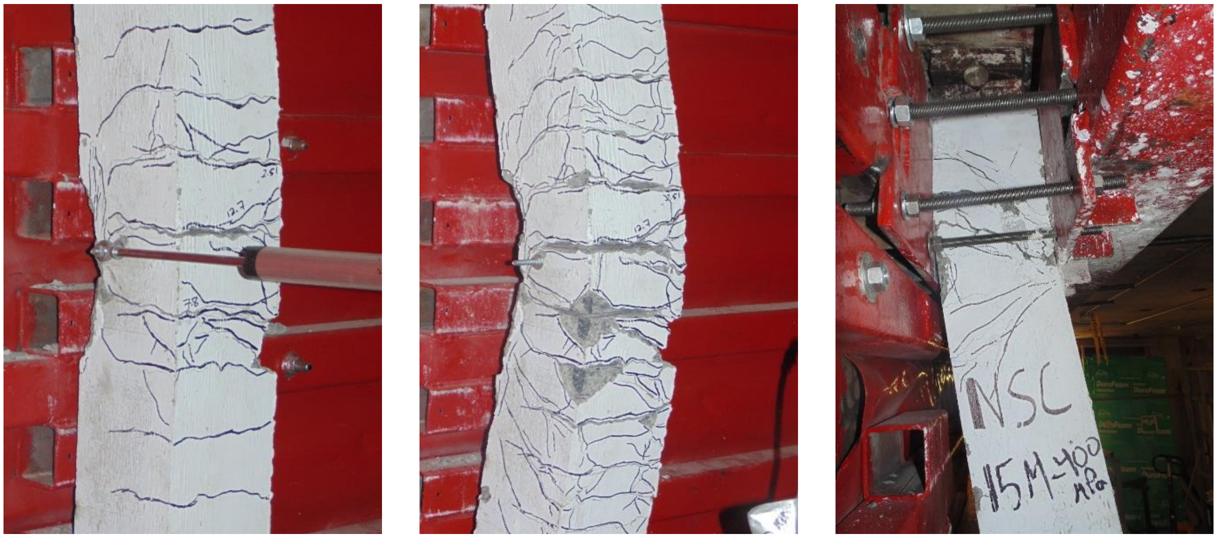

e) Mid-span at blast 3 f) Mid-span at blast 4 g) Top hinge at blast 4

Figure 4-4 NSC-0%-NSS-15M: Photographs at the end of blasts 1-4

4.3.2 HSC-NSS Series

4.3.2.1 HSC-0%-NSS-10M

This first specimen of the series was cast with plain high-strength concrete (without fibers). Hoops were spaced at 75 mm, corresponding to non-seismic detailing. The column included 10M normal-strength steel bars (ρ= 1.72%). A total of three blasts were used to test this column until failure. The shockwave and displacement data can be found in Table 4-2. Figure 4-5 shows complete reflected pressure and impulse time histories along with reflected pressure and displacement time histories. Photographs after each test are also available in Figure 4-6.

At blast 1 (17 psi), the recorded mid-span displacement was 8.38 mm, while the residual was 1.31 mm. Thin hairline cracks formed along the tension face of the middle third of the column.

Blast 2 (35 psi) resulted in a maximum mid-span displacement of 33.83 mm. Recorded residual displacement was 14.54 mm, while the cumulative residual was 15.85 mm. Wide cracks formed after this blast; the maximum crack width measured were 3.5 mm while other cracks ranged between 0.8 mm to 1.6 mm. As for other cracks, they continued to surface on the columns' face and followed a spacing at which the hoops were assembled, with the biggest cracks located at the mid-height of the specimen.

Blast 3 (80 psi) led to the failure of the column where the maximum displacement was 132.66 mm. The column was not able to recover from the large deformation it was subjected to and the residual displacement remained as 118.08mm, which brought the total cumulative residual to 133.93 mm. Three major crack openings were observed at the mid-span region of the column as shown in Figure 4-6 (d) and (e). The locations of the three openings corresponded to the locations of the widest cracks that were detected after blast 2. Two large pieces of tension concrete spalled in this region as shown in Figure 4-6 (e). As for the compression zone, concrete crushing was visible, and the compression bars were exposed. Compression bars seemed to be a little bent under the compression forces generated, but it was not critical enough to be classified as buckling. The top and bottom supports experienced hinging, with the formation of cracks on the tension side which extended across the cross-section in an inclined manner (Figure 4-6 (f)). The damage in the hinge regions followed the same pattern noticed for the previous specimen (i.e. NSC-0%-NSS-15M), with the formation of inclined cracks due to the combination of flexural and shear stresses at the column ends.

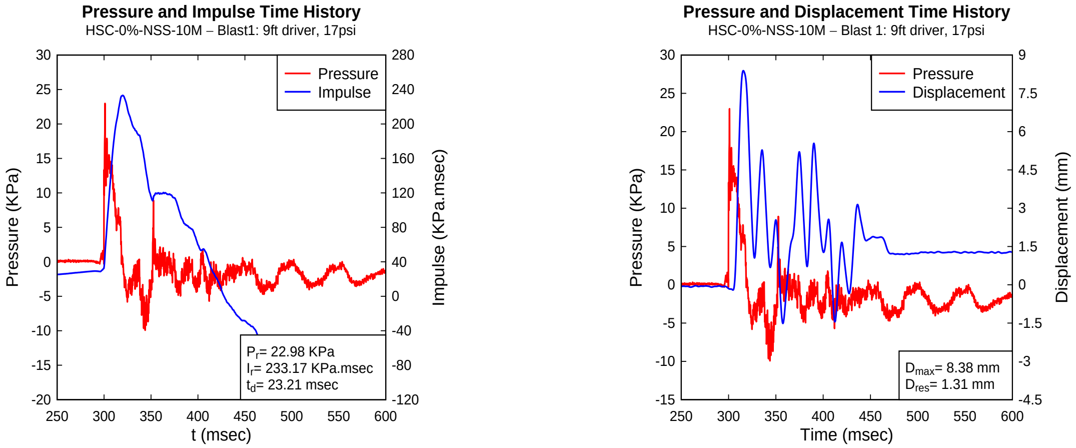

a) Blast 1: Reflected pressure, impulse, and displacement time histories

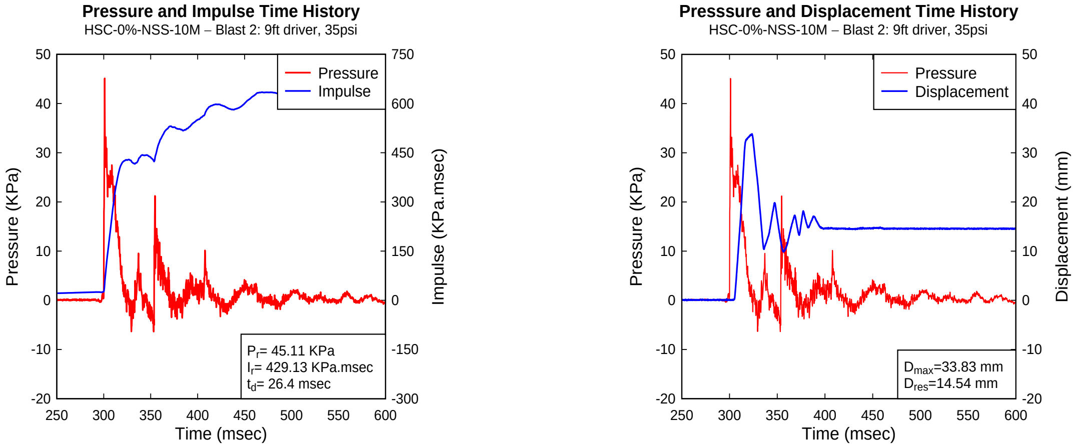

b) Blast 2: Reflected pressure, impulse, and displacement time histories

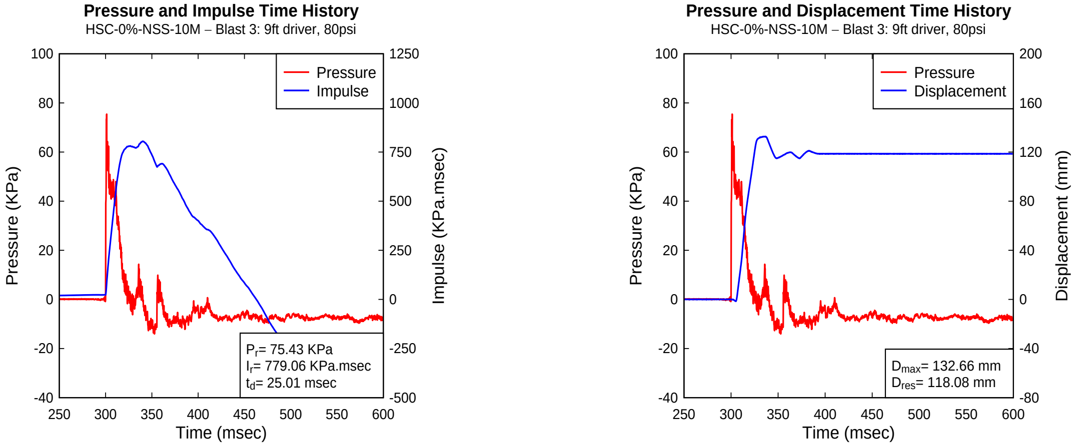

c) Blast 3: Reflected pressure, impulse, and displacement time histories

Figure 4-5 HSC-0%-NSS-10M: Recorded reflected pressure, impulse, and displacement for blasts 1-3

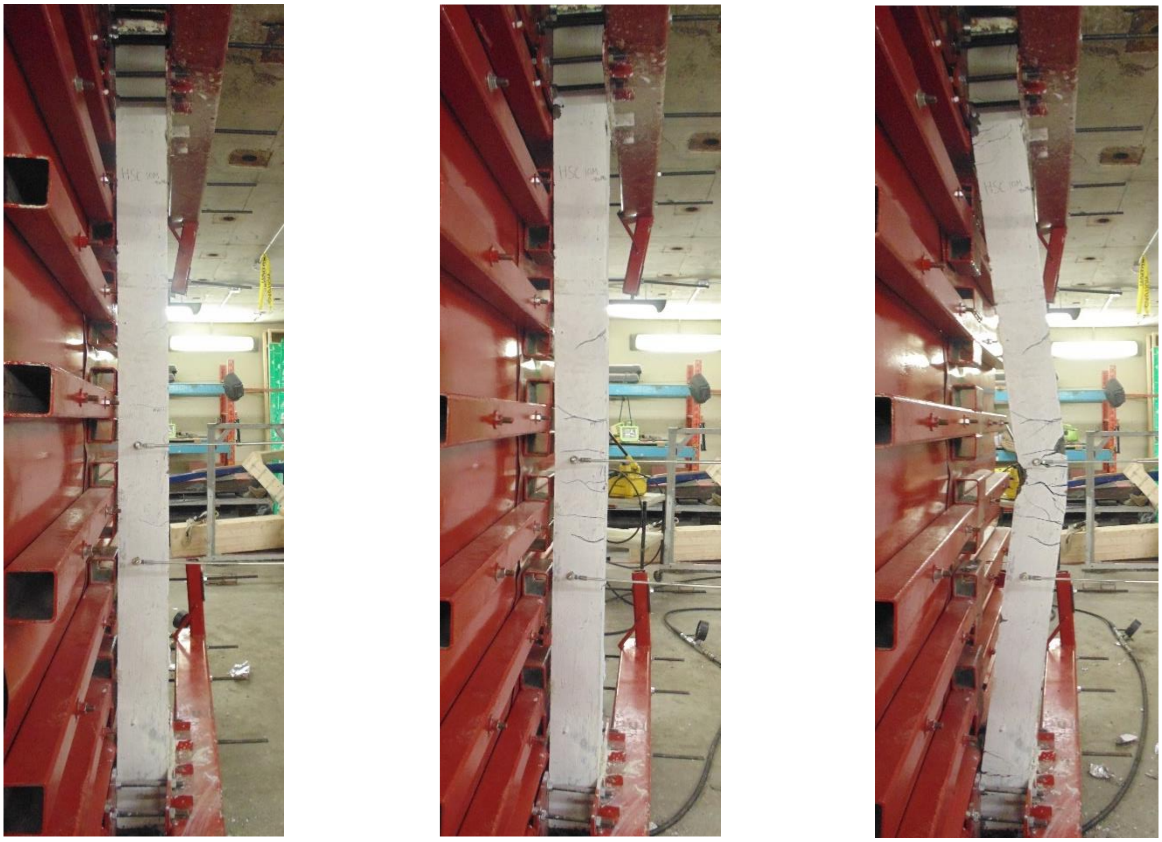

a) Blast 1 (17 psi) b) Blast 2 (35 psi) c) Blast 3 (80 psi)

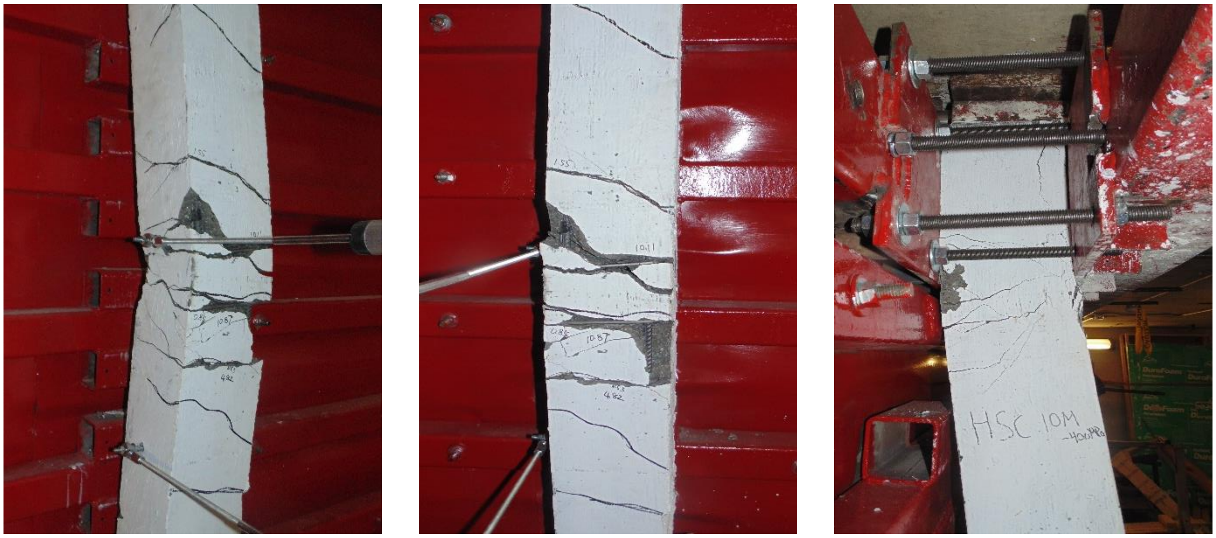

d) Mid-span at blast 3 e) Mid-span at blast 4 f) Top hinge at blast 4

Figure 4-6 HSC-0%-NSS-10M: Photographs at the end of blasts 1-3

4.3.2.2 HSC-0%-NSS-10M-S

This column had a similar configuration to the companion HSC-0%-NSS-10M specimen (plain high-strength concrete and 10M normal-strength bars) with the only difference being the provision of seismic detailing (tie spacing, s= 38 mm) in this column. A total of 3 blasts were performed to test this specimen. The shockwave and displacement data could be found in Table 4-2. Complete reflected pressure and impulse time histories along with reflected pressure and displacement time histories are available in Figure 4-7. Selected photographs from various stages of testing are also available in Figure 4-8.

At blast 1 (17 psi), the specimen's mid-span displacement was 9.49 mm, while the residual displacement was 2.41 mm. Several cracks formed in the middle third of the column, all of them were thin and can be classified as hair-line cracks.

Blast 2 (35 psi) led to a maximum mid-span displacement of 20.81 mm with 4.60 as residual. The cumulative residual displacement was equal to 7.01 mm. After this shot, cracks from the previous blast propagated along the effective depth of the section, along with further cracking appearing on the tension face of the column. Maximum crack width recorded was 0.3 mm. As for cracking pattern, cracks could be observed to be forming at the location of the seismically spaced hoops (spaced at ≈38 mm).

The final blast (80 psi) was the failure shot for this column. The maximum mid-span displacement was equal to 106.13 mm with 87.14 mm as residual. The total residual displacement for the specimen after testing finalized as 94.15 mm. Two major crack openings occurred right below the mid-height as shown in Figure 4-8 (e), corresponding to the locations of the widest cracks from the previous shot and to the locations of two consecutive hoops. The two openings extended all the way to reach the compression zone at the back of the column. Crushing was also observed on the compression side (although core integrity was maintained). Fragmentation and spalling of concrete from this zone was observed when examining the high-speed video, with the resulting damage is visible in Figure 4-8 (d) and (f). The top and bottom supports also exhibited cracking and hinges could be noticed through Figure 4-8 (c).

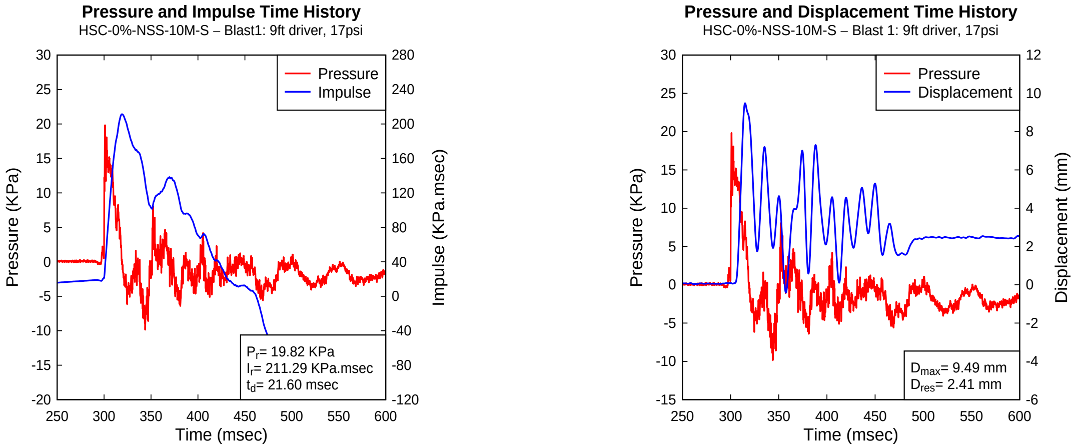
Pressure and Impulse Time History

HSC-0%-NSS-10M-S – Blast1: 9ft driver, 17psi

Pressure and Displacement Time History

HSC-0%-NSS-10M-S – Blast 1: 9ft driver, 17psi

a) Blast 1: Reflected pressure, impulse, and displacement time histories

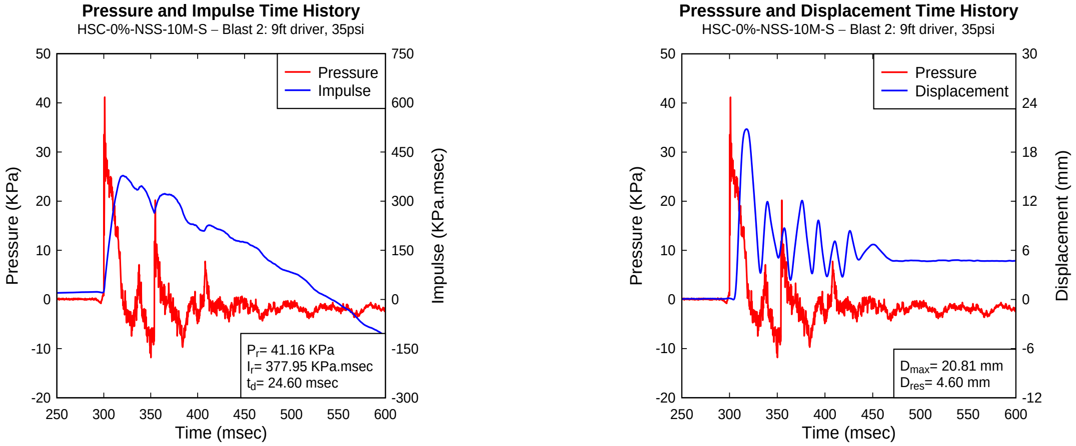
Pressure and Impulse Time History

HSC-0%-NSS-10M-S – Blast 2: 9ft driver, 35psi

Presssure and Displacement Time History

HSC-0%-NSS-10M-S – Blast 2: 9ft driver, 35psi

b) Blast 2: Reflected pressure, impulse, and displacement time histories

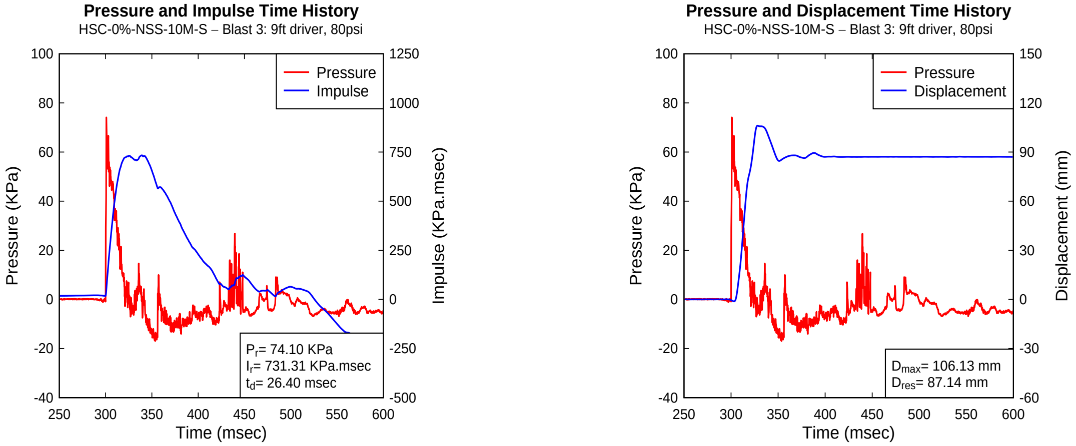
Pressure and Impulse Time History

HSC-0%-NSS-10M-S – Blast 3: 9ft driver, 80psi

Pressure and Displacement Time History

HSC-0%-NSS-10M-S – Blast 3: 9ft driver, 80psi

c) Blast 3: Reflected pressure, impulse, and displacement time histories

Figure 4-7 HSC-0%-NSS-10M-S: Recorded reflected pressure, impulse, and displacement for blast 1-3

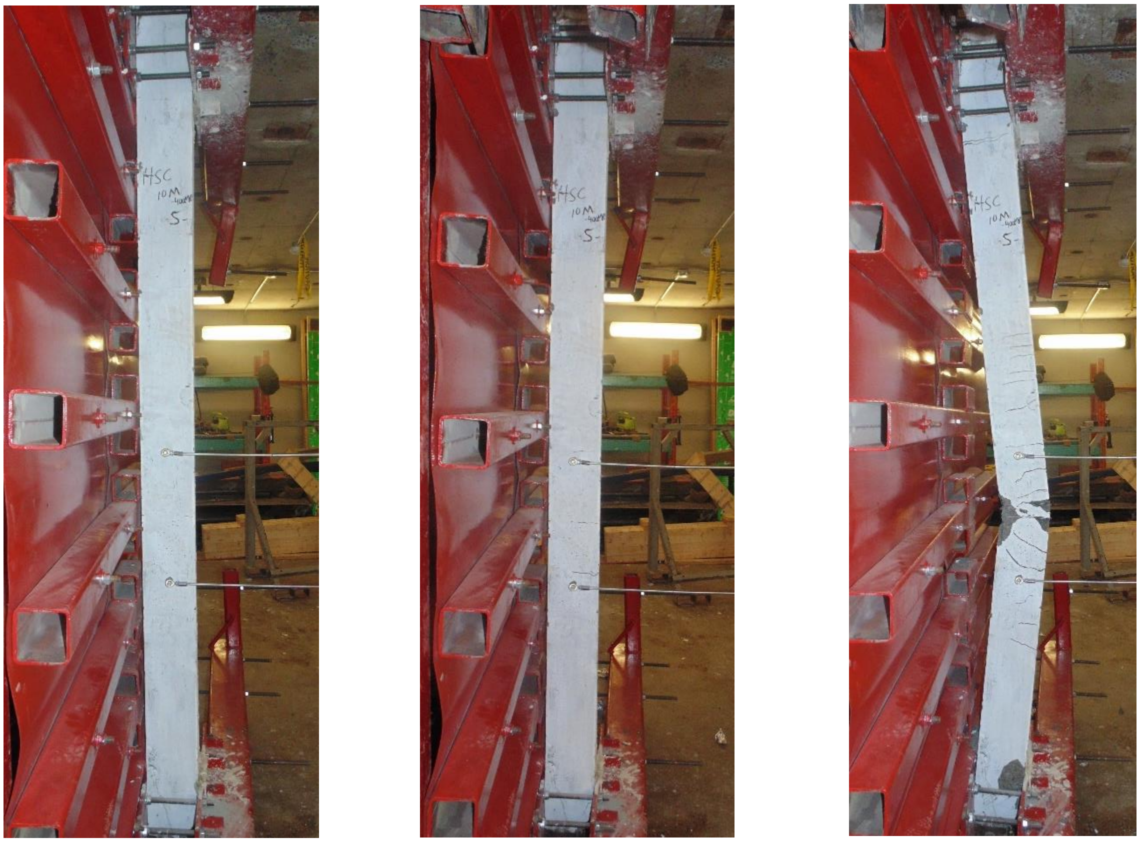

a) Blast 1 (17 psi) b) Blast 2 (35 psi) c) Blast 3 (80 psi)

d) Mid-span at blast 3 e) Tension Face at blast 3 f) Major openings at blast 3

Figure 4-8 HSC-0%-NSS-10M-S: Photographs at the end of Blasts 1-3

4.3.2.3 HSC-0%-NSS-#4

The third column in this series was cast using plain high-strength concrete and included #4 (ρ= 2.22%) normal-strength steel bars, resulting in a slightly larger reinforcement ratio when compared to the specimen with 10M bars (ρ= 1.72%). This specimen allows to observe the effect of steel reinforcement ratio when compared to the 10M and 15M companions, but more importantly, the effect of steel reinforcement type will be observed when compared to the specimen with #4 high-strength steel reinforcement. The shockwave and displacement data can be found in Table 4-2. Figure 4-9 shows complete reflected pressure and impulse time histories and reflected pressure and displacement time histories. Selected photographs of testing are shown in Figure 4-10.

Blast 1 (17 psi) was meant to test the specimen in the elastic range, a maximum displacement of 7.21 mm was recorded with 1.96 mm as residual displacement. Hair-line cracks formed in the middle third of the column, especially at mid-span where the cracks were more visible but still very thin. The strain gauge data showed a maximum strain at the time of maximum displacement equal to 0.0020 mm/mm, which is indeed within the bar's elastic range.

Blast 2 (35 psi) resulted in a maximum mid-span displacement of 20.07 mm and a residual displacement of 7.84 mm. The cumulative residual displacement was 9.8 mm. Further hair-line cracks formed along the middle third of the column, while cracks due to blast 1 widened and propagated. Maximum crack width recorded was 0.2 mm. Steel bars also surpassed their elastic capacity reaching yield levels as the maximum strain recorded was 0.0137 mm/mm.

At blast 3 (80 psi), the maximum mid-span displacement recorded was 82.35 mm. Serious damage occurred to the column where it couldn't recover its high maximum displacement and the residual displacement remained as 44.29 mm (cumulative= 54.09 mm). Cracking occurred all over the tension face and propagated all the way along the effective depth of the column. Two major cracks formed with widths of 16.2 and 12.7 mm, along with a small piece of concrete spalling on the left edge of the column's tension face as shown in Figure 4-10 (e). Cracking was visible at the top and bottom supports and the compression face was subjected to some crushing.

Blast 4 (100 psi) was meant to fail the specimen. Severe damage and fragmentation occurred. The tension face was completely damaged where the steel bars were left exposed over a length of about 500 mm at mid-span. LVTDs were removed during this test to avoid damaging them due to the expected high deformation. However, the maximum mid-span displacement was obtained from the high-speed video and found to be approximately 211 mm. Residual displacement was recorded through taking measurements with respect to the anchor of the LVTD before and after the test, the value was 138.45 mm, which left the specimen with a cumulative residual displacement equal to 192.54 mm. As shown in Figure 4-10 (f), steel bars experienced high deformations but no rupture happened. The compression zone of the column also showed significant crushing. As for the top and bottom supports, hinges formed at both locations and important cracking was visible.

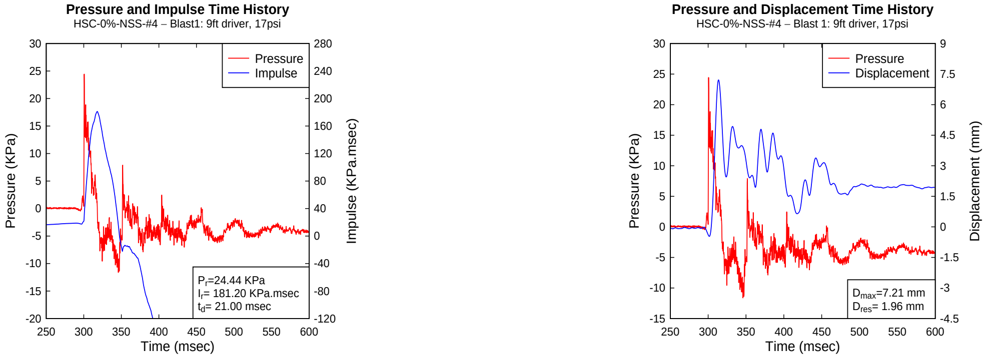

a) Blast 1: Reflected pressure, impulse, and displacement time histories

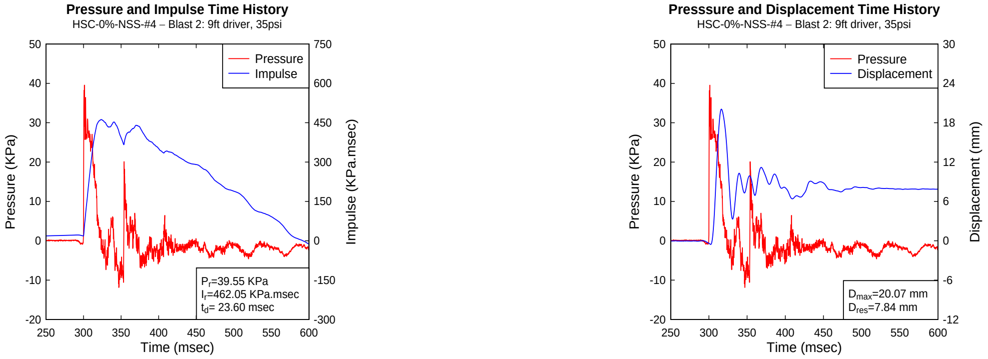

b) Blast 2: Reflected pressure, impulse, and displacement time histories

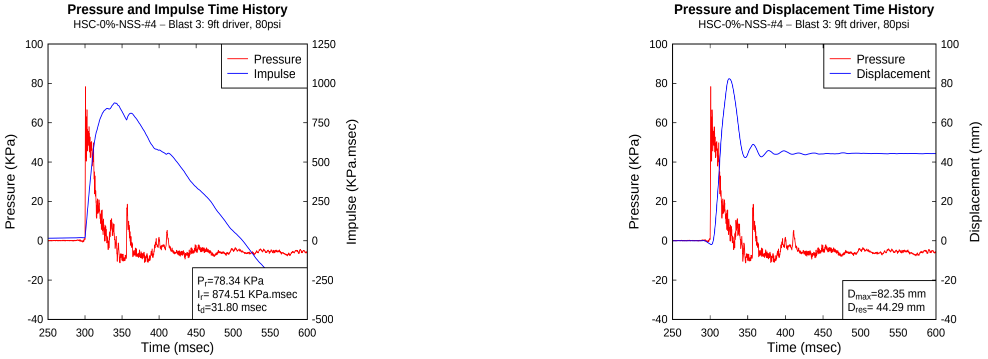

c) Blast 3: Reflected pressure, impulse, and displacement time histories

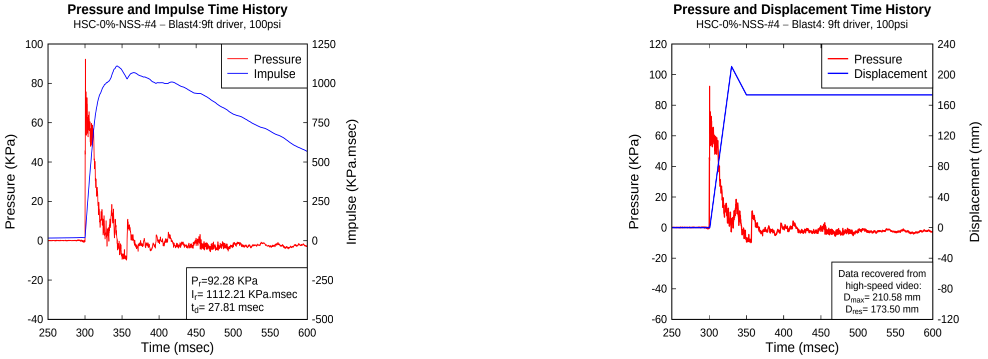

d) Blast 4: Reflected pressure, impulse, and displacement time histories

Figure 4-9 HSC-0%-NSS-#4: Recorded reflected pressure, impulse, and displacement for blasts 1-4

a) Blast 1 (17 psi) b) Blast 2 (35 psi) c) Blast 3 (80 psi) d) Blast 4 (100 psi)

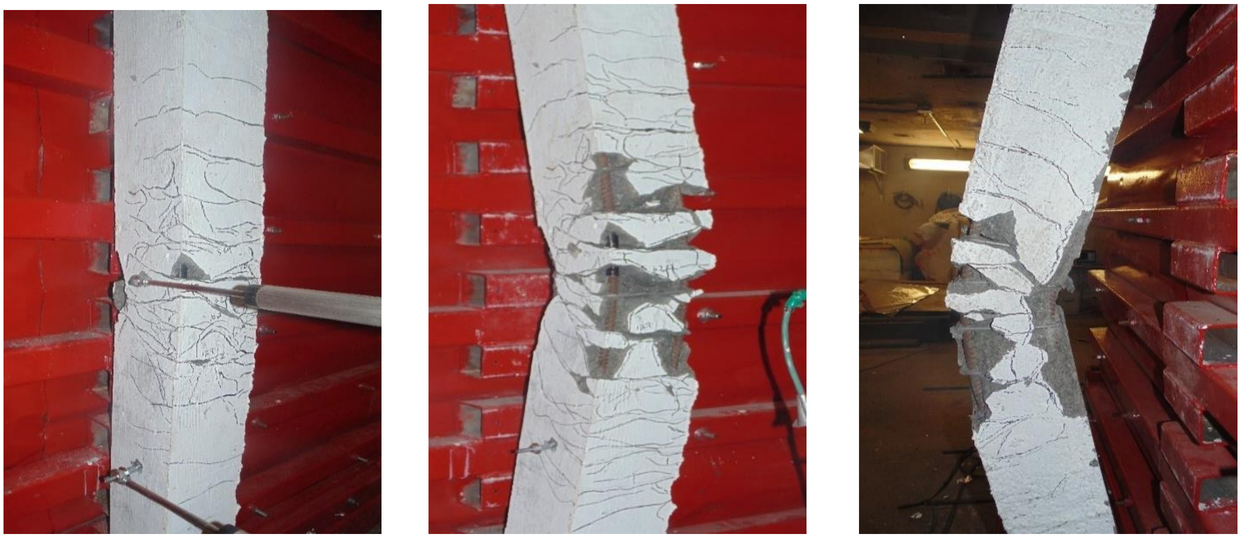

e) Tension face at blast 3 f) Tension face at blast 4 g) Mid-span at blast 4

Figure 4-10 HSC-0%-NSS-#4: Photographs at the end of blasts 1-4

4.3.2.4 HSC-0%-NSS-15M

The last specimen in this series was built with plain high-strength concrete and 15M normal-strength steel bars, resulting in a reinforcement ratio of ρ= 3.44% (the largest in this series). Non-seismic detailing was also provided (s= 75 mm). The column was tested under a total of 4 blasts. The shockwave and displacement data are available in Table 4-2. Complete reflected pressure and impulse time histories, along with reflected pressures and displacement time histories are shown in Figure 4-11. Selected photographs from various stages of testing are also shown in Figure 4-12.

Blast 1 (17 psi) was the first shot for this column. A maximum displacement of 7.57 mm was recorded, while the residual was 1.72 mm. No signs of cracking were observed.

The second shot was at 35 psi. Maximum mid-span displacement recorded was 16.02 mm, residual displacement was 3.41 mm, and the cumulative residual displacement was 5.13 mm. Hair-line cracks formed on the tension face on the middle third of the column after this shot.

Blast 3 (80 psi) was a damaging shot for the specimen, but did not lead to total failure. The maximum mid-span displacement was 77.70 mm. The residual mid-span displacement was 54.45 mm, which added up to a total cumulative residual displacement of 59.58 mm. Compression zone experienced some crushing as shown in Figure 4-12 (c). Cracks formed all over the tension face, especially at the exact mid span where they formed intensely. Also, significant flexural cracking was observed at mid-span, where the crack patterns changed from horizontal to inclined as they extended from the tension face to the neutral axis. Major crack widths measured were 5.5 and 5.1 mm. A small piece of concrete cover with a width of 31mm spalled of the left edge of the front face of column as shown in Figure 4-12 (e).

For blast 4 (100 psi), the middle LVDT was removed as the failure was expected to be severe. This shot led to total failure of column. Maximum mid-span displacement was recovered from the high-speed video and was found to be 141 mm. The residual displacement was estimated to be 117 mm, which brings the total cumulative residual displacement of the column to around 177 mm. Footage from high speed video shows that significant fragments from the mid-span region burst away from the specimen and travelled long distances across the test area upon column failure. Concrete spalled of the tension face and steel bars were left exposed over the mid-span hinge. Compression zone experienced more crushing and lost a significant portion of its volume. Hinging also formed on top and bottom supports. Figure 4-12 (d), (f), and (g) show the damage that happened after this shot.

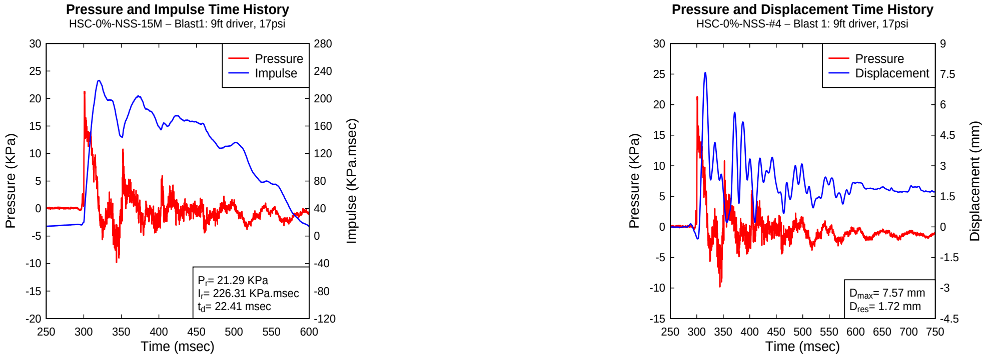

a) Blast 1: Reflected pressure, impulse, and displacement time histories

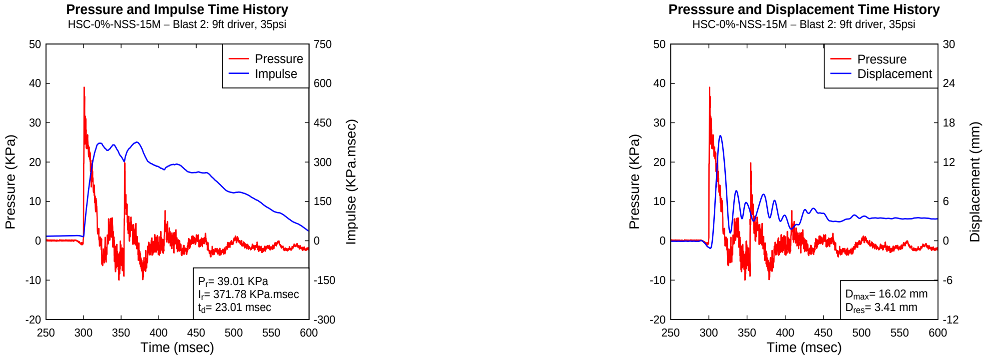

b) Blast 2: Reflected pressure, impulse, and displacement time histories

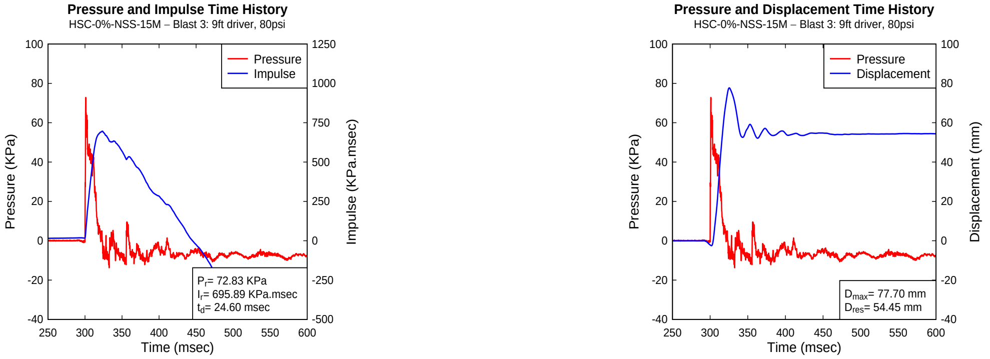

c) Blast 3: Reflected pressure, impulse, and displacement time histories

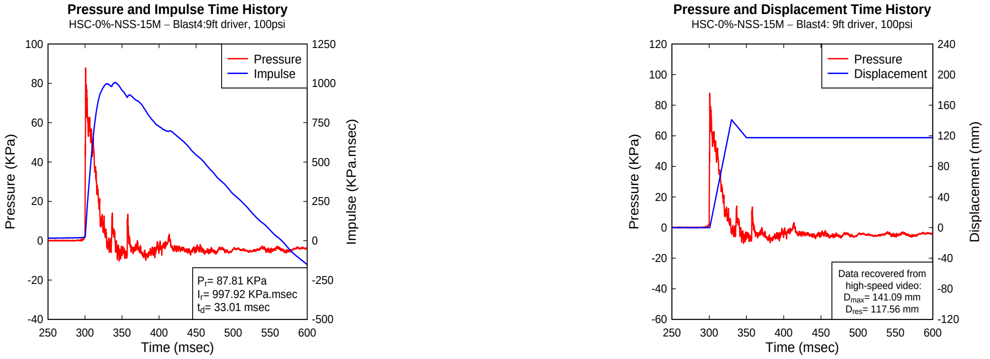

d) Blast 4: Reflected pressure, impulse, and displacement time histories

Figure 4-11 HSC-0%-NSS-15M: Recorded reflected pressure, impulse, and displacement for blasts 1-4

a) Blast 1 (17 psi) b) Blast 2 (35 psi) c) Blast 3 (80 psi) d) Blast 4 (100 psi)

e) Mid-span at blast 3 f) Mid-span at blast 4 g) Tension Face at blast 4

Figure 4-12 HSC-0%-NSS-15M: Photographs at the end of blasts 1-4

4.3.3 HSFRC-NSS Series

4.3.3.1 HSC-0.5%-NSS-10M

The first column of the HSFRC series included 10M normal-strength steel bars (ρ= 1.72%). The column was built with high-strength fiber-reinforced concrete (HSFRC) with a steel fiber content equal to 0.5%. Non-seismic detailing was provided to this column (s= 75 mm). Including this column in the experimental program allows for an investigation into the effect of fiber content on blast behaviour when compared to the companions with 0% and 1% fibers. A total of three blasts were used during the testing of this column. The shockwave and displacement data are available in Table 4-3. Complete reflected pressure and impulse time histories as well as reflected pressure and displacement time histories are provided in Figure 4-13. Selected photographs of the specimen during testing are also shown in Figure 4-14.

Blast 1 (17 psi) tested the specimen within the elastic range of its properties. The maximum mid-span displacement recorded was 9.08 mm with 1.25 mm as residual. Hair-line cracks formed in the middle third of the column. Strain gauge data recorded a maximum strain equal to 0.0018 mm/mm at the time of maximum displacement.

Blast 2 (35 psi) resulted in a maximum mid-span displacement equal to 22.85 mm, while the residual displacement was equal to 2.78 mm. The cumulative residual displacement after this shot was 4.03 mm. More cracks along the tension face occurred after this shot and spread over the cross-section of the column. Strain gauge data recorded a maximum strain of 0.004 mm/mm, which implies that the tension steel bars entered their plastic range of behaviour.

The third and final blast (80 psi) resulted in the failure of the column through an opening in the mid-span as shown in Figure 4-14 (f). The maximum displacement after this test was 75.43 mm. The column couldn’t recover much of its displaced value and the residual displacement remained as 62.13 mm. The overall residual displacement was 66.16 mm. The strain gauge stopped working at this stage. The width of the opening at mid-span was equal to 32 mm with fibers pulled out at that spot. Along with the major opening, cracks formed on the whole tension face and propagated further. Unlike what happened with previous specimens with no fibers included, the compression zone experienced some damage but the presence of fibers kept the concrete mostly intact with limited fragmenting and crushing. Both supports displayed the same behaviour as noted in previous specimens with regards to cracking and formation of hinges.

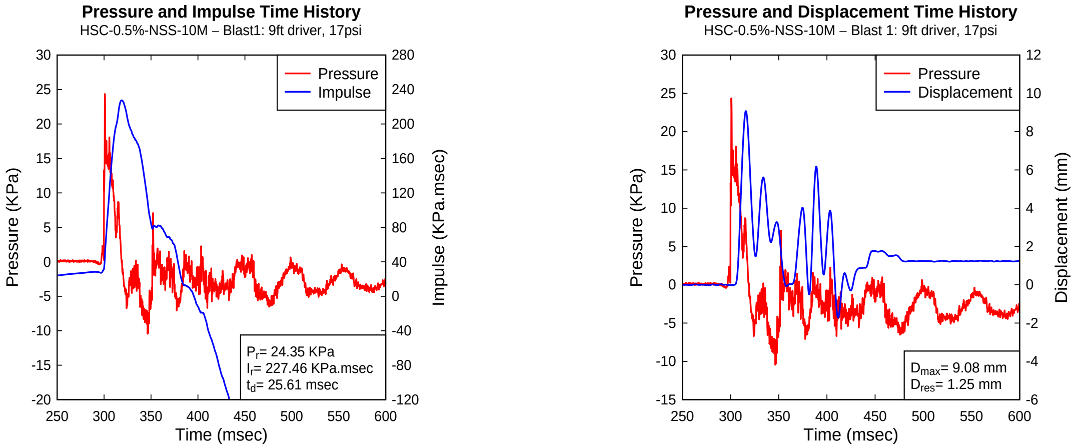

a) Blast 1: Reflected pressure, impulse, and displacement time histories

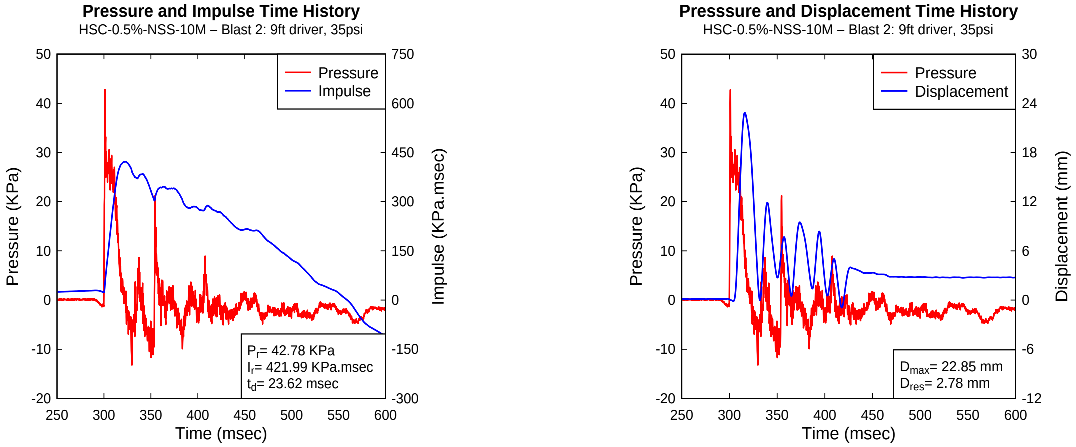

b) Blast 2: Reflected pressure, impulse, and displacement time histories

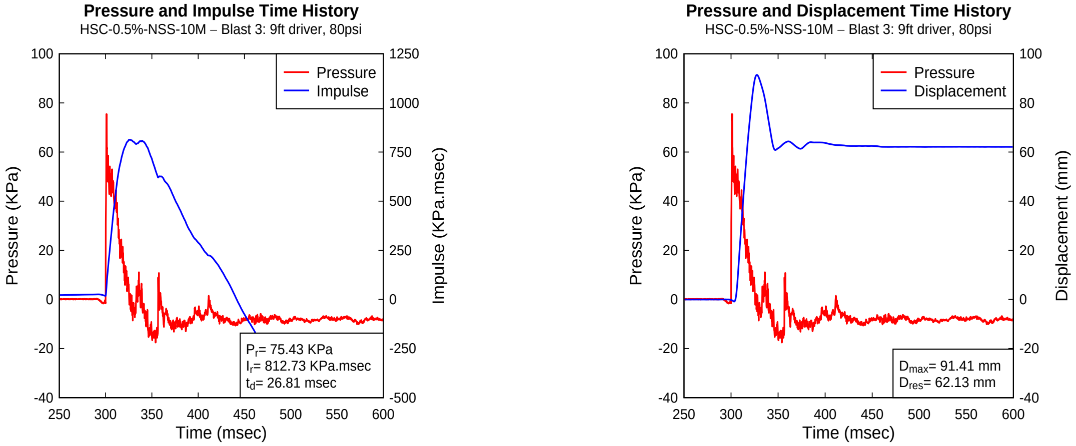

c) Blast 3: Reflected pressure, impulse, and displacement time histories

Figure 4-13 HSC-0.5%-NSS-10M: Recorded reflected pressure, impulse, and displacement for blast 1-3

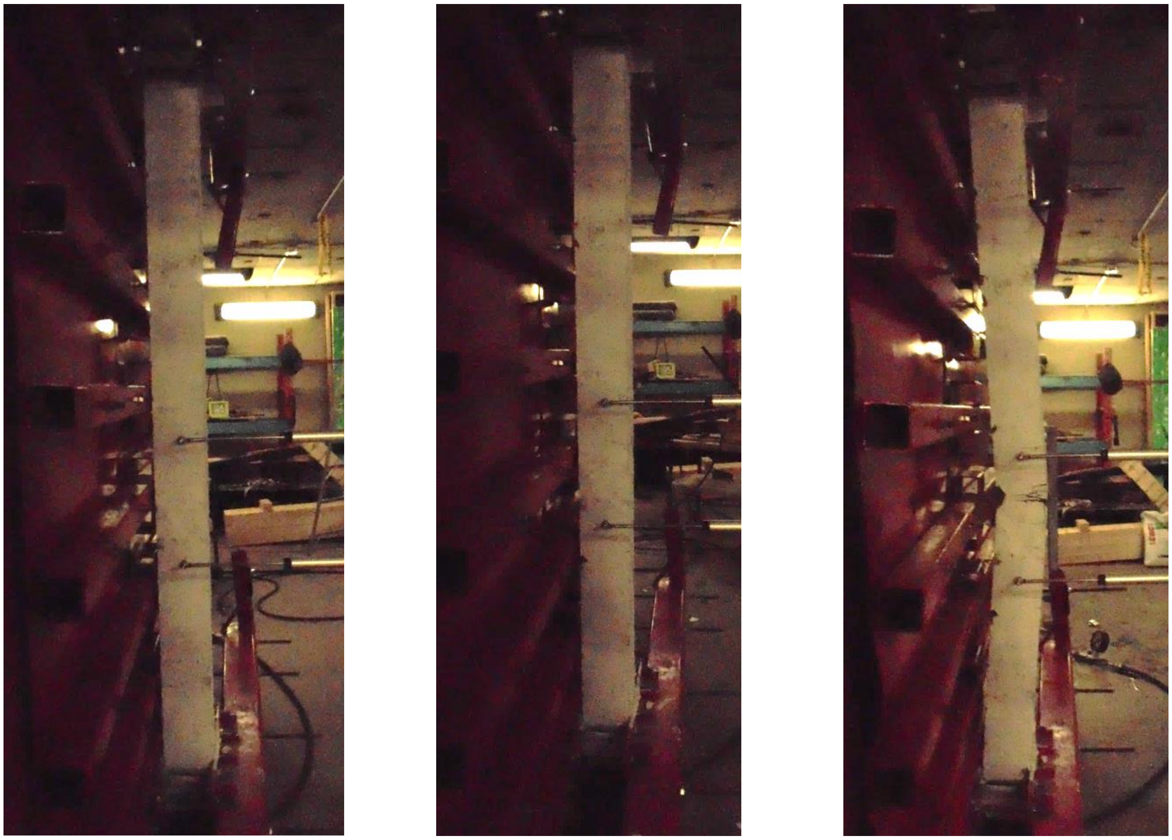

a) Blast 1 (17 psi) b) Blast 2 (35 psi) c) Blast 3 (80 psi)

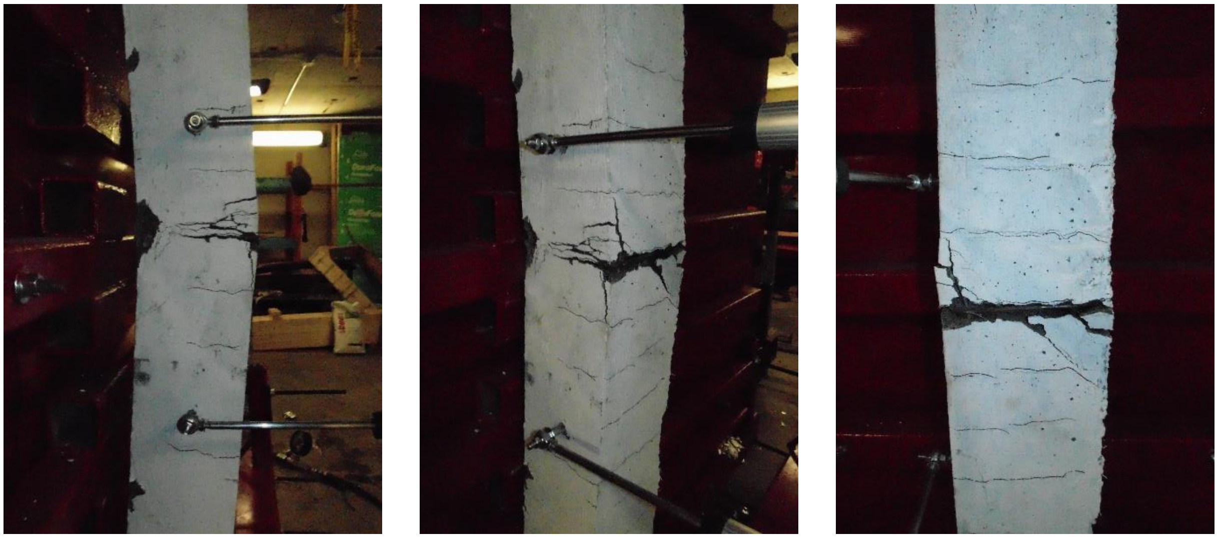

d) Mid-span at blast 3 e) Mid-span at blast 3 f) Tension Face at blast 3

Figure 4-14 HSC-0.5%-NSS-10M: Photographs at the end of blasts 1-3

4.3.3.2 HSC-1%-NSS-10M

As with the previous column, this specimen was built with high-strength fiber-reinforced concrete (HSFRC), 10M normal-strength steel bars (ρ= 1.72%) with the hoops spaced at s= 75 mm (non-seismic detailing). However, the fiber content was increased to 1% in this column. The shockwave and displacement data are available in Table 4-3. Complete reflected pressure and impulse time histories as well as reflected pressure and displacement time histories are provided in Figure 4-15. Selected photographs for the specimen after each blast are available in Figure 4-16. Strain gauge data is not available for this specimen.

Blast 1 (17 psi) barely caused any damage for the column. The maximum mid-span displacement recorded was 7.07 mm with 0.52 mm as residual. A couple of hair-line cracks showed at mid-span but no major cracks were detected.

The second Blast (35 psi) resulted in a maximum mid-span displacement equal to 19.41 mm. The residual displacement recorded was 6.70 mm (cumulative = 7.22 mm). Hair-line cracks from blast 1 widened and several more cracks appeared in the mid-span region. Maximum crack width measured was 0.8 mm just below of mid-span.

The third and final blast (80 psi) resulted in the column's failure. The failure was through a major crack opening occurring just below mid-span (Figure 4-16). Maximum displacement after this shot was 83.78 mm with 52.85 mm as residual. The overall residual displacement settled as 60.07 mm. The crack opening's width was measured to be 24 mm, with fibers pulling out at the location. High-speed video shows that the failure was localized and not severe as the companion with no fibers, where it shows much less fragmentation and damage in the highly-stressed tension zone. The localization of failure reveals the role of fibers in controlling a members' failure mechanism, where damage concentration follows the weakest point rather than manifesting in other areas where steel fibers still contribute to the concrete's strength. As for the compression zone, it experienced some crushing, but the presence of fibers seemed to help resist further crushing to happen. Both top and bottom supports showed signs of hinging, although cracking and damage was more limited when compared to previous specimens. Some photographs showing the failure zone are shown in Figure 4-16.

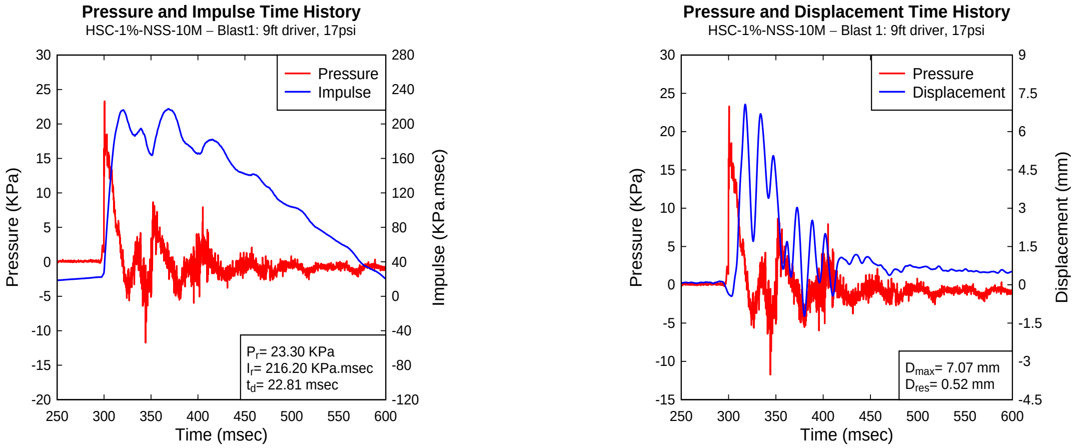

a) Blast 1: Reflected pressure, impulse, and displacement time histories

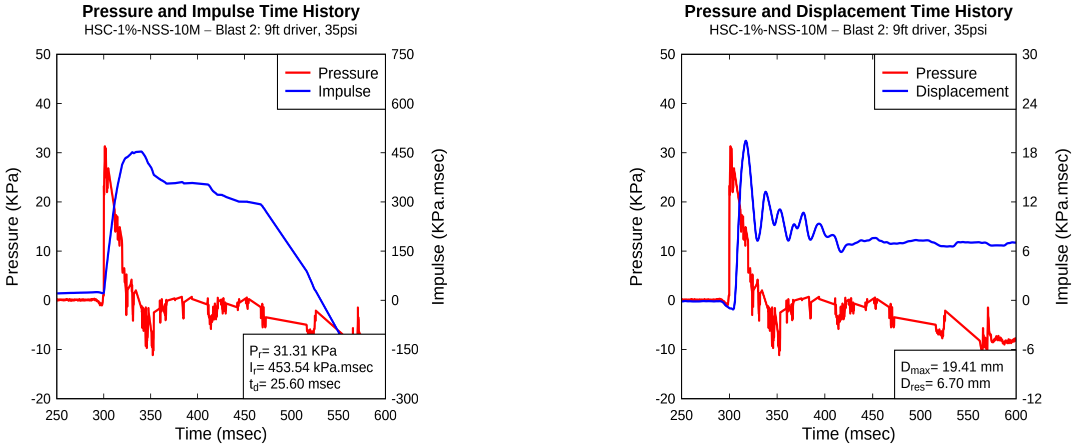

b) Blast 2: Reflected pressure, impulse, and displacement time histories

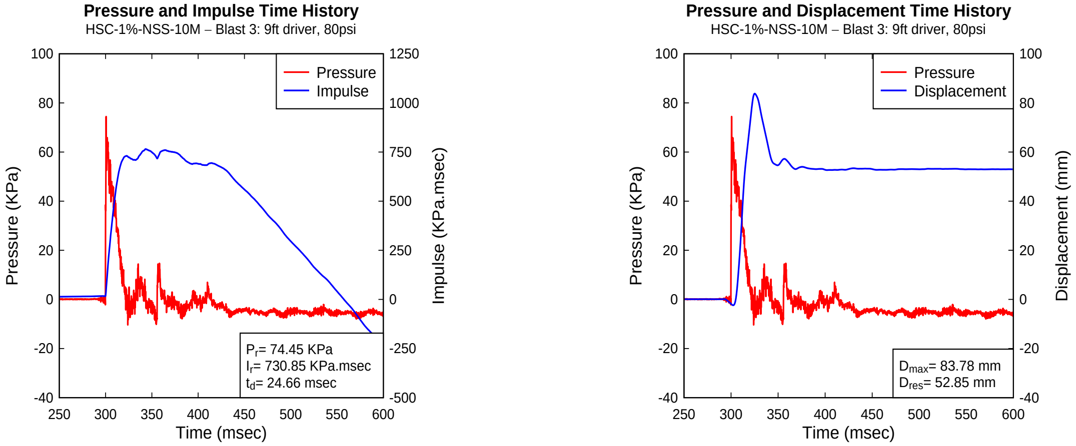

c) Blast 3: Reflected pressure, impulse, and displacement time histories

Figure 4-15 HSC-1%-NSS-10M: Recorded reflected pressure, impulse, and displacement for blast 1-3

a) Blast 1 (17 psi) b) Blast 2 (35 psi) c) Blast 3 (80 psi)

d) Mid-span After blast 3 e) Mid-span After blast 3 f) Tension Face After blast 3

Figure 4-16 HSC-1%-NSS-10M: Photographs at the end of blasts 1-3

4.3.3.3 HSC-1%-NSS-#4

The third column in the HSFRC series was built with #4 normal-strength steel bars (ρ= 2.22%) and a non-seismic detailing (s= 75 mm). Its configuration was similar to that of HSC-0%-NSS-#4 except for adding steel fibers (1%) to the high-strength concrete mix. The column required a total of four blasts to be pushed to failure. The shockwave and displacement data could be found in Table 4-3. Complete reflected pressure and impulse time histories in addition to pressure and displacement time histories are shown in Figure 4-17. Selected photographs from various stages of testing are available in Figure 4-18. No strain gauge data is available for this column.

Blast 1 (17 psi) resulted in a maximum mid-span displacement equal to 7.62 mm, and a residual displacement equal to 2.50 mm. No significant cracks were detected after this blast.

After the second blast (35 psi), cracks formed in the middle third of the column, but none of them was major. The observed cracks formed on the tension face and did not extend much on the column's depth. Mid-span displacements recorded at this stage were 15.37 mm for maximum and 4.14 mm for residual (cumulative = 6.64 mm).

Blast 3 (80 psi) caused some damage in the column but not to the extent of failure. The displacements recorded were 67.09 mm for maximum and 29.11 mm for residual. The cumulative residual displacement was 35.75 mm. Further cracking formed along the tension face of the column, with cracks from blast 2 widening and propagating along the section. Two major cracks were detected at mid span and were spaced at 75 mm (spacing of hoops) as shown in Figure 4-18 (e). Their widths were measured as 8.2 and 4.5 mm. A close examination of the fibers at the location of the cracks showed that the fibers did not pull out completely and were still partially grabbing concrete together.

Blast 4 (100 psi) led to the failure of the specimen through rupture of tension steel as shown in Figure 4-18 (g). The middle LVDT was pushed away from the column due to the major opening propagating and passing through its anchor point. Therefore, LVDT data is not available for this shot, however displacements were recovered from the high-speed video. Maximum mid-span displacement obtained was 153 mm, while the residual was 130 mm, which adds up to a cumulative residual displacement of 166 mm. The specimen opened up at two locations, corresponding to the two major cracks from the previous blast. The larger opening was at mid-height and measured 30 mm (rupture of steel bars could be observed at this location). The compression zone on the other side remained without serious crushing due to the presence of fibers. For supports, both top and bottom experienced cracking. Photographs of failure are shown in Figure 4-18 (f) and (g).

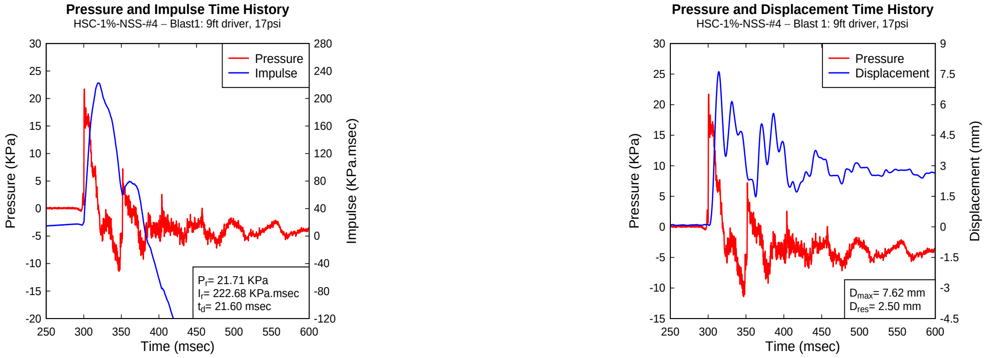
Pressure and Impulse Time History
HSC-1%-NSS-#4 – Blast1: 9ft driver, 17psi

Pressure and Displacement Time History
HSC-1%-NSS-#4 – Blast 1: 9ft driver, 17psi

a) Blast 1: Reflected pressure, impulse, and displacement time histories

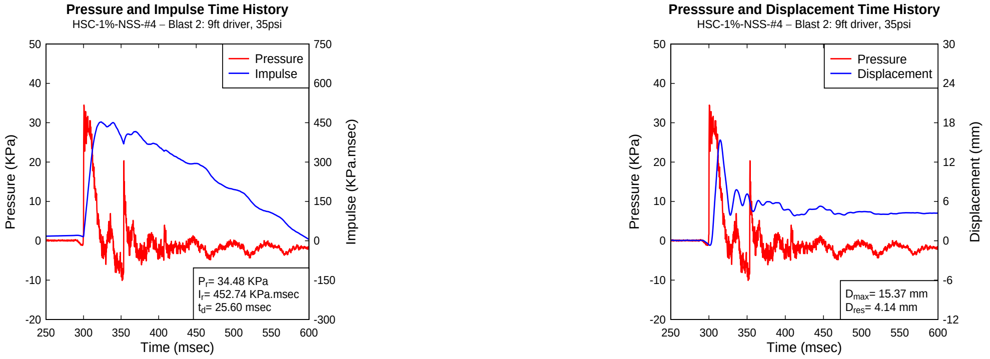
Pressure and Impulse Time History
HSC-1%-NSS-#4 – Blast 2: 9ft driver, 35psi

Presssure and Displacement Time History
HSC-1%-NSS-#4 – Blast 2: 9ft driver, 35psi

b) Blast 2: Reflected pressure, impulse, and displacement time histories

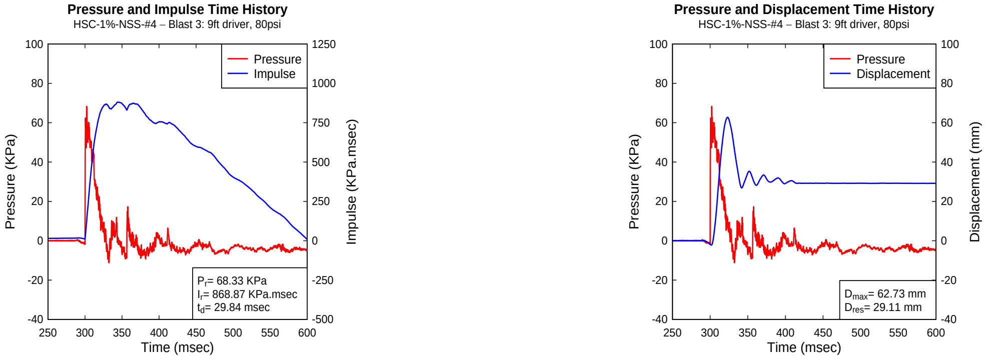
Pressure and Impulse Time History
HSC-1%-NSS-#4 – Blast 3: 9ft driver, 80psi

Pressure and Displacement Time History
HSC-1%-NSS-#4 – Blast 3: 9ft driver, 80psi

c) Blast 3: Reflected pressure, impulse, and displacement time histories

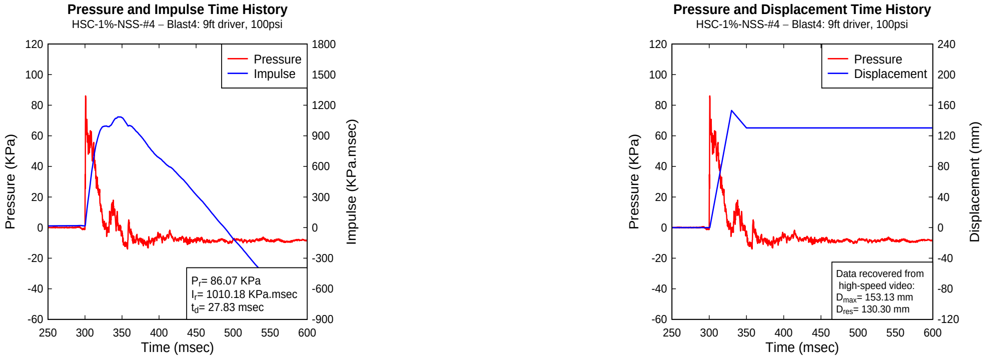
Pressure and Impulse Time History
HSC-1%-NSS-#4 – Blast4: 9ft driver, 100psi

Pressure and Displacement Time History
HSC-1%-NSS-#4 – Blast4: 9ft driver, 100psi

d) Blast 4: Reflected pressure, impulse, and displacement time histories

Figure 4-17 HSC-1%-NSS-#4: Recorded reflected pressure, impulse, and displacement for blasts 1-4

a) Blast 1 (17 psi) b) Blast 2 (35 psi) c) Blast 3 (80 psi) d) Blast 4 (100 psi)

e) Tension face at blast 3 f) Mid-span at blast 4 g) Bar rupture at blast 4

Figure 4-18 HSC-1%-NSS-#4: Photographs at the end of blasts 1-4

4.3.3.4 HSC-1%-NSS-15M

This column was the final specimen of the series built with HSFRC and conventional steel bars. Specimen configuration included high-strength fiber-reinforced concrete (1% fibers), 15M normal-strength steel bars (ρ= 3.44%), and non-seismic detailing (s= 75 mm). A total of four blasts were performed to test this specimen. The shockwave and displacement data are available in Table 4-3. Complete reflected pressure and impulse time histories and reflected pressure and displacement time histories are available in Figure 4-19. Photographs at the end of each blast along with close photographs of the affected regions are also available in Figure 4-20.

For blast 1 (17 psi), no visible effects were observed. The maximum mid-span displacement after this shot was 8.07 mm. The residual mid-span displacement was 0.41 mm. The strain gauge read a maximum strain of 0.0016 mm/mm (elastic behaviour).

Blast 2 (35 psi) resulted in a maximum mid-span displacement of 17.52 mm and a residual displacement of 4.01 mm (cumulative= 4.42 mm). Several hair-line cracks appeared at the maximum positive moment region, and their spacing followed the spacing at which the hoops were located. A maximum strain of 0.0092 mm/mm was recorded (plastic behaviour).

After blast 3 (80 psi), some damage appeared on the specimen. The maximum and residual mid-span displacements were 54.62 mm and 34.09 mm respectively. Cumulative residual displacement summed up to 38.49 mm. Two major cracks formed after this test in addition to other minor ones forming along the tension face as Figure 4-20 (e) shows. The major cracks’ widths were measured to be 9.4 and 5.9 mm in width. The compression zone was barely damaged and crushing was limited to only a small amount of concrete powder falling off the column. The strain gauge stopped working at this blast.

The fourth blast was the failure shot for this specimen. The maximum mid-span displacement was 120.52 mm, with a residual mid-span displacement of 92.24 mm, and final cumulative value of 130.73 mm. The failure manifested through two major cracks at mid-span as shown in Figure 4-20 (f) and (g), where the wider crack was 27.4 mm in width, while the other one was at 12 mm. Fibers pulled out at the location of these cracks, and hoops which were at the same location of the cracks were exposed. Despite this, spalling was limited. The compression zone was still in good shape, with the high compression strain capacity of fiber-reinforced concrete resisting the applied compression forces. Hinging occurred at both top and bottom supports, along with cracking on the tension side of those regions.

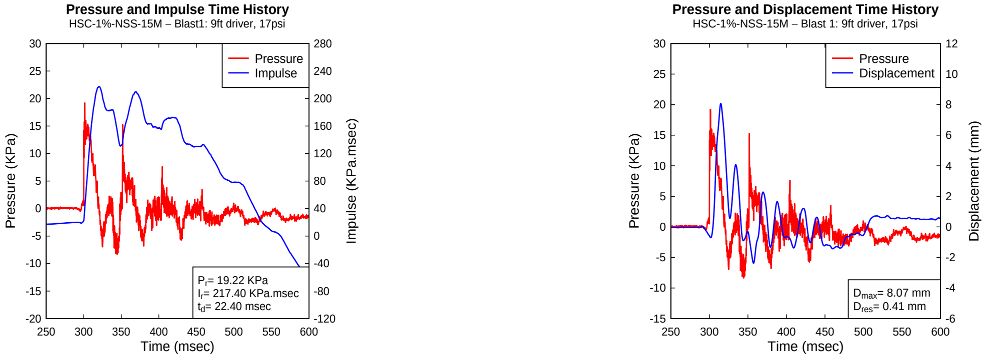

a) Blast 1: Reflected pressure, impulse, and displacement time histories

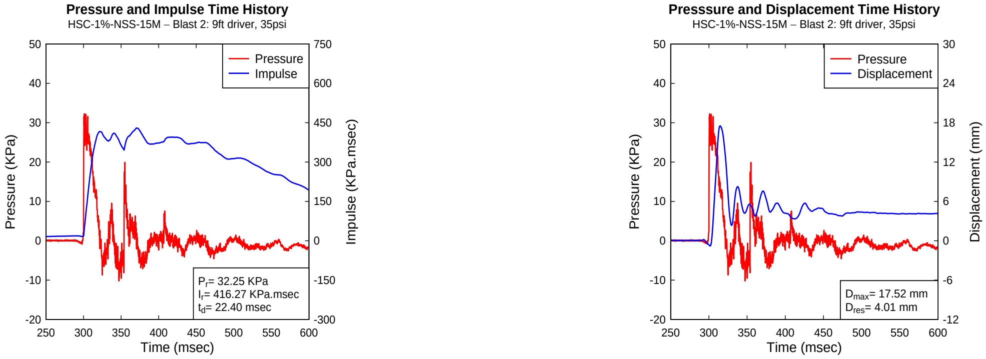

b) Blast 2: Reflected pressure, impulse, and displacement time histories

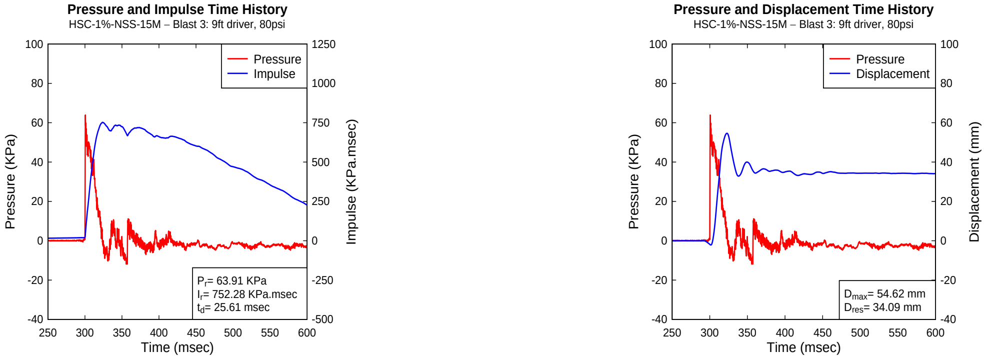

c) Blast 3: Reflected pressure, impulse, and displacement time histories

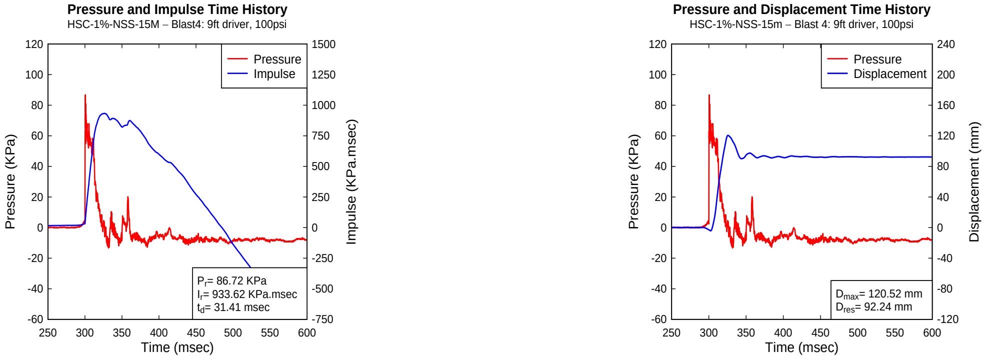

d) Blast 4: Reflected pressure, impulse, and displacement time histories

Figure 4-19 HSC-1%-NSS-15M: Recorded reflected pressure, impulse, and displacement for blasts 1-4

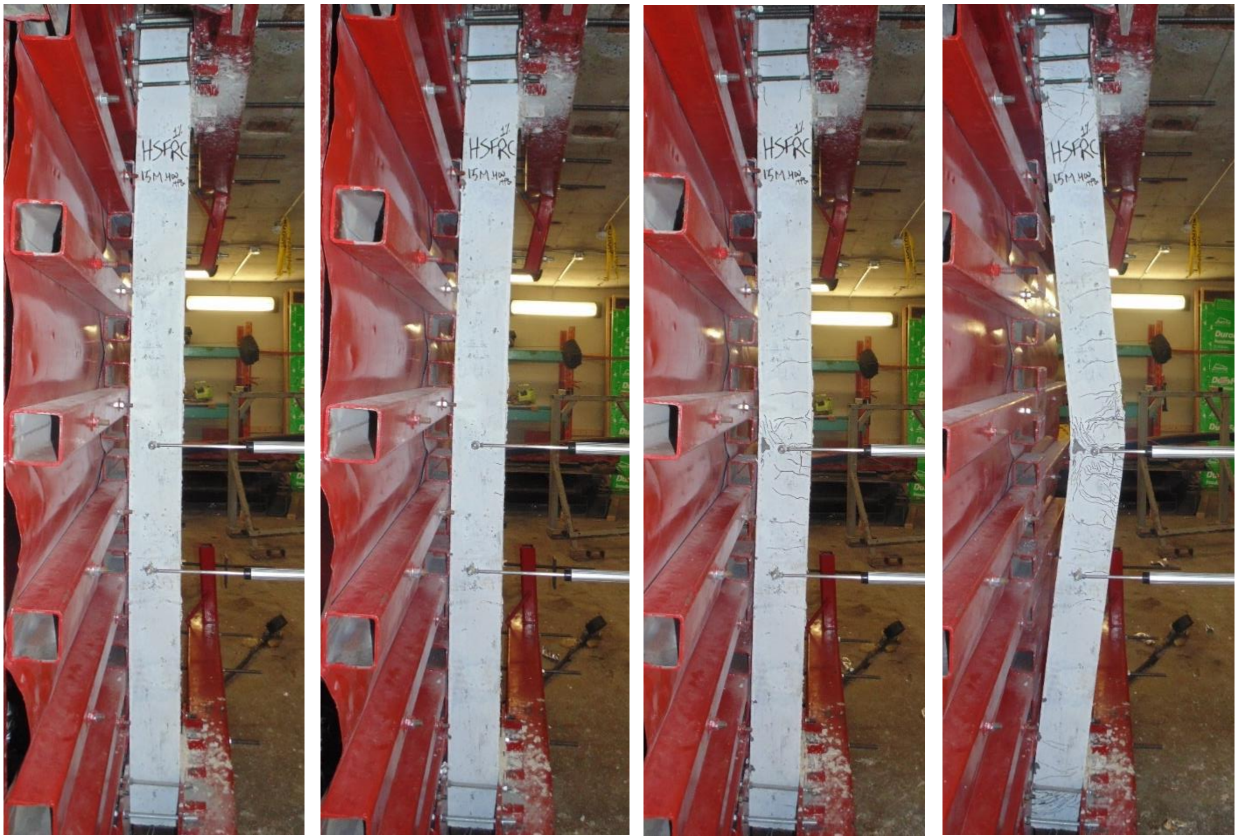

a) Blast 1 (17 psi) b) Blast 2 (35 psi) c) Blast 3 (80 psi) d) Blast 4 (100 psi)

e) Mid-span at blast 3 f) Mid-span at blast 4 g) Tension face at blast 4

Figure 4-20 HSC-1%-NSS-15M: Photographs at the end of blasts 1-4

4.3.4 HSC-MMFX Series

4.3.4.1 HSC-0%-MMFX-#3

The first column of the HSC-MMFX series was built with #3 high-strength bars (ρ= 1.22%) and plain high-strength concrete (no fibers). Non-seismic detailing was provided to the specimen (s= 75 mm). A total of four blasts were used to test the specimen until failure. The shockwave and displacement data can be found in Table 4-4. Complete reflected pressure and impulse time histories, as well as reflected pressure and displacement time histories are available in Figure 4-21. Selected photographs after each blast are also provided in Figure 4-22.

The first blast (17 psi) caused a mid-span maximum displacement of 9.15 mm and a residual displacement of 2.49 mm. Three hair-line cracks formed on the mid-height face; they were very thin and barely visible. Strain gauge indicated a strain of 0.0022 mm/mm which is well within the high elastic range of the MMFX bars.

Blast 2 (35 psi) caused further cracking on the tension face but they were all very thin and no major cracks were found among them. The maximum and residual displacement after this shot were 18.35 mm and 3.84 mm respectively, while the cumulative residual displacement was 6.33 mm. The strain gauge recorded a maximum value within the bar's elastic range equal to 0.0050 mm/mm.

Blast 3 (80 psi) resulted in some visible damage to the column. The maximum displacement was equal to 67.28 mm, while the residual displacement was equal to 25.74, which added up to be 32.07 mm as the column's cumulative residual displacement. Strain recorded was 0.0256 mm/mm, which is in the plastic range just below the strain gauge's capacity (0.0270 mm/mm). Random cracking appeared all over the tension face with the widest crack measuring 15.3 mm. Cracks propagated on the effective depth of the section, especially at mid-span, where cracks can be seen heading towards the very well damaged compression zone. Significant crushing of concrete occurred in that zone as shown by the high-speed video, where significant number of concrete fragments appear ejecting out of there.

Blast 4 (100 psi) was expected to have a severe impact on the specimen, so LVDTs were removed to save them from getting damaged. As expected, blast 4 inhibited a severe failure in the specimen, resulting in rupture of tension steel at both the mid-span region and the top support. Furthermore, the specimen completely pulled out of the bottom support (Figure 4-22 (d)), where the steel bars slipped out of the concrete base that was left in place in between the two bottom HSS supports. At mid-span, tension steel bars ruptured, which led to the fragmentation of the concrete in that region across the test area. At that region, the two halves of the column remained connected only through the two compression bars at the back, where no concrete remained after the intense fragmentation took place. The top support experienced rupture of tension steel (Figure 4-22 (g)), while the bottom support pulled out as mentioned before.

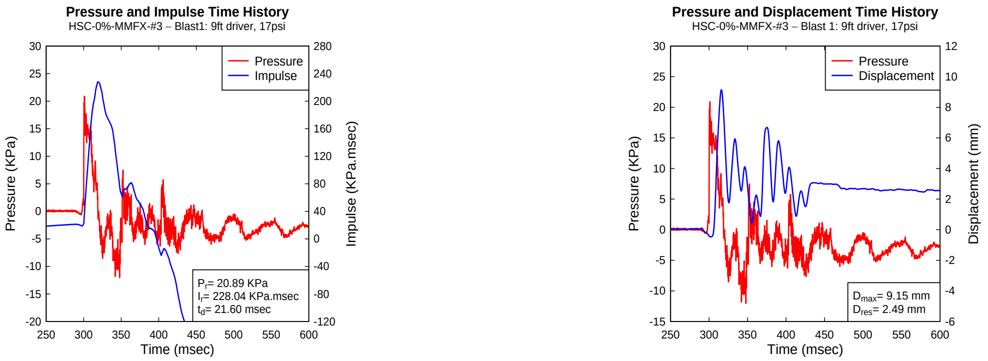

a) Blast 1: Reflected pressure, impulse, and displacement time histories

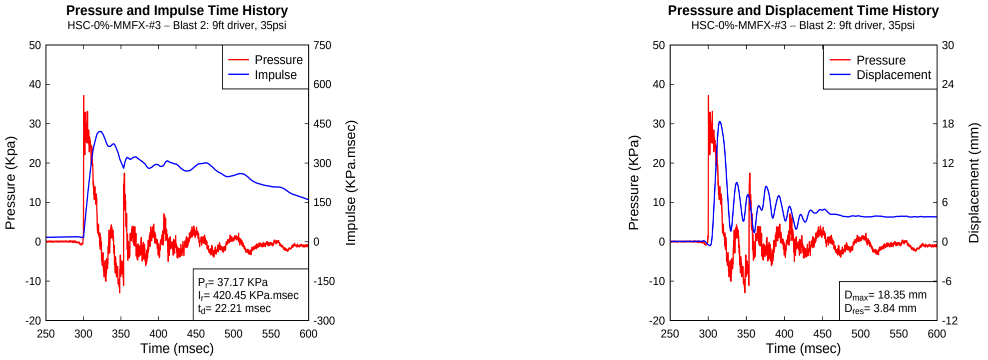

b) Blast 2: Reflected pressure, impulse, and displacement time histories

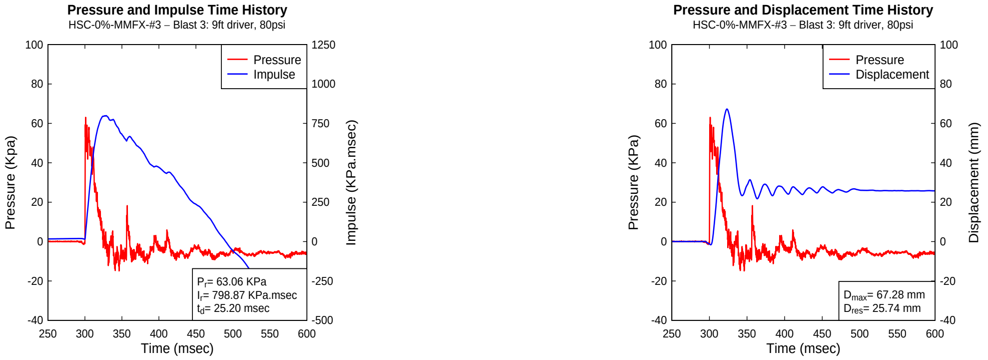

c) Blast 3: Reflected pressure, impulse, and displacement time histories

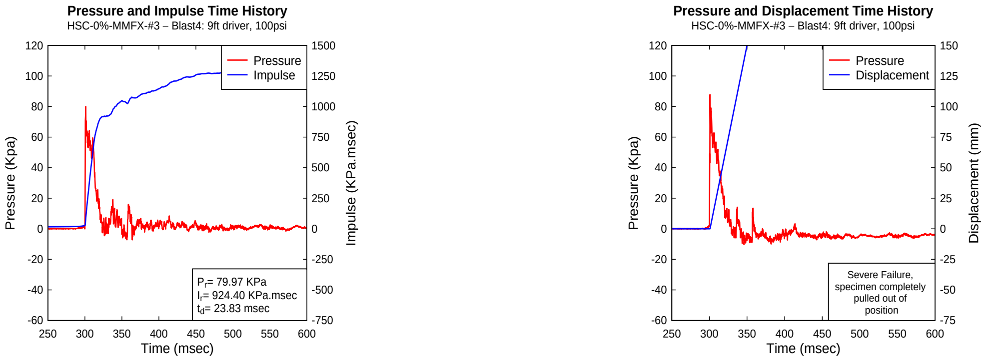

d) Blast 4: Reflected pressure, impulse, and displacement time histories

Figure 4-21 HSC-0%-MMFX-#3: Recorded reflected pressure, impulse, and displacement for blasts 1-4

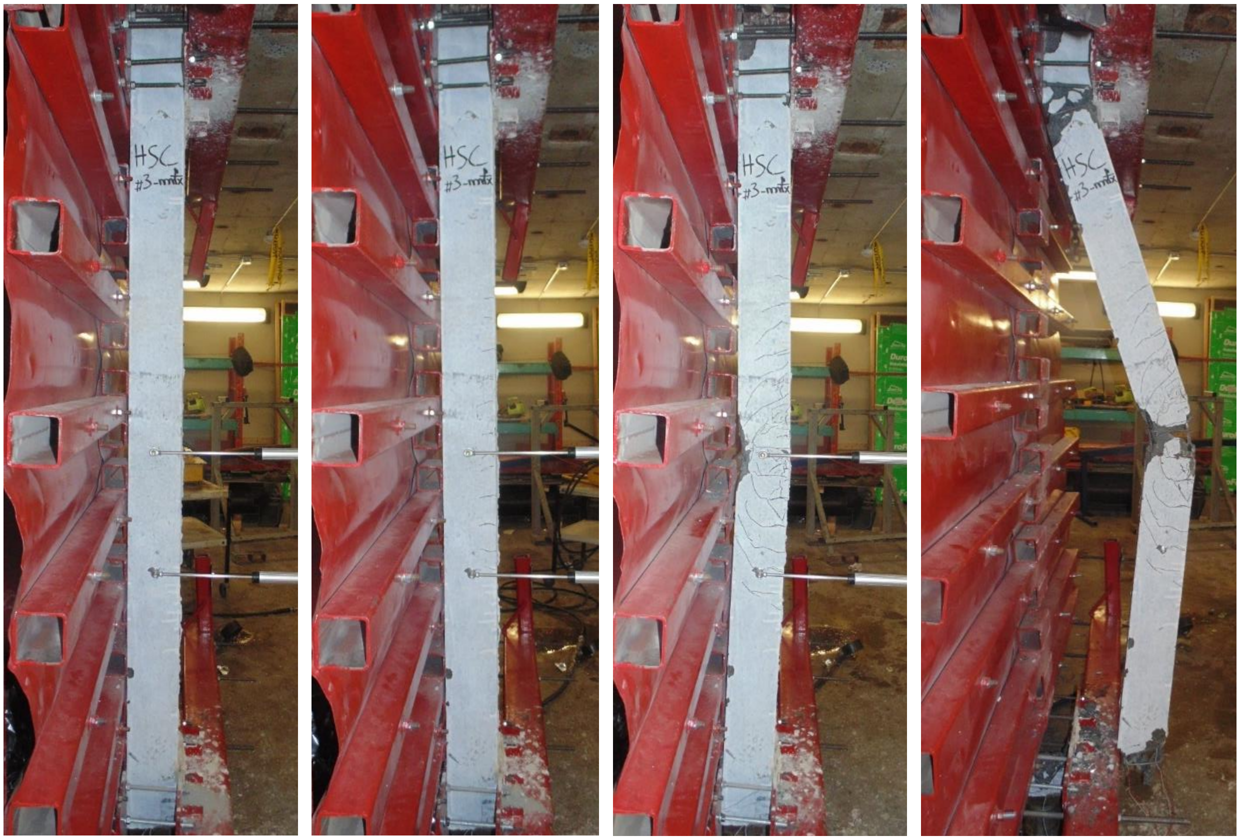

a) Blast 1 (17 psi) b) Blast 2 (35 psi) c) Blast 3 (80 psi) d) Blast 4 (100 psi)

e) Tension face at blast 3 f) Mid-span bar rupture at blast 4 g) Top support bar rupture at blast 4

Figure 4-22 HSC-0%-MMFX-#3: Photographs at the end of blasts 1-4

4.3.4.2 HSC-0%-MMFX-#4

The second column of this series was constructed with plain high-strength concrete, #4 MMFX bars (ρ= 2.22%) and non-seismic detailing (s=75 mm). It serves as a companion to column HSC-0%-NSS-#4 which had identical properties except for reinforcement type. It was tested under the effect of four blasts. The shockwave data and displacement are included in Table 4-4. Complete reflected pressure and impulse time histories along with reflected pressure and displacement time histories are provided in Figure 4-23. Photographs after various stages of testing are also available in Figure 4-24.

As usual, the first blast (17 psi) was to test the specimen within its elastic range. Mid-span displacements obtained were 9.65 mm for maximum and 3.16 mm for residual. The strain gauge recorded at the time of maximum displacement a maximum strain of 0.0022 mm/mm (elastic range). No visible effect was spotted on the specimen.

Blast 2 (35 psi) resulted in maximum and residual displacements equal to 16.76 mm and 3.33 mm respectively. The cumulative residual displacement was 6.49 mm. Several hair-line cracks formed along the tension face of the column, but none of them was major. A maximum strain of 0.0038 mm/mm was recorded, which means the MMFX bars were still within their elastic range.

Blast 3 (80 psi) led to a maximum mid-span displacement equal to 65.39 mm. The residual displacement was 10.97 mm, which left the column with a cumulative residual displacement equal to 17.46 mm. Cracks formed all over the tension face of the middle third of the column (Figure 4-24 (e)), where cracks from the previous shot propagated and widened, and the maximum crack width measured was equal to 1.8 mm. Damage also reached the compression zone through a fair amount of crushing along a 500 mm span. Cracks propagating form the tension side changed their horizontal projection and became inclined as they propagated towards the affected compression zone. Strain records after this shot showed some disturbance as the high strain values got close to the gauge's maximum capacity.

Blast 4 (100 psi) was the final shot for this column. Displacements recorded were 94.24 mm for maximum and 44.11 mm for residual. The specimen settled with a total residual displacement of 61.57 mm. Mid-span region experienced fragmentation as concrete cover spalled as shown in Figure 4-24 (f) and (g), where the two reinforcing bars were left exposed over a length of 75 mm. Unlike the previous specimen with #3 bars, no rupture was present at failure, although a slight amount of necking was visible on one of the exposed bars, indicating that the bars were pushed to near their limit. Significant crushing of concrete also occurred at the compression side of mid-span, where the high-speed video shows the formation of concrete fragments at failure. Compression steel bars were left exposed after concrete was lost from this location. The supports showed signs of hinging with some cracking, though the damage is much less severe when compared to the previous specimen with #3 bars.

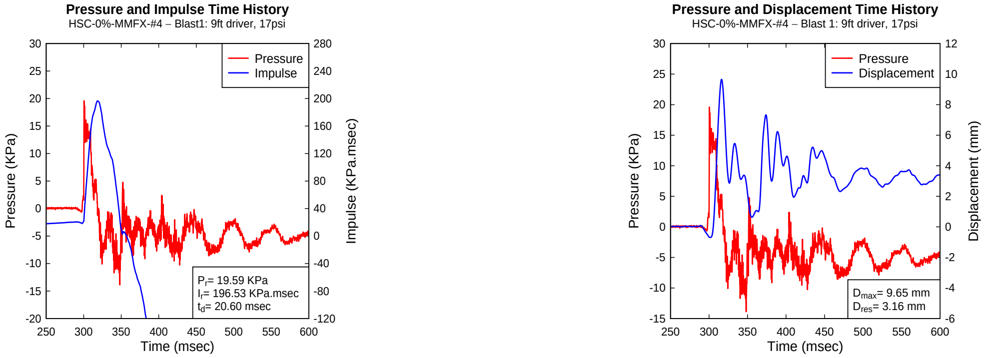
Pressure and Impulse Time History
HSC-0%-MMFX-#4 – Blast1: 9ft driver, 17psi
Pressure and Displacement Time History
HSC-0%-MMFX-#4 – Blast 1: 9ft driver, 17psi

a) Blast 1: Reflected pressure, impulse, and displacement time histories

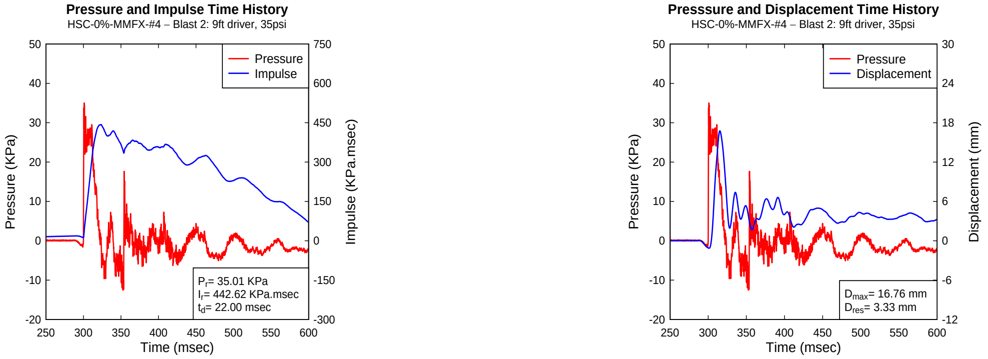
Pressure and Impulse Time History
HSC-0%-MMFX-#4 – Blast 2: 9ft driver, 35psi
Presssure and Displacement Time History
HSC-0%-MMFX-#4 – Blast 2: 9ft driver, 35psi

b) Blast 2: Reflected pressure, impulse, and displacement time histories

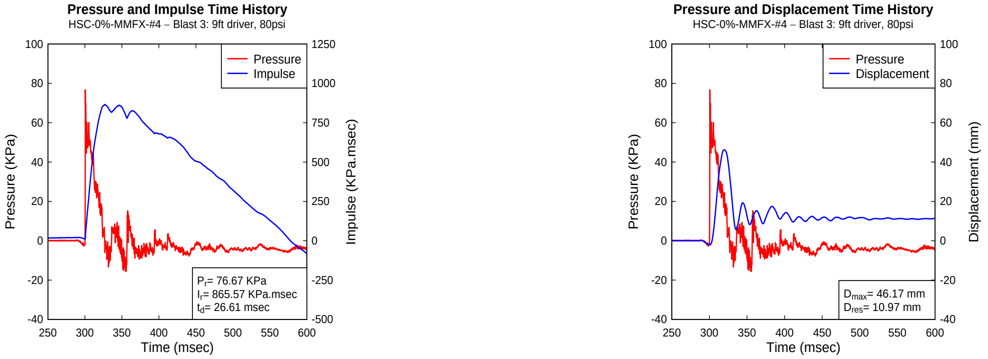
Pressure and Impulse Time History
HSC-0%-MMFX-#4 – Blast 3: 9ft driver, 80psi
Pressure and Displacement Time History
HSC-0%-MMFX-#4 – Blast 3: 9ft driver, 80psi

c) Blast 3: Reflected pressure, impulse, and displacement time histories

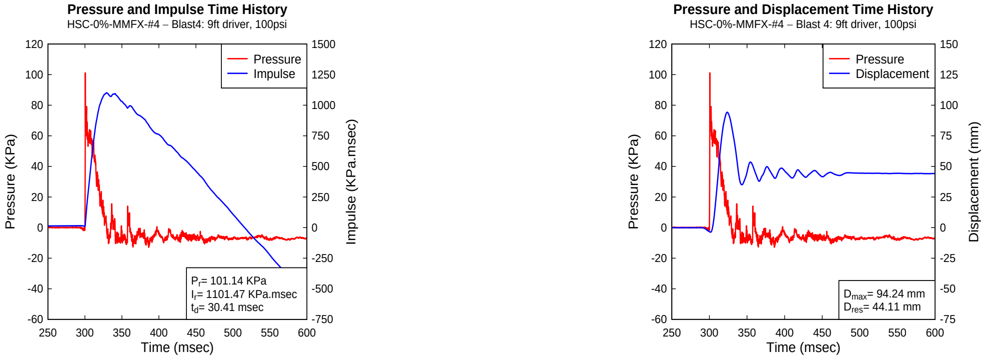
Pressure and Impulse Time History
HSC-0%-MMFX-#4 – Blast4: 9ft driver, 100psi
Pressure and Displacement Time History
HSC-0%-MMFX-#4 – Blast 4: 9ft driver, 100psi

d) Blast 4: Reflected pressure, impulse, and displacement time histories

Figure 4-23 HSC-0%-MMFX-#4: Recorded reflected pressure, impulse, and displacement for blasts 1-4

a) Blast 1 (17 psi) b) Blast 2 (35 psi) c) Blast 3 (80 psi) d) Blast 4 (100 psi)

e) Mid-span at blast 3 f) Mid-span at blast 4 g) Tension face at blast 4

Figure 4-24 HSC-0%-MMFX-#4: Photographs at the end of blasts 1-4

4.3.4.3 HSC-0%-MMFX-#4-S

This column had the same configuration as the previous specimen (plain HSC and #4 MMFX bars), except for the seismic detailing that was provided to this column, with the spacing of hoops set at s= 38 mm. The column was tested under the impact of four shots until failure. The shockwave and displacement data are available in Table 4-4. Complete reflected pressure and impulse time histories are available in Figure 4-25 as well as reflected pressure and displacement time histories. Selected photographs for the specimen after each test could be found in Figure 4-26. No strain gauge data is available for this specimen.

For the first blast (17 psi), the maximum and residual displacements were 6.82 mm and 2.01 mm respectively. No cracks were observed on the column.

Blast 2 (35 psi) resulted in a maximum mid-span displacement equal to 13.28 mm. The residual displacement was 2.16 mm, which makes the cumulative residual displacement equal to 4.17 mm. A few hair-line cracks at the middle of the column appeared but no major cracks were spotted.

For blast 3 (80 psi), a maximum displacement of 39.95 mm and a residual displacement of 8.88 mm were recorded at mid-span. The total residual displacement was 13.05 mm. The tension face of the middle third exhibited a lot of cracks after this shot as shown in Figure 4-26 (e). The widest cracks measured were equal to 1.5 mm and 1.2 mm. The compression zone experienced some signs of crushing as was previously noticed for the other columns of this series; this could be attributed to the high-strength steel bars that develop high-strains, which due to the balancing of tension and compression forces, results in the development of earlier crushing strains in the plain high-strength concrete.

The fourth blast (100 psi) was the failure shot for this specimen through rupture of tension steel at mid-span. The maximum mid-span displacement was equal to 84.30 mm. The residual mid-span displacement was 19.70 mm. Though the overall residual displacement for this specimen was not relatively high compared to other specimens (32.75 mm), the applied load seemed just enough to cause rupture in steel reinforcing bars at mid-span (Figure 4-26(g)). The steel bars could be seen through a wide crack opening at mid-height that extended to reach the crushed compression zone on the other side of the section (Figure 4-26 (f)). At the compression side, concrete fragments were shed during the blast, as also confirmed with the high-speed video. Similar to other columns, cracking is visible on the faces of both supports, but rotations and damage are less significant when compared to previous specimens due to the combined effect of high steel resistance and seismic detailing.

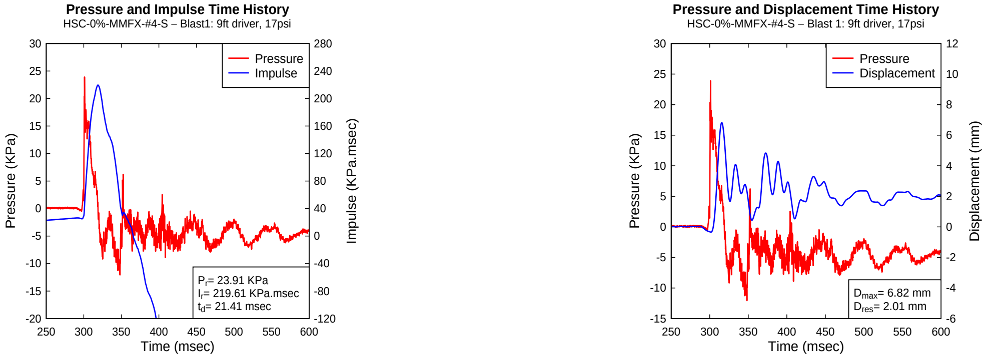

a) Blast 1: Reflected pressure, impulse, and displacement time histories

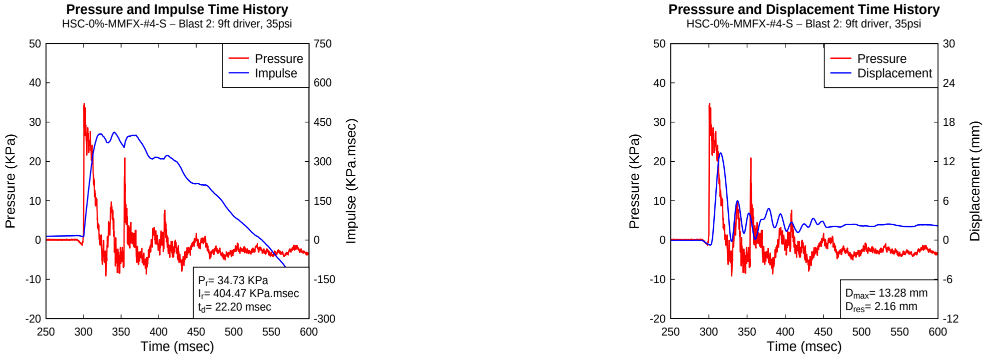

b) Blast 2: Reflected pressure, impulse, and displacement time histories

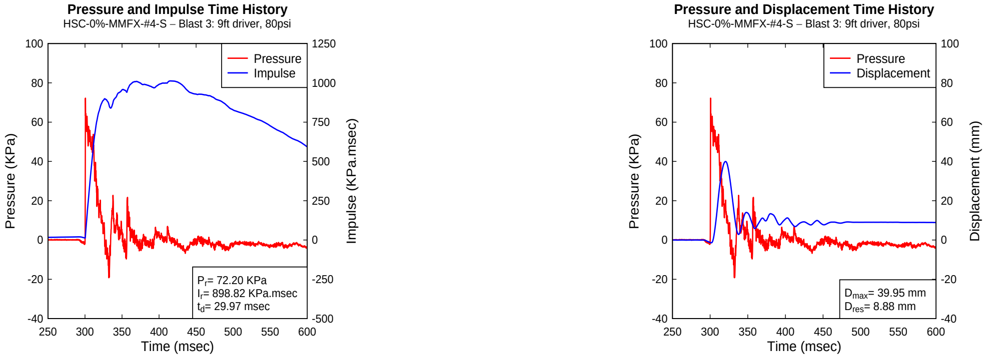

c) Blast 3: Reflected pressure, impulse, and displacement time histories

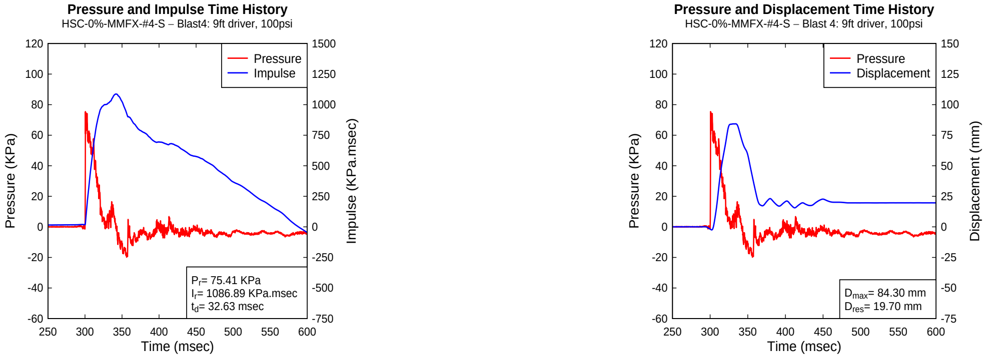

d) Blast 4: Reflected pressure, impulse, and displacement time histories

Figure 4-25 HSC-0%-MMFX-#4-S: Recorded reflected pressure, impulse, and displacement for blasts 1-4

a) Blast 1 (17 psi) b) Blast 2 (35 psi) c) Blast 3 (80 psi) d) Blast 4 (100 psi)

e) Mid-span at blast 3 f) Mid-span at blast 4 g) Bar rupture at blast 4

Figure 4-26 HSC-0%-MMFX-#4-S: Photographs at the end of blasts 1-4

4.3.4.4 HSC-0%-MMFX-#5

The last specimen of this set included the largest reinforcement ratio in the HSC-MMFX series, having #5 high-strength bars (ρ= 3.44%). The column was constructed with plain high-strength concrete, while the transverse reinforcement detailing was non-seismic. A total of five shots were required to push the column to failure. The shockwave data and displacement data are included in Table 4-4. Complete reflected pressure and impulse time histories and complete reflected pressure and displacement time histories are available in Figure 4-27. Selected photographs are also available in Figure 4-28. Strain gauge data is not available for this specimen.

Displacements due blast 1 (17 psi) were 8.74 mm for maximum and 4.09 mm for residual. No visible outcome was observed on the column.

The second blast (35 psi) resulted in maximum and residual displacements of 17.18 mm and 2.42 mm respectively (cumulative= 6.51 mm). Three hair-line cracks appeared on the mid-height face but no major cracks were observed.

Blast 3 (80 psi) outcome was the formation of more cracks along the tension face of the column and small chipping of concrete on the compression side. The displacements recorded after this shot were 37.06 mm for maximum and 11.15 mm for residual (cumulative= 17.66 mm).

As for blast 4 (100 psi), this specimen was the first one to survive it with no major damage. The maximum displacement due to this shot was 62.68 mm. The residual displacement was 24.85 mm, which adds up to a cumulative value of 42.51 mm. Cracks from the previous shot widened and propagated, along with the formation of more cracks all along the column’s face (Figure 4-28 (f)). The widest cracks were equal to 8.3 mm and 2.6 mm, in addition to chipping of a piece of concrete on the left edge of the column. The compression zone experienced some more crushing of concrete and the faces of both supports showed cracking.

The specimen was tested under the impact of an additional blast 5 (110 psi). Since the failure was expected to be severe, LVDTs were removed to save them from getting damaged. As expected, this shot caused severe failure of the specimen as the concrete fragments burst out of the column at the time of impact, which left the steel bars exposed over a length of 600 mm. In addition to the severe fragmentation, steel bars ruptured at mid span as shown Figure 4-28 (h). Displacements were recovered form high-speed video and found to be 183 mm for maximum and 148 mm for residual. The compression zone also went through serious crushing along a span corresponding to that over which tension damage happened (600 mm). Hinges formed at top and bottom supports, extensive cracking happened on their tension sides, and some crushing of concrete occurred on their compression side.

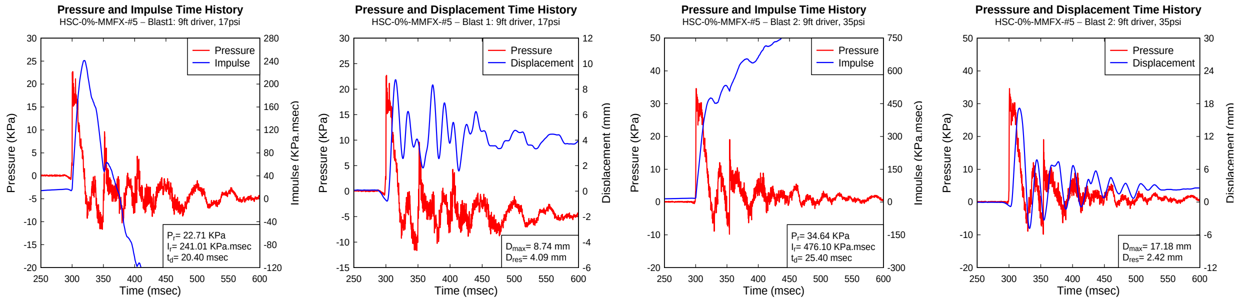

a) Blast 1: Reflected pressure, impulse, and displacement time histories

b) Blast 2: Reflected pressure, impulse, and displacement time histories

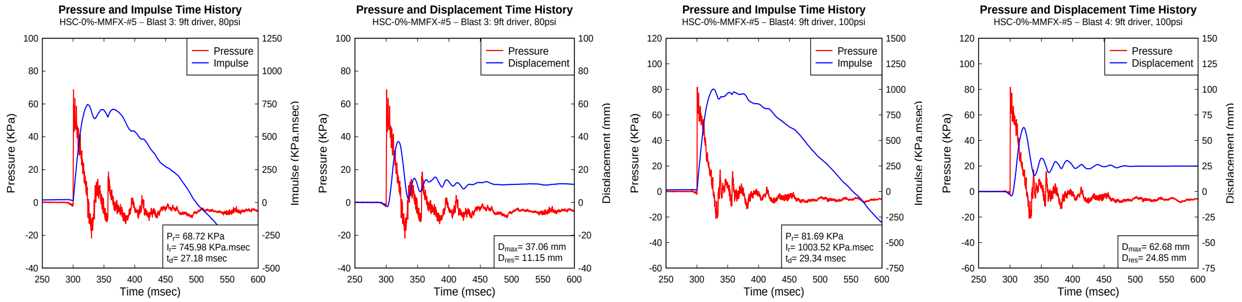

c) Blast 3: Reflected pressure, impulse, and displacement time histories

d) Blast 4: Reflected pressure, impulse, and displacement time histories

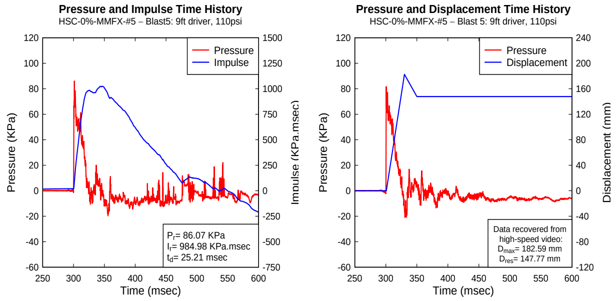

e) Blast 5: Reflected pressure, impulse, and displacement time histories

Figure 4-27 HSC-0%-MMFX-#5: Recorded reflected pressure, impulse, and displacement for blasts 1-5

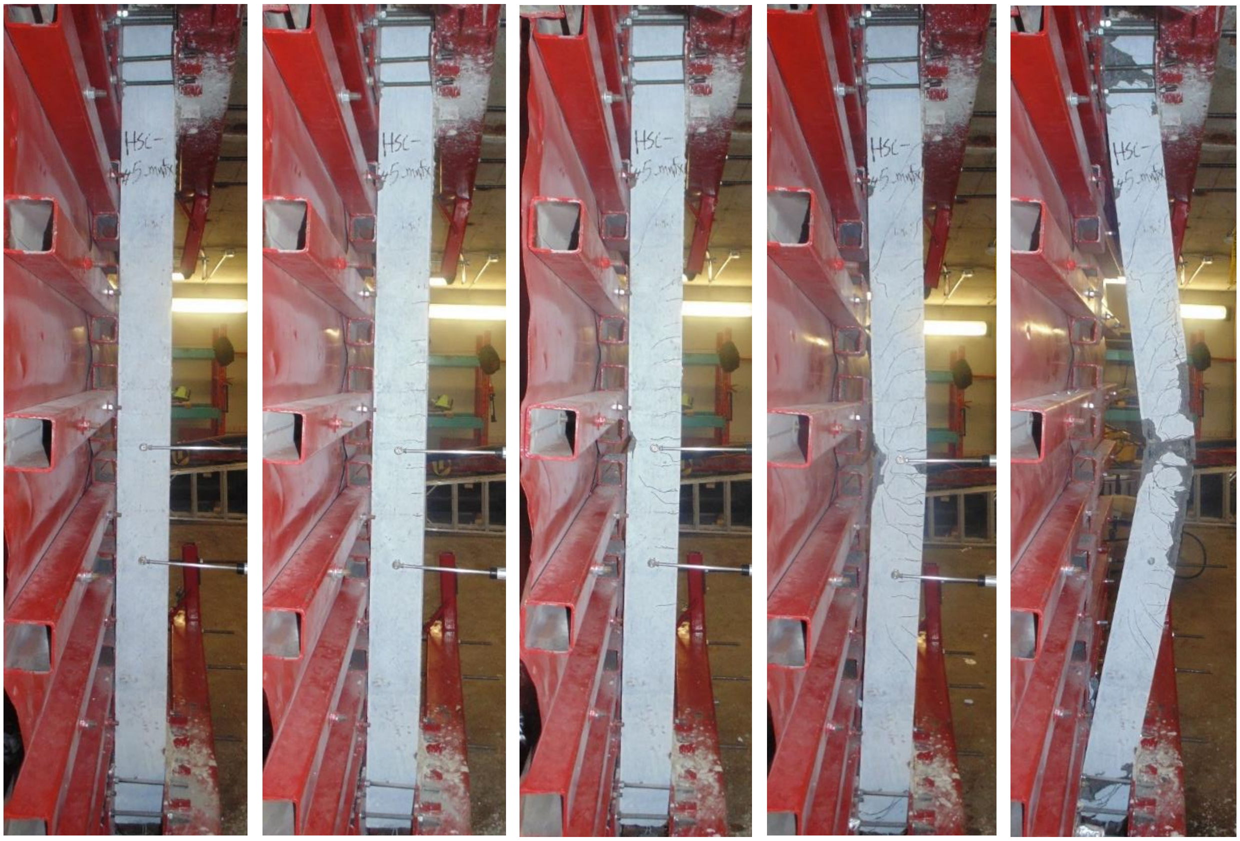

a) Blast 1 (17 psi) b) Blast 2 (35 psi) c) Blast 3 (80 psi) d) Blast 4 (100 psi) e) Blast 5 (110 psi)

f) Mid-span at blast 4 g) Mid-span at blast 5 h) Tension face and bar rupture at blast 5

Figure 4-28 HSC-0%-MMFX-#5: Photographs at the end of blasts 1-5

4.3.5 HSFRC-MMFX Series

4.3.5.1 HSC-1%-MMFX-#3

The last series of specimens was built with high-strength fiber-reinforced concrete (HSFRC) and high-strength MMFX reinforcement. The first column of this series included #3 MMFX bars (ρ= 1.22%). As with all other columns in this series, HSFRC contained 1% steel fibres, while transverse reinforcement had non-seismic detailing (s = 75 mm). The column was tested under the effect of four blasts until failure. The shockwave and displacement data are provided in Table 4-5. Complete reflected pressure and impulse time histories as well as complete reflected pressure and displacement time histories are available in Figure 4-29. Selected photographs for various stages of testing are provided in Figure 4-30. No strain gauge data is available in this column.

Blast 1 (17 psi) resulted in a maximum mid-span displacement of 12.37 mm and a residual displacement of 2.16 mm. Several hair-line cracks were visible on the mid-height of the section.

Blast 2 (35 psi) produced a maximum mid-span displacement of 25.18 mm. The residual displacement was 5.84 mm (cumulative= 8.00 mm). Number of cracks increased along the middle third's face of the specimen, while cracks from previous the blast stretched and widened, but none of these cracks were considered to be major.

Blast 3 (80 psi) caused noticeable damage to the specimen. The maximum and residual mid-span displacements were 98.92 mm and 26.02 mm respectively (cumulative= 34.02 mm). A wide crack opened at the column's mid-height (width = 32 mm) and propagated towards the slightly damaged compression zone as shown in Figure 4-30 (e). The compression zone lost some concrete powder but further crushing was prevented by the presence of fibers.

Blast 4 (100 psi) triggered a severe failure in the column. Tension steel ruptured at mid-span and at both supports. Displacement history data are not available because the LVDTs were removed to avoid getting them damaged, therefore the high-speed video was used to recover displacement values. As for mid-span, the specimen displaced a very high value of 517 mm. Bar rupturing resulted in a straight cut through the concrete at mid-span in which the two halves of the column were kept connected only through the two compression bars. Significant hinging also occurred at both supports, with the steel bars on the tension side rupturing at both locations. Despite the brittle failure, concrete fragmentation was less (i.e. concrete held together) when compared to the companion column built with plain HSC (HSC-0%-MMFX-#3)

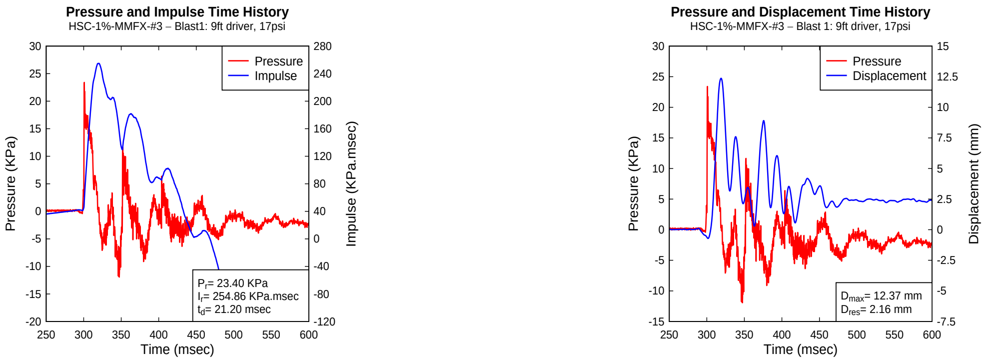

a) Blast 1: Reflected pressure, impulse, and displacement time histories

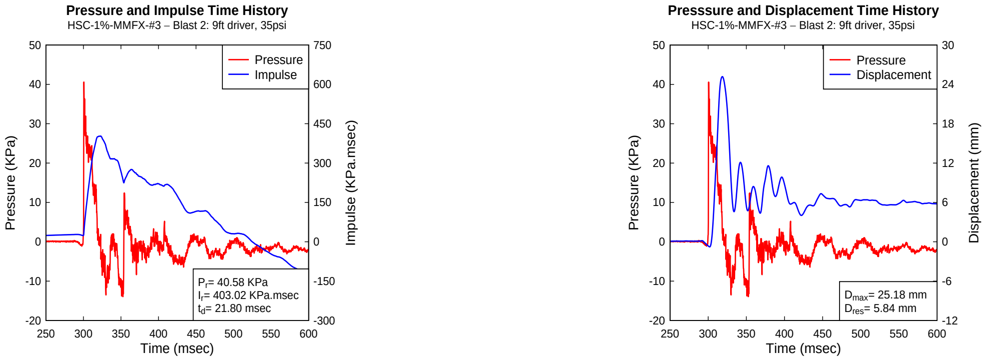

b) Blast 2: Reflected pressure, impulse, and displacement time histories

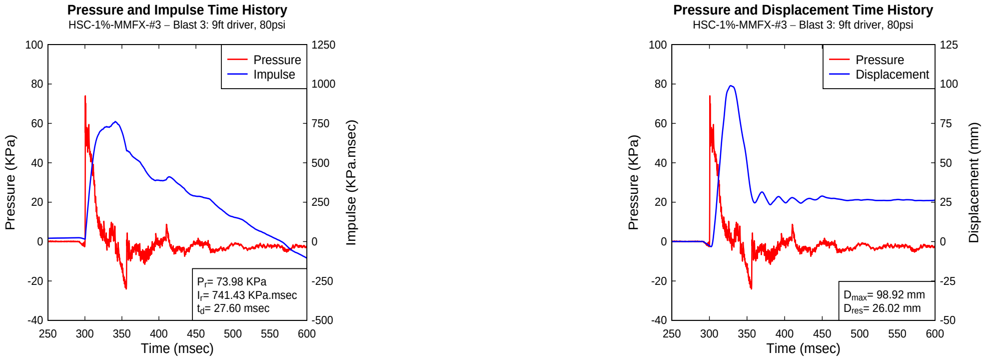

c) Blast 3: Reflected pressure, impulse, and displacement time histories

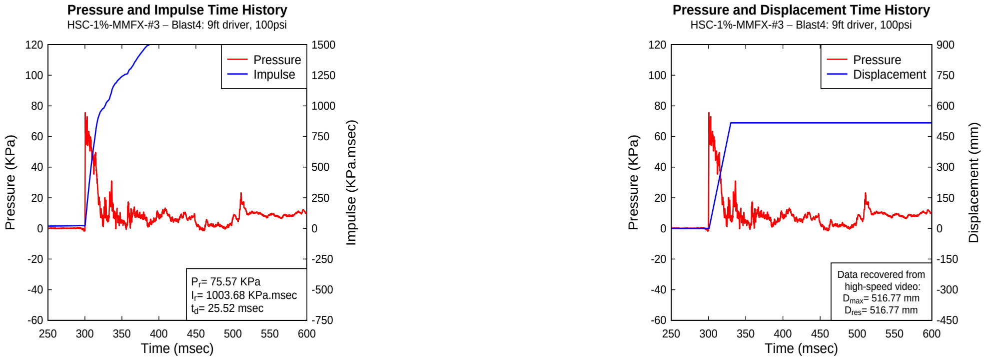

d) Blast 4: Reflected pressure, impulse, and displacement time histories

Figure 4-29 HSC-1%-MMFX-#3: Recorded reflected pressure, impulse, and displacement for blasts 1-4

a) Blast 1 (17 psi) b) Blast 2 (35 psi) c) Blast 3 (80 psi) d) Blast 4 (100 psi)

e) Mid-span at blast 3 f) Mid-span and bar rupture at blast 4 g) Top hinge and bar rupture at blast 4

Figure 4-30 HSC-1%-MMFX-#3: Photographs at the end of blasts 1-4

4.3.5.2 HSC-1%-MMFX-#4

The second HSFRC column of this series increased the high-strength reinforcement ratio to ρ= 2.22% using #4 MMFX bars for the main reinforcement, with hoops assembled at s= 75 mm (non-seismic detailing) and fiber content remaining at 1%. The specimen was tested under four blasts. The shockwave and displacement data are provided in Table 4-5. Complete reflected pressure and impulse time histories and complete reflected pressure and displacement time histories are available in Figure 4-31. Selected photographs of the column after each test are available in Figure 4-32. No strain gauge data is available for this column.

Blast 1 (17 psi) didn’t have any impact on the column as it was within its elastic capacity. The maximum and residual mid-span displacements were 6.07 mm and 2.17 mm respectively.

Blast 2 (35 psi) resulted in several very thin cracks along the tension face of the column. The maximum displacement recorded was 13.25 mm. As for the residual displacement, it was 3.58 mm, which summed up to be 5.75 mm as the cumulative residual displacement.

Blast 3 (80 psi) outcome was the generation of more cracks along the column’s tension side, with cracks form the previous blast propagating and opening-up further (Figure 4-32(e)). The major crack width detected was equal to 3.4 mm. The compression zone was not affected by this shot. The maximum displacement recorded after this shot was 40.65 mm. The residual displacement recorded was 14.64 mm, while the cumulative residual displacement added up to 20.39 mm.

The fourth and final blast (100 psi) was also the failure shot for the column through rupture of tension steel. The displacements recorded were 99.02 mm for maximum and 33.80 mm for residual, which left the column with a total residual displacement of 54.19 mm. Cracks followed the same pattern as before, spaced according to the hoop spacing, and propagating all across the cross section of the column. As for the major crack, it was localized at mid-height, in which it opened-up to a width of 20.5 mm. Fiber pull-out occurred at that spot, but for other cracks, fibers were still holding concrete together and yet to pull-out. Through the opening mentioned, the steel bars could be seen still in contact at the rupture location and did not initially show signs of rupture, but as soon as the specimen was leaned a little while taking it out of the setup, the failure at the rupture location was detected (Figure 4-32 (g)). Both top and bottom supports suffered hinging and showed cracking on their tension sides, while the compression zone remained intact as the fibers augmenting the concrete’s crushing strain-capacity.

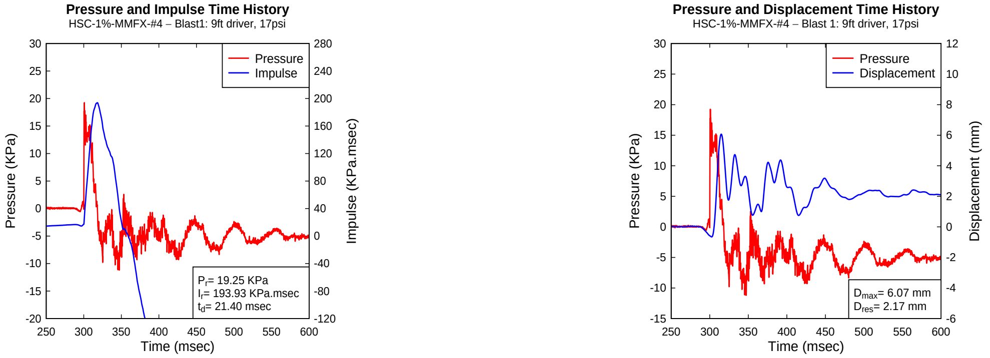

a) Blast 1: Reflected pressure, impulse, and displacement time histories

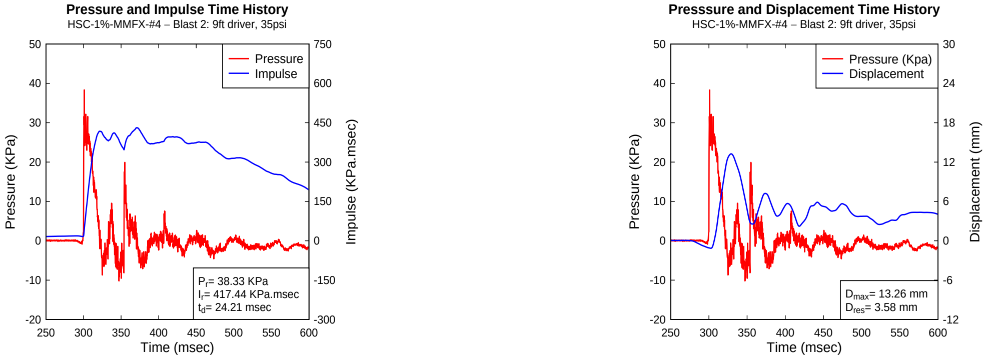

b) Blast 2: Reflected pressure, impulse, and displacement time histories

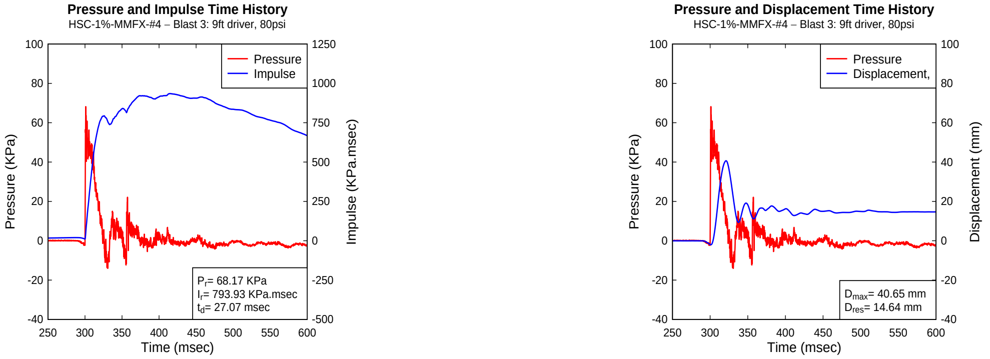

c) Blast 3: Reflected pressure, impulse, and displacement time histories

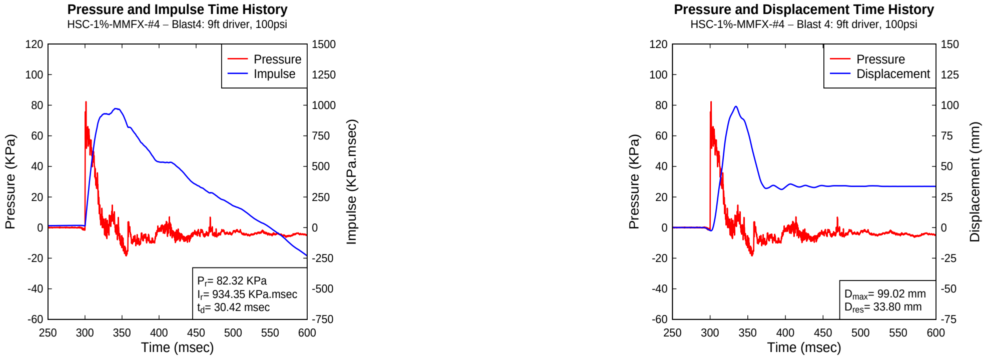

d) Blast 4: Reflected pressure, impulse, and displacement time histories

Figure 4-31 HSC-1%-MMFX-#4: Recorded reflected pressure, impulse, and displacement for blasts 1-4

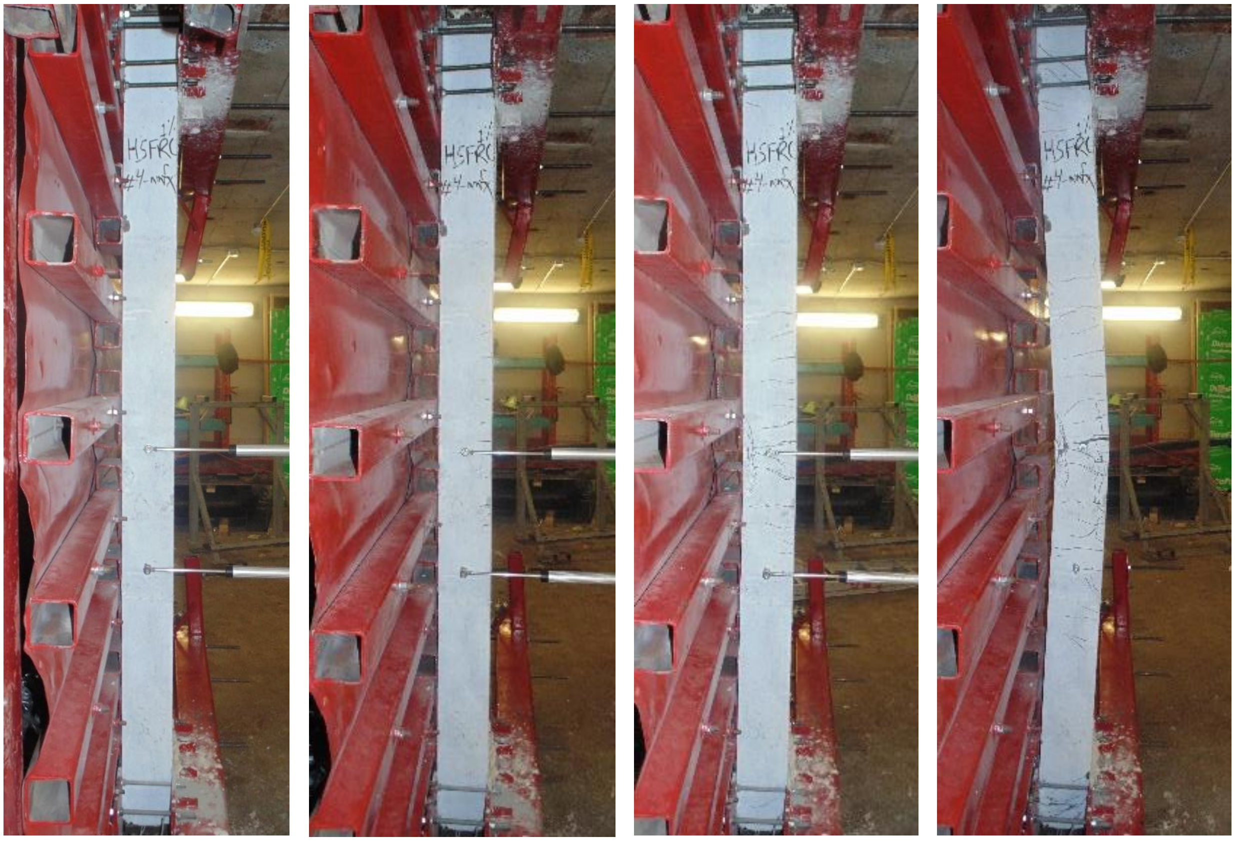

a) Blast 1 (17 psi) b) Blast 2 (35 psi) c) Blast 3 (80 psi) d) Blast 4 (100 psi)

e) Mid-span at blast 3 f) Mid-span at blast 4 g) Bar rupture at blast 4

Figure 4-32 HSC-1%-MMFX-#4: Photographs at the end of blasts 1-4

4.3.5.3 HSC-1%-MMFX-#5

The last specimen of this series and for this experimental program was constructed with #5 MMFX bars (ρ= 3.44%), HSFRC (1% fibers), and had non-seismic detailing (s = 75 mm). The specimen was expected to be the one with the most resistance among its companions, and indeed it needed five blast to be pushed to failure. The shockwave and displacement data are listed in Table 4-5. Figure 4-33 shows the complete reflected pressure and impulse time histories and the complete reflected pressure and displacement time histories. Figure 4-34 shows selected photographs of the specimen after each stage of testing.

Blast 1 (17 psi) did not have any clear influence on the column. The maximum and residual displacements were equal to 9.23 mm and 3.48 mm. Strain gauge data showed a value of a maximum strain within the bar's elastic range equal to 0.0011 mm/mm.

The second blast (35 psi) led to a maximum displacement of 15.59 mm and a residual displacement of 4.36 mm (cumulative= 7.84 mm). Two very thin cracks were spotted at mid-span but they were barely visible. A maximum strain equal to 0.0027 mm/mm was obtained, which is still within the elastic range of the MMFX rebar.

After blast 3 (80 psi), cracks were generated on the tension face but none of them was classified as major. The displacements recorded after this shot were 33.20 mm for maximum and 10.04 mm for residual (cumulative= 17.88 mm), respectively. The strains in tension steel bars showed a maximum strain of 0.0040 mm/mm at the time of maximum displacement (still within elastic range).

The specimen survived blast 4 (100 psi) with no major damage. Cracks continued to propagate and widen due to this shot, and the major crack width measured was equal to 5.7 mm. Displacements recorded due to this blast were 55.39 mm for maximum and 21.54 mm for residual (cumulative= 50.92 mm). The compression zone was not affected by the blast, and cracks formed on the tension side at the face of the supports.

A fifth test was conducted on the specimen. Blast 5 (110 psi) pushed the tension steel bars to rupture. The maximum mid-span displacement for this shot was 87.89 mm. The residual displacement was equal to 42.44 mm, which left the column with a final residual displacement of 138.81 mm. Rupture of tension steel was examined through a major crack (width = 18.2 mm) at mid-span (Figure 4-34 (g) and (h)). The identification of steel rupture was not possible until the specimen was taken out of position as the major crack opened up more during the process (i.e., the crack was not initially wide enough to detect bar rupture with the steel bar remaining in contact at the rupture location). Other cracks formed on the tension face, two of them classified as major and located above the primary one at mid-span as shown in Figure 4-34 (g). The compression zone remained nearly intact with high-speed video showing only the formation of fine concrete powder at the time of failure. Both supports developed hinging and cracks formed along their tension sides.

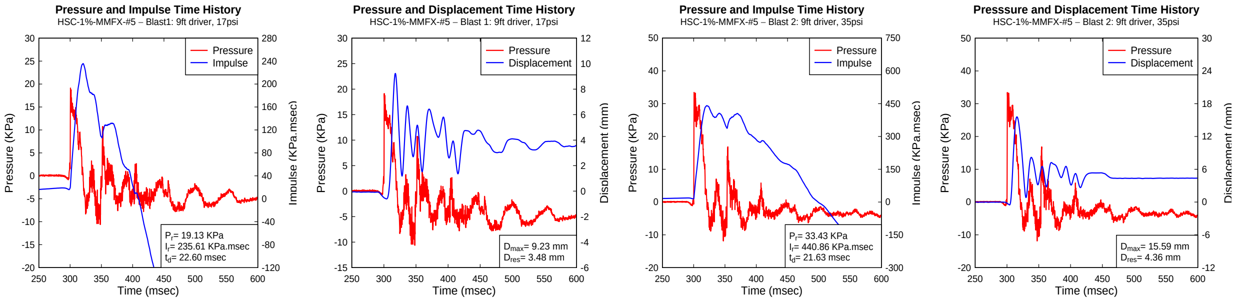

a) Blast 1: Reflected pressure, impulse, and displacement time histories

b) Blast 2: Reflected pressure, impulse, and displacement time histories

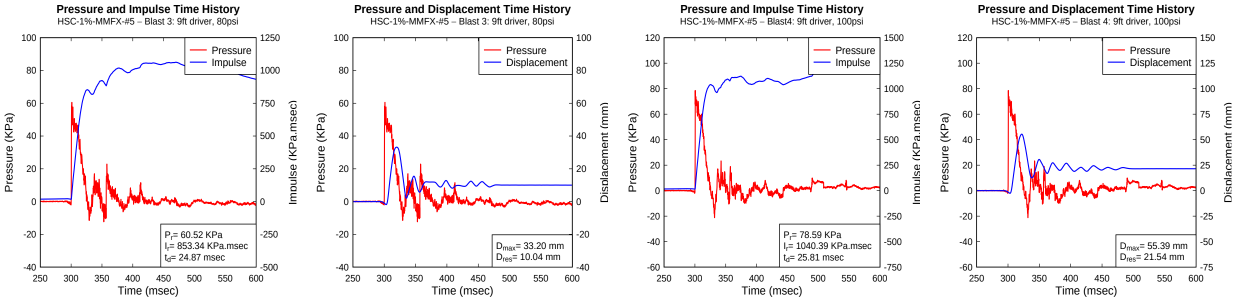

c) Blast 3: Reflected pressure, impulse, and displacement time histories

d) Blast 4: Reflected pressure, impulse, and displacement time histories

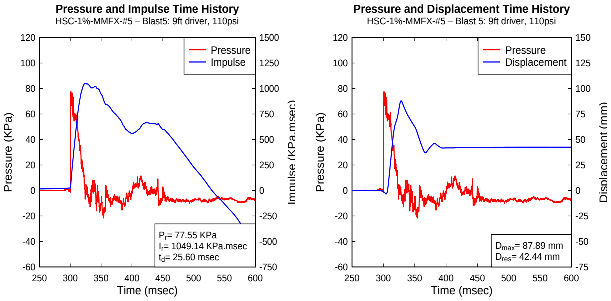

e) Blast 5: Reflected pressure, impulse, and displacement time histories

Figure 4-33 HSC-1%-MMFX-#5: Recorded reflected pressure, impulse, and displacement for blasts 1-5

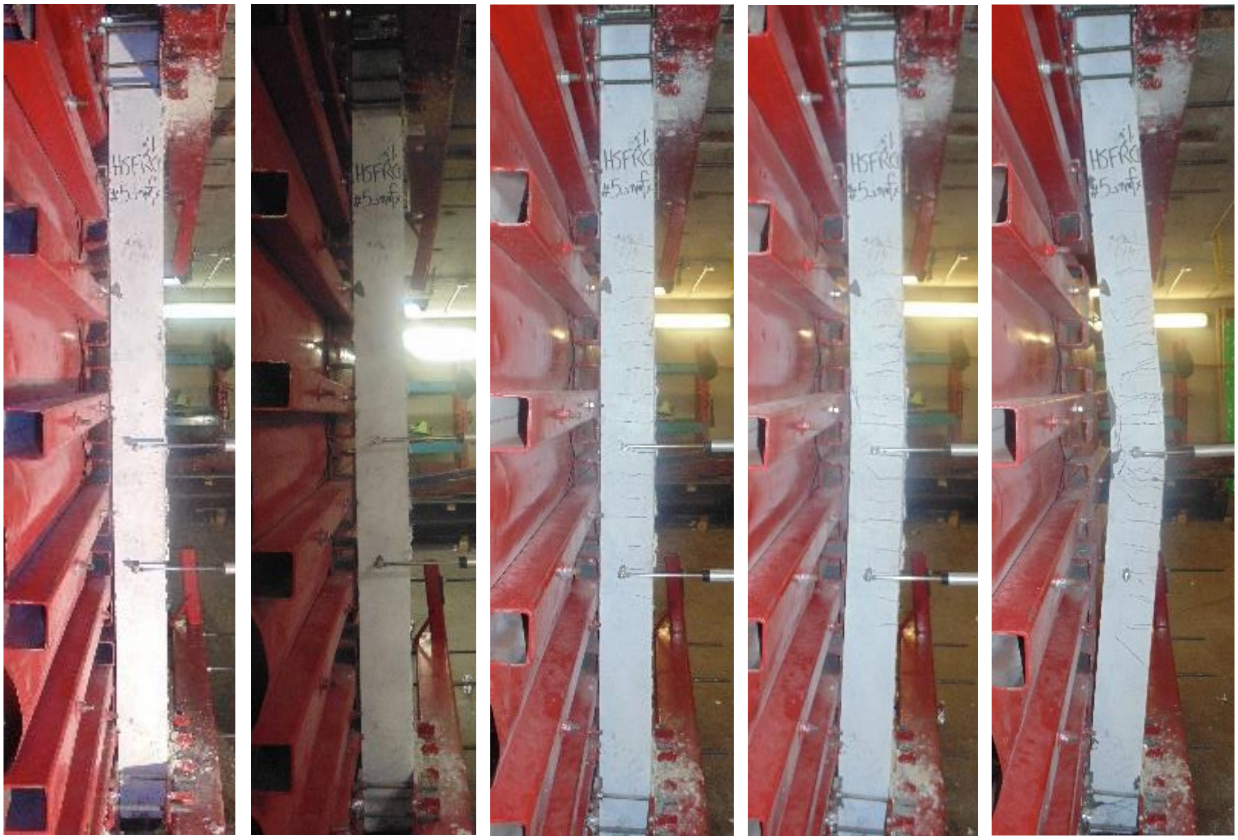

a) Blast 1 (17 psi)

b) Blast 2 (35 psi)

c) Blast 3 (80 psi)

d) Blast 4 (100 psi)

e) Blast 5 (110 psi)

f) Mid-span at blast 4

g) Mid-span at blast 5

h) Bar rupture at blast 5

Figure 4-34 HSC-1%-MMFX-#5: Photographs at the end of blasts 1-4

CHAPTER 5. DISCUSSION OF EXPERIMENTAL RESULTS

5.1 Chapter Overview

This chapter compares and discusses the experimental results presented in the previous chapter. Comparisons between different specimens is carried out to examine the effect of different parameters on the blast performance of the high-strength reinforced concrete columns. Parameters studied include the effect of longitudinal steel reinforcement ratio, longitudinal steel reinforcement type, steel fibers, steel fiber content, concrete strength, and seismic detailing. The criteria used in the discussion of results includes the mid-span displacements at equivalent blasts, overall blast resistance, failure modes and damage. This chapter is divided into several sections as follows:

<u>Effect of steel reinforcement ratio</u>

- Effect of normal-strength steel reinforcement ratio
    - In HSC series: HSC-0%-NSS-10M vs. HSC-0%-NSS-#4 vs. HSC-0%-NSS-15M
    - In HSFRC series: HSC-1%-NSS-10M vs. HSC-1%-NSS-#4 vs. HSC-1%-NSS-15M
- Effect of high-strength steel reinforcement ratio (MMFX)
    - In HSC series: HSC-0%-MMFX-#3 vs. HSC-0%-MMFX-#4 vs. HSC-0%-MMFX-#5
    - In HSFRC series: HSC-1%-MMFX-#3 vs. HSC-1%-MMFX-#4 vs. HSC-1%-MMFX-#5

<u>Effect of steel reinforcement type</u>

- In HSC series:
    - HSC-0%-NSS-#4 vs. HSC-0%-MMFX-#4
    - HSC-0%-NSS-15M vs. HSC-0%-MMFX-#5
- In HSFRC series:
    - HSC-1%-NSS-#4 vs. HSC-1%-MMFX-#4
    - HSC-1%-NSS-15M vs. HSC-1%-MMFX-#5
- In HSC series with different reinforcement ratios:
    - HSC-0%-NSS-10M vs. HSC-0%-MMFX-#3
    - HSC-0%-NSS-#15M vs. HSC-0%-MMFX-#4

<u>Effect of steel fibers</u>

- In columns with NSS bars
    - HSC-0%-NSS-10M vs. HSC-1%-NSS-10M
    - HSC-0%-NSS-#4 vs. HSC-1%-NSS-#4
    - HSC-0%-NSS-15M vs. HSC-1%-NSS-15M

- In columns with MMFX bars
    - HSC-0%-MMFX-#4 vs. HSC-1%-MMFX-#4
    - HSC-0%-MMFX-#5 vs. HSC-1%-MMFX-#5

Effect of steel fibers content

- In columns with 10M NSS bars
    - HSC-0%-NSS-10M vs. HSC-0.5%-NSS-10M vs. HSC-1%-NSS-10M

Effect of Concrete strength

- In NSC and HSC columns
    - NSC-0%-NSS-#4 vs. HSC-0%-NSS-#4
    - NSC-0%-NSS-15M vs. HSC-0%-NSS-15M

Effect of seismic detailing

- In columns with 10M NSS and #4 MMFX bars
    - HSC-0%-NSS-10M vs. HSC-0%-NSS-10M-S
    - HSC-0%-MMFX-#4 vs. HSC-0%-MMFX-#4-S

5.2 General Observations

Figure 5-1 to Figure 5-5 show a summary of the results acquired for all the columns. The results are displayed in comparative bar charts of mid-span displacements (maximum and residual) for each of the blast intensities used in this experimental program.

As expected the increase in reinforcement ratio leads to improvements in blast performance, for columns with both normal-strength and high-strength reinforcement, and for all concrete types.

Enhancements are also observed whenever innovative materials (like high-strength steel and steel fibers) were utilized over traditional materials.

The effects of concrete strength and seismic detailing are not as significant.

The trends are not as clear for the first blast (17 psi) which aimed at testing the specimens under elastic conditions, and therefore the discussions in the subsequent sections will focus on the results from Blasts 2 to 5.

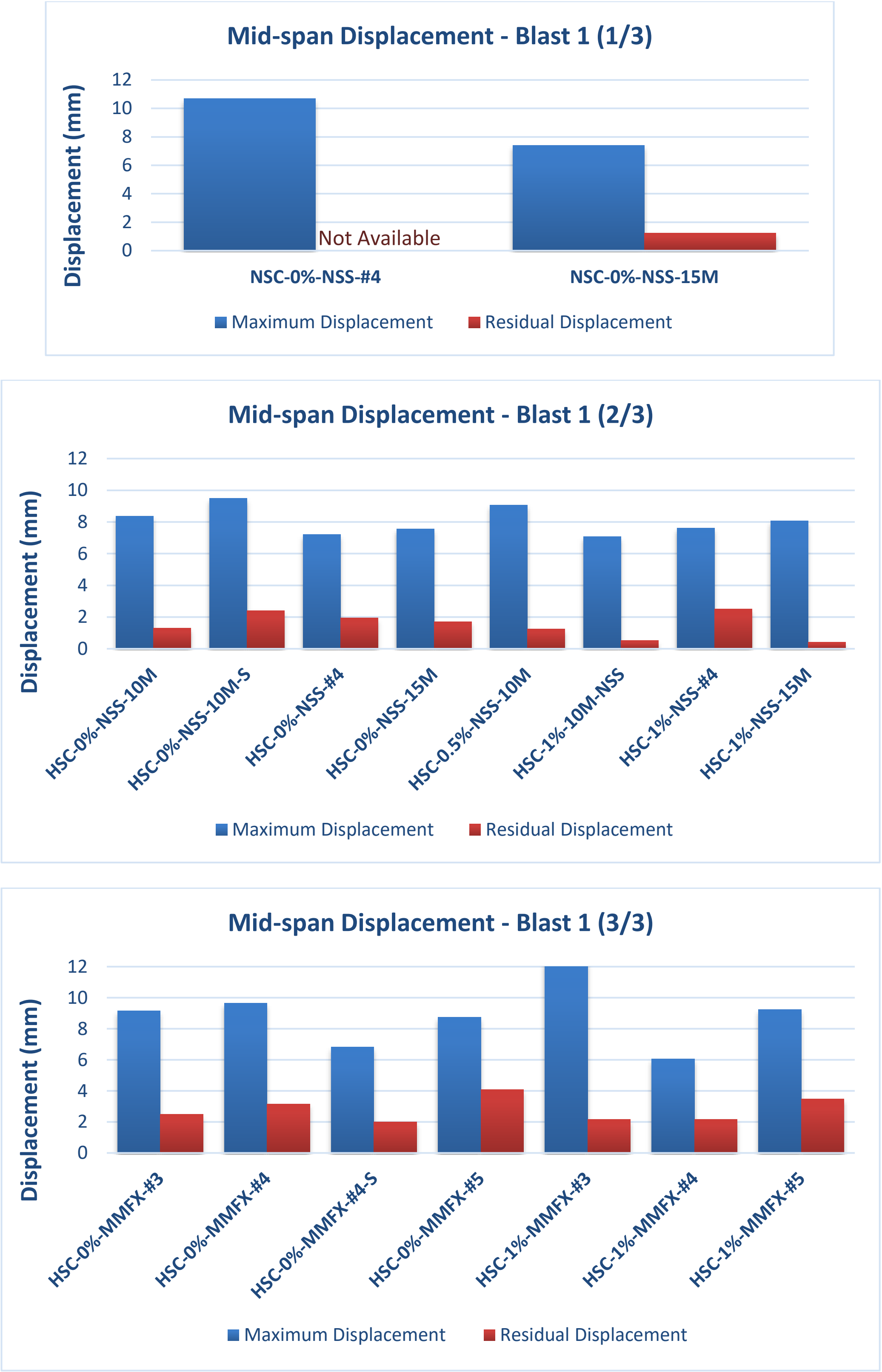

Figure 5-1 Mid-span displacements for all columns for blast 1

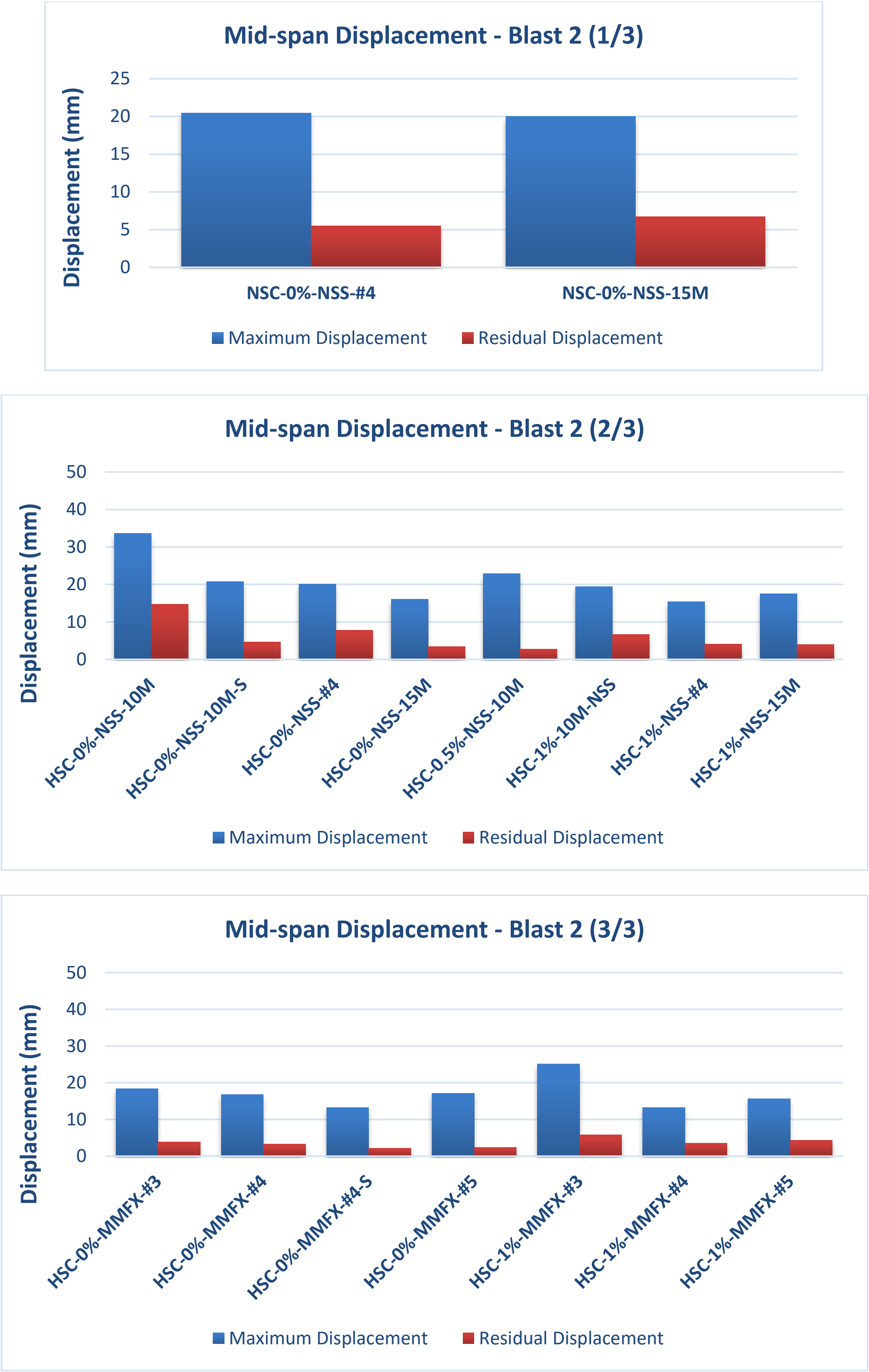

Figure 5-2 Mid-span displacements for all columns for blast 2

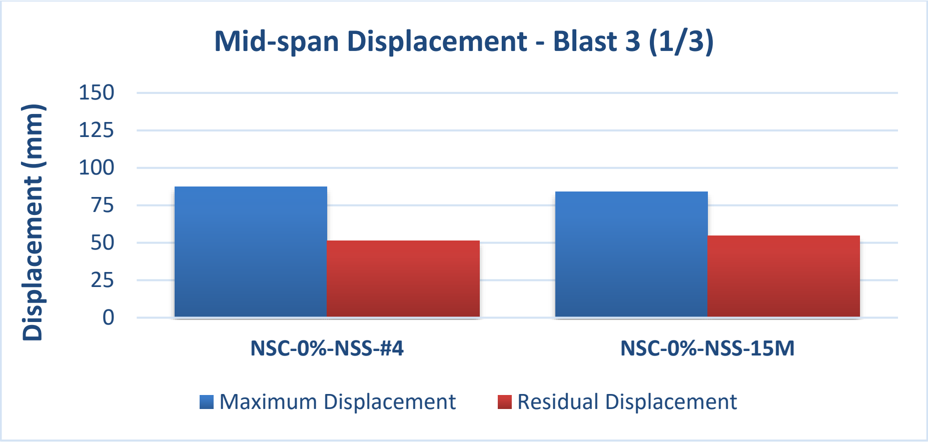

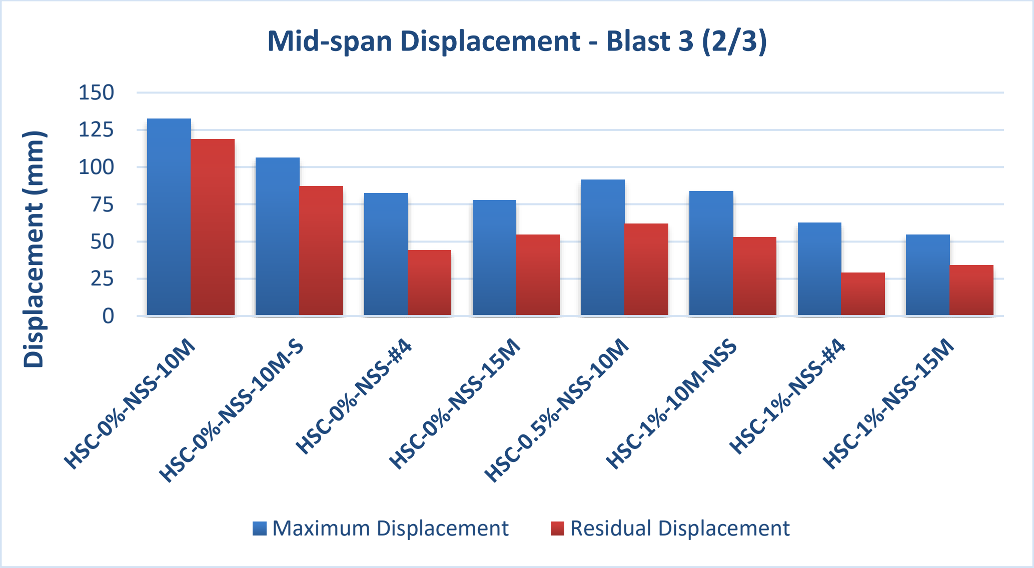

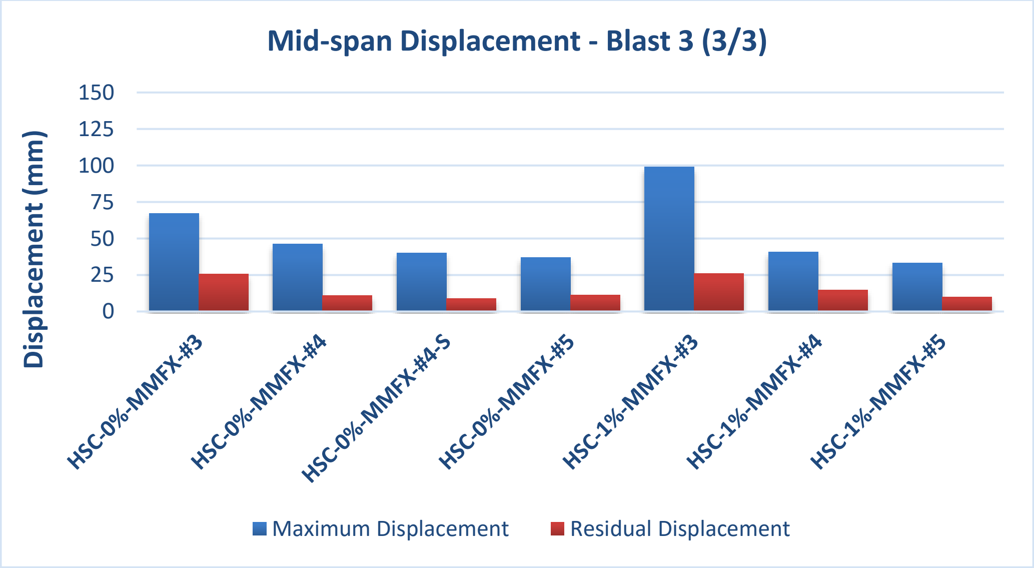

Figure 5-3 Mid-span displacements for all columns for blast 3

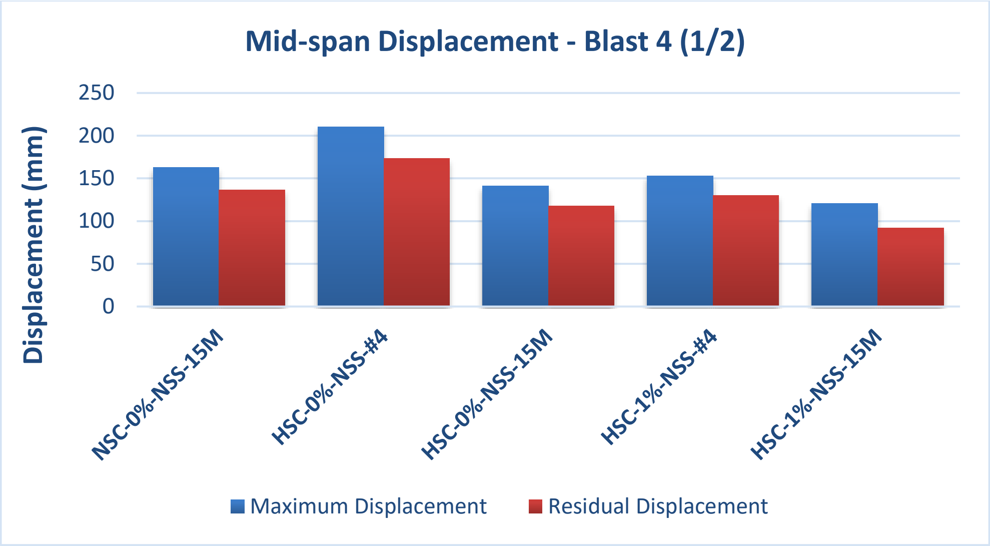

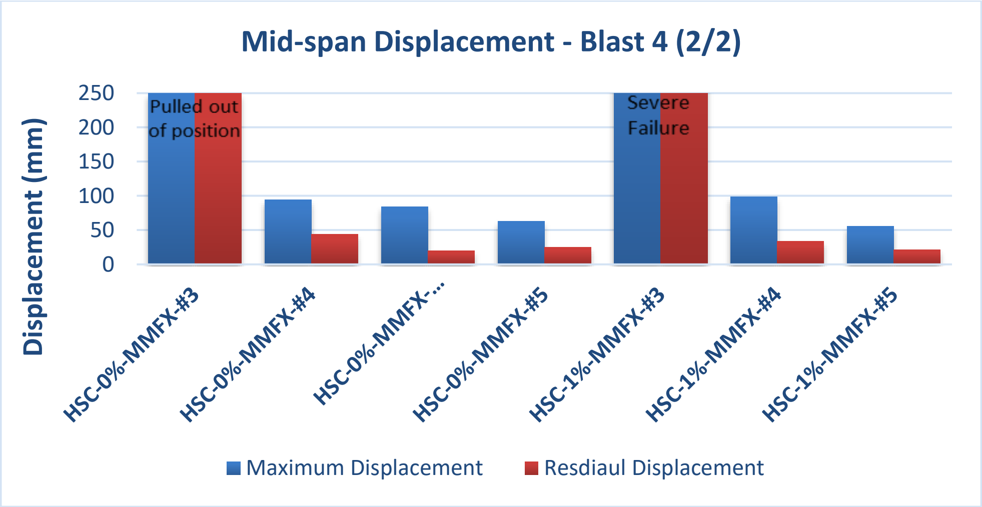

Figure 5-4 Mid-span displacements for all columns for blast 4

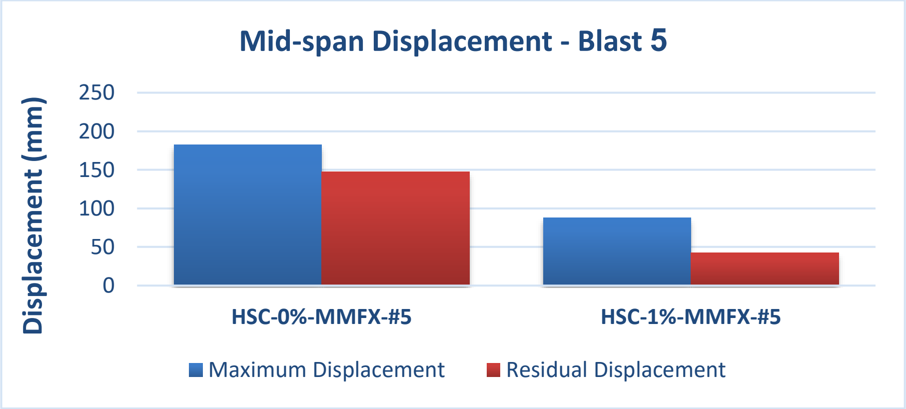

Figure 5-5 Mid-span displacements for all columns for blast 5

5.3 Effect of Steel Reinforcement Ratio

5.3.1 Effect of Normal-Strength Steel Reinforcement Ratio

The role of longitudinal steel reinforcement ratio in improving a member's resistance to blast loads was a main parameter investigated in this research. The effect of normal-strength steel (NSS) ratio is examined through two sets of specimens constructed with varied steel bar sizes between 10M (ρ= 1.72%), #4 (ρ= 2.22%), and 15M (ρ= 3.44%). All specimens in this comparison had non-seismic detailing with a hoop spacing of s= 75mm and were built with high-strength concrete, with the only difference being the addition of steel fibers at a ratio of 1% in the HSFRC columns.

- HSC series: HSC-0%-NSS-10M vs. HSC-0%-NSS-#4 vs. HSC-0%-NSS-15M
- HSFRC series: HSC-1%-NSS-10M vs. HSC-1%-NSS-#4 vs. HSC-1%-NSS-15M

Comparisons of results are shown through comparative bar charts and displacement time histories in Figure 5-6 and Figure 5-7. Photos comparing damage and failure are supplied in Figure 5-8.

After blast 2, the role of NSS reinforcement ratio started to take effect. Maximum displacements between the 10M and #4 specimens had decreased by 40.3% (from 33.64 mm to 20.07 mm) for the HSC columns with larger bar area. A similar observation is made for the HSFRC columns but with a lower reduction ratio of 20.8% when using #4 bars (from 19.41 mm to 15.37 mm). A further enhancement in displacement control occurred when shifting from #4 to 15M bars in the HSC specimens, where a decrease of 20.2% in maximum displacements took place (from 20.07 mm to 16.02 mm) when bar sizes were increased from #4 to 15M bars. The same trend is not observed for the HSFRC columns, where the maximum displacements shows a higher value of 17.52 mm for the 15M specimen, when compared to the value of 15.37 mm recorded for the #4 specimen.

Blast 3 shows more clear improvements when increasing the NSS reinforcement ratio. For the HSC columns, a 37.9% cut in maximum displacement was achieved when the longitudinal reinforcement was changed from 10M to #4 bars (from 132.57 mm to 82.35 mm), with a further reduction of 5.6% through the transition to 15M bars instead of #4 bars (from 82.35 mm to 77.70 mm). This shot caused failure in the specimen with 10M bars, with a residual displacement remained equal to 118.68 mm. The other two columns showed reduced residual displacement, settling as 44.29 mm for the #4 specimen and 54.45 mm for the 15M specimen. For crack patterns, the 10M specimen suffered from some very wide cracks and spalling, while the maximum cracks widths recorded were 16.2 mm and 5.5 mm for the #4 and the 15M specimens respectively. Hence, in addition to reduced displacements achieved by increasing the reinforcement ratio, additional crack control could be obtained reducing damage in the HSC specimens.

As for the HSFRC columns, reduced maximum displacements were obtained when increasing reinforcement form 10M to #4 bars (25.1%; from 83.78 mm to 62.73mm) under Blast 3, and the same applied when bar size was increased form #4 to 15M (12.9%; from 62.73 mm to 54.62mm). The 10M specimen failed after the third blast due to a wide opening and a high displacement value, with a residual displacement of 52.85 mm, a much higher value than in the case of the #4 (29.11 mm) and 15M companions (34.09mm).

The #4 and 15M specimens in both the HSC and HSFRC sets were tested under the impact of an additional blast 4 (100 psi). The final test further exemplified the benefit of increasing the NSS reinforcement ratio (Figure 5-8 (a, b)). For the HSC series, the maximum displacement acquired for the 15M column was 141.09 mm, which is 33% less than the 210.58 mm recorded for the #4 specimen. Residual displacements were also cut significantly, as the 15M specimen settled with around 60 mm less than the #4 (117.56 mm for the 15M, 173.50 mm for the #4). As for cracking and fragmentation, the 15M specimen performed slightly better, but as the blast pushed both columns to failure, severe fragmentation and damage occurred to both specimens.

Again, for the HSFRC specimens, increased reinforcing ratios enhanced column performance under blast 4 pressures. A decrease from 153.13 mm to 120.52 mm took place in maximum displacements when the reinforcing bars were changed form #4s to 15Ms (a reduction of 21.3%). Both specimens failed at this blast, where the 15M recorded a smaller residual value of 92.24 mm than the 130.30 mm recorded for the #4 column (a reduction of 29.2%). As for cracking and fragmentation, the 15M specimen performed slightly better than the #4 specimen, but the control in crack widths and secondary fragmentation is due to the presence of fibers in the HSFRC specimens, which will be discussed in a later section of this chapter.

In summary, increasing the amount of NSS longitudinal steel reinforcement in high-strength concrete and fiber-reinforced concrete columns leads to reduced displacements for the same intensity of loading. In addition, it can lead to increased blast capacity saving a member from failure as seen in the case of 10M specimens which failed at blast 3 loads, whilst companion specimens constructed with #4 and 15M bars survived this blast, failing under blast 4 pressures.

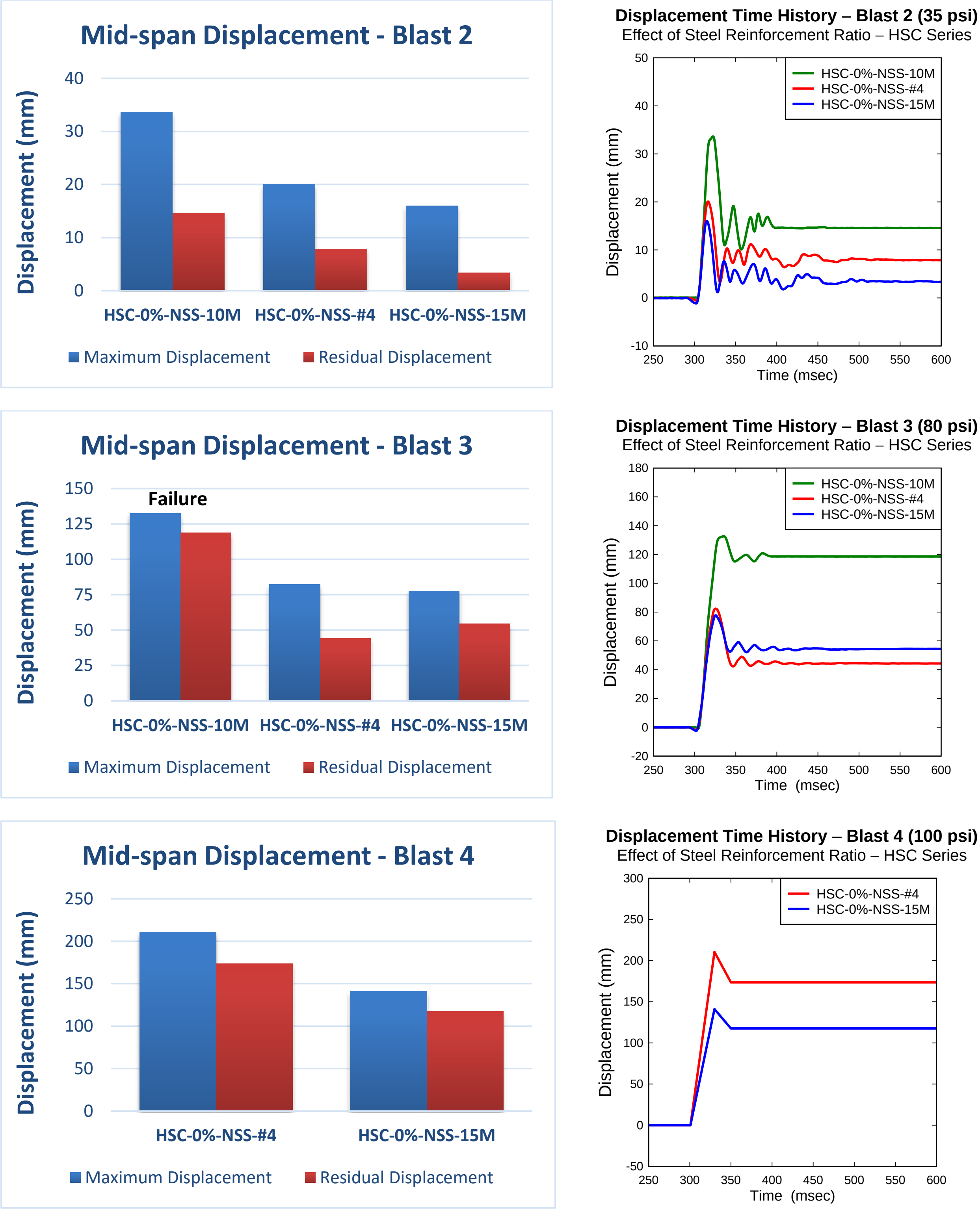

Figure 5-6 Effect of normal-strength steel reinforcement ratios for the HSC series: Comparisons of mid-span displacements and displacement time histories for blasts 2-4

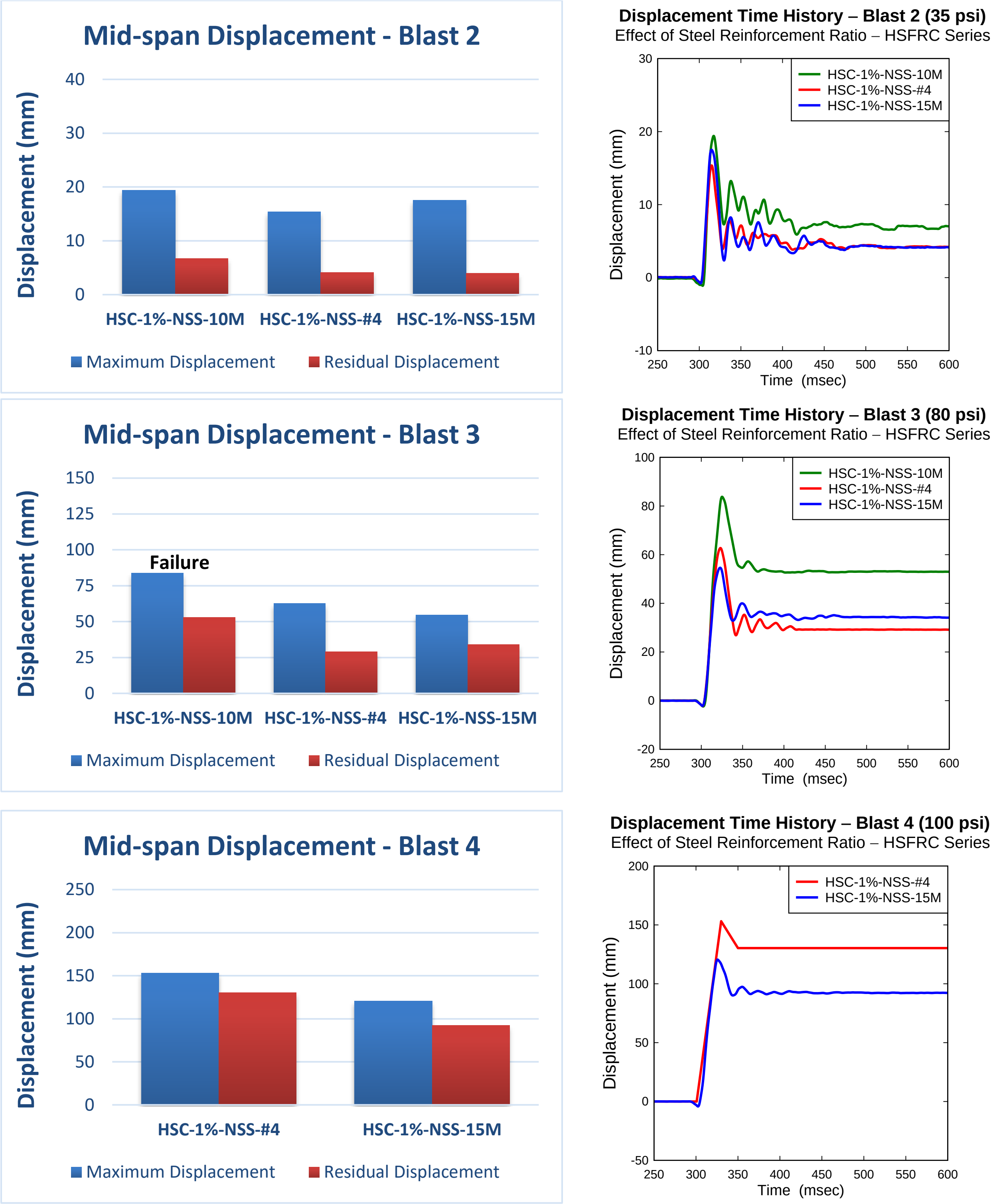

Figure 5-7 Effect of normal-strength steel reinforcement ratios for the HSFRC series: Comparisons of mid-span displacements and displacement time histories for blasts 2-4

HSC-0%-NSS-10M *HSC-0%-NSS-#4* *HSC-0%-NSS-15M*

a) Blast 3

HSC-0%-NSS-#4 *HSC-0%-NSS-15M*

b) Blast 4

HSC-1%-NSS-10M *HSC-1%-NSS-#4* *HSC-1%-NSS-15M*

c) Blast 3

HSC-1%-NSS-#4 *HSC-1%-NSS-15M*

d) Blast 4

Figure 5-8 Effect of normal-strength steel reinforcement ratios: Selected photographs after testing

5.3.2 Effect of High-Strength Steel Reinforcement Ratio

The effect of increased high-strength steel (HSS) reinforcement ratio was monitored in this research through varying MMFX bar sizes from #3 (ρ= 1.22%), #4 (ρ= 2.22 %), and #5 (ρ= 3.44%) in two different series:

- <u>HSC series</u>: HSC-0%-MMFX-#3 vs. HSC-0%-MMFX-#4 vs. HSC-0%-MMFX-#5
- <u>HSFRC series</u>: HSC-1%-MMFX-#3 vs. HSC-1%-MMFX-#4 vs. HSC-1%-MMFX-#5

Comparative bar charts along with comparative displacement time histories are shown in Figure 5-9 and Figure 5-10. Photographs showing companion specimens after testing are provided in Figure 5-11.

Blast 2 did not fully demonstrate the role of increasing HSS bar sizes in both series. Though a decrease between maximum displacements occurred when changing form #3 bars to #4 bars in the HSC series (8.7%; from 18.35 mm to 16.76 mm), the same effect could not be detected when changing from #4 to #5 bars, where approximately the same displacements were recorded for both specimens (16.76 mm for the #4 specimen and 17.18 mm for the #5 specimen). The same trend was noticed for the HSFRC series where a reduction of 47.3% in maximum displacements happened when switching to #4 bars instead of #3 bars (from 25.18 mm to 13.26 mm), while the increase of the reinforcement ratio from #4 to #5 bars recorded an increase of around 2 mm in maximum displacement (13.26 mm for the #4 specimen and 15.59 mm for the #5 specimen). These results could be justified since 35-psi blast is meant to push the high-strength steel reinforcement in the columns with #4/#5 bars only near their elastic limit.

Blast 3 was clearer in revealing the effect of HSS longitudinal reinforcement ratio in controlling displacements in the columns. For the HSC series, a significant reduction in the displaced values between the three specimens occurred as the bar sizes increased gradually. A 31.4% reduction in maximum displacements was achieved by increasing MMFX bar size from #3 to #4 (from 67.28 mm to 46.17 mm). Similarly, a 19.7% reduction was achieved when #5 bars were used instead of #4 bars (form 46.17mm to 37.06 mm). As for residual displacements, an important reduction of 57.4% was observed between specimens with #3 and #4 bars, whereas specimens with #4 and #5 bars showed very close residual displacements (10.97 mm for the #4 specimen and 11.15 mm for the #5 specimen). Figure 5-11 (a) shows photographs after this blast for the specimens.

A similar trend was observed in the HSFRC series at this blast intensity (Figure 5-11 (b)). Using #4 bars instead of #3 reduced the maximum displacement considerably by 58.9% (40.65 mm vs. 98.92 mm). A similar improvement is evident when replacing #4 bars with #5 bars, where the maximum displacement decreased form 40.65 mm to 33.20 mm (a reduction of 18.3%). As for residual displacement, it was also better controlled as the HSS reinforcement ratio gradually increased, with residual displacements of 26.02 mm, 14.64 mm, and 10.04 mm recorded for the #3, #4, and #5 specimens, respectively.

The effect of HSS reinforcement ratio is also observed in both series of columns under blast 4 pressures (100 psi). In the HSC series, the specimen constructed with #3 bars experienced severe failure through rupture of tension steel at mid-span and at the top support, with the steel bars pulling out of the bottom support. In comparison, the specimen constructed with #4 bars managed to prevent bar rupture, although the specimen was still considered to have failed due to excessive maximum deformation of 92.24 mm. The HSC specimen with #5 MMFX bars managed to reduce displacements by 33.5% when compared to the #4 companion (from 94.24 mm to 62.68 mm), in addition to effectively bringing down residual displacements by 43.7% (from 44.11 mm to 24.85 mm). It is worth mentioning that the #5 specimen survived blast 4 with minor damage (limited cracking and crushing), and was tested against blast 5 pressures later (110 psi). In contrast, the #4 specimen failed at blast 4, and showed major cracking and spalling at failure (Figure 5-11 (b)).

The same trend continued in the HSFRC series at blast 4. The specimen with #3 HSS bars failed severely through rupture of tension steel at all three maximum moment regions (mid-span and both supports). Rupture of tension steel also took place in the specimen with #4 bars, but at mid-span only, with the load seeming to be just enough to trigger rupture in the tension steel. The #5 specimen effectively prevented failure, and resulted in reduced maximum and residual displacements of 55.39 mm and 21.54 mm when compared to 99.02 mm and 33.80 mm for the #4 companion. This reduction of 44.1 % and 36.3% in maximum and residual displacements respectively allowed the #5 specimen to survive the blast and be tested under an additional blast (110 psi). Similarly, the #5 specimen showed reduced cracking and damage, passing with a relatively good condition into to the next test.

In summary, the increase in high-strength steel (HSS) longitudinal steel reinforcement had an important effect in upgrading the blast performance of the columns. It has a decisive role in reducing maximum and residual displacements, while also leading to an ability to survive greater blast pressures before failure as seen with the #5 specimens in both the HSC and HSFRC series.

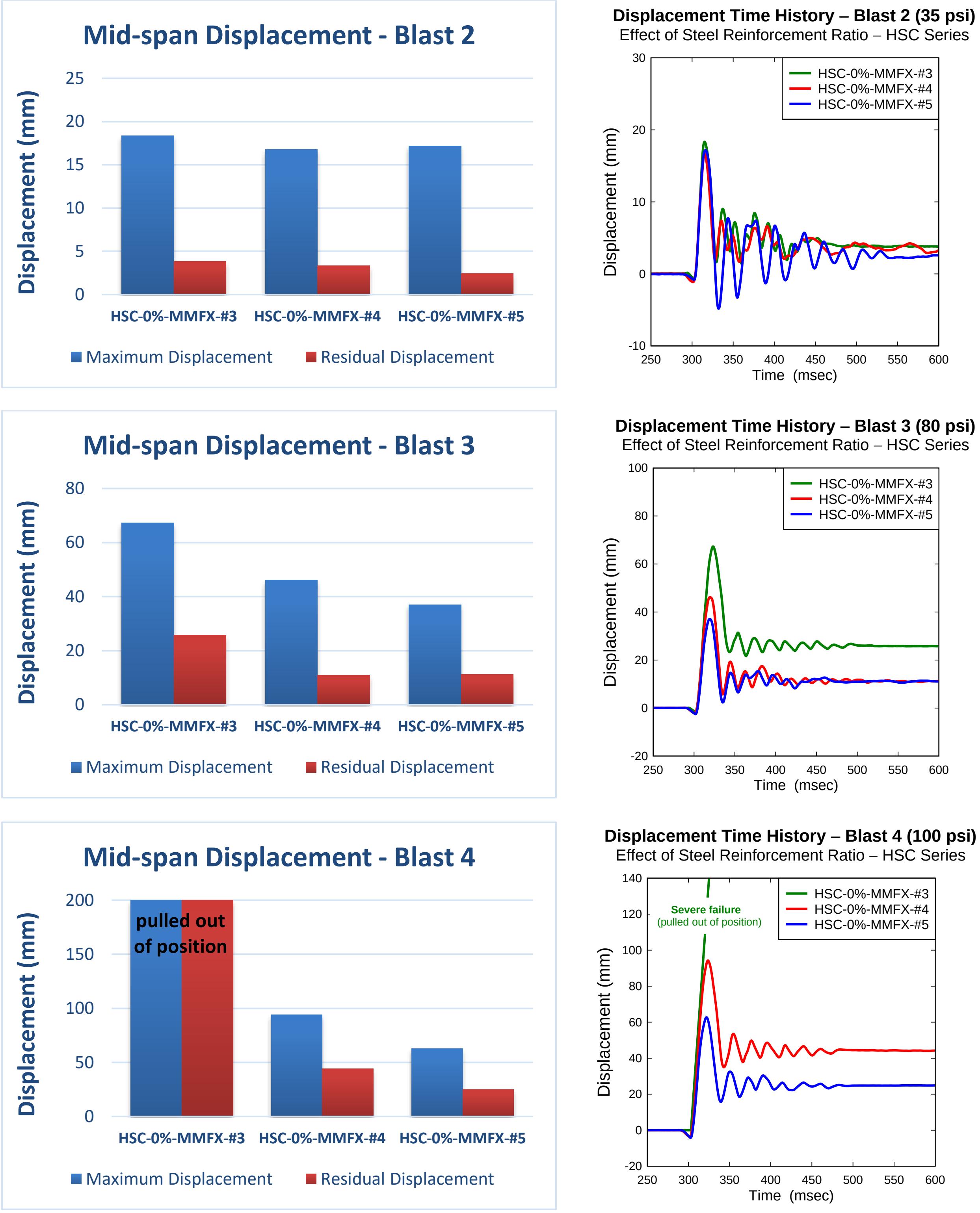

Figure 5-9 Effect of high-strength steel reinforcement ratios for the HSC Series: Comparisons of mid-span displacements and displacement time histories for blasts 2-4

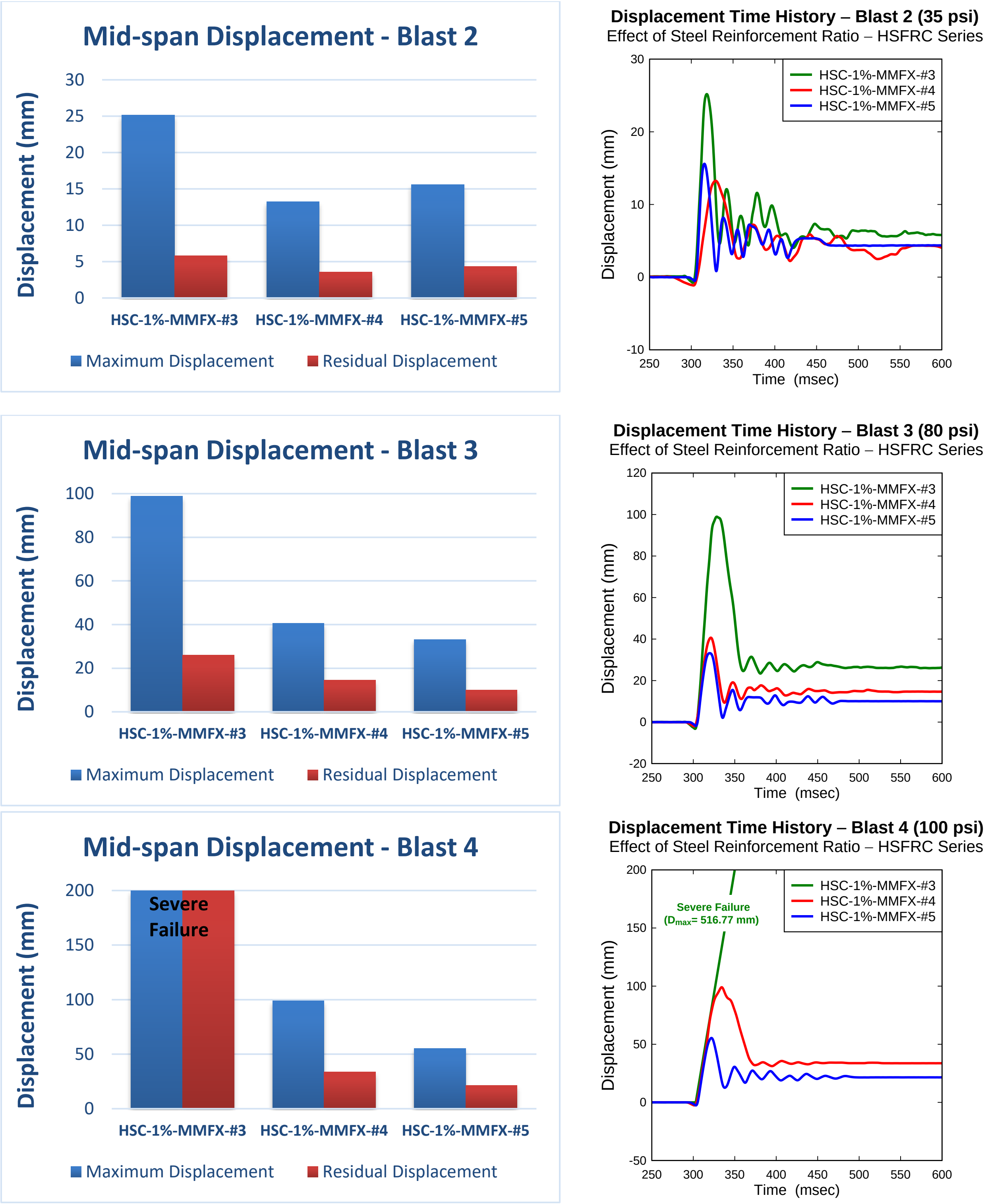

Figure 5-10 Effect of high-strength steel reinforcement ratios for the HSFRC Series: Comparisons of mid-span displacements and displacement time histories for blasts 2-4

HSC-0%-MMFX-#3 *HSC-0%-MMFX-#4* *HSC-0%-MMFX-#5* *HSC-0%-MMFX-#3* *HSC-0%-MMFX-#4* *HSC-0%-MMFX-#5*

a) Blast 3 b) Blast 4

HSC-1%-MMFX-#3 *HSC-1%-MMFX-#4* *HSC-1%-MMFX-#5* *HSC-1%-MMFX-#3* *HSC-1%-MMFX-#4* *HSC-1%-MMFX-#5*

c) Blast 3 d) Blast 4

Figure 5-11 Effect of high-strength steel reinforcement ratios: Selected photographs after testing

5.4 Effect of Steel Reinforcement Type

5.4.1 Effect of Steel Type: HSC Series

A second parameter investigated in this study was the role of longitudinal reinforcement type (normal vs. high-strength reinforcement) on the blast performance of columns. The effect of this parameter is first studied by comparing the response of companion HSC specimens with #4 (ρ= 2.22%) and 15M/#5 bars (ρ= 3.44%):

- HSC-0%-NSS-#4 vs. HSC-0%-MMFX-#4
- HSC-0%-NSS-15M vs. HSC-0%-MMFX-#5

Companion columns were cast with plain high-strength concrete (no fibers) and had non-seismic detailing (s = 75 mm), with the only difference being the reinforcement type (NSS vs. MMFX). Comparative bar charts of mid-span displacements and displacements time histories for each companion set are provided in Figure 5-12 and Figure 5-13. Photographs showing the specimens after selected blasts are also available in Figure 5-14.

After blast 2, the HSC column with #4 MMFX bars showed improved control of displacements over the one with #4 conventional bars, where the maximum mid-span displacement was reduced form 20.07 mm to 16.76 mm (a reduction of 16.5%). The residual displacement for the MMFX specimen showed a smaller value of 3.33 mm, while a value of 7.84 mm was recorded for the specimen with normal-strength bars. The same pattern did not show after this blast for the companions with ρ= 3.44%, where the specimen with #5 MMFX bars displaced 1.16 mm more than its companion (15M: 16.02 mm, #5 MMFX: 17.18 mm). This could be justified again since this blast tested the 15M/#5 specimens near their elastic domain.

Blast 3 displays a clearer trend regarding the effectiveness of high-strength steel. The maximum displacement recorded for the #4 MMFX specimen shows an important reduction of 43.9% when compared to the column with #4 conventional reinforcement (from 82.35 mm to 46.17 mm). The same influence was observed for the residual displacement, where it showed a lower value of 10.97 mm, versus the 44.29 mm for the specimen with #4 normal-strength bars (a reduction of 75.2%). The decrease in residual displacements is due to the increased elastic strain capacity of the MMFX bars, which allows the columns to recover displacements at moderate blast levels. It also interesting to observe through the displacement time histories provided in Figure 5-12, that the high-strength MMFX specimen shows relatively more cycles when undergoing vibrations before coming to rest when compared to the column with conventional steel.

The same trend is observed in the 15M/#5 HSC set. At blast 3, the specimen with #5 MMFX bars managed to produce reductions of 52.3% (from 77.70 mm to 37.06 mm) and 79.5% (54.45 mm to 11.15 mm) in maximum and residual displacements when compared to the companion with 15M normal-strength bars. The specimen with #5 MMFX bars also lowered the amount of damage when compared to the 15M NSS specimen as shown in Figure 5-14 (c), through less crushing in the compression zone and smaller cracks widths on the tension face.

All four specimens were tested under a fourth blast. As expected, specimens with MMFX rebar behaved much better than the ones with normal-strength steel. The #4 MMFX specimen showed a reduced maximum displacement of more than 50% when compared to the specimen with #4 NSS bars (94.24 mm vs. 210.58 mm). This was the last blast for both specimens, where the MMFX column settled with a residual displacement of 44.11 mm, compared to 173.50 mm for its companion. In terms of damage, the MMFX specimen exhibited a lot of cracks with two locations experiencing spalling of concrete on the tension face. In comparison, the normal steel specimen went through major deformations resulting in damage all along the middle third of the column, where concrete fragmented exposing the tension steel bars showing signs of excessive stressing. Crushing was more important, with more significant hinging and damage at the supports.

As for the 15M/#5 set, the specimen with #5 MMFX bars showed superior control in resisting blast 4 loading. It recorded 62.68 mm for maximum displacement, a reduction of 55.6 % when compared to the column with normal-strength 15M bars which displaced 141.09 mm. Damage for the 15M specimen after this blast was severe. The permanent deformation at mid-span reached 117.56 mm, with concrete lost over the column's tension side, and rebar exposed over the middle third of the column. In contrast, the #5 MMFX specimen survived the blast with relatively minor damage (residual of 24.85 mm) and was tested under an additional impulse (blast 5).

In summary, the results from this companion set demonstrates important improvements in column blast performance when transitioning from normal-strength to high-strength reinforcement in high-strength concrete (HSC) columns. The provision of high-strength MMFX not only improves control of mid-span displacements, but can also increase blast capacity as observed in the 15M and #5 companion set.

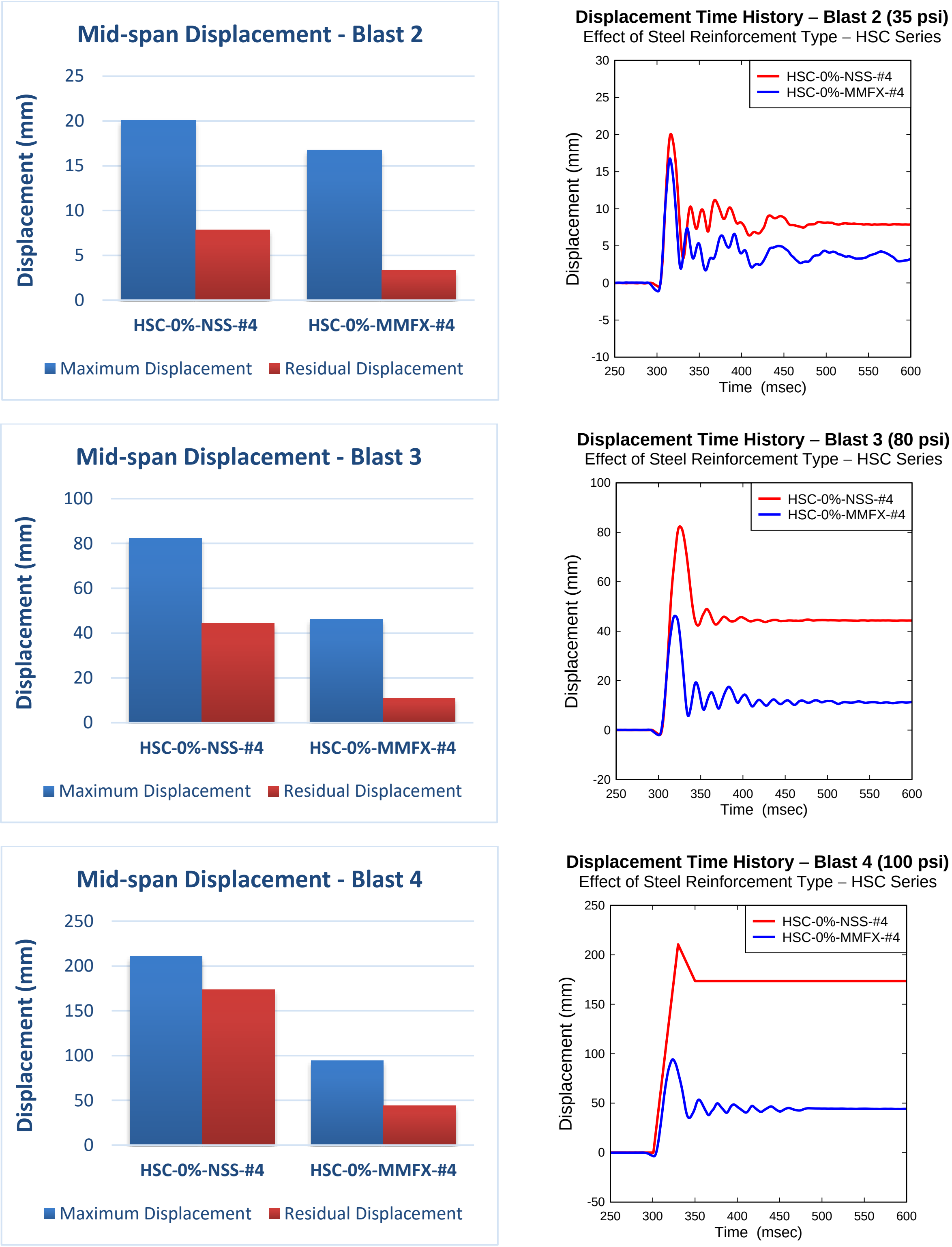

Figure 5-12 Effect of steel reinforcement type for HSC-0%-NSS-#4 vs. HSC-0%-MMFX-#4: Comparisons of mid-span displacements and displacement time histories for blasts 2-4

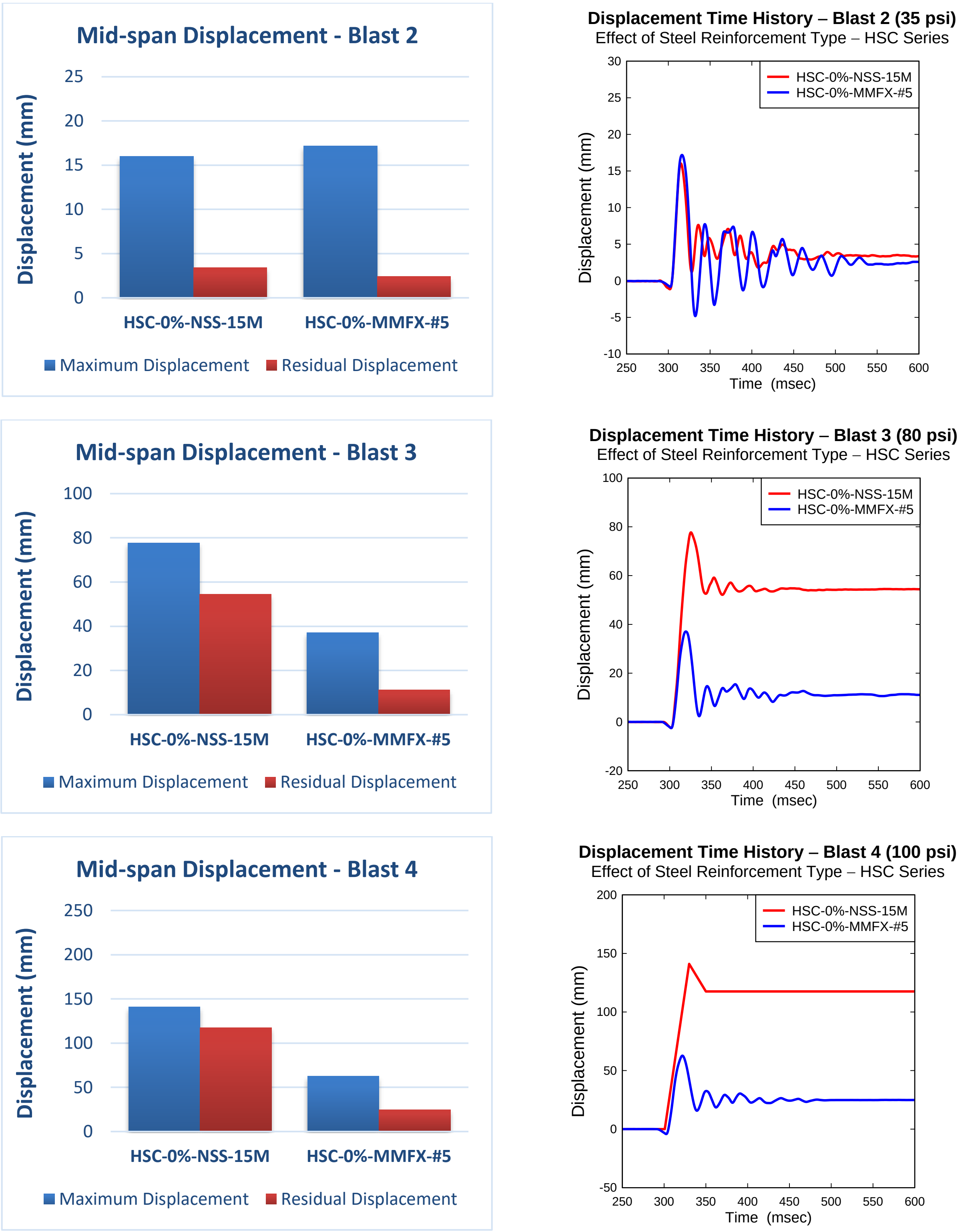

Figure 5-13 Effect of steel reinforcement type for HSC-0%-NSS-15M vs. HSC-0%-MMFX-#5: Comparisons of mid-span displacements and displacement time histories for blasts 2-4

HSC-0%-NSS-#4 *HSC-0%-MMFX-#4*

a) Blast 3

HSC-0%-NSS-#4 *HSC-0%-MMFX-#4*

b) Blast 4

HSC-0%-NSS-#15M *HSC-0%-MMFX-#5*

c) Blast 3

HSC-0%-NSS-15M *HSC-0%-MMFX-#5*

d) Blast 4

Figure 5-14 Effect of steel reinforcement type for the HSC series: Selected photographs after testing

5.4.2 Effect of Steel Type: HSFRC Series

The effect of steel type was also monitored by comparing the response of companion HSFRC columns with #4 and 15M normal vs. high-strength (MMFX) bars:

- HSC-1%-NSS-#4 vs. HSC-1%-MMFX-#4
- HSC-1%-NSS-15M vs. HSC-1%-MMFX-#5

The companions in each set where constructed with the same reinforcement ratios. Concrete type was HSFRC with a steel fiber ratio of 1%. All hoops spacing corresponded to non-seismic details (s = 75 mm). Comparative bar chars of mid-span displacements are provided along with comparative displacement time histories in Figure 5-15 and Figure 5-16. Figure 5-17 shows photographs to reveal the impact of blasts on the columns.

For blast 2, the mid-span displacements were reduced by around 13% for both maximum and residual when #4 MMFX bars were used instead of #4 NSS bars (maximum: from 15.37 mm to 13.26 mm, residual: from 4.41 to 3.58 mm). For the 15M/#5 specimens, the maximum displacement was decreased by 11% (17.52 mm to 15.59 mm), whereas the residual displacement settled close to 4 mm for both specimens.

At Blast 3 levels, maximum displacements were decreased by 35.2 % (from 62.73 to 40.65 mm) for the column with the #4 MMFX bars when compared to the normal-strength companion, with a similar reduction ratio of 39.2% for the #5 MMFX specimen against the normal-strength 15M specimen (from 54.62 mm to 33.20 mm). The same trend was noticed regarding the residual displacements, where a 49.7% reduction of displacement was obtained with the #4 MMFX bars (from 29.11 mm to 14.64 mm), while a 70.6 % reduction was obtained with #5 MMFX bars (from 92.24 mm to 21.54 mm) when comparing to the normal-strength companions.

As for blast 4, the MMFX high-strength steel reinforcement continued to show its effectiveness in minimizing mid-span displacements in the HSFRC columns. The specimen with #4 MMFX bars showed a 35.3 % reduction in maximum displacement over the #4 normal-strength specimen (form 153.13 mm to 99.02 mm), with a residual displacement of 33.80 mm, which is significantly less than its companion by around 100 mm (a reduction of 74.1%). Similarly, in the 15M/#5 set, the transition to MMFX bars reduced the mid-span displacements significantly by 54% (from 120.52 mm to 55.39 mm), while residual displacement also decreased by 76.6 % (from 92.24 mm to 21.54 mm). It should be noted that this blast was the last blast for the #4 pair of specimens and for the normal-strength 15M specimen, while the specimen with #5 MMFX bars endured the blast with limited damage, with this column tested under one more blast (110 psi).

In summary, just as in the HSC series, the use of high-strength steel reinforcement proved to be a major upgrade for the blast resistance of columns built with high-strength fiber-reinforced concrete. The use of MMFX bars in HSFRC columns leads to lower displacements when compared to normal-strength steel (by not less than 30% at high intensity blasts such as blasts 3 and 4), while also controlling permanent deformations. In addition, it can increase blast capacity. Indeed, the combined use of high-strength reinforcement and steel fibers seems to be ideal in high-strength concrete columns, where the fibers allow the concrete to keep up and fully utilize the increased capacity of the MMFX bars.

Figure 5-15 Effect of steel reinforcement type for HSC-1%-NSS-#4 vs. HSC-1%-MMFX-#4: Comparisons of mid-span displacements and displacement time histories for blasts 2-4

Figure 5-16 Effect of steel reinforcement type for HSC-1%-NSS-15M vs. HSC-1%-MMFX-#5: Comparisons of mid-span displacements and displacement time histories for blasts 2-4

HSC-1%-NSS-#4 *HSC-1%-MMFX-#4*

Blast 3

HSC-1%-NSS-#4 *HSC-1%-MMFX-#4*

Blast 4

HSC-1%-NSS-15M *HSC-1%-MMFX-#5*

Blast 3

HSC-1%-NSS-15M *HSC-1%-MMFX-#5*

Blast 4

Figure 5-17 Effect of steel reinforcement type for the HSFRC series: Selected photographs after testing

5.4.3 Effect of Steel Type: Ability to Reduce Reinforcement

The enhancement provided by high-strength steel is not only limited to specimens with the same reinforcement ratios. It also showed an ability of achieving similar performance with lesser amount of steel when compared to columns with normal-strength bars. This effect is examined through comparing the results of two sets of columns: HSC-0%-NSS-10M (ρ= 1.72%) vs. HSC-0%-MMFX-#3 (ρ= 1.22%) and HSC-0%-NSS-15M (ρ= 3.44%) vs. HSC-0%-MMFX-#4 (ρ= 2.22%), which were all built with plain high-strength concrete. It is noted that the MMFX columns in these companion sets has ~ 30% reduction in the amount of longitudinal reinforcement. Comparative bar charts for mid-span displacements and comparative displacement time histories for both specimens after selected blasts are shown in Figure 5-18 and Figure 5-20. Figure 5-19 and Figure 5-21 also include selected photographs to show the different outcomes.

After blast 2, the specimen with the MMFX #3 bars showed a noticeable reduction of 45.5% in maximum displacements (from 33.64 mm to 18.35) when compared to the specimen with the 10M normal-strength bars. The same applied for the residual displacements where the specimen with #3 MMFX bars settled with a lower value of 3.84 mm than the 14.69 mm obtained for its companion. The third blast emphasized again the benefits of high-strength steel. Whilst the specimen with 10M bars failed after this blast due to major deformations and a maximum displacement of 132.57 mm, the specimen with #3 MMFX bars was able to survive and record around half of the maximum displacement of its companion (a reduction of 49.2%: from 132.57 mm to 67.28 mm). Moreover, residual displacements followed the same trend, where the column with #3 MMFX bars settled with only 25.74 mm, much less than the 118.68 mm of the 10M NSS column. Failure of the #3 MMFX specimen would eventually occur at blast 4 due to bar rupture.

Similar benefits are observed when comparing companion HSC columns with #4 MMFX steel and 15M normal-strength steel (HSC-0%-MMFX-#4 vs. HSC-0%-NSS-15M). While both columns failed at the same blast intensity, the MMFX column shows reductions of 33.2% and 62.48% in maximum and residual displacements at blast 4 despite the 1.22% reduction in ρ (see Figure 5-20 and Figure 5-21).

This comparison demonstrates the ability of high-strength steel to reduce reinforcement requirements in columns tested under blast loads, where reduced amounts of MMFX bars showed an ability to better control displacements, while also allowing for an increase in blast capacity in some cases.

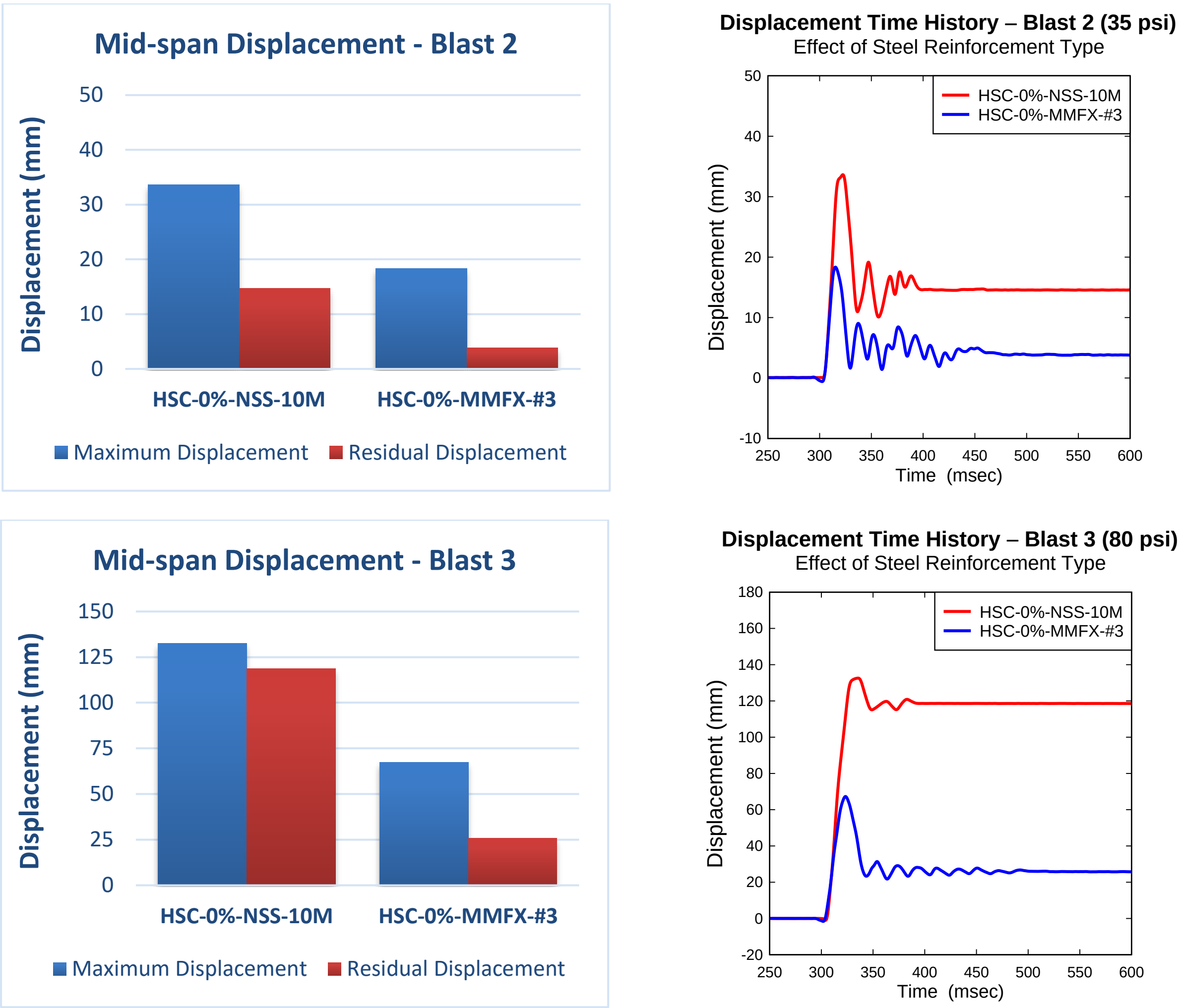

Figure 5-18 Effect of steel reinforcement type for HSC-0%-NSS-10M vs. HSC-0%-MMFX-#3: Comparison of mid-span displacements and displacement time histories for blasts 2-3

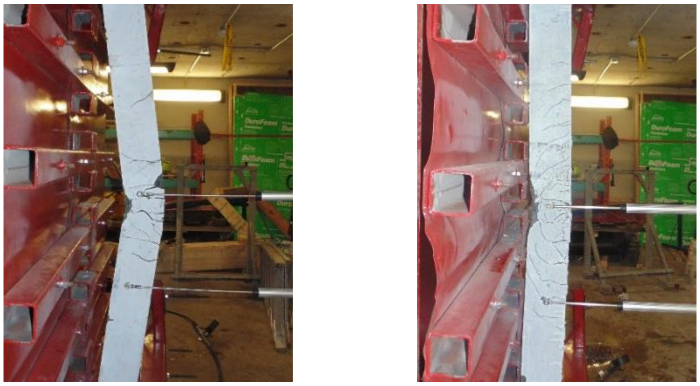

HSC-0%-NSS-10M *HSC-0%-MMFX-#3*

Figure 5-19 Effect of steel reinforcement type for HSC-0%-NSS-10M vs. HSC-0%-MMFX-#3: Photographs after blast 3

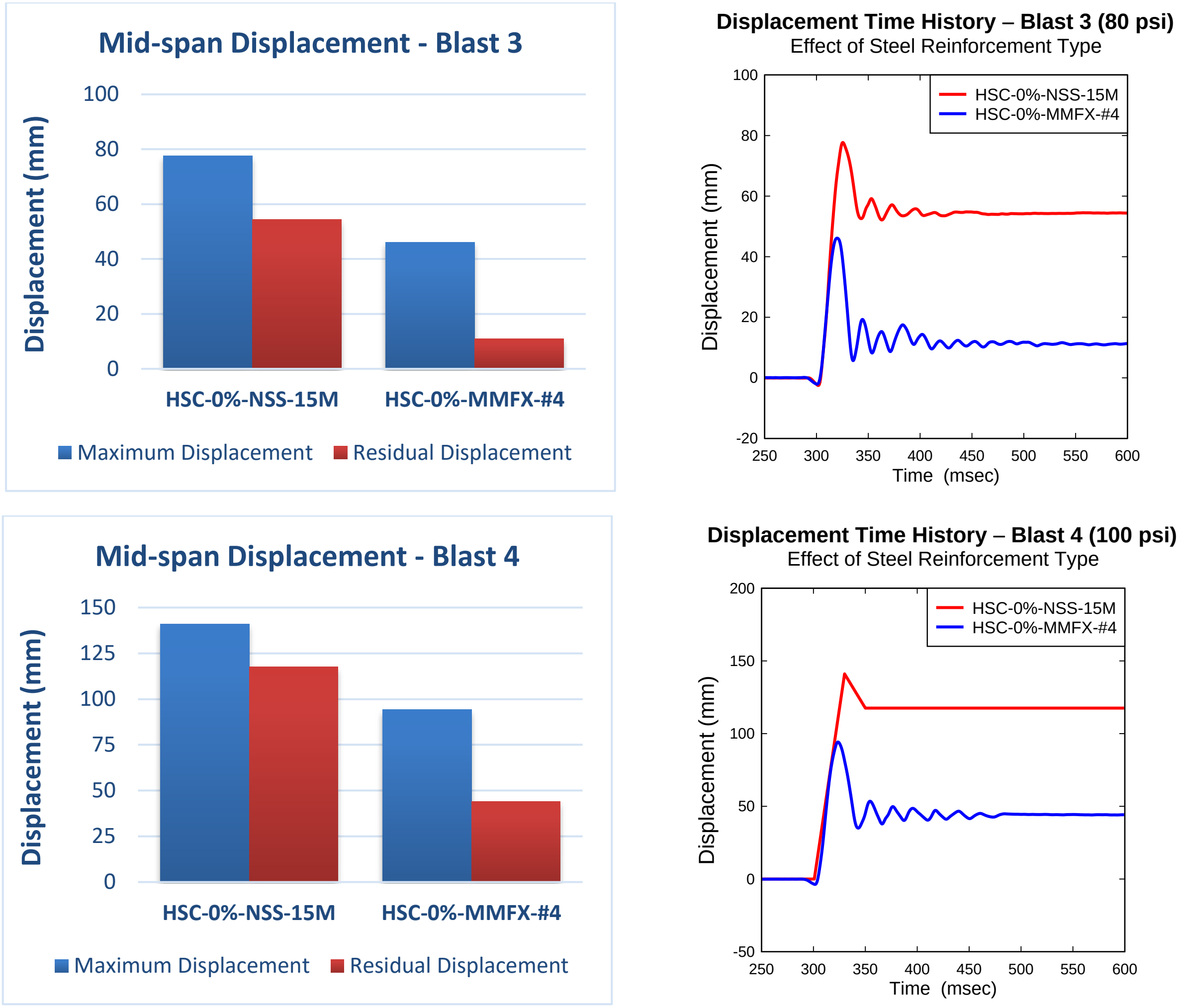

Figure 5-20 Effect of steel reinforcement type for HSC-0%-NSS-15M vs. HSC-0%-MMFX-#4: Comparison of mid-span displacements and displacement time histories for blasts 3-4

HSC-0%-NSS-15M *HSC-0%-MMFX-#4*

Figure 5-21 Effect of steel reinforcement type for HSC-0%-NSS-15M vs. HSC-0%-MMFX-#4: Photographs after blast 4

5.4.4 Effect of Steel Type on Failure Mode and Secondary Fragmentation

As demonstrated in the preceding sections, utilization of high-strength steel reinforcement leads to significant improvements in the blast resistance of columns. However, the use of this high-performance steel material can affect failure mechanisms at extreme blast pressures. Figure 5-22 shows selected photographs after failure for companion specimens with normal-strength steel bars and high-strength bars in both the HSC and HSFRC series.

In the plain HSC series, while columns with both normal-strength and high-strength steel show concrete damage due to crushing and spalling, the damage at failure is more significant for the specimens with high-strength reinforcement. These specimens also show greater amounts of secondary fragments at failure as displayed in the high-speed video stills shown in Figure 5-23. This can partly be explained by the high tensile stresses that develop in the MMFX bars, which in turn lead to high compressive strains in the high-strength concrete, leading to more explosive failures. This effect is less evident when comparing the failure photos of companion HSFRC columns, where the fibers improve the damage tolerance of the concrete when high-strength reinforcement is used. An important observation in both series is that failure of columns with high-strength steel can be associated with rupture of tension reinforcement, which is a brittle mode of failure.

The high-strength steel used in this study shows significant increase in ultimate stress which allows for increased blast resistance, however it comes at the cost of a relative reduction in ductility due to reduced strain capacity (smaller rupture strains) when compared to normal-strength reinforcement. This results in the columns behaving quasi-elastically without significant damage prior to ultimate failure. However, once capacity is reached, failures can be brittle due to the sudden release of energy, particularly if rupture of the tension steel reinforcement occurs. Brittle failure through rupture of steel is undesirable as it leaves a structural member with no residual capacity. Care should therefore be taken when designing columns with high-strength reinforcement to avoid this brittle failure mechanism.

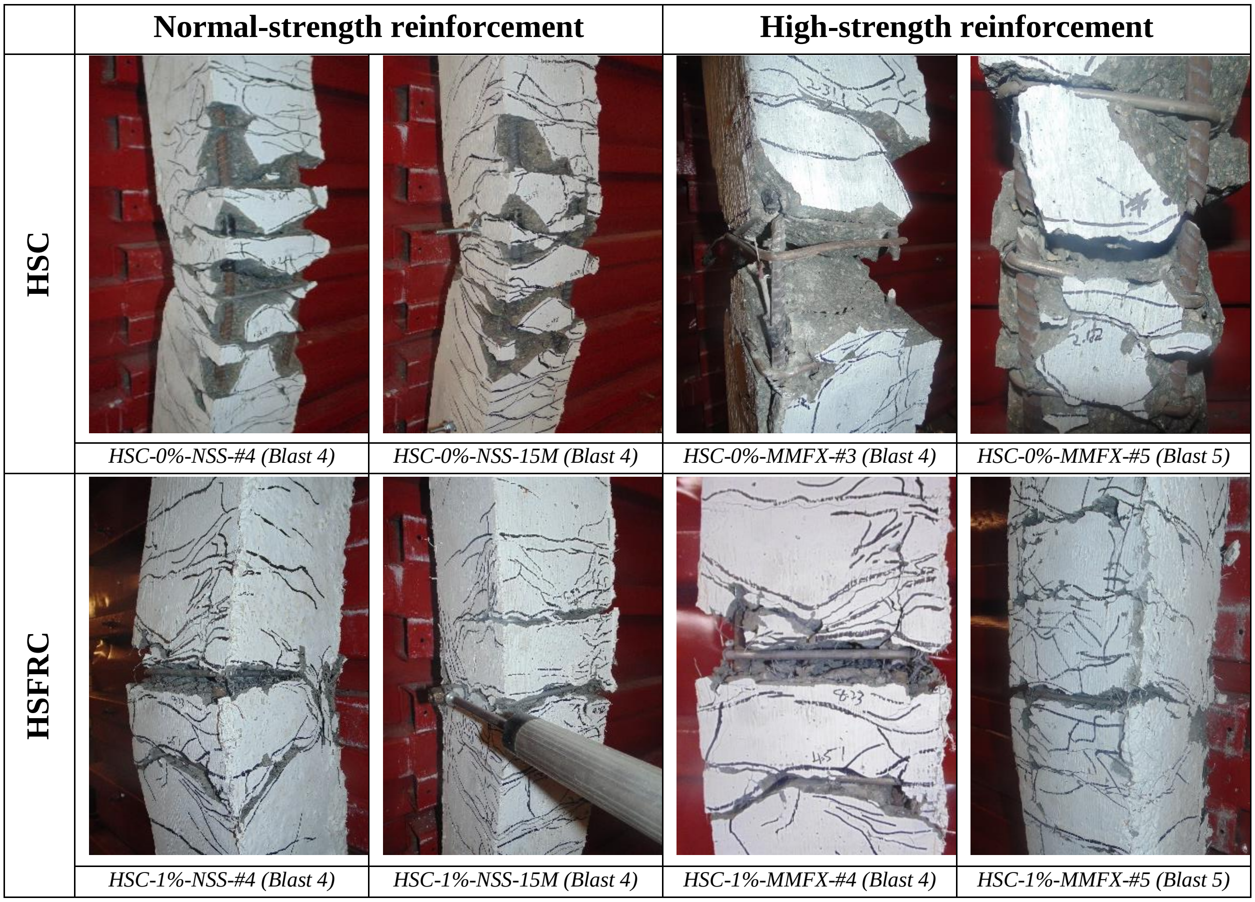

HSC-0%-NSS-#4 (Blast 4) *HSC-0%-NSS-15M (Blast 4)* *HSC-0%-MMFX-#3 (Blast 4)* *HSC-0%-MMFX-#5 (Blast 5)*

HSC-1%-NSS-#4 (Blast 4) *HSC-1%-NSS-15M (Blast 4)* *HSC-1%-MMFX-#4 (Blast 4)* *HSC-1%-MMFX-#5 (Blast 5)*

Figure 5-22 Effect of steel type: Photographs at failure with the corresponding blast number

HSC-0%-NSS-#4 (Blast 4) *HSC-0%-NSS-15M (Blast 4)* *HSC-0%-MMFX-#4 (Blast 4)* *HSC-0%-MMFX-#5 (Blast 5)*

Figure 5-23 Effect of steel reinforcement type on secondary fragmentation through high-speed video footage

5.5 Effects of Steel Fibers

5.5.1 Effect of Steel Fibers in Specimens with NSS Bars

As demonstrated in previous sections, the failure of high-strength concrete columns can be brittle; the combined use of HSC and fibers is one potentaial solution to this problem. The contribution of steel fibers on enhancing the blast performance of columns was examined through several pairs of specimens built with plain HSC and HSFRC, respectively. In this section, this parameter is investigated in columns built with normal-strength steel reinforcement. Three column sets with 10M, #4, and 15M bars are compared:

- 10M set: HSC-0%-NSS-10M vs. HSC-1%-NSS-10M
- #4 set: HSC-0%-NSS-#4 vs. HSC-1%-NSS-#4
- 15M set: HSC-0%-NSS-15M vs. HSC-1%-NSS-15M

The columns in each set have the same reinforcement ratio and transverse reinforcement (s = 75 mm), but were constructed with high-strength concrete containing 0% and 1% steel fibers, respectively. Comparative bar charts and displacement time histories for the three pairs after blast 2-4 are provided in Figure 5-24, Figure 5-25, and Figure 5-26. Photographs to examine the impact of fibers on damage and failure mode are provided in, Figure 5-27, Figure 5-28, and Figure 5-29.

For blast 2, starting with the 10M set, the HSFRC column showed lower maximum and residual displacements by margins of 42.3% (from 33.64 mm to 19.41 mm) and 54.39% (from 14.69 mm to 6.70 mm) when compared to its plain HSC companion. As for the #4 set, a more modest reduction of 23.4% in maximum displacement occurred when steel fibers were added to the concrete mix (from 20.07 mm to 15.37 mm). Residual displacement also reduced by 47.2% (form 7.84 mm to 4.14 mm) when comparing to the column without fibers. As for the 15M pair, similar maximum displacements were obtained for both specimens, where the plain HSC specimen recorded a value of 16.02 mm, versus the 17.52 mm obtained for HSFRC column.

At blast 3, all specimens cast with fiber-reinforced concrete showed improvements over the ones cast with plain concrete. The 10M HSFRC specimen reduced the maximum displacement obtained for the specimen without fibers by 36.8% (from 132.57 mm to 83.78 mm). Also, the residual was cut significantly by 55.5% (form 118.68 mm to 52.85 mm). It is worth mentioning that the two 10M specimens were considered failed after this blast. The improved control of displacement is also observed in the #4 and 15M sets, where the HSFRC specimens in the respective sets recorded reductions in maximum displacement of 23.8% (from 82.35 mm to 62.73 mm) and 29.7% (form 77.70 mm to 54.62 mm) when compared to companion specimens cast with plain HSC. As for residual, a reduction from 44.29 mm to 29.11 mm took place in the #4 pair (a reduction of 34.3%). Similarly, for the 15M pair, residual displacements were reduced (a reduction of from 54.45 to 34.09 mm (a reduction of 37.4%).

This trend continues when examining the #4 and 15M pairs at blast 4. In the #4 set the HSFRC specimen recorded reductions of 27.3% (from 210.58 mm to 153.13 mm) and 24.9% (from 173.50 mm to 130.30 mm) in maximum and residual displacements when compared to the plain HSC companion. The HSC column failed during this blast due to excessive deformations and with significant damage. The HSFRC column showed reduced concrete damage, though failure occurred due to rupture of tension steel. This could be explained by the role of fibers in improving the compressive toughness of the high-strength concrete, which in turn leaves the steel bars with more stresses to deal with, and in this case, it eventually led to rupture. As for the 15M set, reductions in mid-span displacements are also observed at blast 4when fibers are provided, with the HSFRC column recording maximum and residual displacements which were reduced by 14.6% (from 141.09 to 120.52 mm) and 21.54% (from 117.56 mm to 92.24 mm). Once again damage tolerance is greater in the HSFRC companion, and in this case the use of larger reinforcing bars prevents brittle rupture of the tension reinforcement.

In summary, the results demonstrate clear benefits associated with the use of steel fibers in HSC columns. The presence of fibers in HSFRC effectively improves blast performance through reduction of mid-span displacements. It also has an important role in increasing damage tolerance. Spalling and cracking are better controlled when fibers are added. Fiber reinforcement also delays damage in the compression zone due to the increased toughness of HSFRC in compression, which further enhances the blast resistance of columns.

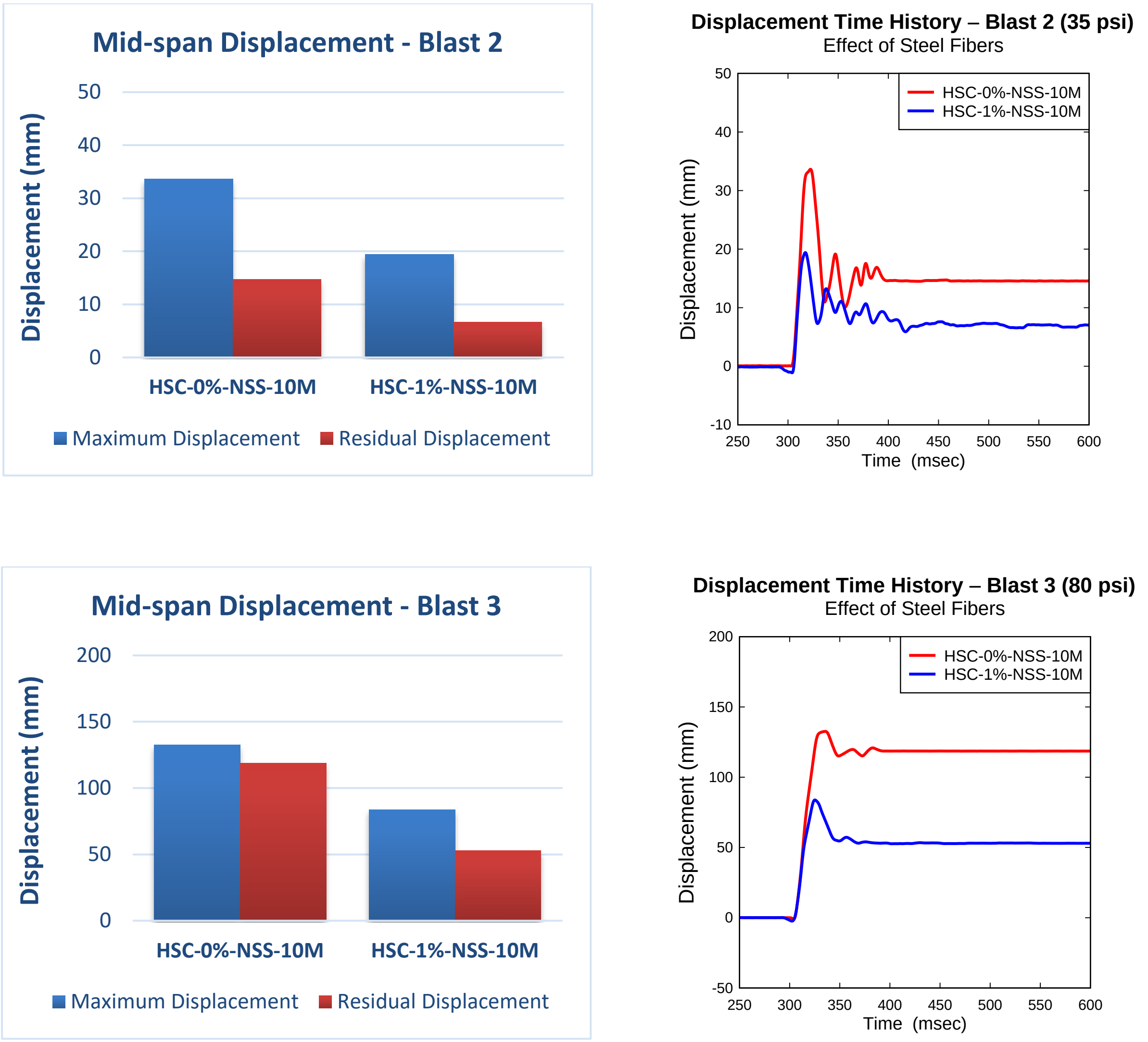

Figure 5-24 Effect of steel fibers for HSC-0%-NSS-10M vs. HSC-1%-NSS-10M: Comparisons of mid-span displacements and displacement time histories for blasts 2-3

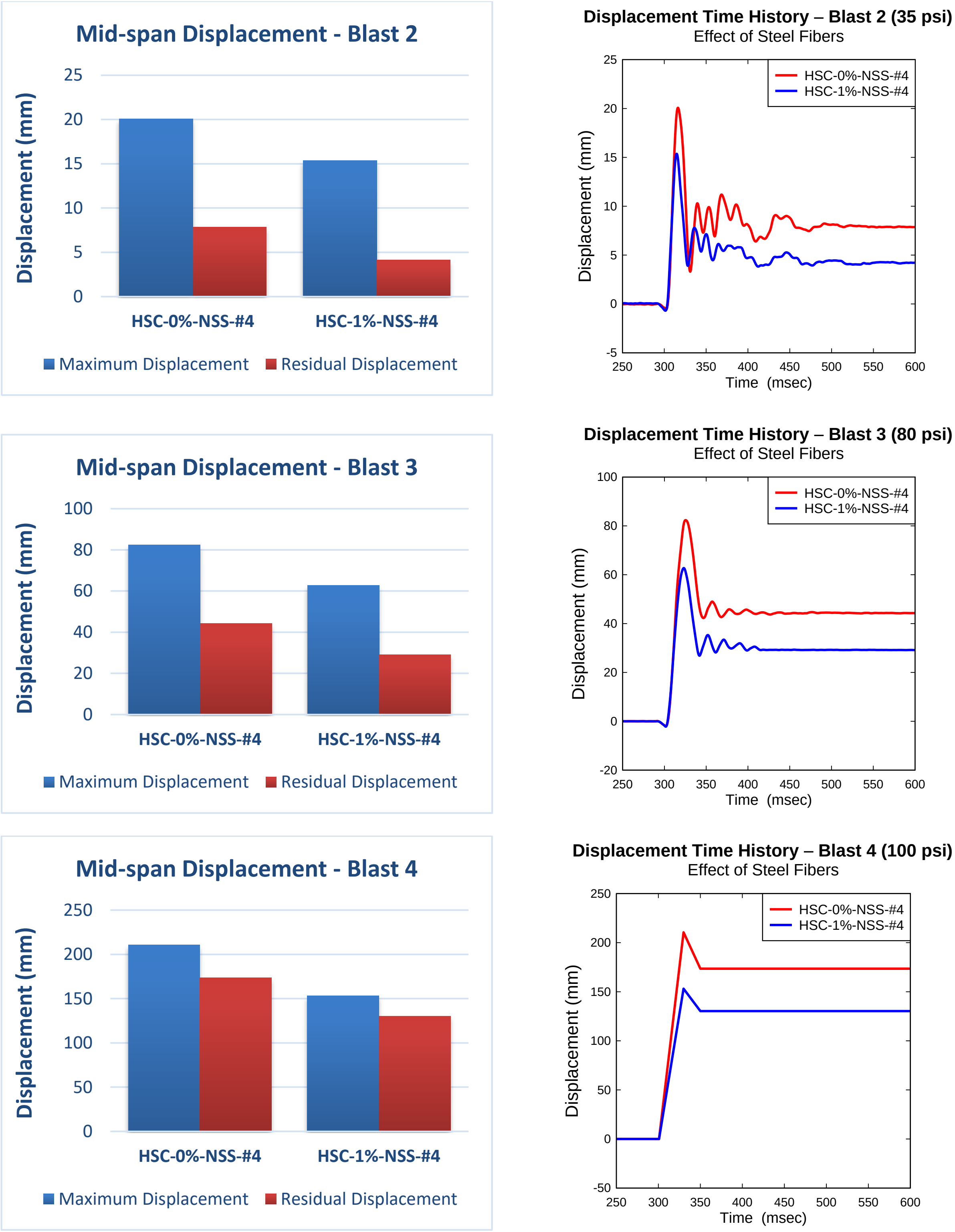

Figure 5-25 Effect of steel fibers for HSC-0%-NSS-#4 vs. HSC-1%-NSS-#4: Comparisons of mid-span displacements and displacement time histories for blasts 2-4

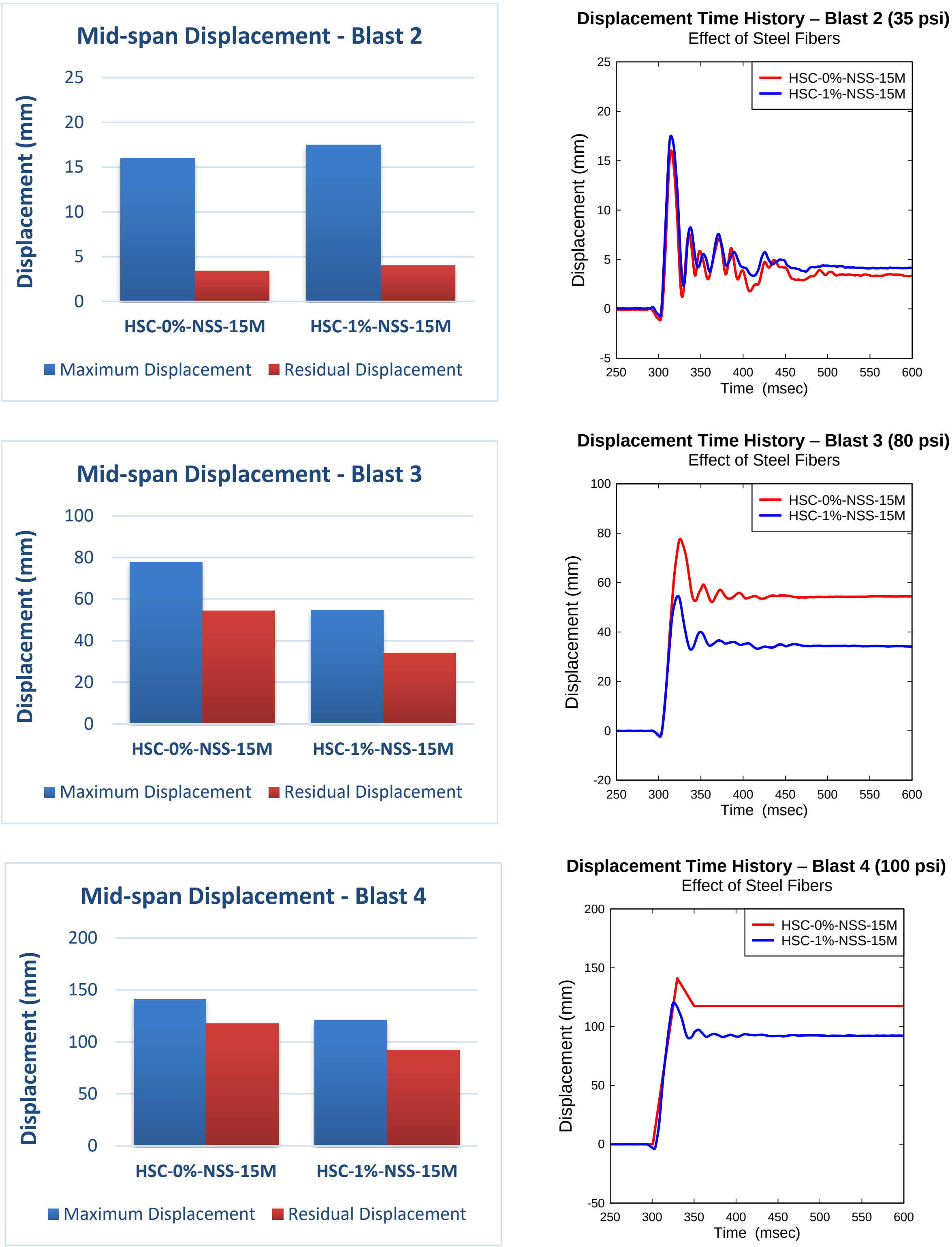

Figure 5-26 Effect of steel fibers for HSC-0%-NSS-15M vs. HSC-1%-NSS-15M: Comparisons of mid-span displacements and displacement time histories for blasts 2-4

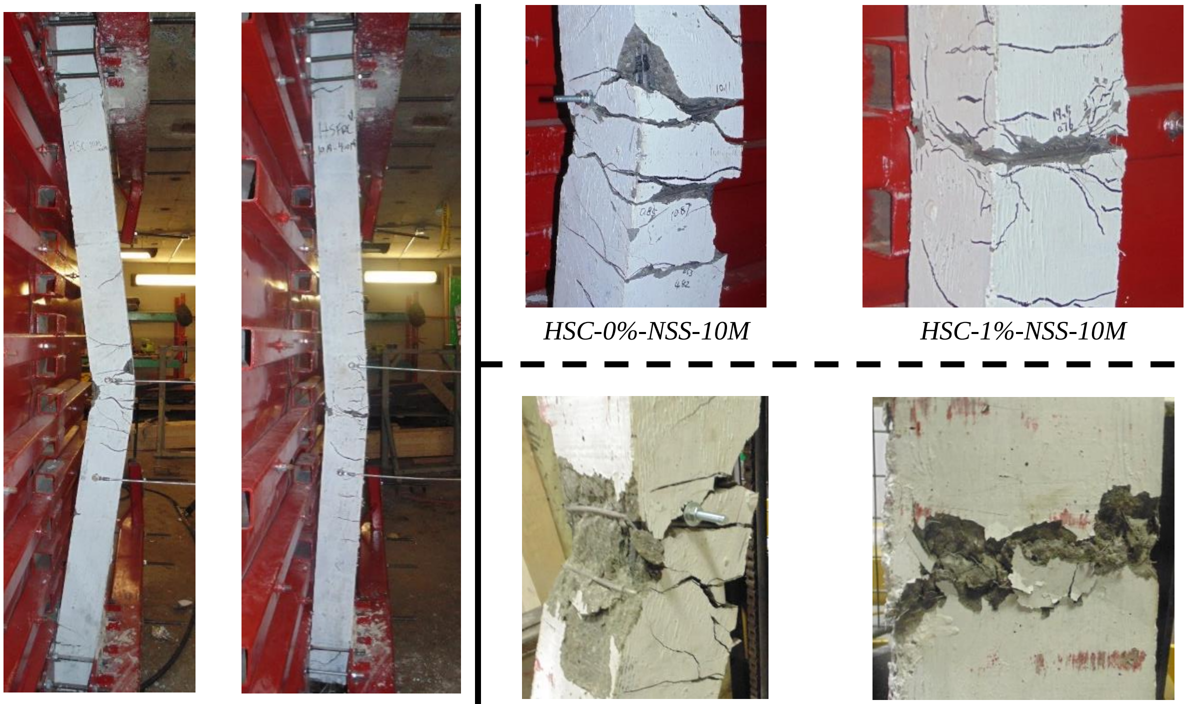

HSC-0%-NSS-10M *HSC-1%-NSS-10M* (top row, panel b)

HSC-0%-NSS-10M *HSC-1%-NSS-10M* *HSC-0%-NSS-10M* *HSC-1%-NSS-10M*

a) Blast 3 b) Mid-span result after blast 3

Figure 5-27 Effect of steel fibers for HSC-0%-NSS-10M vs HSC-1%-NSS-10M: Photographs after blast 3

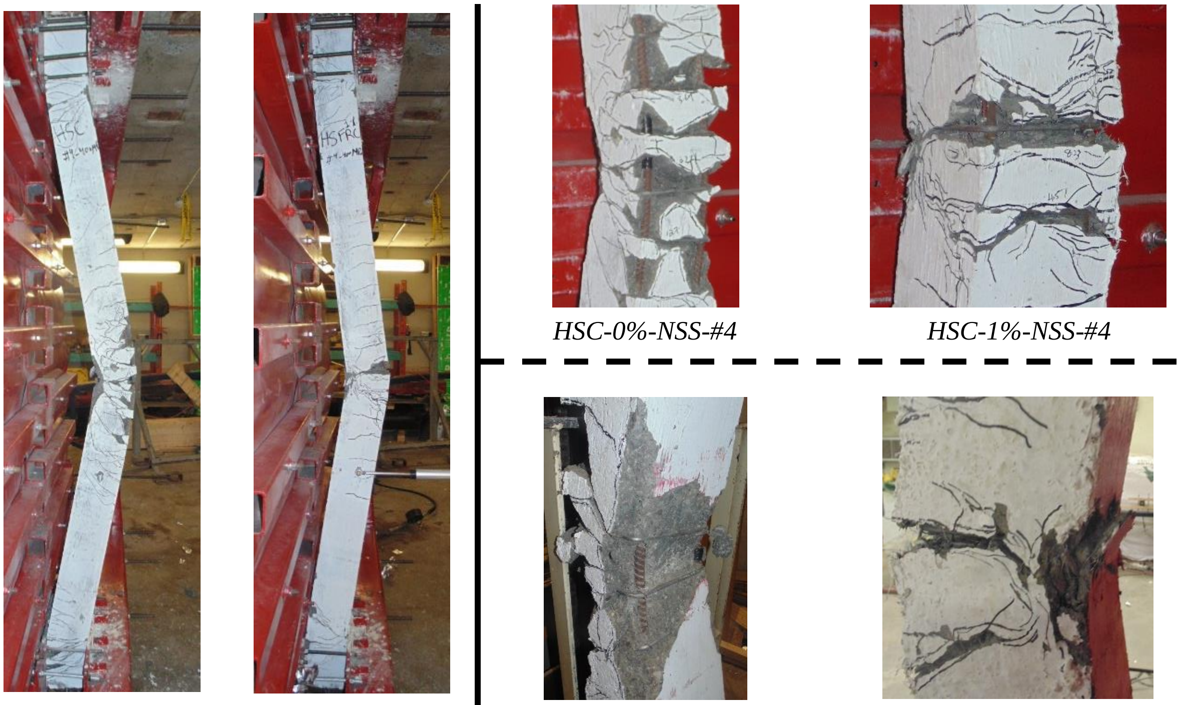

HSC-0%-NSS-#4 *HSC-1%-NSS-#4*

HSC-0%-NSS-#4 *HSC-1%-NSS-#4* *HSC-0%-NSS-#4* *HSC-1%-NSS-#4*

a) Blast 4 b) Mid-span result after blast 4

Figure 5-28 Effect of steel fibers for HSC-0%-NSS-#4 vs HSC-1%-NSS-#4: Photographs after blast 4

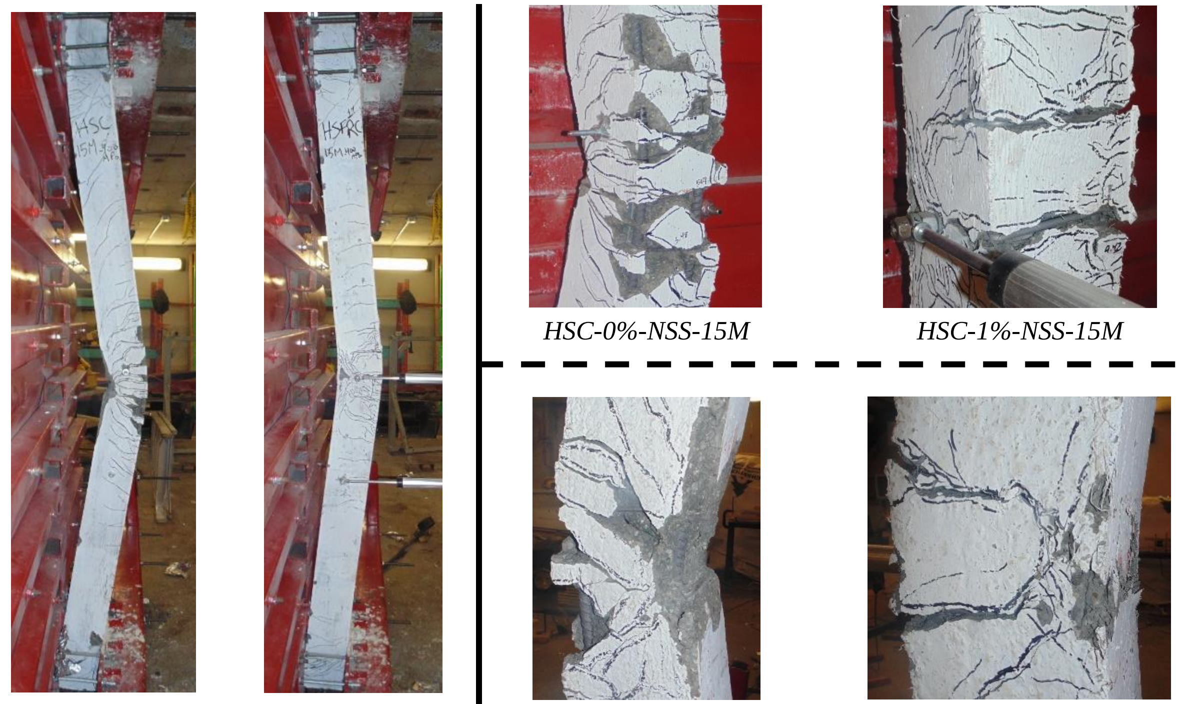

HSC-0%-NSS-15M HSC-1%-NSS-15M

HSC-0%-NSS-15M HSC-1%-NSS-15M

HSC-0%-NSS-15M HSC-1%-NSS-15M

a) Blast 4 b) Mid-span result after blast 4

Figure 5-29 Effect of steel fibers for HSC-0%-NSS-15M vs HSC-1%-NSS-15M: Photographs after blast 4

5.5.2 Effect of Steel Fibers in Specimens with MMFX Bars

In this section, the effect of fibers is investigated in columns with high-strength reinforcement. Two pairs of columns are compared, with #4 and #5 MMFX bars:

- #4 MMFX set: HSC-0%-MMFX-#4 vs. HSC-1%-MMFX-#4
- #5 MMFX set: HSC-0%-MMFX-#5 vs. HSC-1%-MMFX-#5

The columns in each companion set have the same high-strength reinforcement ratio and transverse reinforcement but were cast with plain HSC and HSFRC (1% fibers). Comparative bar charts and displacement time histories for both pairs after blasts 2-5 are available in Figure 5-30 and Figure 5-31. Photographs after testing are provided in Figure 5-32 and Figure 5-33.

The HSFRC specimens showed better behaviours when compared to the HSC companions after blast 2. For the HSC specimen with #4 MMFX bars, the maximum displacement was 16.76 mm, while the HSFRC column with #4 MMFX bars decreased that displacement by 20.9% and recorded a value 13.26 mm. As for residual, both specimens showed similar displacements after this shot (3.33 mm and 3.58 mm). With regards to the #5 MMFX set, the HSFRC specimen showed a 9.3% reduction in maximum displacement when compared to the plain HSC specimen (from 17.18 mm to 15.59 mm). As for the residual, the column with fibers had a higher displacement (4.36 mm) than the column without fibers (2.42 mm).

Blast 3 produced a similar trend with regards to the effect of fibers on displacement control in the MMFX series. The #4 HSFRC specimen showed a 12.0% reduction in maximum displacement when compared to the #4 specimen with plain concrete (from 46.17 mm to 40.65 mm). The same applied for residual, where it settled with ~ 4 mm less deformation compared to the plain HSC column. For the #5 pair, addition of fibers also led to lower displacements, with an improvement of 10.4% (from 37.06 mm to 33.20 mm) for maximum displacement, whereas both columns showed similar residual deformations (from 11.15 mm to 10.04 mm).

Blast 4 was considered a failure blast to the #4 pair. At failure, the HSFRC specimen did not show improved behaviour when compared to the companion with plain concrete, where its maximum displacement was 99.24 mm, which is a higher number than the 94.24 mm recorded for the HSC specimen. The counter-trend can be explained by examining the failure modes of the two specimens. The HSFRC specimen experienced bar rupture at mid-span, whereas the HSC specimen did not. Comparing the failure photos, the HSC specimen shows important crushing, cracking and spalling of concrete, while the concrete damage is limited in the HSFRC column. It is understood that forces must balance in a reinforced concrete member under flexural loading; the increased strength and strain capacity of HSFRC in compression leads to the development of higher tensile stresses in the high-strength reinforcement, which eventually leads to bar rupture. Another possible reason for the bar rupture is that the stresses seemed to concentrate at the critical crack opening (where fibers pulled out) in the HSFRC column with limited cracking and damage outside this region; this concentration of stresses could have been a factor in eventually driving tension steel bars to rupture.

As for the #5 pair of specimens, failure was delayed to blast 5. At blast 4, the HSFRC column showed lower displacements when compared to its HSC companion, with reductions of 11.6% for maximum (from 62.68 mm to 55.39mm) and 13.3% residual displacement (form 24.85 mm to 21.54 mm). Both specimens would eventually fail due to bar rupture under application of the fifth blast. Despite the brittle failure through bar rupture, the HSFRC specimen recorded less displacement and damage during the test. Its maximum displacement was 87.89 mm, a reduction of 51.9% when compared to the 182.59 mm recorded for the HSC specimen. Similarly, for the residual displacement, a reduction of 71.3% was obtained (form 147.77 mm to 42.44mm). Damage on the column was significantly reduced for the fiber-reinforced specimen, as seen through photographs shown in Figure 5-33.

In summary, the benefit of fibers in improving the blast performance of columns with high-strength reinforcement was demonstrated in this set. The provision of fibers reduced displacements at equivalent blasts, while also enhancing damage tolerance. Nonetheless, the increased compression strain capacity of HSFRC combined with the less ductile high-strength bars can lead to earlier rupture of tension steel reinforcement at failure.

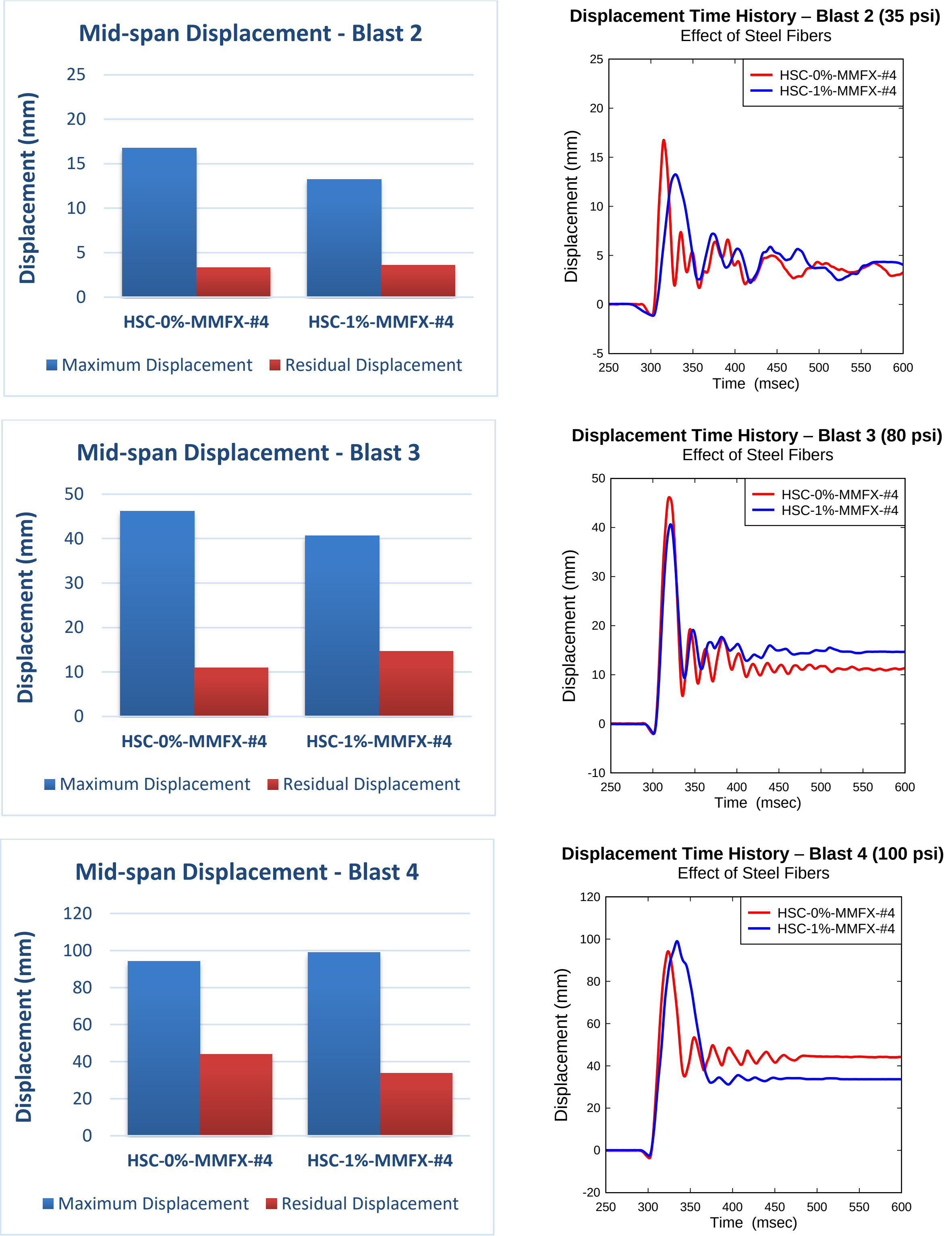

Figure 5-30 Effect of steel fibers for HSC-0%-MMFX-#4 vs. HSC-1%-MMFX-#4: Comparisons of mid-span displacements and displacement time histories for blasts 2-4

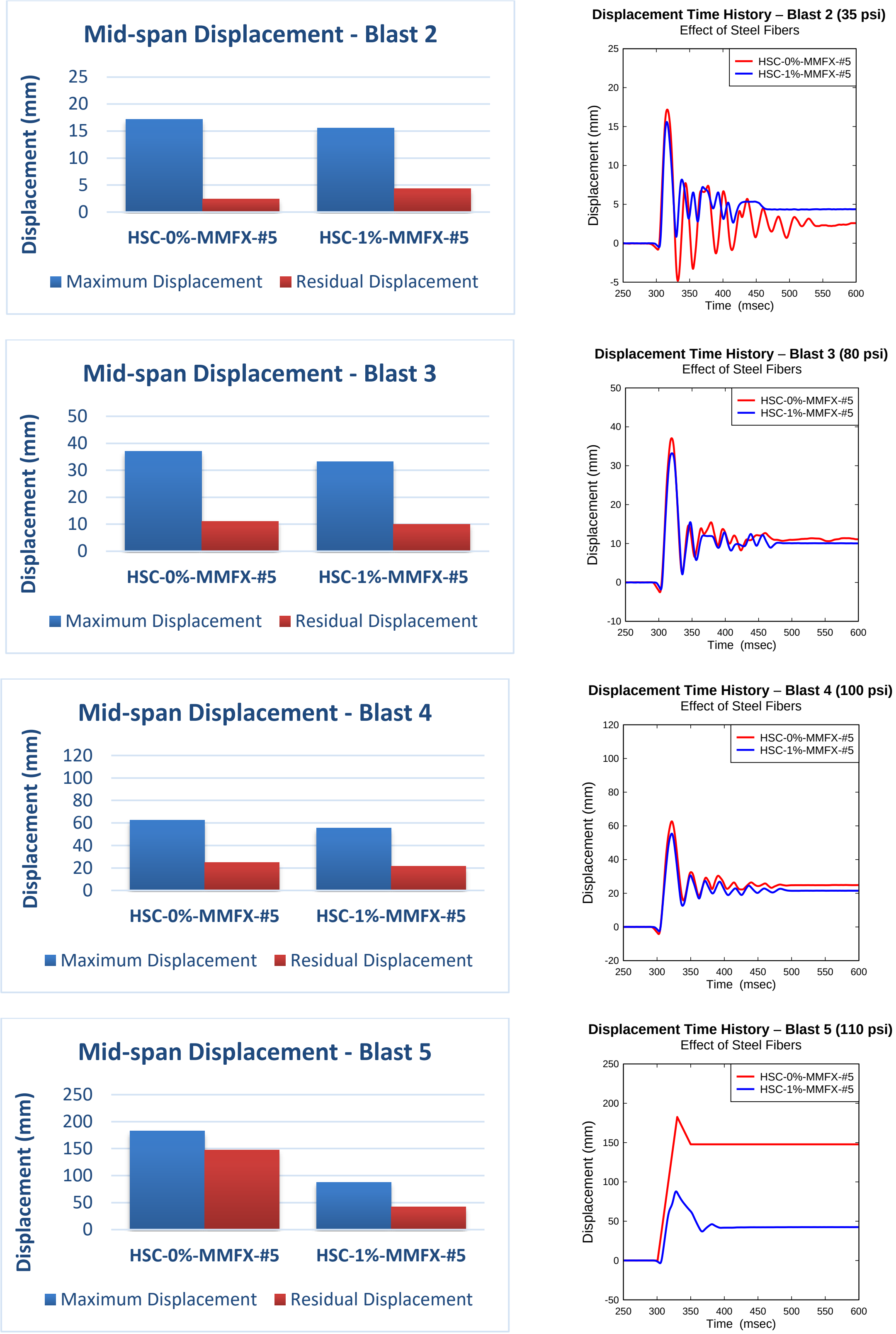

Figure 5-31 Effect of steel fibers for HSC-0%-MMFX-#5 vs. HSC-1%-MMFX-#5: Comparisons of mid-span displacements and displacement time histories for blasts 2-5

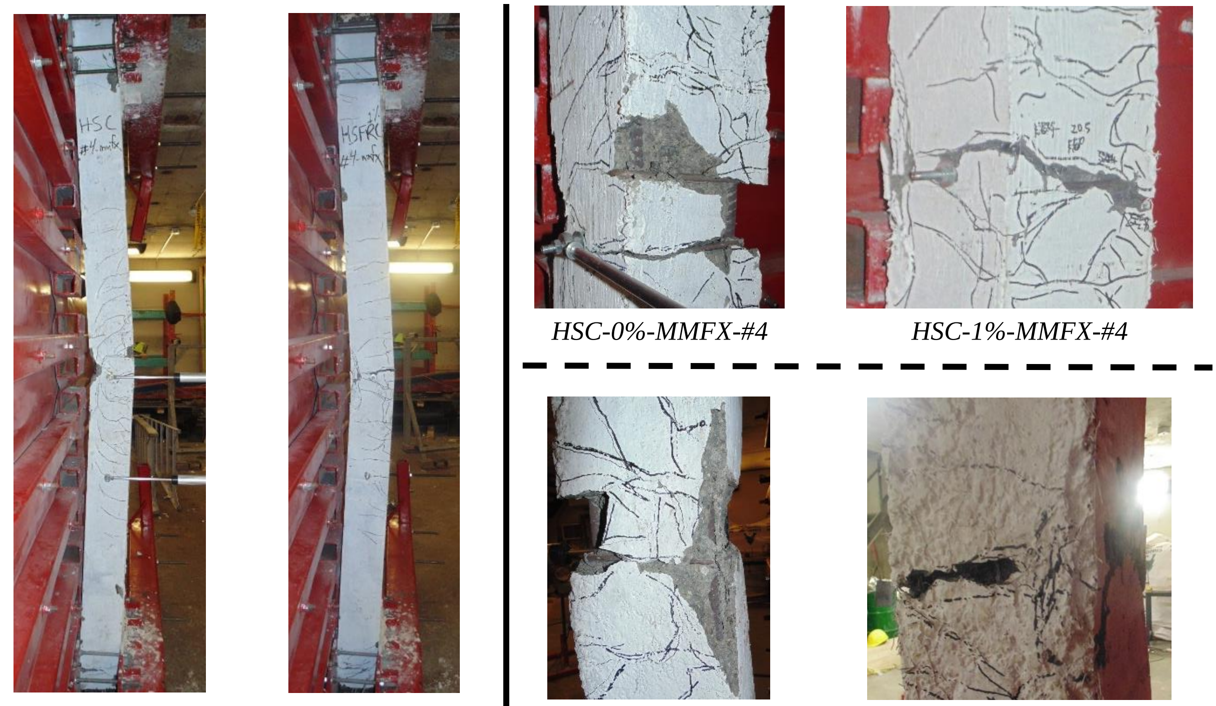

HSC-0%-MMFX-#4 *HSC-1%-MMFX-#4*

a) Blast 4

HSC-0%-MMFX-#4 *HSC-1%-MMFX-#4*

HSC-0%-MMFX-#4 *HSC-1%-MMFX-#4*

b) Mid-span results after blast 4

Figure 5-32 Effect of steel fibers for HSC-0%-MMFX-#4 vs. HSC-1%-MMFX-#4: Photographs after blast 4

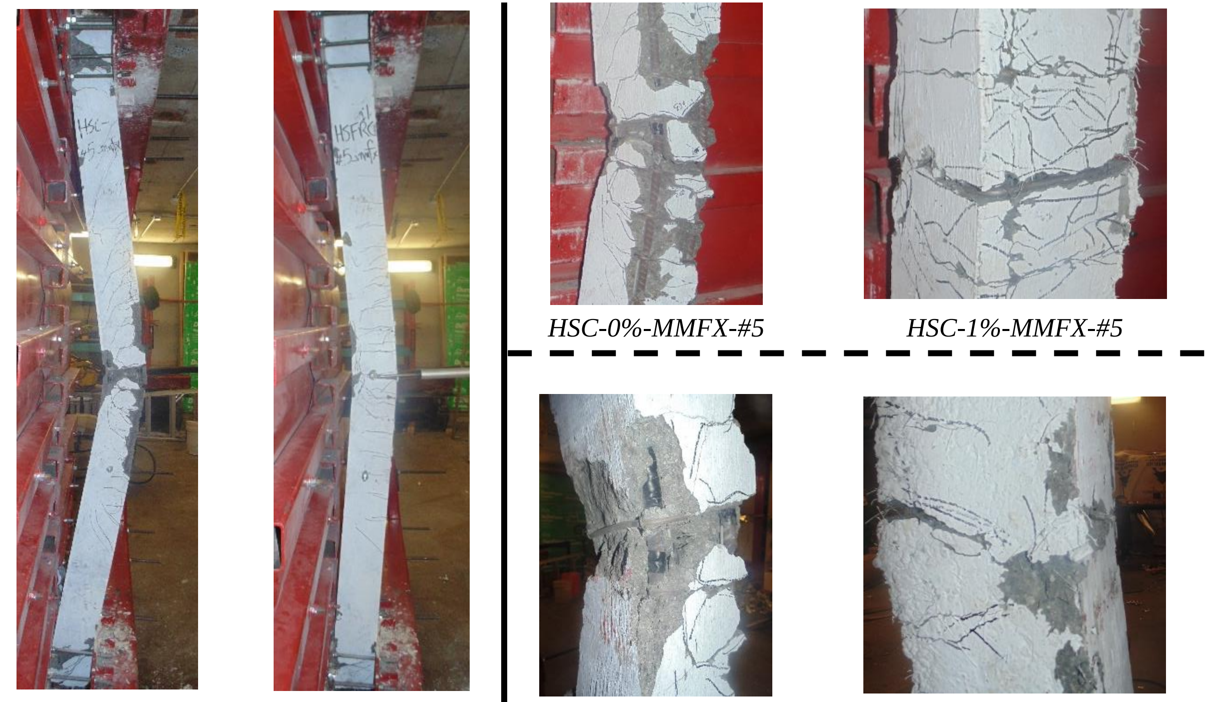

HSC-0%-MMFX-#5 *HSC-1%-MMFX-#5*

a) Blast 5

HSC-0%-MMFX-#5 *HSC-1%-MMFX-#5*

HSC-0%-MMFX-#5 *HSC-1%-MMFX-#5*

b) Mid-span results after blast 5

Figure 5-33 Effect of steel fibers for HSC-0%-MMFX-#5 vs. HSC-1%-MMFX-#5: Photographs after blast 5

5.5.3 Effect of Steel Fibers on Failure Mode and Secondary Fragmentation

High-strength concrete shows brittle behaviour in compression, with limited tensile resistance. The addition of steel fibers improves the post-caking capacity of high-strength concrete which leads to enhanced ductility in compression, with superior tensile resistance and post-cracking capacity. because of these characteristics, the use of fibers showed an ability to significantly reduce and control crushing, cover spalling and cracking in the high-strength concrete columns; this is clearly demonstrated in the failure photos of companion HSC and HSFRC specimens (see Figure 5-32 and Figure 5-33).

The increased toughness of HSFRC also leads to significant reduction in the amount of secondary fragmentation when compared to plain HSC. This is clear in Figure 5-34 which shows high-speed video stills of the failure process of companion HSC and HSFRC specimens. Fragments are reduced - if not eliminated - whenever fibers were present in the concrete mix. On the other hand, the opposite happens in the plain high-strength concrete specimens, where large pieces of concrete go flying across the test area at high speeds, a situation which could harm building occupants.

However, the provision of fibers in concrete can also influence failure mode of columns under blast loading. In the case of conventional reinforced concrete members, energy dissipation occurs through cracking and damage over a well-defined plastic hinge region over the column's mid-span. This hinging mechanism is different in HSFRC, where damage concentrates at a critical crack location where fiber pullout and failure occurs. Furthermore, the equilibrium of compressive and tensile forces in bending means that the increased compressive toughness of HSFRC can lead to high stresses in tension steel, making the tensile reinforcing bars more susceptible to rupture (this was, for example, demonstrated in the companion HSFRC/HSC columns with #4 MMFX bars and the HSFRC/HSC columns #4 NSS bars).

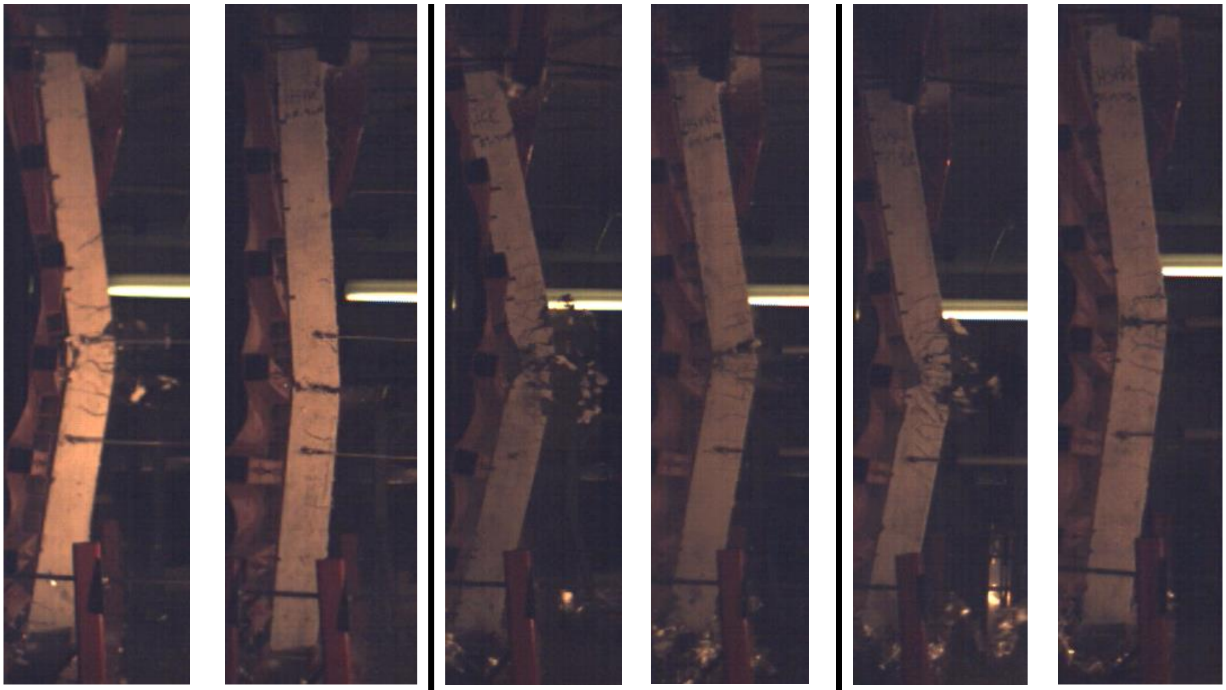

HSC-0%-NSS-10M *HSC-1%-NSS-10M* *HSC-0%-NSS-#4* *HSC-1%-NSS-#4* *HSC-0%-NSS-15M* *HSC-1%-NSS-15M*

Blast 3 Blast 4 Blast 4

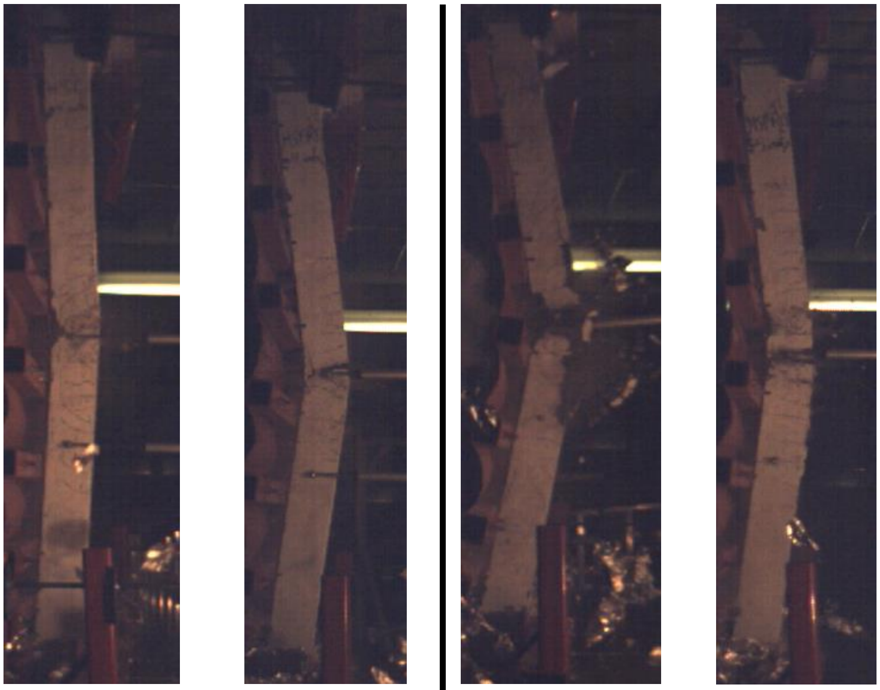

HSC-0%-MMFX-#4 *HSC-1%-MMFX-#4* *HSC-0%-MMFX-#5* *HSC-1%-MMFX-#5*

Blast 4 Blast 5

Figure 5-34 Effect of steel fibers on secondary fragmentation through high-speed video footage

5.5.4 Effect of Steel Fibers Content

Another aspect studied in this research was the effect of fiber content. The parameter was investigated through specimens HSC-0.5%-NSS-10M and HSC-1%-NSS-10M, which had similar properties (normal-strength 10M bars, hoops at s = 75 mm) but were built with HSFRC having 0.5% and 1% steel fibers by volume of concrete, respectively. The response of the columns is also compared to the companion column built with plain HSC (HSC-0%-NSS-10M), i.e. 0% fibers. Comparative bar charts and comparative displacement time histories for blast 2 and 3 are available in Figure 5-35. Figure 5-36 also shows photographs of the specimens after testing.

At blast 2, the control specimen without fibers sustained the largest maximum displacement of 33.64 mm. The column with 0.5% fibers reduced this displacement by 32.07% and recorded a maximum displacement of 22.85 mm. A further increase in fiber content to 1% of fibers led to a further reduction in displacement to 19.41 mm. As for the residual deformation, the highest displacement was recorded for the plain concrete column at 14.69 mm, whereas for the fiber-reinforced specimens settled with limited displacements (although the trend is not clear as the fiber content is increased from 0.5% to 1%; 2.78 mm vs. 6.70 mm, respectively).

The third blast led to the failure of all three specimens. The trend in displacement control followed the gradual variation of fiber content in the columns. The specimen without fibers failed with a maximum displacement equal to 132.57 mm, while the specimen with 0.5% fibers reduced that displacement by 31.05% to 91.41 mm, and finally the specimen with 1% fibers further reduced the displacement to 83.78 mm. Similarly, for residual displacements, the column without fibers showed the highest permanent deformation at 118.68 mm, while values of 62.13mm and 52.85 mm were recorded for the columns with 0.5% and 1% fibers, respectively.

The above results demonstrate that the performance generally improves as the fiber content is gradually increased. The results also show that even a small amount of fibers is sufficient to enhance the blast performance of HSC columns. Indeed, the enhancement in displacement control is clear when transitioning from plain concrete (0% fibers) to 0.5% fibers. However, the effect on displacements upon the transition from 0.5% to 1% is less significant (i.e. doubling the fiber content does not cut the displacements by half). This is clear when examining the outcomes from blasts 2 and 3, where the relative reduction in displacements due to the doubling of the fiber content (from 0.5% to 1% fibres) is 15.1% for blast 2 and 8.4% for blast 3. Similarly, both fiber-reinforced concrete columns showed reduced cracking, spalling and fragmentation, regardless of whether the columns were reinforced with 0.5% or 1% fibers, demonstrating that even a relatively low amount of steel fibers is effective in improving the damage tolerance of high-strength concrete columns.

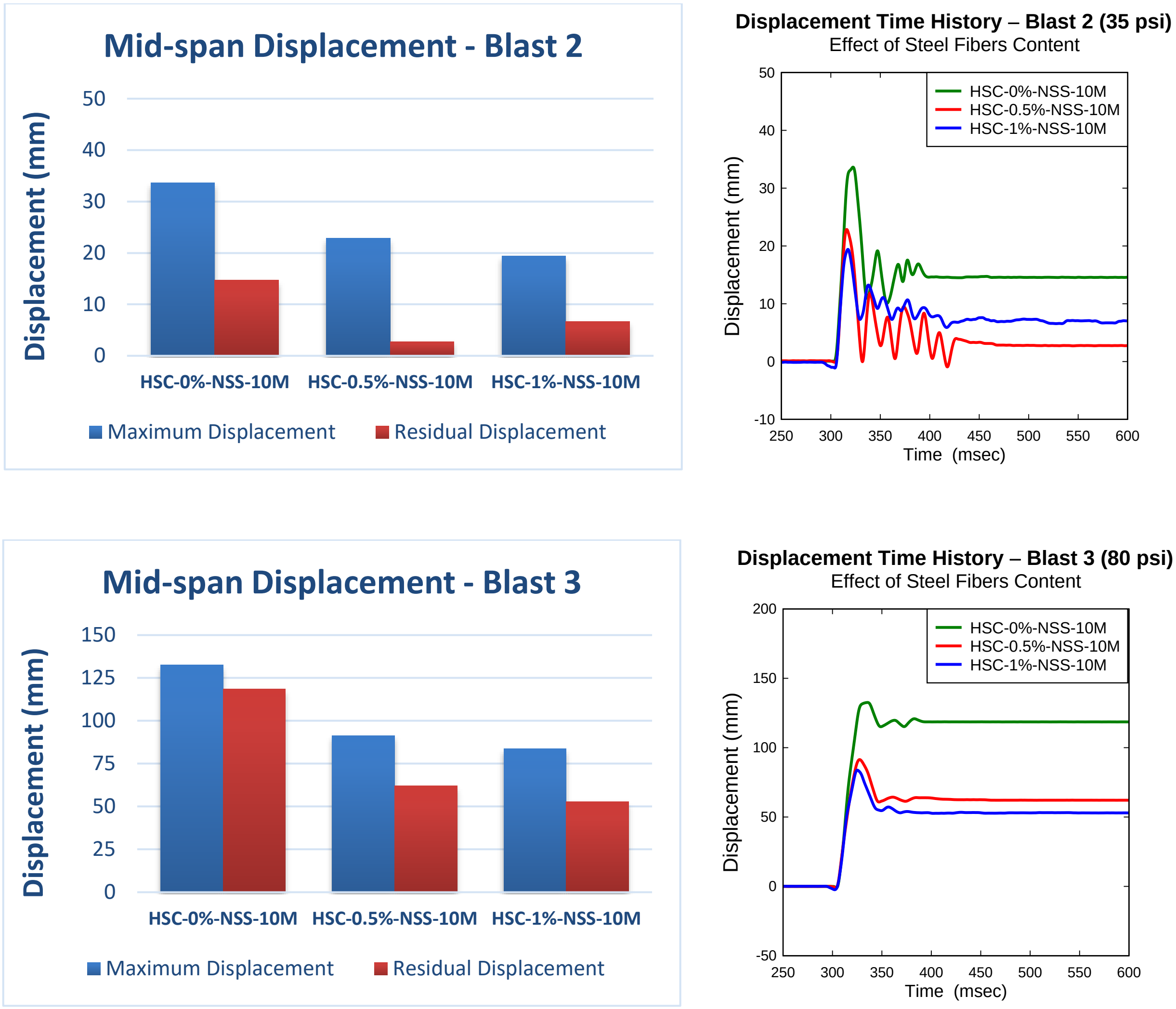

Figure 5-35 Effect of steel fibers content: Comparisons of mid-span displacements and displacement time histories for blasts 2-3

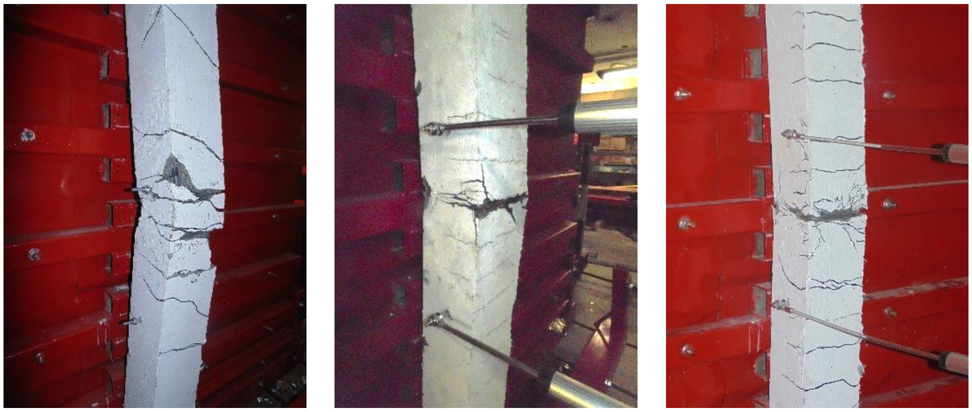

HSC-0%-NSS-10M *HSC-0.5%-NSS-10M* *HSC-1%-NSS-10M*

Figure 5-36 Effect of steel fibers content: Photographs after blast 3

5.6 Effect of Concrete Strength

5.6.1 Effect of Concrete Strength in Columns with NSS Bars

The effect of concrete strength was another aspect studied in this research. The effect of concrete strength is investigated by comparing the response of two companion sets built with normal-strength concrete (NSC) vs. high-strength concrete (HSC) and #4/15M normal-strength reinforcing bars:

- #4 set: NSC-0%-NSS-#4 vs. HSC-0%-NSS-#4
- 15M set: NSC-0%-NSS-15M vs. HSC-0%-NSS-15M

Comparative bar charts and displacement histories for blasts 2-4 are provided in Figure 5-37 and Figure 5-38. Photographs of the columns after testing are shown in Figure 5-39 and Figure 5-40.

For blast 2, the HSC and NSC columns with #4 bars recorded approximately the same maximum displacement (20.07 mm and 20.47 mm, respectively). As for the residual, the HSC specimen settled with a higher value of 7.84 mm compared to the 5.50 mm in the case of the NSC specimen. For the 15M pair, the HSC column showed around 20% reduction in the maximum displacement recorded for the NSC column (from 20.01 mm to 16.02 mm). Residual displacement was less for the HSC column, where it settled with 3.41 mm versus the 6.71 mm for the NSC column.

After blast 3, displacement data shows slight improvements for the HSC columns over the NSC columns. The #4 HSC column displaced a maximum value of 87.38 mm, which is 5.8% less than the displacement for the NSC column which was equal to 82.35 mm. Residual displacement settled for the HSC specimen with a value of 51.31 mm versus 44.29 mm for the NSC specimen. In the 15M companion set, the HSC column also achieved a slight reduction in maximum displacement of 7.5% over the NSC column (from 83.96 mm to 77.70 mm). However, the residual displacements were similar after this shot for both specimens (~ 54 mm displacement for both).

As for blast 4, a comparison for the #4 pair of specimens in not available. That is because only the HSC column was tested under the impact of a fourth blast, whilst a decision to not test the NSC specimen for a fourth time was taken due to relatively high damage that the specimen went through after blast 3. In the case of the 15M pair, both specimens were tested for a fourth time. The HSC specimen continued to show a slight improvement over the NSC companion, where it recorded a maximum displacement equal to 141.09 mm compared to the 162.77 mm obtained for the NSC specimen (a reduction of 13.3%). Residual displacement was also reduced by a similar margin when using higher strength concrete, where the HSC column settled at 117.56 mm, a value which is 13.9% less than the 136.60 mm recorded for the NSC specimen.

In summary, the results demonstrate that concrete strength has a relatively minor role on the blast resistance of columns. While the use of HSC results in slight improvements in displacement control at equivalent blasts, overall blast capacity is not affected. The slight improvement could be related to the increased elastic modulus and tensile strength of HSC which can enhance stiffness and flexural capacity before yielding. It should be noted that the columns in this study were flexural dominant, as such the behaviour was dictated by the longitudinal steel reinforcement properties. The effect of concrete strength could be more significant in shear dominant columns, where HSC is expected to show increased shear resistance. The use of HSC can also be beneficial in columns with high-strength reinforcement, where the use of HSC can increase the balanced reinforcement ratio and allow for greater amounts of steel – further research is recommended.

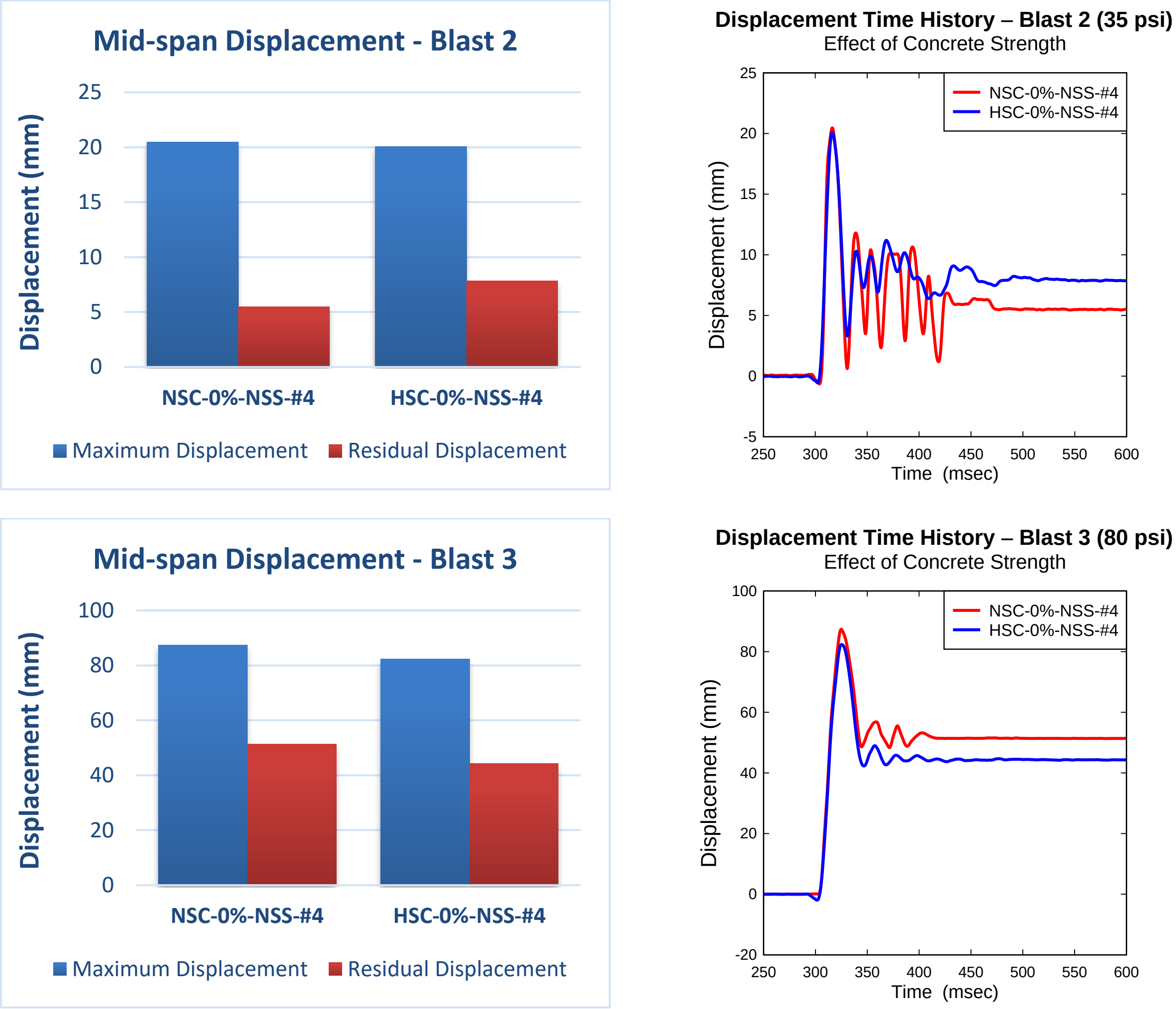

Figure 5-37 Effect of concrete strength for NSC-0%-NSS-#4 vs. HSC-0%-NSS-#4: Comparison of mid-span displacements and displacement time histories for blasts 2-3

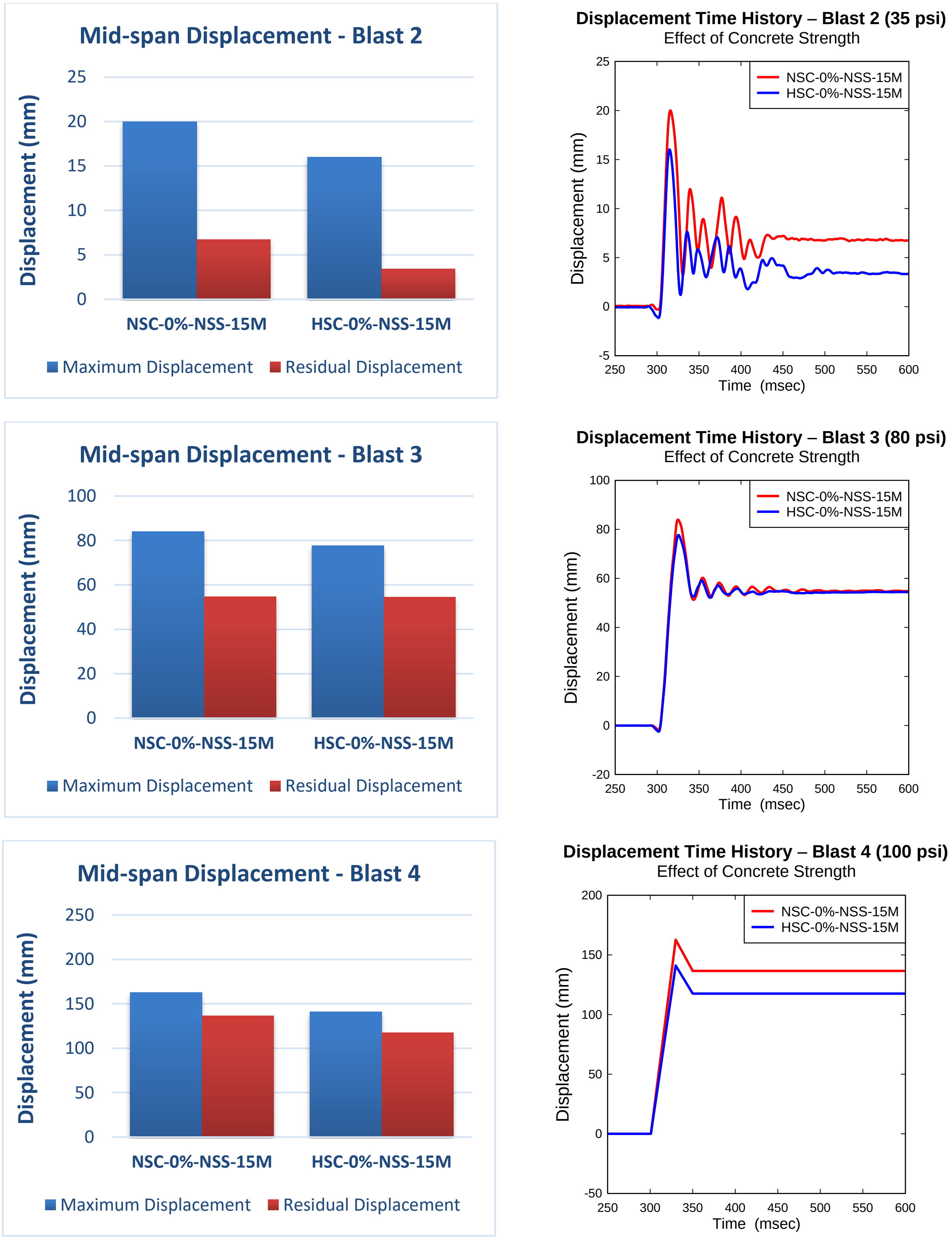

Figure 5-38 Effect of concrete strength for NSC-0%-NSS-15M vs. HSC-0%-NSS-15M: Comparison of mid-span displacements and displacement time histories for blasts 2-4

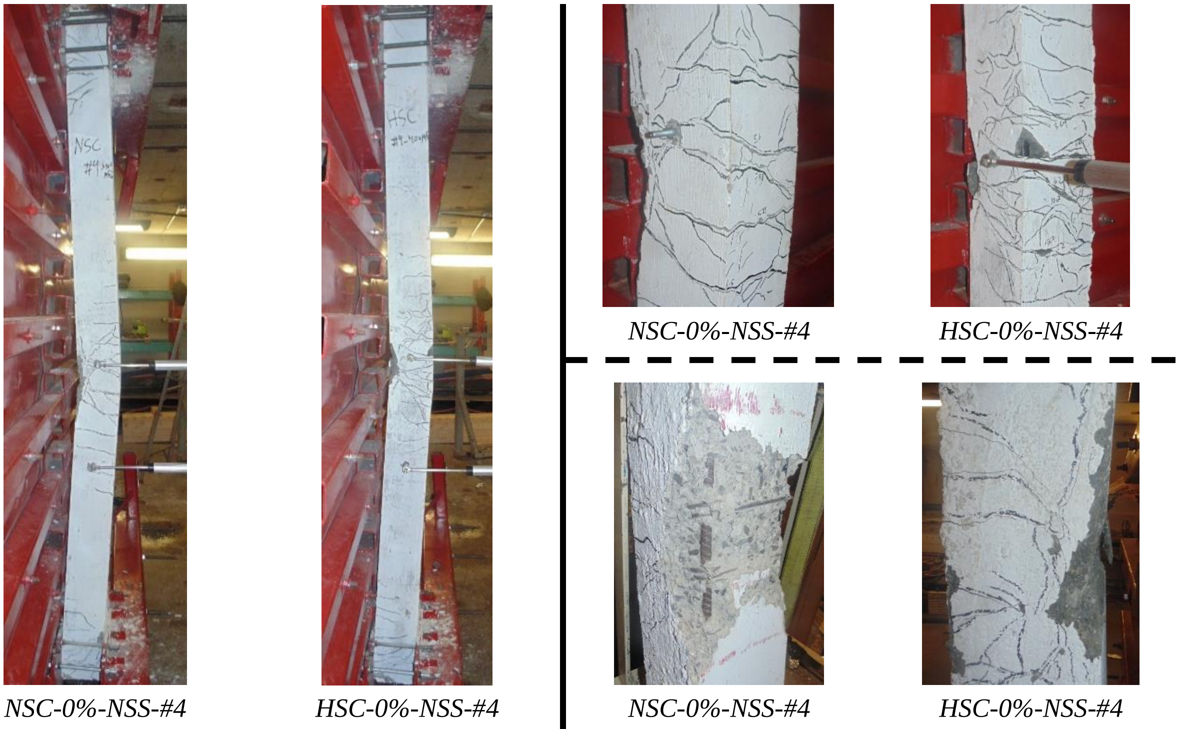

a) Blast 3 b) Mid-span result after Blast 3

Figure 5-39 Effect of concrete strength for NSC-0%-NSS-#4 vs. HSC-0%-NSS-#4: Photographs after blast 3

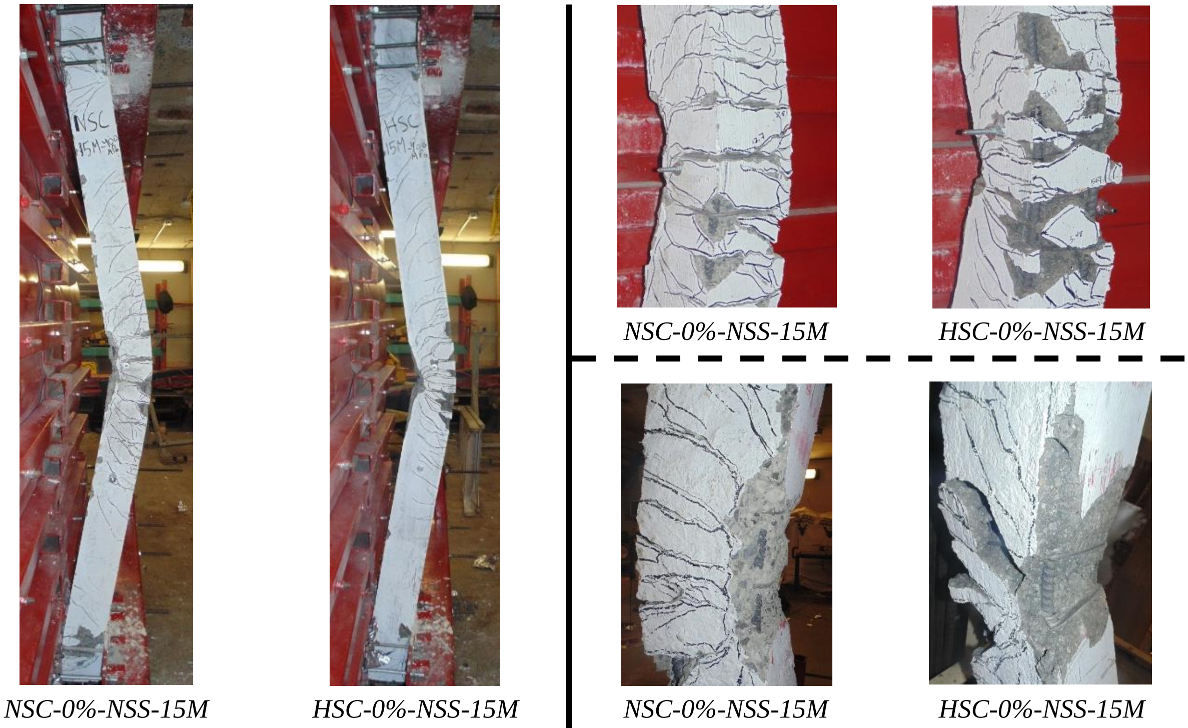

a) Blast 4 b) Mid-span result after Blast 4

Figure 5-40 Effect of concrete strength for NSC-0%-NSS-15M vs. HSC-0%-NSS-15M: Photographs after blast 4

5.6.2 Effect of Concrete Strength on Failure Mode and Secondary Fragmentation

It is accepted that concrete’s behaviour becomes more brittle as strength is increased. This was observed in the compression stress-strain relationships of NSC and HSC presented in Ch.3, where HSC showed brittle crushing failure soon after peak capacity. In the columns tested in this research study, this translated into relatively more brittle failure and greater damage for the HSC columns in comparison to their NSC counterparts. This can be observed when examining the damaged state of the compression zone or tension face of the columns at mid-span (refer to Figure 5-39 and Figure 5-40). This effect was more evident in the 15M companion set.

Similarly, for secondary fragmentation, a comparison of the high-speed video stills for the 15M specimens at failure shows that more severe fragmentation occurs for the high-strength concrete specimen (see Figure 5-41). The still shows larger pieces of concrete shattering off the specimen’s highly stressed mid-span region (tension zone and compression zone), compared to the relatively smaller pieces of concrete in the case of normal-strength concrete column.

NSC-0%-NSS-15M *HSC-0%-NSS-15M*

Blast 4

Figure 5-41 Effect of concrete strength on secondary fragmentation through high speed footage

5.7 Effect of Seismic Detailing

5.7.1 Effect of Seismic Detailing in HSC Columns with NSS and MMFX Bars

The last parameter investigated in this research program was transverse reinforcement detailing. The effect of this variable is studied by comparing the response of companion columns with non-seismic (s = 75 mm) and seismic detailing (s = 38 mm). Two sets of columns with normal-strength 10M bars and #4 MMFX high-strength bars are examined:

- NSS set with 10M bars: HSC-0%-NSS-10M vs. HSC-0%-NSS-10M-S
- MMFX set with #4 bars: HSC-0%-MMFX-#4 vs. HSC-0%-MMFX-#4-S

The columns in each set had the same longitudinal reinforcement ratio and type, and were built with high-strength concrete. The "S" in the nomenclature indicates the use of seismic detailing. Comparative bar charts and displacement time histories are provided in Figure 5-42 and Figure 5-43. Photographs of the columns after testing are provided in Figure 5-44 and Figure 5-45.

Specimens with seismic detailing showed improvement in performance in terms of displacement control after blast 2. In the set with normal-strength bars, the 10M seismic column recorded a maximum displacement of 20.81 mm, a value which is 38.1% less than the one recorded for the non-seismic column (33.64 mm). The same applied for the residual displacement, where HSC-0%-NSS-10M-S settled with only 4.60 mm, versus 14.69 mm for HSC-0%-NSS-10M (a reduction of 68.7%). A similar trend is observed in the #4 MMFX pair, where the maximum displacements recorded were 16.76 mm and 13.28 mm for the non-seismic and seismic columns, respectively (a reduction of 20.8% for HSC-0%-MMFX-#4-S). Residual displacements were similar for both columns after this shot (3.33 mm for the non-seismic column vs. 2.16 mm for the seismic one).

The outcome of blast 3 also showed enhanced behaviour for the seismic columns. For the NSS set with 10M bars, the seismic column reduced maximum displacements by 19.9% when compared to non-seismic companion (form 132.57 mm to 106.13 mm). Residual displacements were also reduced by 26.6% for the seismic specimen (from 118.68 mm to 87.14 mm). It should be noted that this shot was the failure shot for both 10M specimens. The #4 MMFX specimens produced the same trend, where the seismic column showed reductions of 13.5% for maximum displacement (from 46.17 mm to 39.95 mm) when compared to its non-seismic companion. Residual displacement was also slightly reduced for the seismic column (from 10.97 to 8.88 mm).

The two #4 MMFX columns were tested under a fourth blast. Once again displacements were better controlled in the column with seismic detailing. The maximum mid-span displacement sustained by HSC-0%-MMFX-#4-S was 84.30 mm, which was a 10.5% lower than the displacement recorded by the non-seismic HSC-0%-MMFX-#4 column (94.24 mm). The closely spaced hoops in the seismic column were also able to better restrict permanent deformations, with a 55.3% reduction in residual displacement. The seismic column settled with 19.70 mm of permanent displacement while its companion with non-seismic details suffered a permanent deformation of 44.11 mm. While both columns failed during this blast, the failure mechanism was different, where HSC-0%-MMFX-#4 failed due to crushing and spalling of concrete, while the seismic HSC-0%-MMFX-#4-S experienced rupture of tension steel.

In summary, the results demonstrate benefits associated with the use of seismic detailing, where the use of closely spaced hoops results in improvements in displacement control at equivalent blasts. The improvements can be related to the enhanced core confinement in the seismically-detailed columns which were tested under combined flexural and axial loads. Nonetheless, it should be noted that the columns in this test program were tested under relatively low axial load levels due to limitations in the jack capacity and the high-strength of the concrete used in the columns (the axial load corresponded to around 16% of the nominal capacity of the HSC columns).

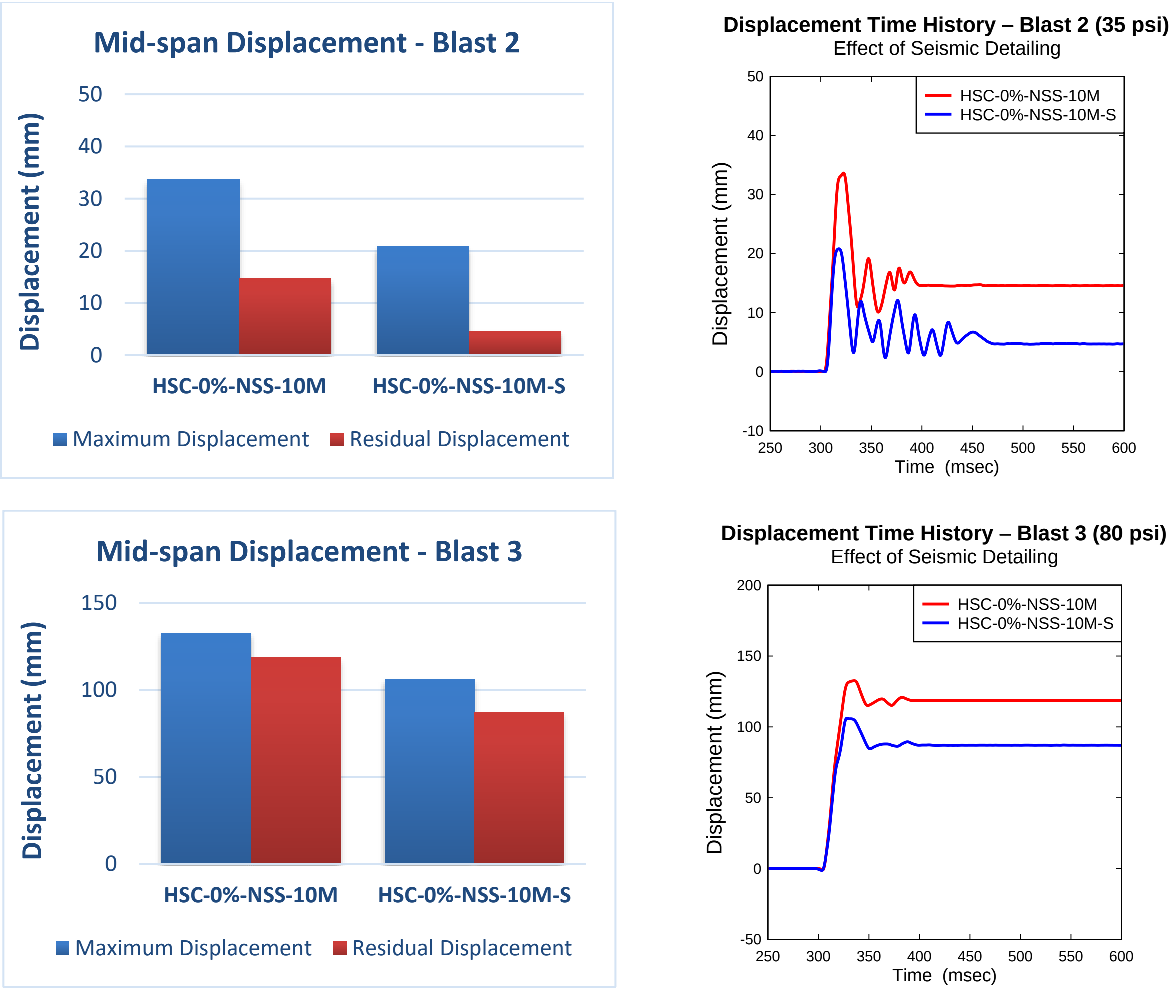

Figure 5-42 Effect of seismic detailing for HSC-0%-NSS-10M vs. HSC-0%-NSS-10M-S: Comparison of mid-span displacements and displacement time histories for blasts 2-3

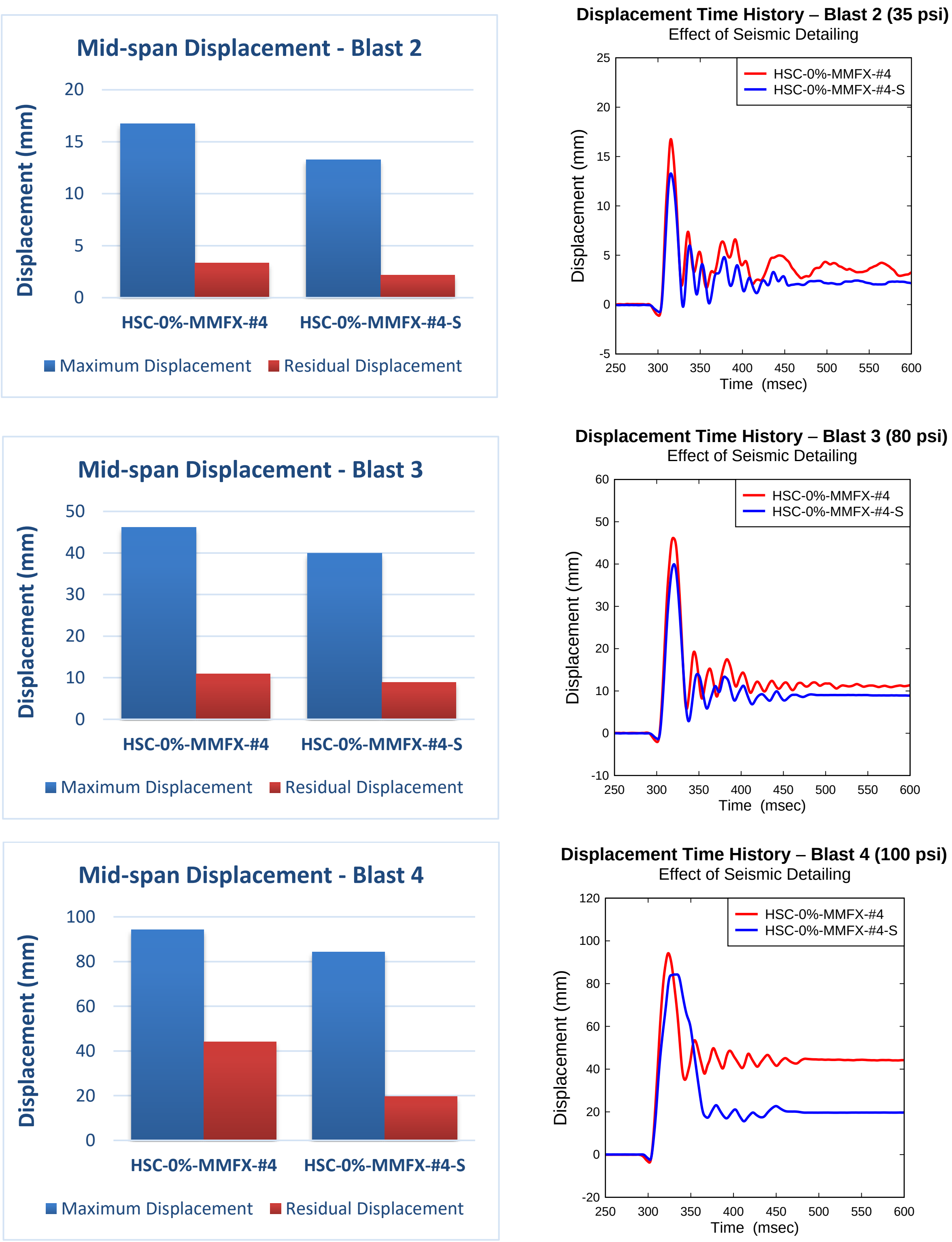

Figure 5-43 Effect of seismic detailing for HSC-0%-MMFX-#4 vs. HSC-0%-MMFX-#4-S: Comparison of mid-span displacements and displacement time histories for blasts 2-4

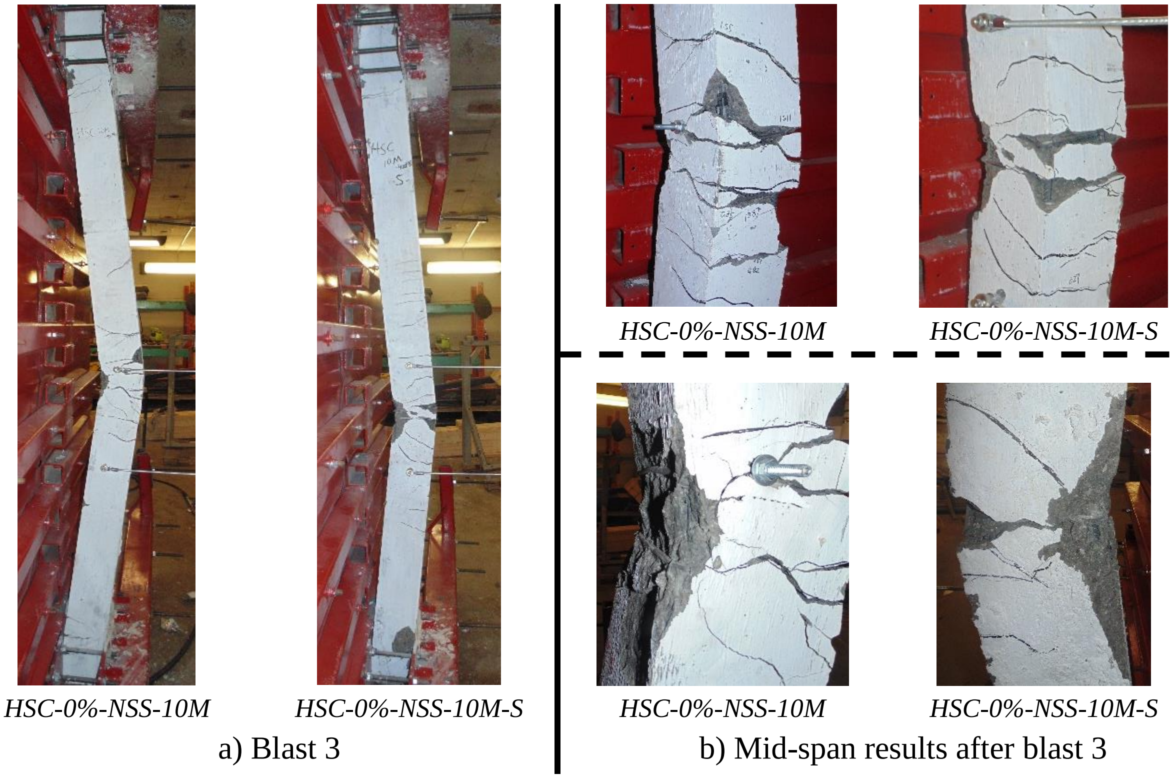

HSC-0%-NSS-10M HSC-0%-NSS-10M-S

a) Blast 3

HSC-0%-NSS-10M HSC-0%-NSS-10M-S

HSC-0%-NSS-10M HSC-0%-NSS-10M-S

b) Mid-span results after blast 3

Figure 5-44 Effect of seismic detailing for HSC-0%-NSS-10M vs. HSC-0%-NSS-10M-S: Photographs after blast 3

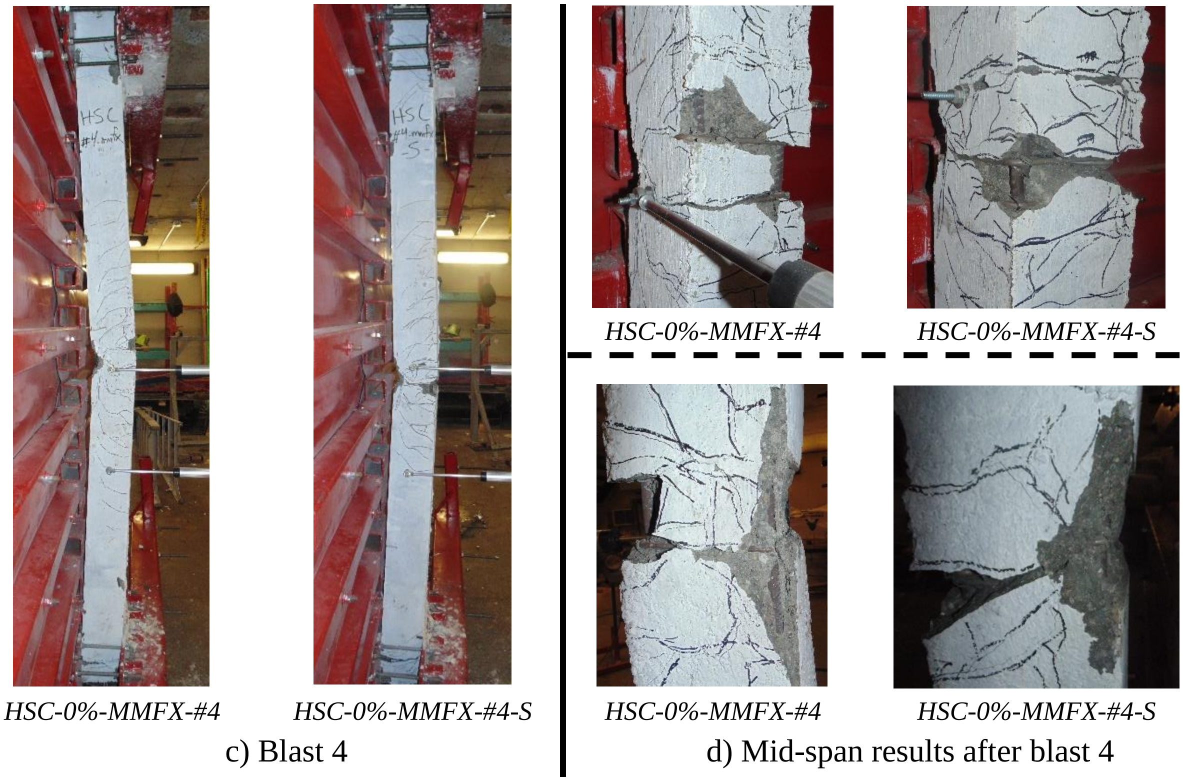

HSC-0%-MMFX-#4 HSC-0%-MMFX-#4-S

c) Blast 4

HSC-0%-MMFX-#4 HSC-0%-MMFX-#4-S

HSC-0%-MMFX-#4 HSC-0%-MMFX-#4-S

d) Mid-span results after blast 4

Figure 5-45 Effect of seismic detailing for HSC-0%-MMFX-#4 vs. HSC-0%-MMFX-#4-S: Photographs after blast 4

5.7.2 Effect of Seismic Detailing on Failure Mode and Secondary Fragmentation

This use of seismic detailing had some effects on damage and failure mode in the tested columns. In terms crack formation at moderate blast levels, traverse cracks were generally spaced according to the locations of the hoops, and therefore seismic columns in this test program tended to show more closely spaced cracks (i.e. at s = 38 mm vs. 75 mm in the non-seismic companions). The use of seismic detailing also affected damage and failure mode. For the specimens with normal-strength 10M bars, damage was more localized when using seismic detailing, with reduced crushing and spalling, the damage was also more localized when compared to the specimen with non-seismic detailing (see Figure 5-44). Similarly, the tie spacing affected fragmentation. As shown in Figure 5-46 , the 10M non-seismic column (HSC-0%-NSS-10M) produced greater fragments at failure when compared to the seismic column (HSC-0%-NSS-10M-S); the amount of fragmentation was greater because of the larger damaged at mid-span in the non-seismic column.

As for the pair with #4 MMFX bars, the detailing of the transverse reinforcement affected failure mode. For the non-seismic column, failure was associated with spalling and crushing of concrete, while for the column with seismic detailing, bar rupture was triggered at mid-span. This could be explained by the increased toughness of confined concrete in the seismic specimen which in turn results in larger tensile strains in the high-strength steel bars, eventually leading to bar rupture. Because of the difference in failure modes, the seismic column showed greater fragmentation at failure as shown in Figure 5-46.

HSC-0%-NSS-10M *HSC-0%-NSS-10M-S*
Blast 3

HSC-0%-MMFX-#4 *HSC-0%-MMFX-#4*
Blast 4

Figure 5-46 Effect of seismic detailing on secondary fragmentation through high-speed footage

CHAPTER 6. ANALYTICAL RESULTS

6.1 Chapter Overview

This chapter presents the dynamic inelastic analysis of the seventeen columns tested in this research program. The blast analysis is conducted using a single degree of freedom (SDOF) analysis, with member resistance functions developed using dynamic material properties for high-strength concrete, high-strength fiber-reinforced concrete and normal/high-strength steel. The chapter begins with a description of the materials models and dynamic increase factors (DIF) used in the analysis. An overview of the member analysis and SDOF procedure as implemented in software RCBlast (Jacques 2014) is then presented. A sensitivity analysis which examines the effect of accumulated damage, DIF models and material models is also presented.

6.2 Materials Models

This section describes the stress-stain models used in the analysis. Models for plain concrete, high-strength fiber-reinforced concrete, and normal/high-strength steel reinforcement are presented.

6.2.1 Plain Concrete Models

<u>Model for unconfined NSC in compression:</u>

To model the response of unconfined concrete in compression, the cover region of the plain NSC columns is considered using the model proposed by Hognestad (1951). Equation 6-1 is used to define the ascending branch of the stress-strain curve:

$$f_{cu} = \begin{cases} f'_{cu}\left(2(\varepsilon_{cu}/\varepsilon'_{cu}) - (\varepsilon_{cu}/\varepsilon'_{cu})^2\right), & \varepsilon_{cu} \le \varepsilon'_{cu} \\ f'_{cu} - \left(\dfrac{0.15f'_{cu}}{0.0038-\varepsilon'_{cu}}\right)(\varepsilon_{cu} - \varepsilon'_{cu}), & \varepsilon_{cu} \ge \varepsilon'_{cu} \end{cases} \qquad 6\text{-}1$$

Where, $$\varepsilon'_{cu} = {2f'_{cu}}/{E_c} \qquad 6\text{-}2$$

$$E_c = 3300\sqrt{f'_{cu}} + 6900 \qquad 6\text{-}3$$

Where f_{cu} is the unconfined stress at a given strain ε_{cu} , f'_{cu} is the peak unconfined stress (taken as 85% of the 28-day compressive strength of the concrete), and ε'_{cu} is the peak strain of unconfined concrete. Beyond ε'_{cu}, the descending branch is linear and defined by a line that connects the peak stress to $0.85f'_{cu}$ at a strain ε_{cu85} which is taken equal to 0.0038 mm/mm. A typical stress strain curve for unconfined NSC is shown in Figure 6-1 (a).

Model for unconfined HSC in compression:

The unconfined concrete model developed by Popovics (1973) was considered for the cover region in the plain high-strength concrete columns. This model was chosen since it is applicable for concrete with strength up to 125 MPa. Equation 6-4 is used for both the ascending and descending branches of the stress-strain curve. The relationships to calculate the different parameters that are part of equation 6-4 are listed in equations 6-5, 6-6, 6-7, and 6-8, where k controls the slope of the descending branch of the stress-strain curve, n is a curve-fitting factor, ε'_{cu} is the strain corresponding to the peak stress f'_{cu}, and E_c is the initial tangent modulus of unconfined concrete in compression. A typical stress strain curve for unconfined HSC as obtained using this model is shown in Figure 6-1 (b).

$$f_{cu} = \frac{n(\varepsilon_{cu}/\varepsilon'_{cu})}{n-1+(\varepsilon_{cu}/\varepsilon'_{cu})^{nk}} f'_{cu} \tag{6-4}$$

$$k = \begin{cases} 1.0 & \varepsilon_{cu}/\varepsilon'_{cu} \leq 1.0 \\ 0.67 + \dfrac{f'_{cu}}{62} & \varepsilon_{cu}/\varepsilon'_{cu} > 1.0 \end{cases} \tag{6-5}$$

$$n = 0.8 + \frac{f'_{cu}}{17} \tag{6-6}$$

$$\varepsilon'_{cu} = \frac{f'_{cu}}{E_c}\left(\frac{n}{n-1}\right) \tag{6-7}$$

$$E_c = 3300\sqrt{f'_{cu}} + 6900 \tag{6-8}$$

Taking into consideration that this unconfined model was used for the cover region of the columns, the model was modified to account for the spalling that may be experienced in HSC in that region. Once the strain on the original curve reaches 0.003 mm/mm, the stress drops down to a stress equal to $0.4f'_{cu}$, and then descends following a linear relationship according to equation 6-9 until zero stress is reached at a strain of 0.004 mm/mm.

$$f_{cu} = \left(\frac{0-(0.4f'_{cu})}{(0.004-0.0031)}\right) * \ \varepsilon_{cu} + \frac{(0.4f'_{cu})}{(0.004-0.0031)} \quad for\ 0.003 < \varepsilon_{cu} \leq 0.004 \tag{6-9}$$

Model for confined NSC and HSC in compression:

The behaviour of core concrete in the plain NSC and HSC columns is modeled using the stress-strain model proposed by Légeron and Paultre (2003). This model accounts for the confinement provided by transverse reinforcement to the concrete core and its effect on improved compressive strength and post-peak ductility. The relationships, which extend an earlier model proposed by Cusson and Paultre (1995), account for important parameters affecting the performance of confined concrete, including the yield stress and volumetric ratio of transverse reinforcement, hoop spacing and configuration, bar arrangement, and concrete strength. In this model, the peak confined compressive strength (f'_{cc}) and corresponding strain (ε'_{cc}) are computed using the following expressions:

$$f'_{cc} = f'_{cu}(1 + 2.4(I'_E)^{0.7}) \tag{6-10}$$

$$\varepsilon'_{cc} = \varepsilon'_{cu}(1 + 35(I'_E)^{1.2}) \tag{6-11}$$

$$I'_E = \frac{f'_{le}}{f'_{cu}} \tag{6-12}$$

$$f'_{le} = K_e \times f'_l \tag{6-13}$$

$$f'_l = \frac{f_{hcc}}{s}\left(\frac{A_{shy} + A_{shx}}{c_x + c_y}\right) \tag{6-14}$$

$$K_e = \frac{\left(1 - \frac{\sum w^2}{6c_x c_y}\right)\left(1 - \frac{s'}{2c_x}\right)\left(1 - \frac{s'}{2c_y}\right)}{(1 - \rho_c)} \tag{6-15}$$

Where I'_E is the effective confinement index and f'_{le} is the effective confinement pressure acting on the core. f'_{le} is in turn a function of the nominal lateral pressure provided by the transverse reinforcement multiplied by the effective confinement coefficient K_e as originally proposed by Sheikh and Uzumeri (1982) and defined in equations 6-14 and 6-15. Parameters used in the derivation of f'_{le} and K_e include the stress in the transverse steel reinforcement at maximum strength of confined concrete f_{hcc}, the total corss-sectional areas of transverse reinforcement perpendicular to the x and y directions A_{shy} and A_{shx}, and the ratio of longitudinal reinforcement in the core region ρ_c, as well as dimensional parameters which include: s and s' as the center-to center and clear spacing of the transverse reinforcement, c_x and c_y as the widths of the concrete core parallel to the x and y axis, and $\sum w^2$ as the sum of the squares of the clear spacing between adjacent longitudinal bars.

The following equations are used to compute the stress in the transverse steel reinforcement at peak concrete stress, f_{hcc}, where the magnitude of the stress is proportional to the confinement provided to the section:

$$f'_{hcc} = \begin{cases} f_{hy} \; for \; \kappa \leq 10 \\ \dfrac{0.25 f'_{cu}}{\rho_{sey}(\kappa - 10)} \geq 0.43 \varepsilon'_{cu} E_s \; for \; \kappa > 10 \end{cases} \tag{6-16}$$

$$\kappa = \frac{f'_{cu}}{\rho_{sey} E_s \varepsilon'_{co}} \tag{6-17}$$

$$\rho_{sey} = \frac{K_e A_{shy}}{sc} \tag{6-18}$$

where ρ_{sey} is the effective ratio of confinement reinforcement in the y direction, κ is a parameter used to determine if yielding of the transverse reinforcement occurs at the maximum strength of confined concrete, and E_s is the modulus of elasticity of the transverse reinforcement.

The model uses two different equations for the ascending and the descending branches of the stress-strain curve. The ascending branch follows the same format of the model proposed by Popovics (1973):

$$f_{cc} = \frac{f'_{cc} \times \left(k \times \frac{\varepsilon_{cc}}{\varepsilon'_{cc}}\right)}{k - 1 + \left(\frac{\varepsilon_{cc}}{\varepsilon'_{cc}}\right)^{k}} \quad for\ \varepsilon_{cc} \le \varepsilon'_{cc} \qquad \text{6-19}$$

Where k is a parameter which controls the slope of the ascending branch and is calculated as:

$$k = \frac{E_c}{E_c - \left(\frac{f'_{cc}}{\varepsilon'_{cc}}\right)} \qquad \text{6-20}$$

The descending branch of the confined concrete stress-strain curve is modelled using the following expression:

$$f_{cc} = f'_{cc} \times \exp\left(k_1 (\varepsilon_{cc} - \varepsilon'_{cc})^{k_2}\right) \quad for\ \varepsilon_{cc} > \varepsilon'_{cc} \qquad \text{6-21}$$

Parameters k_1 and k_2 are defined using the expressions below, where I_{E50} is the effective confinement index evaluated at post-peak strain ε'_{cc50}, and ε'_{cu50} represents the post-peak strain measured at 50% of maximum unconfined stress, taken equal to 0.004. Typical stress strain curves for confined NSC and confined HSC as obtained using this model are shown in Figure 6-1 (b).

$$k_1 = \frac{ln(0.5)}{(\varepsilon'_{cc50} - \varepsilon'_{cc})^{k_2}} \qquad \text{6-22}$$

$$k_2 = 1 + 25(I_{E50})^2 \qquad \text{6-23}$$

$$\varepsilon'_{cc50} = \varepsilon'_{cu50}\left(1 + 60(I_{E50})\right) \qquad \text{6-24}$$

$$I_{E50} = \rho_{sey} \frac{f_{hy}}{f'_{cu}} \qquad \text{6-25}$$

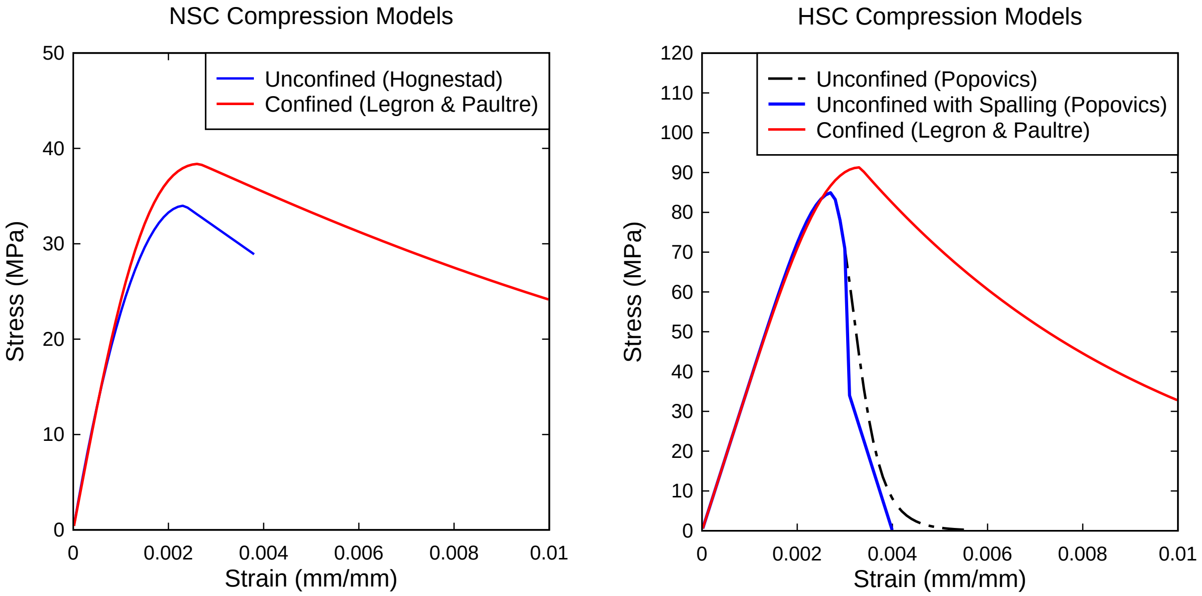

(a) Unconfined and confined NSC

(b) Unconfined and confined HSC

Figure 6-1 Plain concrete compression stress-strain curves

6.2.2 Steel-Fiber Reinforced Concrete Models

Model for unconfined SFRC in compression:

The model proposed by Mansur et al. (1999) was used to predict the stress-strain response for unconfined steel-fiber reinforced concrete (SFRC) in the cover region of the HSFRC columns. The model is applicable for SFRC having compressive strengths ranging from 70 to 120 MPa. This model includes two sets of relationships to determine the ascending and the descending branches of the stress-strain curve (ε_{cuf} , f_{cuf}) as shown below:

$$f_{cuf} = \begin{cases} f'_{cuf}\left(\dfrac{n\left(\dfrac{\varepsilon_{cuf}}{\varepsilon_{0f}}\right)}{\beta - 1 + \left(\dfrac{\varepsilon_{cuf}}{\varepsilon_{0f}}\right)^{n}}\right), & for\ \varepsilon_{cuf} \leq \varepsilon_{0f} \\ f'_{cuf}\left(\dfrac{k_{f1}n\left(\dfrac{\varepsilon_{cuf}}{\varepsilon_{0f}}\right)}{k_{f1}n - 1 + \left(\dfrac{\varepsilon_{cuf}}{\varepsilon_{0f}}\right)^{k_{f2}n}}\right), & for\ \varepsilon_{cuf} > \varepsilon_{0f} \end{cases} \quad 6\text{-}26$$

where n is a curve fitting parameter, which is a function of the modulus of elasticity, peak stress and peak strain of unconfined SFRC (E_{cf}, f'_{cuf} and ε'_{cuf}, respectively) as defined below. Parameters k_{f1} and k_{f2} control the slope of the descending branch as defined in the equations below. The effect of steel fibers is accounted for using the steel fiber volumetric ratio v_f, fiber length L_f, and fiber diameter d_f. A typical stress strain curve is shown in Figure 6-2 (a).

$$n = \frac{E_{cf}}{E_{cf} - \left(\frac{f'_{cuf}}{\varepsilon_{0f}}\right)} \tag{6-27}$$

$$E_{cf} = \left(10300 - 400v_f\right){f'_{cuf}}^{1/3} \tag{6-28}$$

$$\varepsilon'_{cuf} = \left(0.00050 + 0.00000072\left(\frac{v_f L_f}{d_f}\right)\right){f'_{cuf}}^{0.35} \tag{6-29}$$

$$k_{f1} = \left(\frac{50}{f'_{cuf}}\right)^{3.0}\left(1 + 2.5\left(\frac{v_f L_f}{d_f}\right)^{2.5}\right) \tag{6-30}$$

$$k_{f2} = \left(\frac{50}{f'_{cuf}}\right)^{1.3}\left[1 - 0.11\left(\frac{v_f L_f}{d_f}\right)^{-1.1}\right] \tag{6-31}$$

Model for confined SFRC in compression:

The model proposed by Aoude (2008) was used to predict the compressive stress-strain response of confined steel-fiber reinforced concrete in the core region of the high-strength HSFRC columns. The model is an extension of the confinement model proposed by Légeron and Paultre (2003) and accounts for the additional confining effect provided by steel fibers. The increase in compressive strength due to the addition of steel fibers can be calculated through the following set of equations, where f'_{ccf} is the peak stress of confined SFRC at strain ε'_{ccf} and $f_{l,fib}$ is the confining pressure provided by the steel fibers (which is function of the number of fibers per unit area and the bond pullout strength of the fibers):

$$f'_{ccf} = f'_{cc} + 4.1\times\left(f_{l,fib}\right) \tag{6-32}$$

$$\varepsilon'_{ccf} = \varepsilon'_{cc} = \varepsilon'_{cu}\left(1 + 35\left(\frac{f'_{le}}{f'_{cu}}\right)^{1.2}\right) \tag{6-33}$$

$$f_{l,fib} = \frac{3}{8}\times\left(\frac{v_f L_f}{d}\right)\times\left(0.6\times\left(f'_{cuf}\right)^{\frac{2}{3}}\right) \tag{6-34}$$

The ascending branch of the stress-strain curve is obtained by substituting f'_{ccf} and ε'_{ccf} in the original expressions proposed by Légeron and Paultre (2003), as defined in the previous section:

$$f_{ccf} = \frac{f'_{ccf}\times\left(k\times\frac{\varepsilon_{ccf}}{\varepsilon'_{ccf}}\right)}{k - 1 + \left(\frac{\varepsilon_{ccf}}{\varepsilon'_{ccf}}\right)^{k}}, \quad for\ \varepsilon_{ccf} \le \varepsilon'_{ccf} \tag{6-35}$$

$$k = \frac{E_c}{E_c - \left(\frac{f'_{ccf}}{\varepsilon'_{ccf}}\right)} \tag{6-36}$$

The descending branch is adjusted using a modified confinement index which accounts for the contribution of the steel fibers on post-peak ductility, where the parameters $\varepsilon'_{cc50,fib}$ and $I'_{E50,fib}$ are used to adjust k_1 and k_2 in the model originally proposed by Légeron and Paultre (2003). The model assumes that the fibers contribute primarily to confinement in the ineffectively confined core region ($A_{ineff} = (1 - K_e) \times A_{core}$, where K_e is the previously defined effective confinement coefficient), with a much lesser contribution in the effectively confined core. A typical stress-strain curve for confined HSFRC obtained using this model is shown in Figure 6-2 (a).

$$f_{ccf} = f'_{ccf} \times exp\left(k_1\left(\varepsilon_{ccf} - \varepsilon'_{ccf}\right)^{k_2}\right), \quad for\ \varepsilon_{ccf} > \varepsilon'_{ccf} \tag{6-37}$$

$$k_1 = \frac{ln(0.5)}{\left(\varepsilon'_{cc50,fib} - \varepsilon'_{ccf}\right)^{k_2}} \tag{6-38}$$

$$k_2 = 0.58 + 16\left(I'_{E,fib}\right)^{1.4} \tag{6-39}$$

$$\varepsilon'_{cc50,fib} = \varepsilon'_{cu50}\left(1 + 60\left(I'_{E50,fib}\right)\right) \tag{6-40}$$

$$I'_{E50,fib} = I'_E + \left(\frac{f_{l,fib}}{f'_{cu}}\right)(1 - K_e) \tag{6-41}$$

<u>Model for SFRC in tension:</u>

The improved tensile response of steel-fiber reinforced concrete is accounted for through the model proposed by Lok and Pei (1998). The stress-strain response follows a tri-linear relationship, where the first branch starts from zero stress and increases linearly up to the cracking stress of HSFRC (f_{ctf}), with a slope equal to the modulus of elasticity of SFRC (E_{cf}). After reaching the cracking stress, a bi-linear response follows with either an ascending or a descending branch depending on the steel fiber content. The first linear part of the bi-linear response ends at strain and stress values corresponding to ε_2^* and f_2^*. The final part of the curve descends linearly to reach zero stress at a maximum strain equal to 0.02. Parameters f_{ctf}, τ_{bond}, f_2^*, and ε_2^* are calculated using the equations below. Other parameters in the equations include the steel fiber volumetric ratio v_f, the fiber length l_f, fiber diameter d_f, and the modulus of elasticity of steel fibers E_{fp}, taken as 200 GPa. Figure 6-2 (b) shows a typical curve for SFRC in tension.

$$f_{ctf} = 0.3\left(f'_{cuf}\right)^{2/3} \tag{6-42}$$

$$\tau_{bond} = 0.6\left(f'_{cuf}\right)^{2/3} \tag{6-43}$$

$$\varepsilon_2^* = \tau_{bond} \frac{l_f}{d_f} \frac{1}{E_{fp}} \qquad \text{6-44}$$

$$f_2^* = \frac{1}{2} \, v_f \tau_{bond} \frac{l_f}{d_f} \qquad \text{6-45}$$

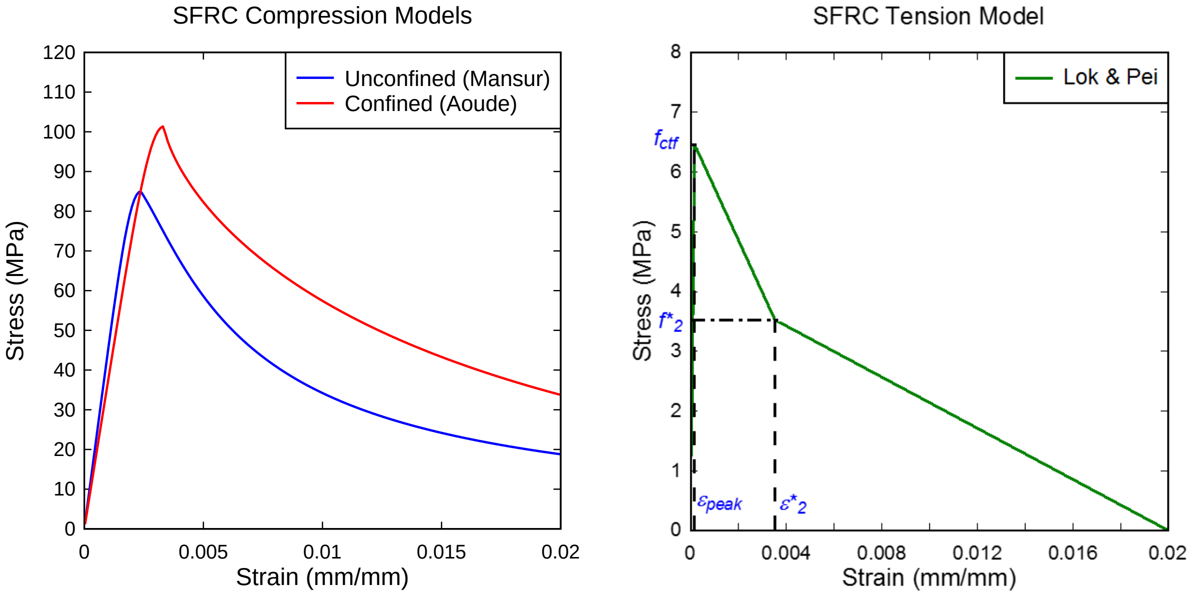

(a) SFRC in compression (b) SFRC in tension

Figure 6-2 SFRC compression and tension stress-strain curves

6.2.3 Steel Reinforcement Models

Normal-strength steel reinforcement in tension:

The stress-strain relationship for normal-strength steel reinforcement in tension is taken into account using either the experimental data obtained from testing steel coupons or using the generic stress-strain model proposed by Jacques et al. (2012) which is pre-defined in RCBlast. Figure 6-3 shows the stress-strain curves for the 10M, No. 4, and 15M reinforcement for both cases. The model proposed by Jacques et al. (2012) includes two linear segments and a parabolic function to plot the stress-strain curve of the steel reinforcement as shown in the equations below, where f_y, f_{sh}, f_u are the stresses at yield, strain-hardening and ultimate, and $\varepsilon_y, \varepsilon_{sh}, \varepsilon_u$ are the corresponding strains.

$$f_s = E_s \varepsilon_s \qquad for\ \varepsilon_s \le \varepsilon_y \qquad \text{6-46}$$

$$f_s = f_y + (\varepsilon_s - \varepsilon_y)\left(\frac{\varepsilon_{sh} - \varepsilon_y}{\varepsilon_{sh} - \varepsilon_y}\right) \qquad for\ \varepsilon_y < \varepsilon_s \le \varepsilon_{sh} \qquad \text{6-47}$$

$$f_s = f_y + (\varepsilon_u - \varepsilon_y)\left(2\left(\frac{\varepsilon_s - \varepsilon_{sh}}{\varepsilon_u - \varepsilon_{sh}}\right) - \left(\frac{\varepsilon_s - \varepsilon_{sh}}{\varepsilon_u - \varepsilon_{sh}}\right)^2\right) \; for \; \varepsilon_{sh} < \varepsilon_s \le \varepsilon_u \qquad \text{6-48}$$

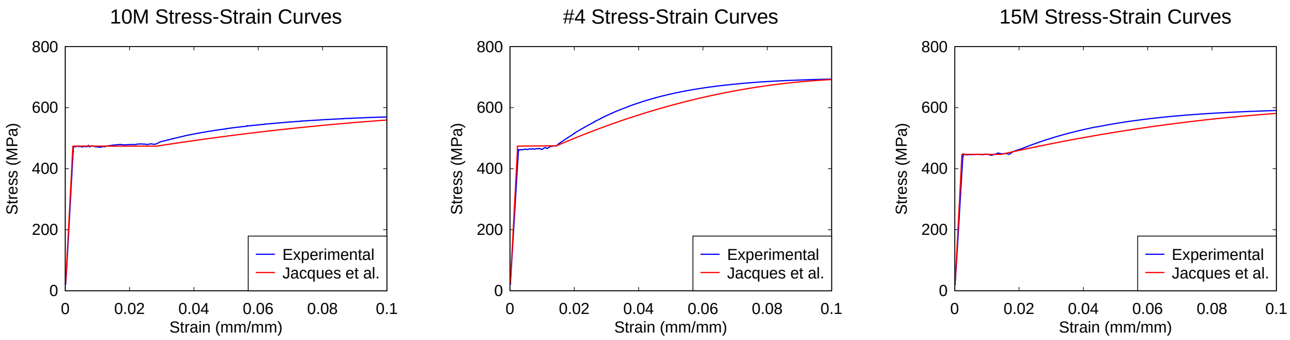

a) 10M b) #4 c) 15M

Figure 6-3 Normal-strength steel stress-strain curves

<u>High-strength steel reinforcement (MMFX) in tension:</u>

The tensile stress-strain relationship for the high-strength MMFX bars was considered using either the experimental data obtained from coupon testing or using the model proposed by the ACI Task Group ITG-6R (2010) for ASTM A1035 high-strength reinforcement. The model proposed by the ACI ITG-6R (2010) design guidelines includes three segments as shown in Equation 6-53. The first portion follows a linear-elastic relationship with a slope equal to the modulus od elasticity of steel until a strain of ε_s =0.0024 is reached. This is followed by a second non-linear parabolic portion which ends at a strain of ε_s =0.02, with an ultimate stress of 1040 MPa. The final part of the curve maintains the stress at 1040 MPa until reaching the rupture strain, which is taken equal to 0.06. It is noted that the model is not a function of bar size. Figure 6-4 compares the results obtained from the experimental coupon tests with the model proposed by ACI ITG-6R (2010).

$$f_s = \begin{cases} 200{,}000\varepsilon_s (MPa) & \text{for } \varepsilon_s \le 0.0024 \\ 1170 - \dfrac{2.96}{\varepsilon_s + 0.0019} (MPa) & \text{for } 0.0024 < \varepsilon_s \le 0.02 \\ 1040 (MPa) & \text{for } 0.02 < \varepsilon_s \le 0.06 \end{cases} \qquad \text{6-49}$$

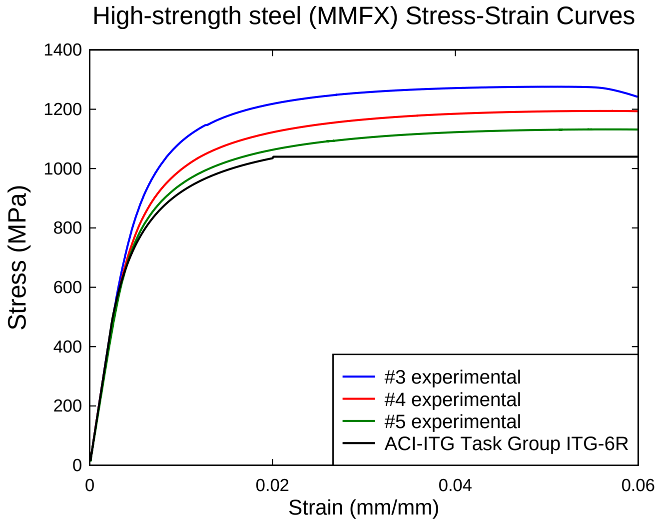

Figure 6-4 High-strength steel stress-strain curves

Steel reinforcement in compression:

The behaviour of steel reinforcement in compression was predicted based on the model proposed by Yalcin and Saatcioglu (2000) and as summarized in the following equations. As shown in Figure 6-5, the stability of bars and their ability to develop strength after yield depends on the aspect ratio (*s/d_b*)). An aspect ratio larger than 8 will lead to the loss of stability of the bars after yielding, whereas stability after yielding is maintained for an aspect ratio equal to 8, with the development of strain hardening as the ratio decreases further.

$$f_s = f_y + \left(f_{s/Du} - f_{sh}\right)\left(2\frac{\varepsilon_s-\varepsilon_{sh}}{\varepsilon_{s/Du}-\varepsilon_{sh}} - \left(\frac{\varepsilon_s-\varepsilon_{sh}}{\varepsilon_{s/Du}-\varepsilon_{sh}}\right)^2\right), \quad \varepsilon_s > \varepsilon_y \qquad \text{6-50}$$

$$f_{s/Du} = f_{sh} + (f_u - f_{sh})\left(48e^{-0.9(s/d_b)}\right) \qquad \text{6-51}$$

$$\varepsilon_{s/Du} = \varepsilon_{sh} + (\varepsilon_u - \varepsilon_{sh})\left(6e^{-0.4(s/d_b)}\right) \qquad \text{6-52}$$

where $f_{s/Du}$ and $\varepsilon_{s/Du}$ are the limiting values on stress and strain respectively.

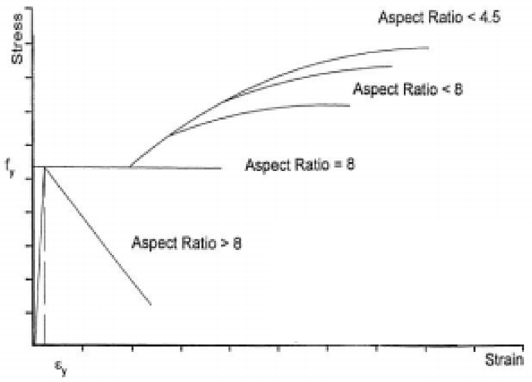

Figure 6-5 Steel compression model (Jacques el al. (2012))

6.3 Dynamic Increase Factors

High strain-rate loading results in an increase in material strength. This section summarizes the dynamic increase factors (DIF) considered in the analysis.

6.3.1 Design Dynamic Increase Factors

In addition to the strain-rate sensitive models described in the next sub-section, “design” dynamic increase factors proposed in the UFC-3-340-02 (2008) documentation for reinforcing steel and concrete were considered in the analysis. These factors are intended for the design of reinforced concrete members subjected to blast loadings and are therefore generally considered to be conservative. As shown in Table 6-2, the DIFs are sorted based on the type of stress applied (bending, compression) and on the design range of the blast (far vs. close-in design range). For the shock-tube columns tests, the stress type was taken as “bending” with the blasts considered in the far design range. The resulting dynamic increase factors based on the UFC recommendations are found to be: DIF_y =1.17 and DIF_u = 1.05 for steel reinforcement at yield and ultimate, and DIF_c= 1.19 for concrete in compression.

Table 6-1 Dynamic increase factors for design of reinforced concrete elements (UFC-3-340-02)

Type of stress	Far design range			Close-in design range		
	Reinforcing bars		Concrete	Reinforcing bars		Concrete
	f_{dy}/f_y	f_{du}/f_u	f'_{dc}/f'_c	f_{dy}/f_y	f_{du}/f_u	f'_{dc}/f'_c
Bending	1.17	1.05	1.19	1.23	1.05	1.25
Diagonal tension	1.00	-	1.00	1.10	1.00	1.00
Direct shear	1.10	1.00	1.10	1.10	1.00	1.10
Bond	1.17	1.05	1.00	1.23	1.05	1.00
Compression	1.10	-	1.12	1.13	-	1.16

6.3.2 Strain-Rate Sensitive Dynamic Increase Factor Models

CEB (1990) model for plain concrete in compression:

Concrete in compression shows an increase in strength and stiffness as strain-rate increases. The Euro-international Concrete Committee (Comité euro-international du Béton, CEB) proposes equations 6-53 and 6-54 to compute the dynamic increase factor for plain concrete in compression (DIF_c), where $\dot{\varepsilon}$ represents the dynamic strain rate, and $\dot{\varepsilon}_s$ is a constant that represents the quasi-static strain rate and is equal to $30x10^{-6}$ s^{-1}. According to this model, the increase in strength is affected by f'_{cu} (as considered in the factor α), with reduced strain-rate sensitivity for higher strength concrete. Assuming a strain rate of $\dot{\varepsilon}_s$ = 1 s^{-1} for the shock-tube tests, the DIF_c for plain normal-strength and high-strength concrete are computed to be 1.26 and 1.14 using this model.

$$DIF_c = \begin{cases} \left(\frac{\dot{\varepsilon}}{\dot{\varepsilon}_s}\right)^{1.026\alpha} & \text{for } \dot{\varepsilon} \leq 30s^{-1} \\ \gamma\left(\frac{\dot{\varepsilon}}{\dot{\varepsilon}_s}\right)^{1/3} & \text{for } \dot{\varepsilon} > 30s^{-1} \end{cases} \qquad 6\text{-}53$$

$$log\,\gamma = 6.156\alpha - 2,\ \ \alpha = \frac{1}{\left(5 + \frac{9\,\mathrm{f}'_{\mathrm{cu}}}{10}\right)},\ \ \dot{\varepsilon}_s = 30 \cdot 10^{-6}s^{-1} \qquad 6\text{-}54$$

Zhang and Mindness (2011) model for SFRC in compression:

Zhang and Mindness (2011) developed expressions to predict the dynamic increase factor for high-strength steel-fiber reinforced concrete (HSFRC) subjected to dynamic compression. The model follows the bi-linear relationship shown in equations 6-55 and 6-56. The dynamic strength is affected by the strain rate $\dot{\varepsilon}$ and the static compressive strength of HSFRC f'_{cuf}, which in turn affects parameters β and $\dot{\varepsilon}_{BLT}$. Using this model and an assumed strain-rate of 1 s^{-1}, a $DIF_c = 1.28$ was predicted for the HSFRC used in this study.

$$DIF_c = \begin{cases} (\phi\dot{\varepsilon})^{\alpha} & \text{for } \dot{\varepsilon} < \dot{\varepsilon}_{BLT} \\ \beta(\dot{\varepsilon})^{1/3} & \text{for } \dot{\varepsilon} \geq \dot{\varepsilon}_{BLT} \end{cases} \qquad 6\text{-}55$$

$$\alpha = \frac{ln\left(\beta \cdot \dot{\varepsilon}_{BLT}{}^{1/3}\right)}{ln(\phi \cdot \dot{\varepsilon}_{BLT})},\ \ \beta = \frac{5}{9} \cdot exp\left(\frac{-f'_{cuf}}{230}\right),\ \ \phi = 10^5, \dot{\varepsilon}_{BLT} = 25 \cdot exp\left(\frac{f'_{cuf}}{130}\right) \qquad 6\text{-}56$$

Malvar and Ross (1998) for concrete in tension:

As tensile contribution becomes important in the presence of steel fibers, the tensile response of HSFRC was adjusted using a dynamic increase factor for concrete in tension (DIF_t). For the current study, the model proposed by Malvar and Ross (1998) for conventional concrete is used to predict the dynamic strength of HSFRC in tension. The model follows a bi-linear relationship as shown in equations 6-57 and 6-58.

$$\delta = \frac{1}{\left(5 + \frac{8 \cdot f'_{cu}}{f'_{cr}}\right)} .., \ log\,\beta^* = 6\delta - 222, f'_{cr} = 101MPa\ , \dot{\varepsilon}_s = 10^{-6}s^{-1} \qquad 6\text{-}58$$

Using the assumed strain rate of $\dot{\varepsilon} = 1s^{-1}$, this model predicts $DIF_t = 1.22$ for the HSFRC in tension.

$$DIF_t = \begin{cases} \left(\frac{\dot{\varepsilon}}{\dot{\varepsilon}_s}\right)^{\delta} & \text{for } \dot{\varepsilon} \leq 1s^{-1} \\ \beta^*\left(\frac{\dot{\varepsilon}}{\dot{\varepsilon}_s}\right)^{1/3} & \text{for } \dot{\varepsilon} > 1s^{-1} \end{cases} \qquad 6\text{-}57$$

$$\delta = \frac{1}{\left(5 + \frac{8 \cdot f'_{cu}}{f'_{cr}}\right)}, \;\; \log \beta^* = 6\delta - 2, \;\; f'_{cr} = 10\ MPa, \;\; \dot{\varepsilon}_s = 10^{-6}s^{-1} \qquad \text{6-58}$$

Saatcioglu et al. (2011) model for steel reinforcement in tension:

The model proposed by Saatcioglu et al. (2011) is used to account for the increased strength of the normal-strength steel reinforcement in tension (see Equation 6-59). According to this model, the increase in strength is assumed to be greater at yield than at ultimate. At the assumed strain rate of $\dot{\varepsilon} = 1s^{-1}$, the dynamic increase factors are calculated to be $DIF_y = 1.30$ and $DIF_u = 1.10$ at yield and ultimate, respectively.

$$\begin{aligned} DIF_y &= 0.034 ln(\dot{\varepsilon}) + 1.30 \geq 1.0 \\ DIF_u &= 0.010 ln(\dot{\varepsilon}) + 1.10 \geq 1.0 \end{aligned} \qquad \text{6-59}$$

There is no model in the literature specified to predict the DIF of high-strength MMFX steel reinforcement. Since this type of reinforcement does not have a well-defined yield plateau, the dynamic increase factor at ultimate ($DIF_u = 1.10$) from the Saatcioglu et al. (2011) model was used for the entire static stress-strain curve. This approximation is also reasonable based on the observations made by previous researchers that higher-grade steels tend to show lower DIFs when compared to lower grade steel reinforcement (Malvar, 1998).

6.4 Dynamic Analysis Procedure

The dynamic analysis of the columns was conducted using single degree of freedom (SDOF) analysis and software RCBlast (Jacques, 2014). The equation of motion used in the analysis is shown in equation 6-60:

$$K_{LM}\big(u(t)\big) m\ddot{u}(t) + R\big(u(t)\big) = AP_r(t) \qquad \text{6-60}$$

$$K_{LM} = \frac{K_M}{K_L} \qquad \text{6-61}$$

$$K_M = \frac{M_e}{M} = \frac{\int_0^L m(x)[\varphi(x)]^2 dx}{mL} \qquad \text{6-62}$$

$$K_L = \frac{P_e}{P(x)} = \frac{\int_0^L p(x)\varphi(x) dx}{pL} \qquad \text{6-63}$$

where $u(t)$ is the displacement at mid-height, $\ddot{u}(t)$ is the acceleration at mid-height, K_{LM} is the load mass transformation factor calculated using equation 6-61 (where K_M represents the mass factor calculated as the equivalent mass divided by the actual total mass, and K_L represents the load factor calculated as the force on the equivalent SDOF system divided by the actual force).

Furthermore, $R\big(u(t)\big)$ is the resistance of the member as a function of the member's displacement, $P_r(t)$ is the reflected pressure as a function of time and m is the total mass of the system, taken as 315 kg based on the mass of the column (105 kg) and the mass of the load transfer device (210 kg). Finally, A is the area impacted by the blast pressure and set equal to the shock-tube opening that is covered by the load transfer device (4.12 m^2).

Analysis in RCBlast begins by inputting the specimen dimensions, boundary conditions, axial load level, cross-section properties and reinforcement arrangement (see Figure 6-7(a-b)). Thereafter, the concrete and steel reinforcement properties are defined using either built-in or user-defined stress-strain relationships (see Figure 6-7(c)). In the current study, user-defined dynamic material properties as described in the previous sections were used in the sectional analysis. Based on these inputs, the software generates the moment-curvature relationships for the member's cross-section (see Figure 6-7(d)).

Member resistance functions are then developed for the column by assuming a plastic hinge length and using the lumped inelasticity approach as described by Jacques et al. (2012). In this approach, the column is idealized as a half-span symmetric elastic flexural member with non-linear rotational springs at the column's critical sections as shown in Figure 6-6.

The flexural rigidity EI of the member is computed based on the pre-yield slope of the column's moment-curvature relationship, while post-yield sectional analysis is used to define idealized hinge moment-rotation relationships. Equation 6-64 is used calculate the ultimate rotational capacity and post-yield rotations necessary to generate the force-displacement relationship:

$$\theta_u = \left(\varphi_u - \varphi_y\right) * L_{pl} + \frac{M_y}{k_{rot}} \tag{6-64}$$

where θ_u is the ultimate rotational capacity, φ_y and φ_u are curvatures at yield and ultimate, $L_{pl}$is the plastic hinge length, M_y is the moment at yield, and finally k_{rot} is the rotational stiffness of the column's supports. For analysis, the rotational stiffness of the partially-fixed shock-tube supports was taken equal to 903 kN·m/rad (Burrell, 2012), while the plastic hinge length was set equal to 135.5 mm, corresponding to the distance measured from the tension steel to the extreme compression fiber of the column's cross-section.

The software derives the force-deflection relationship by solving the governing Euler-Bernoulli equations for the half-span beam-column considering the support and loading conditions. Resistance functions and equivalent SDOF transformation factors are obtained by solving the force-deflection equation at incrementally increasing load stages.

In accordance with previous research conducted by Lloyd (2010) and Burrell (2012), the effect of variable axial load was considered when deriving the member resistance functions. This was considered using an available option to "consider the effect of variable axial load" in software

RCBlast (Jacques, 2014). The “composite” resistance curve was determined using 5 intermediate axial load steps between 0 KN and 294 KN, resulting in seven resistance functions (at axial load levels of 0, 49, 98, 147, 196, 245 and 294 KN). Figure 6-6 (b) shows typical resistance functions for different levels of axial load, and the resulting composite curve for a sample column.

An equivalent triangular blast load, having the same peak reflected pressure and impulse found in the experimentally recorded pressure time history, was used for analysis (idealized blast properties are shown in the next section). The equation of motion was then solved using the average acceleration numerical integration method (Jacques et al., 2012). An example showing the typical output window from RCBlast is shown in Figure 6-7(e).

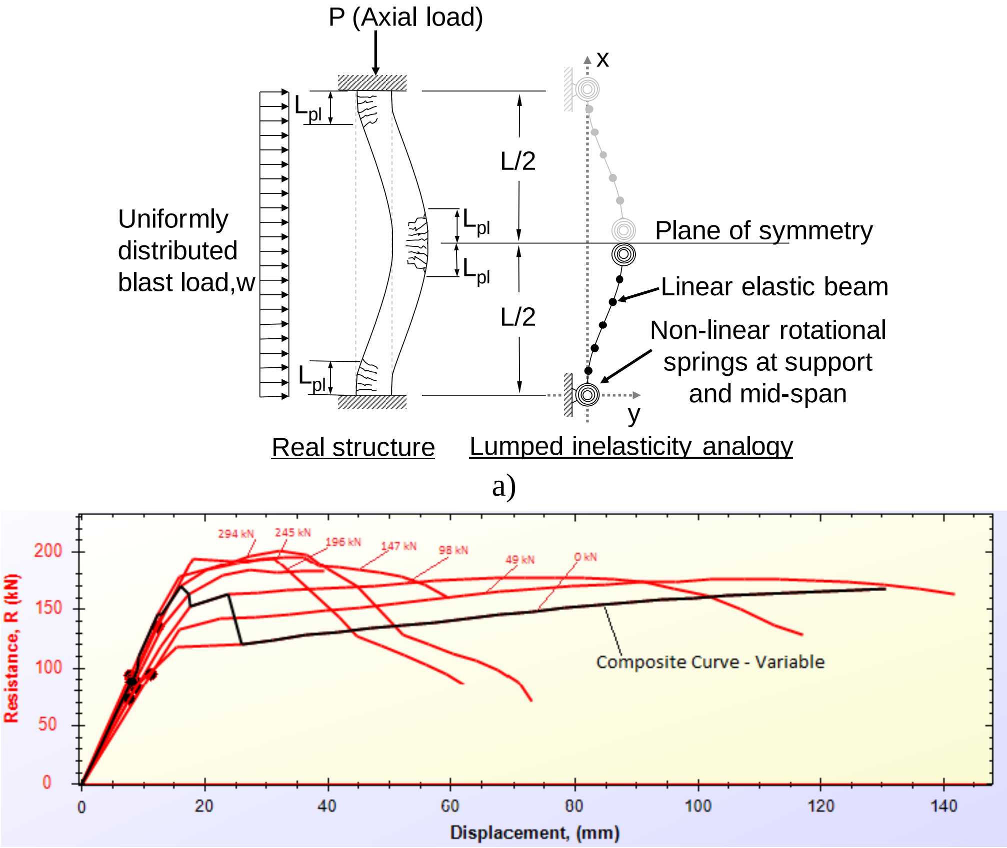

a)

b)

Figure 6-6 a) Beam-column idealized lumped inelasticity approach (Jacques et al. 2012), b) Typical moment-curvature and resistance functions for different levels of axial load

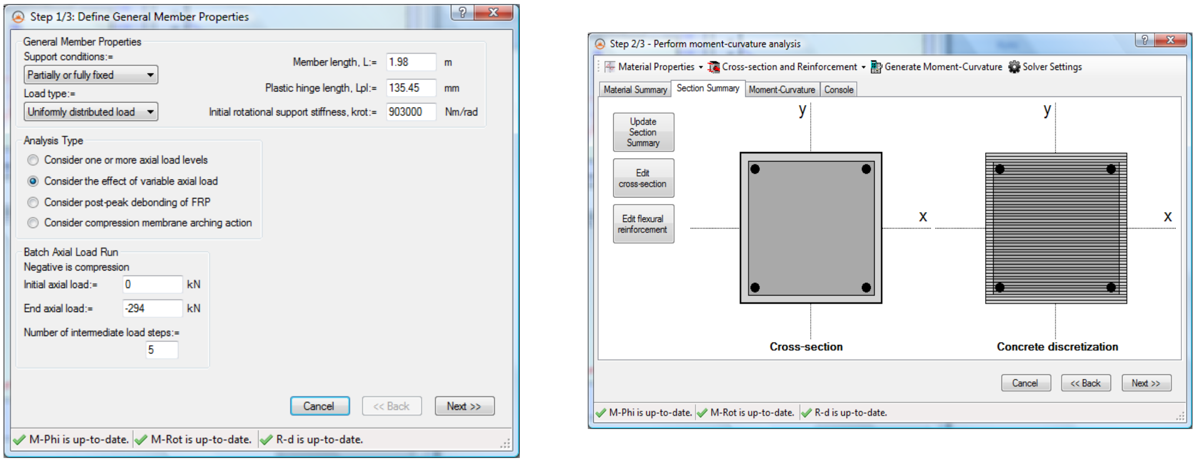

Support conditions:= Partially or fully fixed

Load type:= Uniformly distributed load

Member length, L:= 1.98 m

Plastic hinge length, Lpl:= 135.45 mm

Initial rotational support stiffness, krot:= 903000 Nm/rad

○ Consider one or more axial load levels

● Consider the effect of variable axial load

○ Consider post-peak debonding of FRP

○ Consider compression membrane arching action

Negative is compression

Initial axial load:= 0 kN

End axial load:= -294 kN

Number of intermediate load steps:= 5

✓ M-Phi is up-to-date. ✓ M-Rot is up-to-date. ✓ R-d is up-to-date.

✓ M-Phi is up-to-date. ✓ M-Rot is up-to-date. ✓ R-d is up-to-date.

a) RC blast input: General properties

b) RC blast input: Section summary

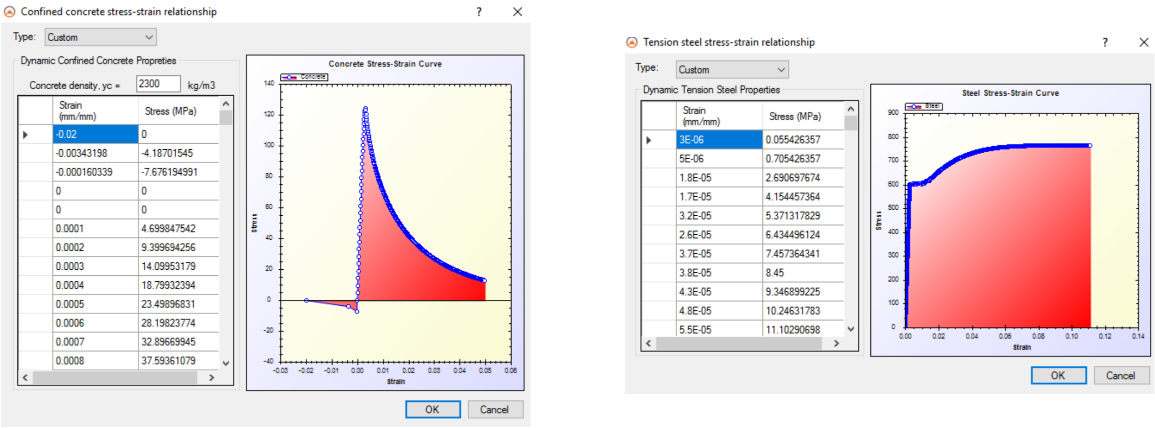

Type: Custom

Concrete density, yc = 2300 kg/m3

Strain (mm/mm)	Stress (MPa)
-0.02	0
-0.00343198	-4.18701545
-0.000160339	-7.676194991
0	0
0	0
0.0001	4.699847542
0.0002	9.399694256
0.0003	14.09953179
0.0004	18.79932394
0.0005	23.49896831
0.0006	28.19823774
0.0007	32.89669945
0.0008	37.59361079

Type: Custom

Strain (mm/mm)	Stress (MPa)
3E-06	0.055426357
5E-06	0.705426357
1.8E-05	2.690697674
1.7E-05	4.154457364
3.2E-05	5.371317829
2.6E-05	6.434496124
3.7E-05	7.457364341
3.8E-05	8.45
4.3E-05	9.346899225
4.8E-05	10.24631783
5.5E-05	11.10290698

c) RCBlast input: user-defined materials stress-strain relationships

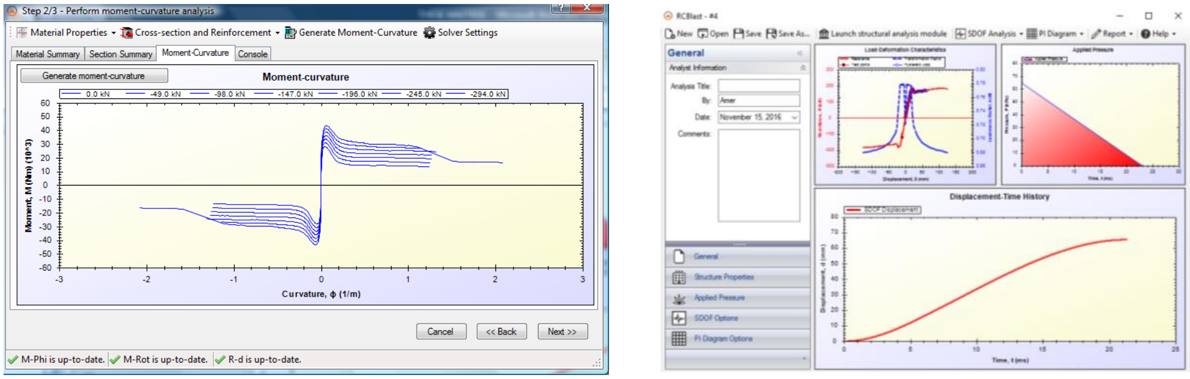

✓ M-Phi is up-to-date. ✓ M-Rot is up-to-date. ✓ R-d is up-to-date.

Analysis Title:

By: Amer

Date: November 15, 2016

Comments:

d) RCBlast output: Generated moment-curvature relationships

e) RCBlast output: Idealized shock-wave properties and displacement-time history

Figure 6-7 RCBlast modelling steps

6.5 Dynamic Analysis Results

6.5.1 Default Case and General Observations

This section summarizes the results obtained from the SDOF dynamic analysis. The default material models and dynamic increase factors used for each series in the analysis are listed in Table 6-2 and sample curves with and without DIF are shown in Figure 6-8. The results for each series are presented in the sub-sections that follow, however an overall summary based on the results for all specimens is provided in Table 6-3. The table reports the mean ratio of the analytical-to experimental maximum displacements (D_{anls}/D_{exp}) for all blasts as well as individual blasts, along with statistical data related to accuracy of the results which include the absolute error, coefficient of variance and standard deviation.

Considering all 17 specimens and all blasts, the mean D_{anls}/D_{exp} ratio is found to be 0.95, with an average absolute error of 19.41%. When the blasts are considered separately, it can be noticed that the error is acceptable and remains within 15% for blasts 1-3, but becomes considerably greater at the later blasts (blast 4 and 5). The larger errors at blasts 4 and 5 can be explained by blow-out failures in some occasions, and more generally because of the effects of repeated loading which results in reduced member stiffness not accounted for in the analysis. This deterioration in stiffness manifests in analytical displacements which are lower when compared to the experimental displacements due to the effects of accumulated damage (notice that the means of D_{anls}/D_{exp} are below 1.0 for blasts 4-5, while the opposite occurs for blasts 1-2).

Table 6-2 Default material and DIF model combination

Series	Concrete models			Tension steel σ-ε [DIF model]
	Compression		Tension σ-ε [DIF model]	
	Unconfined σ-ε [DIF model]	Confined σ-ε [DIF model]		
NSC	Hognestad [CEB]	Légron & Paultre [CEB]	-	Jacques et al. [Saatcioglu et al.]
HSC-NSS	Popovics [CEB]	Légron & Paultre [CEB]	-	
HSC-MMFX				ACI ITG-6R [Saatcioglu et al.]
HSFRC-NSS	Mansur [Zhang & Mindness]	Aoude [Zhang & Mindness]	Lok & Pei [Malvar & Ross]	Jacques et al. [Saatcioglu et al.]
HSFRC-MMFX				ACI ITG-6R [Saatcioglu et al.]

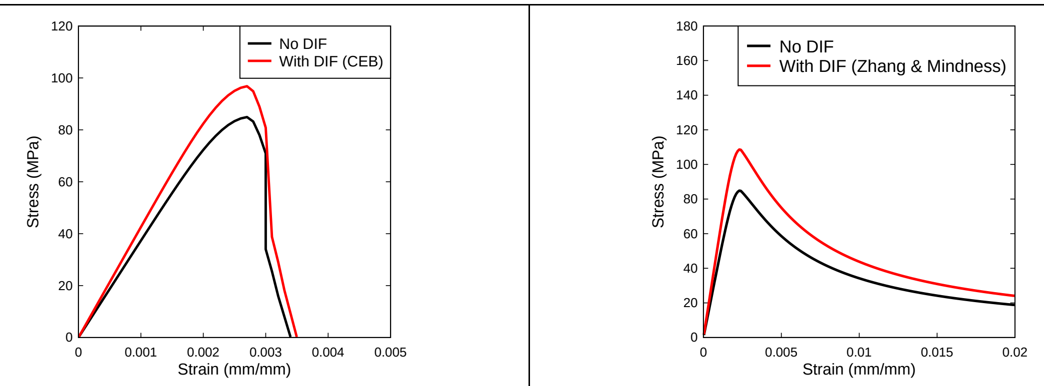

a) Unconfined HSC

b) Unconfined HSFRC

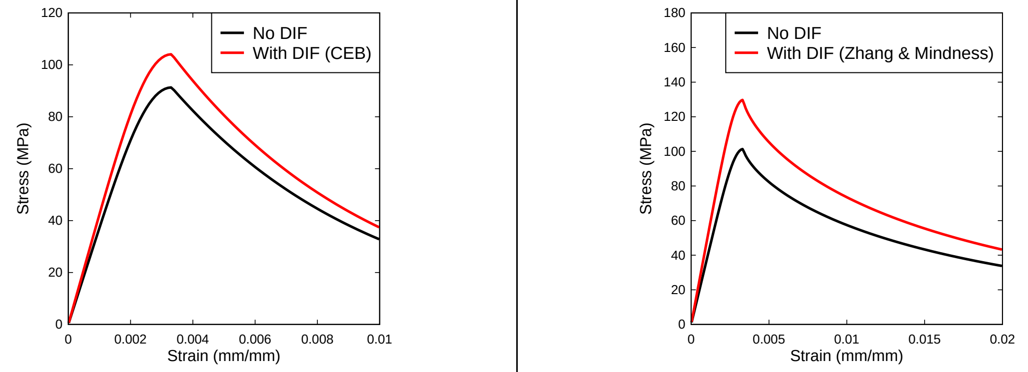

c) Confined HSC

d) Confined HSFRC

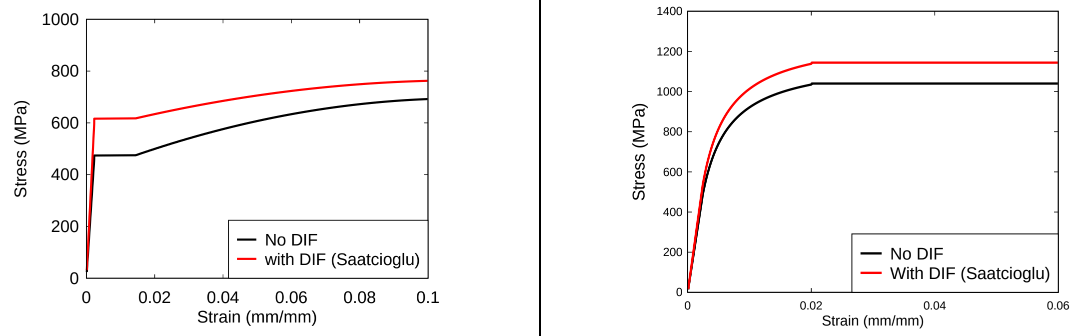

e) Normal-strength reinforcement (#4)

f) High-strength (MMFX) reinforcement

Figure 6-8 Sample stress-strain curves with and without DIF applied (Default case)

Table 6-3 Analysis statistics: All specimens

Blast #	Mean of D_{anls}/D_{exp}	Standard deviation of D_{anls}/D_{exp}	Coefficient of variance	Error
1-5	0.95	0.24	25.74%	18.96%
1	1.13	0.14	12.57%	14.61%
2	1.00	0.17	16.75%	13.22%
3	0.92	0.21	22.76%	15.81%
4	0.68	0.16	23.34%	40.34%
5	0.40	0.19	47.21%	59.86%

6.5.2 Dynamic Analysis Results: NSC Series

The summary of the idealized shockwave properties and analysis results for the NSC specimens are presented in Table 6-4. Statistical data for the analysis is presented in Table 6-5, and Figure 6-9 shows a plot of the analytical vs. experimental displacements. The stress-strain models and DIFs used for this series are as listed in Table 6-2.

The overall accuracy of the analysis for this series is within acceptable limits. The average D_{anls}/D_{exp} ratio considering all blasts and both specimens is 0.90, with an average absolute error of 18.48%. It is worth mentioning that the errors for the first two shots for both specimens were within 12%, with a difference of not more than 2 mm between the analytical and experimental mid-span displacements. The errors become larger for blasts 3 and 4, particularly for the 15M specimen which had relatively large errors at these blasts (34.64% and 45.76%). Blast 1 and 2 tested the specimens within the elastic and yield ranges, while blast 3 resulted in significant damage. The large error at blast 4 can therefore be attributed to the effects of accumulated damage which were not accounted for in the analysis.

Table 6-4 Summary of analysis results: NSC series

Specimen ID	Idealized shockwave properties				Mid-span maximum displacements			
	Blast #	P_r (kPa)	t_d (msec)	I_r (kPa.msec)	D_{exp} (mm)	D_{anls} (mm)	D_{anls}/D_{exp}	Error (%)
NSC-0%-NSS-#4	1	22.12	21.88	242	10.70	11.55	1.08	7.94%
	2	40.34	23.02	464	20.47	22.87	1.12	11.72%
	3	65.10	26.22	854	87.38	78.27	0.90	10.43%
NSC-0%-NSS-15M	1	22.16	17.44	193	7.41	8.25	1.11	11.34%
	2	38.90	21.99	428	20.01	18.51	0.93	7.50%
	3	71.85	23.54	846	83.96	54.88	0.65	34.64%
	4	83.22	26.38	1098	162.77	88.28	0.54	45.76%

Table 6-5 Analysis statistics for D_{anls}/D_{exp} ratio: NSC series

Blast #	Mean	Standard deviation	Coefficient of variance	Error
1-4	0.90	0.23	25.31%	18.48%
1	1.10	0.02	2.19%	9.64%
2	1.02	0.14	13.31%	9.61%
3	0.77	0.17	22.10%	22.53%
4	0.54	-	-	45.76%

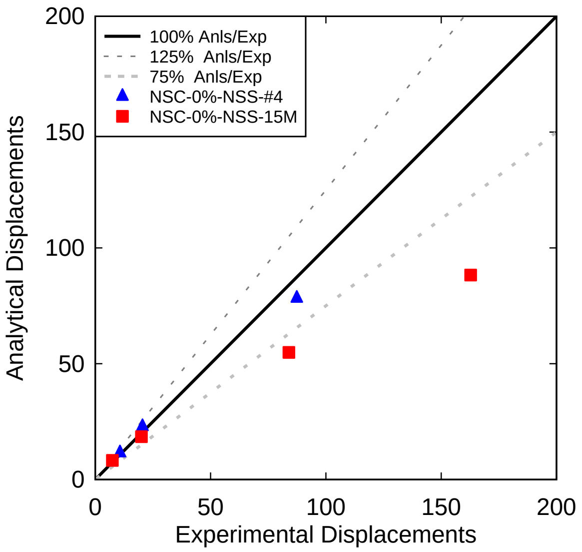

Figure 6-9 Analytical vs. experimental displacements: NSC series

6.5.3 Dynamic Analysis Results: HSC-NSS Series

Table 6-6 presents a summary of the idealized shockwave properties and analytical results for the HSC series constructed with NSS bars. Statistical data related to the accuracy of the analytical predictions is shown in Table 6-7. Comparison of the experimental and analytical results is also displayed graphically in Figure 6-10.

Considering all columns and all blasts in this series, the mean D_{anls}/D_{exp} ratio is found to be 0.94, with an absolute error average of 19.42%. Continuing the trend from the previous series, the results are generally more accurate for blasts 1-2, and blast 3 for most columns. The 10M and the #4 specimens show relatively high errors at blast 1 (29.36% and 24.97% respectively), however one should consider that the mid-span displacements range within 7 - 12 mm at this blast, and therefore a marginal difference of 1-2 mm can produce a large error. The mean D_{anls}/D_{exp} ratio at blast 2 is 0.98 with an average error of 11.21%. Blast 3 showed a mean D_{anls}/D_{exp} ratio of 0.85 with a higher error of 21.34 %, but still within acceptable values considering the limitations of the SDOF method. The error is larger at this blast intensity for the 15M column (46.82%), whereas the errors for the remaining specimens are below 20%. Finally, as expected, blast 4 shows a poor D_{anls}/D_{exp} ratio of 0.61 with the highest average error when compared to all blasts (39.31 %).

Examining the results, it is clear that starting from blast 3 and especially blast 4, the repeated blast testing results in higher errors, where analytical member resistance is over-predicted, resulting in larger margins between the analytically predicted and experimentally obtained displacements. As shown in Table 6-7, the mean D_{anls}/D_{exp} ratios for blast 2, 3, 4 are below 1.0 and generally decrease as the total number of shots increase.

Table 6-6 Summary of analysis results: HSC-NSS series

Specimen ID	Idealized shockwave properties				Mid-span maximum displacements			
	Blast #	P_r (kPa)	t_d (msec)	I_r (kPa.msec)	D_{exp} (mm)	D_{anls} (mm)	D_{anls}/D_{exp}	Error (%)
HSC-0%-NSS-10M	1	22.98	20.29	233	8.38	10.84	1.29	29.36%
	2	45.11	19.03	429	33.64	27.45	0.82	18.40%
	3	75.43	20.66	779	132.57	106.52	0.80	19.65%
HSC-0%-NSS-10M-S	1	19.82	21.32	211	9.49	9.86	1.04	3.90%
	2	41.16	18.36	378	20.81	24.42	1.17	17.35%
	3	74.10	19.74	731	106.13	98.98	0.93	6.74%
HSC-0%-NSS-#4	1	24.44	14.83	181	7.21	9.01	1.25	24.97%
	2	39.55	23.37	462	20.07	20.45	1.02	1.89%
	3	78.34	22.33	875	82.35	92.36	1.12	12.16%
	4	92.28	24.11	1112	210.58	140.00*	0.66	33.52%
HSC-0%-NSS-15M	1	21.29	21.26	226	7.57	7.94	1.05	4.89%
	2	39.01	19.06	373	16.02	14.87	0.93	7.18%
	3	72.83	19.11	696	77.70	41.32	0.53	46.82%
	4	87.81	22.73	998	141.09	77.45	0.55	45.11%

*RCBlast predicts out-of-bound displacement

Table 6-7 Analysis statistics for D_{anls}/D_{exp} ratio: HSC-NSS series

Blast #	Mean	Standard deviation	Coefficient of variance	Error
1-4	0.94	0.24	25.80%	19.42%
1	1.16	0.13	11.46%	15.78%
2	0.98	0.15	15.35%	11.21%
3	0.85	0.25	29.22%	21.34%
4	0.61	0.08	13.50%	39.31%

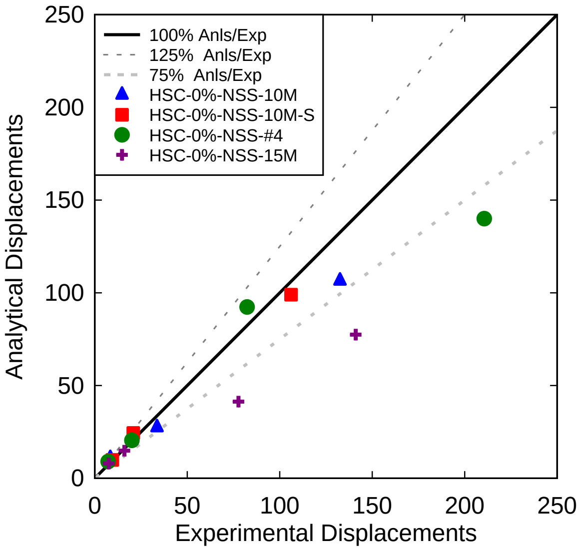

Figure 6-10 Analytical vs. experimental displacements: HSC-NSS series

6.5.4 Dynamic Analysis Results: HSFRC-NSS Series

Table 6-8 summarizes the idealized shockwave properties, experimental and analytical mid-span displacements for the HSFRC columns built with normal-strength reinforcement (NSS bars). Statistical analysis for the results are included in Table 6-9, and analytical and experimental displacements are compared graphically in Figure 6-11.

Considering all specimens and blasts 1-4 for the series, the mean D_{anls}/D_{exp} ratio is found to be 0.95, with an absolute average error of 16.83%. As in the previous series, the predictions at blast 1 and 2 are well within acceptable limits with average errors of 16.84% and 8.70%, respectively. Furthermore, the predictions for blast 3 for this series show an acceptable D_{anls}/D_{exp} ratio of 0.91, with a relatively low average error of 13.33%, which is better than in the previous two series. This could be explained by the presence of fibers which eliminates cracking and damage in the columns for the earlier blasts 1 and 2. Thus the HSFRC specimens reach blast 3 in fairly good shape because of the contribution of fibers in minimizing damage. However, the larger impulse at blast 3 and resulting damage leads to a loss of accuracy in the predictions at blast 4, with a higher error percentage of 40.11% and a mean D_{anls}/D_{exp} ratio of 0.60, where the impact of repeated blasts started taking effect.

Table 6-8 Summary of analysis results: HSFRC-NSS series

Specimen ID	Idealized shockwave properties				Mid-span maximum displacements			
	Blast #	P_r (kPa)	t_d (msec)	I_r (kPa.msec)	D_{exp} (mm)	D_{anls} (mm)	D_{anls}/D_{exp}	Error (%)
HSC-0.5%-NSS-10M	1	24.35	18.68	228	9.08	10.16	1.12	11.89%
	2	42.78	19.73	422	22.85	21.17	0.93	7.35%
	3	75.43	21.55	813	91.41	98.46	1.08	7.71%
HSC-1%-NSS-10M	1	23.30	18.56	216	7.07	9.14	1.29	29.28%
	2	31.31	28.97	454	19.41	20.06	1.03	3.35%
	3	74.45	19.71	734	83.78	75.61	0.90	9.75%
HSC-1%-NSS-#4	1	21.71	20.51	223	7.62	8.87	1.16	16.40%
	2	34.48	26.26	453	15.37	16.16	1.05	5.14%
	3	68.33	25.43	869	62.73	63.30	1.01	0.91%
	4	86.07	23.47	1010	153.13	104.91	0.69	31.49%
HSC-1%-NSS-15M	1	19.22	22.62	217	8.07	8.86	1.10	9.79%
	2	32.25	25.82	416	17.52	14.20	0.81	18.95%
	3	63.91	23.54	752	54.62	35.54	0.65	34.93%
	4	86.72	21.53	934	120.52	61.80	0.51	48.72%

Table 6-9 Analysis statistics for D_{anls}/D_{exp} ratio: HSFRC-NSS series

Blast #	Mean	Standard deviation	Coefficient of variance	Error
1-4	0.95	0.22	23.00%	16.83%
1	1.17	0.09	7.48%	16.84%
2	0.96	0.11	11.65%	8.70%
3	0.91	0.19	20.57%	13.33%
4	0.60	0.12	0.20	40.11%

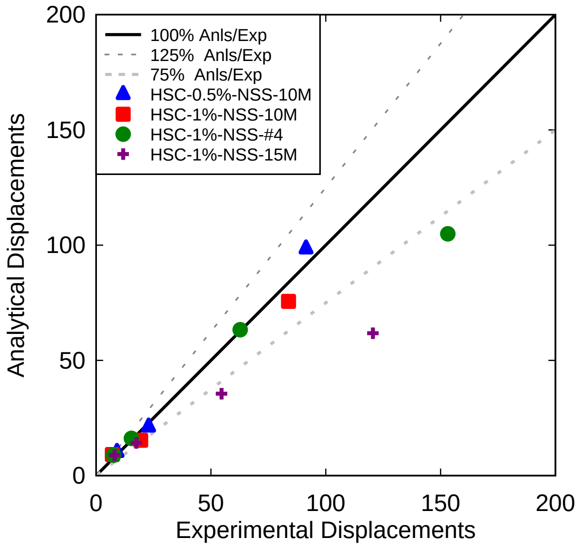

Figure 6-11 Analytical vs. experimental displacements: HSFRC-NSS series

6.5.5 Dynamic Analysis Results: HSC-MMFX Series

The analysis results for the HSC-MMFX series columns which were built with plain high-strength concrete and high-strength bars are summarized in Table 6-10. The table shows the idealized shockwave properties, the analytical and experimental displacements, their ratios and associated errors. Statistical data related to the analysis are shown in Table 6-11, while the accuracy of the predictions can be examined visually in Figure 6-12.

The major challenge faced while modelling columns constructed with MMFX high strength steel reinforcement was the roundhouse stress-strain curve this material is characterized with. The determination of yield points on the moment-curvature relationship will not be as accurate as the normal-strength steel reinforcement due to the absence of a well-defined yield-plateau.

As for the overall predictions for this series, results were reasonably accurate except for the seismic column in which higher errors occurred. The mean D_{anls}/D_{exp} ratio is found to be 0.99 with overall absolute error of 17.27%. The largest error occurs at blast 5 for the #5 specimen; the column experienced a blow-out failure at this shot after undergoing five cycles of testing, with considerable damage and reduction in stiffness from the four previous blasts which was not accounted for in the analysis. In comparison, the average errors for blasts 1, 2, 3, and 4 are below 20%. The results for blast 4 show better accuracy when compared to the previous series. This can be explained by the increased strength of the MMFX bars, which results in elastic behaviour over a wider range of blasts; thus, the columns continue to behave elastically and recover displacements at early shots, leading to better analytical displacement predictions for the MMFX columns at blasts 3 and 4 when compared to the companion set with NSS bars.

Table 6-10 Summary of analysis results: HSC-MMFX series

Specimen ID	Idealized shockwave properties				Mid-span maximum displacements			
	Blast #	P_r (kPa)	t_d (msec)	I_r (kPa.msec)	D_{exp} (mm)	D_{anls} (mm)	D_{anls}/D_{exp}	Error (%)
HSC-0%-MMFX-#3	1	20.89	21.83	228	9.15	9.14	1.00	0.11%
	2	37.17	22.62	421	18.35	18.98	1.03	3.43%
	3	63.06	25.34	799	67.28	68.95*	1.02	2.48%
	4	79.97	23.12	924	-**	-	-	-
HSC-0%-MMFX-#4	1	19.59	20.06	197	9.65	9.18	0.95	4.87%
	2	35.01	25.29	443	16.76	19.01	1.13	13.42%
	3	76.67	22.58	866	46.17	57.33	1.24	24.17%
	4	101.14	21.78	1102	94.24	93.95	1.00	0.31%
HSC-0%-MMFX-#4-S	1	23.91	18.37	220	6.82	9.45	1.39	38.56%
	2	34.71	23.31	405	13.28	16.28	1.23	22.59%
	3	72.20	24.90	899	39.95	47.96	1.20	20.05%
	4	75.41	28.83	1087	84.30	57.87	0.69	31.35%
HSC-0%-MMFX-#5	1	22.71	21.23	241	8.74	9.17	1.05	4.92%
	2	34.64	27.49	476	17.18	15.97	0.93	7.04%
	3	68.72	21.71	746	37.06	35.32	0.95	4.70%
	4	81.69	24.57	1004	62.68	46.98	0.75	25.05%
	5	86.07	22.89	985	182.59	48.83	0.27	73.26%

* RCBlast predicts out-of-bound displacement

** Specimen experienced blow-out failure

Table 6-11 Analysis statistics for D_{anls}/D_{exp} ratio: HSC-MMFX series

Blast #	Mean	Standard deviation	Coefficient of variance	Error
1-5	0.99	0.26	26.44%	17.27%
1	1.10	0.20	17.97%	12.12%
2	1.08	0.13	11.82%	11.62%
3	1.11	0.14	12.51%	12.85%
4	0.81	0.43	52.66%	18.90%
5	0.27	-	-	73.26%

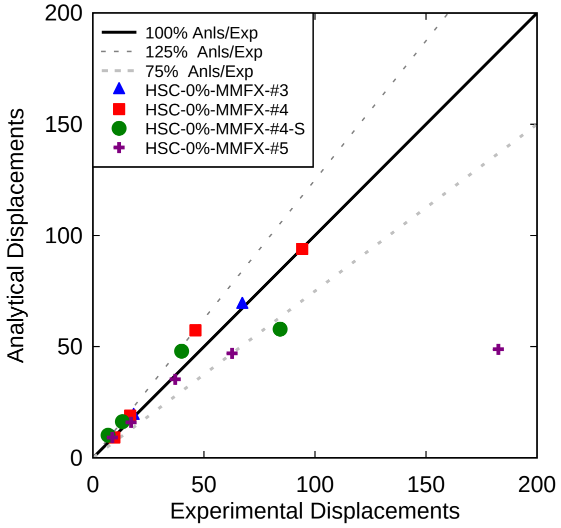

Figure 6-12 Analytical vs. experimental displacement: HSC-MMFX series

6.5.6 Dynamic Analysis Results: HSFRC-MMFX Series

The last series analyzed was the HSFRC-MMFX series which was built with high-strength fiber-reinforced concrete and high-strength MMFX bars. The experimental and analytical predictions for maximum displacements are summarized in Table 6-12 along with the idealized shockwave properties. Statistical data for the analysis is provided in Table 6-13, and finally a graph plotting the analytical versus the experimental displacements is available in Figure 6-13.

Considering the overall results in Table 6-2, the mean D_{anls}/D_{exp} ratio is found to be 0.93 with overall absolute error of 23.45%. However, it is noted the results are associated with a high standard deviation and coefficient of variation. The best results for blast 1-4 are obtained for the column with #5 bars, with absolute errors which are less than 15%, while the last shot (blast 5) results in large error, which is as expected since the column experiences a blow-out failure at this blast. The results are generally acceptable at blast 3, except for the column with #3 bars which shows a D_{anls}/D_{exp} ratio of 0.61 and error of 39.32% (in comparison, the errors for the columns with #4 and #5 bars are below 10%). This can be explained by the fact that blast 2 results in more damage in this less heavily reinforced specimen, while the remaining columns remain elastic at this blast due to the increased reinforcement ratios.

Table 6-12 Summary of analysis results: HSFRC-MMFX series

specimen ID	Idealized shockwave properties				Mid-span maximum displacements			
	Blast #	P_r (kPa)	t_d (msec)	I_r (kPa.msec)	D_{exp} (mm)	D_{anls} (mm)	D_{anls}/D_{exp}	Error (%)
HSC-1%-MMFX-#3	1	23.40	21.78	255	12.37	11.7	0.95	5.42%
	2	40.58	19.86	403	25.18	18.43	0.73	26.81%
	3	73.98	20.04	741	98.92	60.02	0.61	39.32%
	4	75.57	26.56	1004	-**	-	-	-
HSC-1%-MMFX-#4	1	19.25	20.15	194	6.07	8.46	1.39	39.37%
	2	38.33	21.78	417	13.26	17.70	1.33	33.48%
	3	68.17	23.29	794	40.65	38.57	0.95	5.12%
	4	82.32	22.70	934	99.02	52.03	0.53	47.46%
HSC-1%-MMFX-#5	1	19.13	24.63	236	9.23	9.43	1.02	2.17%
	2	33.43	26.38	441	15.59	17.68	1.13	13.41%
	3	60.52	28.20	853	33.20	35.88	1.08	8.07%
	4	78.59	26.48	1040	55.39	47.46	0.86	14.32%
	5	77.55	27.06	1049	87.89	47.06	0.54	46.46%

**Specimen experienced blow-out failure

Table 6-13 Analysis statistics: HSFRC-MMFX series

Blast #	Mean	Standard deviation	Coefficient of variance	Error
1-5	0.93	0.29	31.23%	23.45%
1	1.12	0.24	21.40%	15.65%
2	1.07	0.31	28.77%	24.57%
3	0.88	0.24	27.84%	17.50%
4	0.69	0.43	62.51%	30.89%
5	0.54	-	-	46.46%

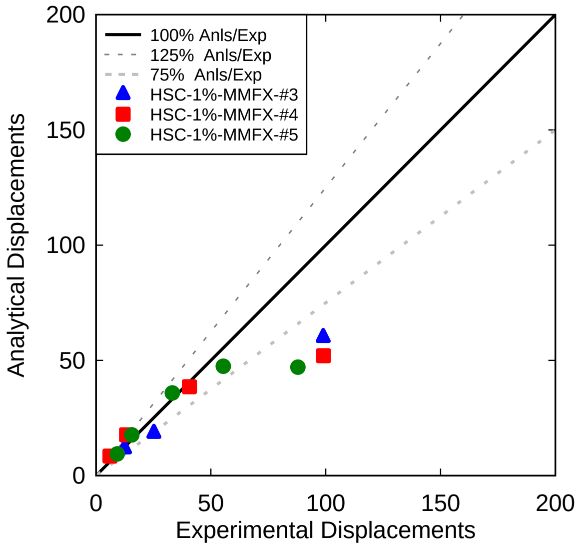

Figure 6-13 Analytical vs. experimental displacements: HSFRC-MMFX series

6.6 Sensitivity Analysis

This section presents a sensitivity analysis which examines the effect of different modeling parameters on the SDOF analysis results. The sensitivity analysis investigates the effect of considering accumulated damage from repeated testing, the effect of different dynamic increase factors (DIFs), and the effect of tension steel model for columns constructed with MMFX rebars.

6.6.1 Sensitivity Analysis: Effect of Accumulated Damage

As discussed previously, the accuracy of the SDOF analysis predictions reduced as the number of blasts increased. In general, the analytical displacement results were smaller than those observed in the experiments for these later blasts (i.e. the analysis overestimated member resistance). One possible explanation for the reduced accuracy is the effect of repeated blast testing which results in a degradation of member stiffness that was not accounted for.

The effect of stiffness degradation due to repeated cycles of blast testing is considered in this section by using the “accumulated damage” option in software RCBlast. This option allows the user to input the inbound and rebound maximum and residual displacements from the previous blast to define the hysteretic response for the columns using the built-in degrading stiffness Clough (1966) hysteretic model for reinforced concrete (Jacques, 2014). The utilization of this option makes it possible to include the loss of stiffness in the specimens due to repeated blasts, which may in turn lead to better predictions of analytical displacements at blasts 4 and 5.

Only columns that were tested under 4 or more blasts were included in this sensitivity analysis, and the analysis was only run for blasts 4 and 5. Two cases of accumulated damage were considered. The first case was run using the “analytical” maximum and residual displacements predicted from the preceding blast, and is referred to as “Case A-A”. The second case used the "experimental" maximum and residual displacements from the previous blast, and is referred to as "Case A-E". The accumulated damage cases were compared to the default case, "Case A" as presented previously. A Summary of results for the three cases is provided in Table 6-14. Bar charts comparing the ratios of analytical to experimental displacements are also included in Figure-6-14.

As seen in Table 6-14, absolute errors were significantly reduced when accumulated damage was accounted for in Cases A-A and A-E, where the hysteretic response managed to get displacement predictions much closer to the experimentally observed displacements. For example, for column NSC-0%-NSS-15M, the 45.76% error obtained through Case A was reduced to more than half in Case A-A to 18.82%. The error is reduced even further to 3.26% when the experimental inbound displacements from the preceding blast were used in Case A-E. In general, the accuracy of the predictions improved when the experimental displacements from the previous blast were used (Case A-E vs. Case A-A). This is justified since the analytical displacements from the preceding blast (Case A-A) already have some errors, while using the experimental displacements from the preceding blast (Case A-E) more closely simulates the actual condition of the specimen before the next blast occurs. It is also worth noting that some of the columns in the table show the same analytical displacements regardless of the case under study (e.g. HSC-0%-NSS-#4 at Blast 4); this is because RCBlast predicts a blow-out failure for all three cases (i.e. inbound displacement has exceeded the ultimate displacement predicted by the sectional analysis).

The sample bar charts supplied in Figure-6-14 further confirm that the predictions improve when accumulated damage is considered. The accuracy is considerably enhanced with most data points falling within the +/- 15% error margins as seen in Figure 6-15 for Case A-E. It is also noticed that the analytical displacements approached the experimental displacements at blast 4, whereas the errors are larger for the two columns tested with a fifth blast, which can be justified by the high intensity blast and blow-out failures experienced by these columns at blast 5.

In summary, the sensitivity analysis demonstrates the importance of considering the previous damage and stiffness degradation of the specimens in the SDOF analysis. Accounting for accumulated damage leads to more accurate predictions of displacements in specimens tested under repeated cycles of blast testing. This method of analysis could also be applied to real-life structures which have been exposed to blast incidents to evaluate the residual capacity of damaged structural members.

Table 6-14 Sensitivity analysis, effect of accumulated damage: Summary of results

Blast #	Specimen ID	D_{exp} (mm)	Case A		Case A-A		Case A-E	
			D_{anls} (mm)	Error (%)	D_{anls} (mm)	Error (%)	D_{anls} (mm)	Error (%)
4	NSC-0%-NSS-15M	162.77	88.28	45.76%	132.14	18.82%	157.47	3.26%
	HSC-0%-NSS-#4	210.58	140.00*	33.52%	140.00*	33.52%	140.00*	33.52%
	HSC-0%-NSS-15M	141.09	77.45	45.11%	109.37	22.48%	140.77	0.23%
	HSC-1%-NSS-#4	153.13	104.91	31.49%	135.00*	11.84%	135.00*	11.84%
	HSC-1%-NSS-15M	120.52	61.80	48.72%	88.09	26.91%	103.41	14.20%
	HSC-0%-MMFX-#4	94.24	93.95	0.31%	98.00*	3.99%	98.00*	3.99%
	HSC-0%-MMFX-#4-S	84.30	57.87	31.35%	83.41	1.06%	75.94	9.92%
	HSC-0%-MMFX-#5	62.68	46.98	25.05%	51.21	18.30%	51.93	17.15%
	HSC-1%-MMFX-#4	99.02	52.03	47.46%	64.33	35.03%	66.27	33.07%
	HSC-1%-MMFX-#5	55.39	47.46	14.32%	48.20	12.98%	48.01	13.32%
5	HSC-0%-MMFX-#5	182.59	48.83	73.26%	61.14	66.52%	69.39	62.00%
	HSC-1%-MMFX-#5	87.89	47.06	46.46%	54.66	37.81%	58.04	33.96%

* RCBlast predicts out-of-bound displacement

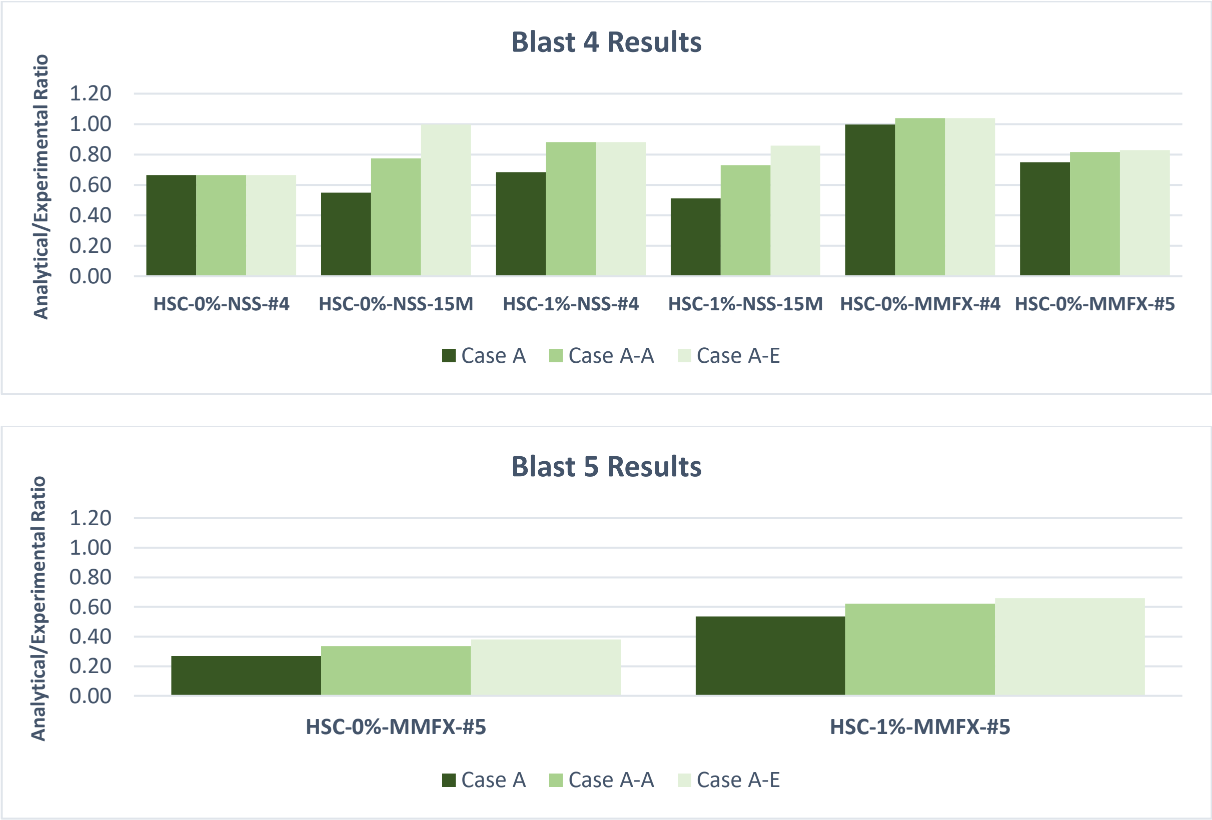

Figure-6-14 Sensitivity analysis, effect of accumulated damage: Sample results for blasts 4 and 5

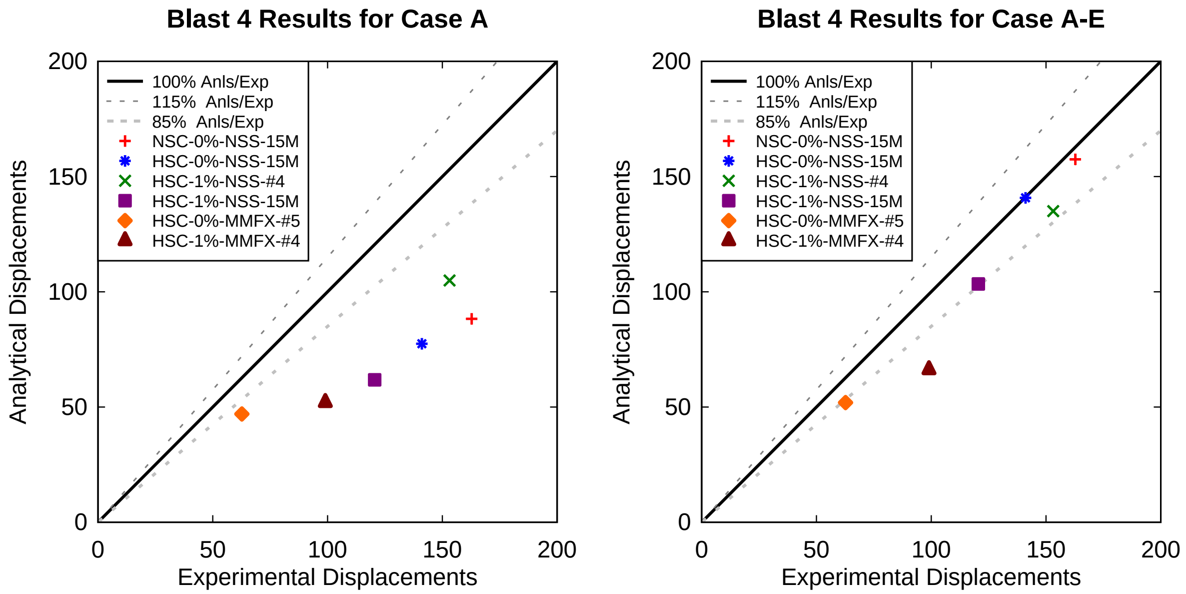

Figure 6-15 Sensitivity analysis, effect of accumulated damage: Blast 4 Case A vs. Case A-E

6.6.2 Sensitivity Analysis: Effect of DIF Selection

The effect of using different DIFs on the SDOF predictions is examined in this section. The default case which was presented in section 6.5 was run using the strain-rate dependant DIF models listed under "Case A" in Table 6-15. Two additional cases are considered in the sensitivity analysis. "Case B" was run using design DIFs as suggested by UFC-3-340-02 (2008). As shown in Table 6-15 this case results in more conservative DIF values when compared to "Case-A" (except for concrete in compression). Finally, "Case C" is run using the materials models without any consideration of high-strain rate effects (i.e. DIF = 1.0). The three cases considered with their corresponding DIFs are listed in Table 6-15**.**

Table 6-15 Sensitivity analysis, effect of DIF selection: DIF models used for each case

CASES	**DIF model**				
	Concrete			**Steel**	
	Compression		**Tension**	**NSS**	**MMFX**
	Plain Concrete	**SFRC**			
A	CEB ***[1.14]***	Zhang & Mindness ***[1.28]***	Malvar ***[1.22]***	Saatcioglu ***[yld: 1.3, ult: 1.1]***	Saatcioglu ***[ult: 1.1]***
B	UFC 03-340-02 ***[1.19]***			UFC 03-340-02 ***[yld: 1.17, ult: 1.05]***	UFC 03-340-02 ***[ult: 1.05]***
C	No DIF			No DIF	

A summary of results for the three cases is provided in Table 6-16. The results are presented by series in terms of average D_{anls}/D_{exp} ratios and errors for all columns within each series. Figure 6-16 shows sample bar charts comparing the results for the three cases.

Furthermore, Table 6-17 includes the statistics obtained for all blasts for all specimens for each of the three cases run. The best average error was obtained with the default case A along with best standard deviation.

As shown in Table 6-16, improved analysis results are observed for cases A and B especially at blasts 1 and 2 and in most cases of blast 3, which is an indicator to the importance of using DIFs to account for dynamic material properties in blast analysis. The results also generally follow the expected trend, with D_{anls}/D_{exp} ratios increasing as the DIF reduce (Case C > Case B > Case A).

Comparing Cases A and B, the D_{anls}/D_{exp} ratios are generally higher for Case B. The difference between the two cases is that the former uses strain-rate dependant DIF models while the later uses design DIFs. This results in lower DIFs for Case B for the steel reinforcement, however it is worth mentioning that the DIF generated for high-strength concrete by the CEB model was 1.14, while the design DIF proposed in the UFC documentation is 1.19. Since the member response of the columns tested in this study was dominated by flexure, the resistance is more sensitive to the longitudinal steel reinforcement and therefore the D_{anls}/D_{exp} ratios are generally higher for Case B when compared to Case A. However, there are a few instances where the opposite trend is observed, especially at the elastic blasts (blast 1 and 2), where the concrete (with higher DIF in Case B) may have a more influential effect on member stiffness and response.

In general, the lowest errors were found for Case A. The largest errors were obtained with Case C, where no DIFs were used. For example, observing the results of blasts 1-4 for the HSC-NSS series in Table 6-16, it can be seen that the lowest average error occurs for Case A with a value of 19.42%, this is followed by Case B with (a close value but higher) error of 20.09%, and finally Case C with the highest error of 25.67%.

As for Blasts 4 and 5, better predictions (D_{anls}/D_{exp} ratios closer to 1.0) were obtained for Case C when compared to the other cases which showed significant underestimation of the displacements. As noted the columns were tested under repeated cycles of loading, therefore the use of no DIF in Case C results in lower member resistance, which in turn leads to higher analytical displacements which are “closer” to those observed in the experiments. The results at these blasts should not be used to draw conclusions on the suitability of Case C since the effects of accumulated damage where not considered in the part of the sensitivity analysis.

In summary, this sensitivity analysis shows the importance of using dynamic increase factors in the blast analysis of reinforced concrete columns. Case C which was run with no DIFs, resulted in a high margin of error. Case A leads to more accurate SDOF analysis predictions, however the more conservative design DIFs used in Case B result in reasonable predictions, and therefore these values may be more suitable for design applications.

Table 6-16 Sensitivity analysis, effect of DIF selection: Summary of results

Series	Blast #	Case A		Case B		Case C	
		Mean (D_{anls}/D_{exp})	Error	Mean (D_{anls}/D_{exp})	Error	Mean (D_{anls}/D_{exp})	Error
NSC	1-4	0.90	18.48%	0.91	17.59%	1.01	18.01%
	1	1.10	9.64%	1.09	8.85%	1.15	15.23%
	2	1.02	9.61%	0.97	13.82%	1.04	17.93%
	3	0.77	22.53%	0.82	18.07%	0.97	14.92%
	4	0.54	45.76%	0.58	41.63%	0.70	29.89%
HSC-NSS	1-4	0.94	19.42%	1.02	20.09%	1.12	25.67%
	1	1.16	15.78%	1.24	24.00%	1.33	32.78%
	2	0.98	11.21%	1.06	9.98%	1.17	19.78%
	3	0.85	21.34%	0.96	18.59%	1.08	22.17%
	4	0.61	39.31%	0.64	35.50%	0.70	30.20%
HSFRC-NSS	1-4	0.95	16.83%	0.95	17.89%	1.07	19.86%
	1	1.17	16.84%	1.11	15.17%	1.17	16.62%
	2	0.96	8.70%	0.92	12.16%	1.03	12.33%
	3	0.91	13.33%	0.98	17.70%	1.18	29.12%
	4	0.60	40.11%	0.65	35.16%	0.77	22.91%
HSC-MMFX	1-5	1.00	17.93%	1.07	22.31%	1.11	24.31%
	1	1.12	14.75%	1.22	21.98%	1.29	28.82%
	2	1.08	11.62%	1.18	19.01%	1.20	19.94%
	3	1.11	12.85%	1.17	17.90%	1.20	20.31%
	4	0.81	18.90%	0.86	16.34%	0.88	13.82%
	5	0.27	73.26%	0.28	72.41%	0.29	71.26%
HSFRC-MMFX	1-5	0.93	23.45%	1.00	24.24%	1.02	23.97%
	1	1.12	15.65%	1.21	20.79%	1.21	21.26%
	2	1.07	24.57%	1.19	28.17%	1.21	28.76%
	3	0.88	17.50%	0.94	14.28%	0.99	14.90%
	4	0.69	30.89%	0.72	27.72%	0.76	24.27%
	5	0.54	46.46%	0.54	45.74%	0.56	44.27%

Table 6-17 Sensitivity analysis, DIF selection: Statistics comparing case A, B, and C

Case	Mean	Standard deviation	Coefficient of variance	Error
A	0.95	0.24	25.74%	18.96%
B	1.00	0.27	26.56%	20.68%
C	1.08	0.27	24.94%	22.86%

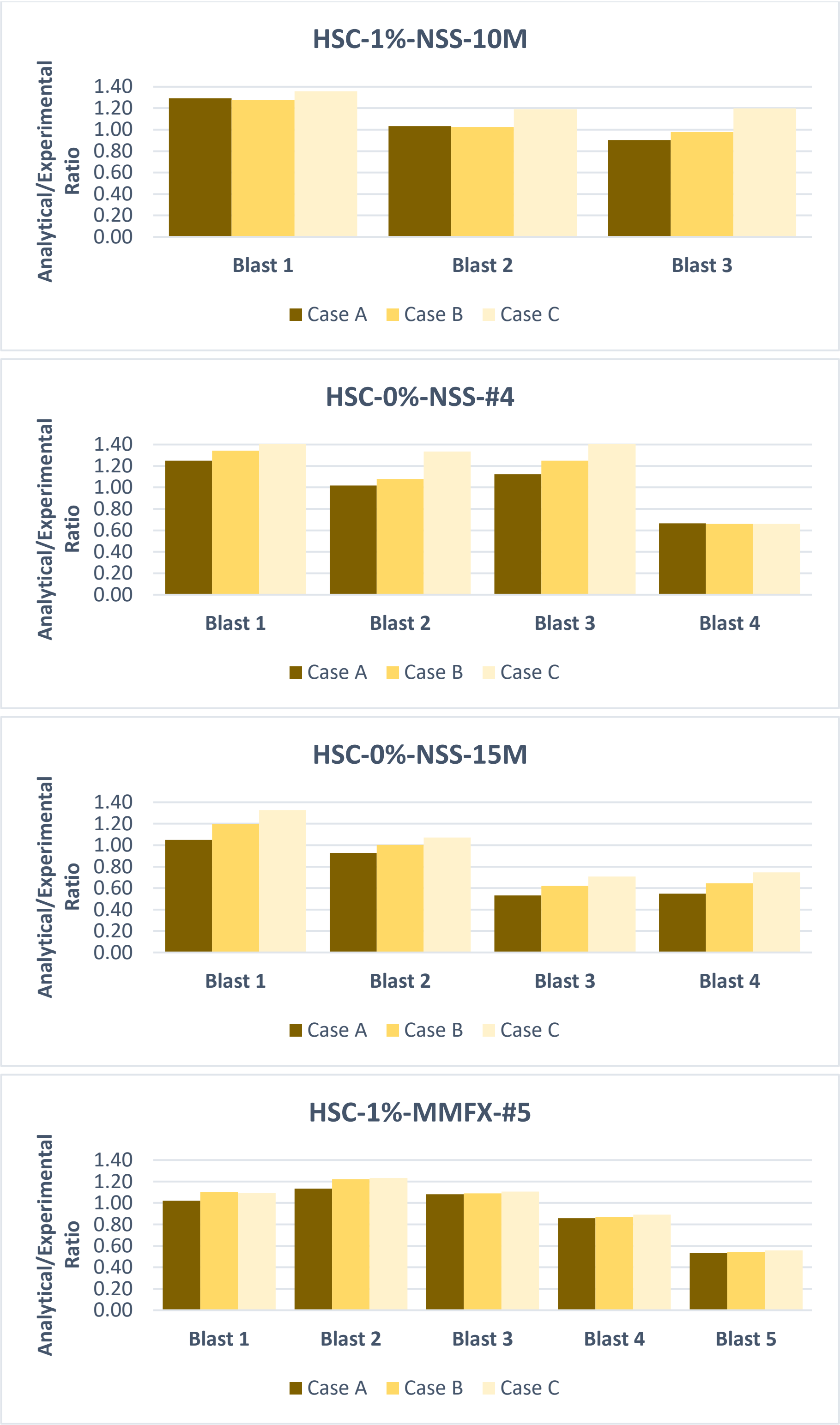

Figure 6-16 Sensitivity analysis, effect of DIF selection: Sample bar charts comparing Cases A, B, and C

6.6.3 Sensitivity Analysis: Effect of Tension Steel Model for MMFX Bars

The effect of using different tension steel models in the case of columns constructed with MMFX high-strength steel reinforcement is examined in the last section of the sensitivity analysis. As shown in Table 6-18, two cases are considered. The first case (“Case A”) is the default case presented earlier, where the analysis was run using the stress-strain relationship proposed by ACI Task Group ITG-6R (2010), whereas the second case (“Case E”) used the actual experimental stress-strain relationships obtained from the MMFX steel coupon tests.

Table 6-18 Sensitivity analysis, effect of tension steel model: Cases and result for columns with MMFX reinforcement

Cases	Steel tension models	Average D_{anls}/D_{exp}	Average absolute error
Case A	ACI-Task Group ITG (2010)	0.97	20.30%
Case E	Experimental curve	0.90	21.07%

A summary of results for the seven columns built with the MMFX reinforcement is shown in Table 6-18. Comparing the average D_{anls}/D_{exp} ratios, Case A with the ACI ITG-6R model delivered better predictions with an average ratio of 0.97. On the other hand, using the experimental stress-strain curve resulted in a lower average ratio of 0.90. The results confirm the validity of using the ACI ITG-6R model which closely approximates the stress-strain response of the MMFX bars. Using the actual coupon data in Case E, generally produced lower analytical displacements due the higher ultimate strength observed in the coupons when compared to the ITG model. The average absolute errors were similar for the two cases; Case A had a slightly lower error of 20.30% when compared to 21.07% for Case E. Figure 6-17 provides bar charts for sample columns which allows for further comparison of the results for the two cases.

Because of lack of models in the literature, the DIF at ultimate stress (DIF =1.1) predicted by the Saatcioglu et al. (2011) model was used when analyzing the columns with high-strength reinforcement. This could have led to an overestimation of the dynamic resistance of the MMFX steel bars, which can explain why the D_{anls}/D_{exp} ratios are generally below 1.0 for both cases. Thus, it may be more conservative to ignore dynamic effects (i.e. use DIF =1.0) when analyzing the blast response of columns with MMFX bars. Indeed, Malvar (1998) has shown that the DIF of steel reinforcement reduces as the strength of steel increases – further research to develop appropriate DIF models for high-strength MMFX bars is recommended.

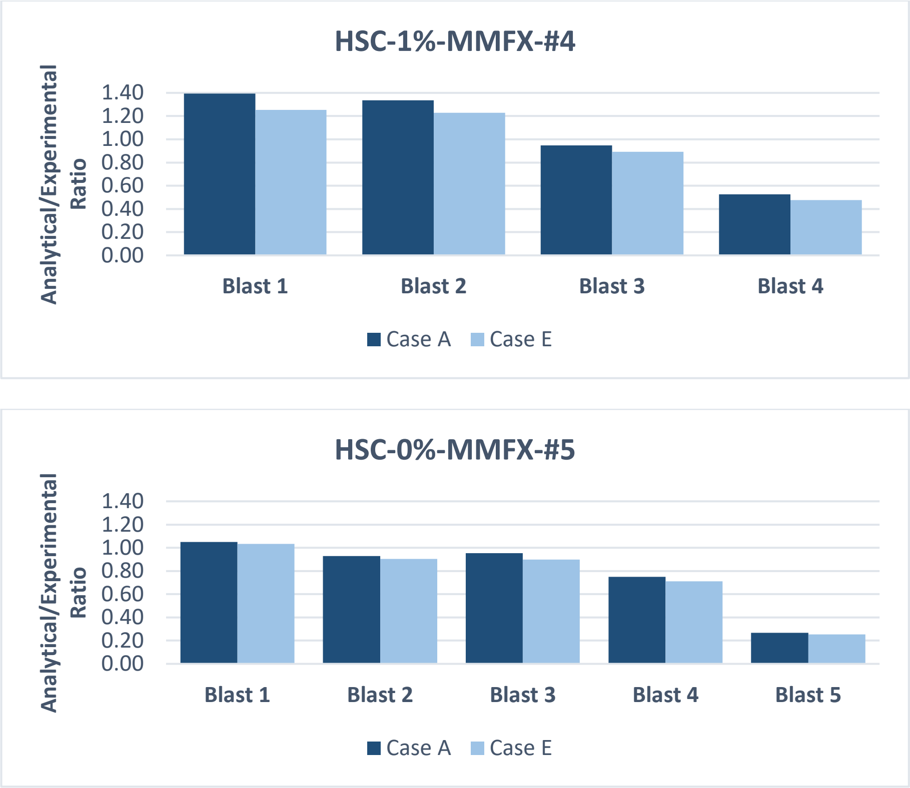

Figure 6-17 Sensitivity analysis, tension steel models selection: Sample bar charts for two specimens with high-strength steel

CHAPTER 7. CONCLUSION

7.1 Conclusion

This research presented an experimental study that examined the blast performance of a series of high-strength reinforced concrete columns. The columns were equipped with different designs in terms of materials and reinforcement, reflecting different concrete types, longitudinal steel reinforcement type and ratios, steel fibers contents and transverse reinforcement ratios. The advantages of using innovative materials and different design parameters were drawn form comparison of the blast performance of corresponding companions.

In total, seventeen columns with different configurations of concrete and steel reinforcement were designed and tested using the University of Ottawa Shock-tube under gradually increased blast loads until failure. The performance criteria used to evaluate the specimens included: overall blast capacity, mid-span displacements at equivalent blasts, failure mode and damage. Several conclusions can be drawn form the experimental results, as follows:

- The use of higher strength concrete (HSC vs. NSC) led to only moderate effects on the blast performance of flexural-dominant reinforced concrete columns. In the current study the use of plain HSC led to some reductions in mid-span displacements at equivalent blasts. However, the brittleness of HSC at the material level manifests into somewhat more brittle column failures, with the plain high-strength concrete columns showing greater fragmentation at failure when compared to NSC companions.
- High-strength longitudinal steel reinforcement provided a major enhancement in the blast performance of the high-strength concrete columns. In addition to reducing mid-span displacements at equivalent blasts, higher blast capacities were achieved when compared to companions built with normal-strength steel. However, the major drawback seen with this type of reinforcement is that their failure can be associated with rupture of tension reinforcement, and thus additional attention is required to design such columns to prevent this brittle failure mode.
- Longitudinal steel reinforcement ratio was found to be the major parameter affecting the blast behaviour of columns, regardless of reinforcement type or concrete type utilized. Increasing the longitudinal steel reinforcement ratios was shown to significantly decrease mid-span displacements at equivalent blasts, and increase overall blast capacities.
- Provision of steel fibers at moderate ratios of 0.5% and 1% significantly improves the blast behaviour of high-strength concrete columns. Maximum and residual mid-span displacements are seen to decrease when steel fibers are added, with an increase in column ductility. The use of fibers also contributes to enhanced crack control and fragmentation resistance, eliminating the significant crushing and spalling associated with plain HSC.

The enhanced ductility and toughness provided by steel fibers is an ideal solution to improve the blast performance of HSC columns.

- Closely spaced transverse reinforcement corresponding to seismic detailing led to modest reductions of mid-span displacements in the HSC columns tested in this study. The increased confinement provides the concrete core with additional ductility and limits mid-span displacements especially in the case of residual displacements. However, the columns in this study had small cross-sections and were tested under low axial loads (with possible loss of axial load during testing), and further research examining the benefits of transverse reinforcement confinement on the blast performance of HSC columns is recommended.
- The results show that the highest blast capacity obtained by the columns tested in this research was achieved through the combination of different high-performance materials (HSC + fibers + MMFX reinforcement). The use of fibers in HSC-MMFX columns is well-suited as the high toughness provided by the fibers allows the tensile strength of the high-strength to be fully utilized and remedies the brittleness of high-strength concrete. However, other alternatives—that were not applied in this research—may offer similar resistance (e.g., higher normal-strength steel reinforcement ratio instead of the high-strength steel might as well produce similar resistance and avoid the risk of bar-rupture associated with the use of high-strength steel bars – further research is recommended).

In addition to the experimental investigation, a SDOF dynamic analysis was conducted to predict the response of the test columns analytically. The dynamic analysis was performed using software RCBlast with member resistance functions developed using dynamic material properties for concrete, HSFRC and steel reinforcement. The following conclusions can be drawn from the analytical study:

- SDOF analysis can be used to predict the blast response of HSC and HSFRC columns reinforced with normal and high-strength steel reinforcement, with acceptable predictions of maximum displacements. The predictions were generally more accurate at early stages of testing (Blasts 1-3), with the analytical predictions showing larger errors at later Blasts (4 and 5) due to the effects of repeated testing.
- The sensitivity analysis showed that consideration of accumulated damage results in improvements in the predictions of maximum displacements, and therefore the effect of stiffness degradation should be considered in the blast analysis of columns tested under repeated blast pressures.
- The sensitivity analysis demonstrated the importance of using dynamic increase factors (DIFs) in the blast analysis of columns. The use of “design” DIFs were found to be slightly more conservative when compared to strain-rate sensitive models. Failing to consider the effects of high-strain on materials lead to an underestimation of column member resistance tested under the effect of blast loading.

- Using the stress-strain relationship proposed ACI Task Group ITG-6R (2010) for the blast analysis of columns with MMFX bars results in reasonable predictions when compared to the use of actual coupon stress-strain data.

7.2 Recommendations for Future Research

The following recommendations for future research are suggested:

- Further experimental studies examining the blast behaviour of other types of structural members built with HSC and HSFRC, such as walls and slabs.
- Further experimental studies examining the effect of high-strength steel on the blast behaviour of other types of structural members, such as walls and slabs.
- Research focused on investigating the effect of high-strain rate loading on high-strength steel material properties, with the development of dynamic increase factors.
- Shock-tube experimental studies that test columns under single high-intensity loads rather than repeated and gradually increased loads to study the effect of accumulated damage experimentally.
- Live blast testing of HSC and HSFRC columns under close-in and far-field blasts.
- Research to examine the effect of steel fiber type on the blast behaviour of HSFRC columns.
- Finite element modelling to predict the blast response of HSC and HSFRC columns as well as well as columns built with high-strength steel reinforcement.

REFERENCES

ACI Concrete Terminology (2013): An ACI Standard (ACI CT-13). American Concrete Institute.

ACI Innovation Task Group 6. (2010). *"ITG-6R-10 Design Guide for the use of ASTM A1035/A1035M Grade 100 (690) Steel bars for structural concrete."* American Concrete Institute.

ASTM A1035/A1035M-11. (2011). "*Standard Specification for Deformed and Plain, Low-Carbon, Chromium, Steel Bars for Concrete Reinforcement.*"

ASTM C 143. (2010). "*Standard Test Method for Slump of Hydraulic-Cement Concrete.*"

ASTM C1609. (2006). "*Standard Test Method for Flexural Performance of Fibre Reinforced Concrete (using Beam with Third-point Loading).*"

ASTM C39 / C39M - 16b. "*Standard Test Method for Compressive Strength of Cylindrical Concrete Specimens.*"

ASTM International. (2016). ASTM A1035/A1035M-16a. *"Standard Specification for Deformed and Plain, Low-Carbon, Chromium, Steel Bars for Concrete Reinforcement."* Retrieved from http://dx.doi.org/10.1520/A1035_A1035M-16A

Aoude H. (2008). *"Structural behaviour of steel fibre reinforced concrete members."* PhD Thesis, McGill University, Montreal.

Banthia, N. P., Mindess, S., and Bentur, A. (1987). *"Impact behaviour of concrete beams."* Materials and Structures/Matériaux et Conctructions, 1987. 20, 293-302.

Banthia, N., Mindess, S., and Trottier, J.-F. (1996). *"Impact resistance of steel fiber reinforced concrete."* ACI Mater. J., 93(5), 472–479.

Bao, X., and Li, B. (2010). *"Residual strength of blast damaged reinforced concrete columns."* International Journal of Impact Engineering, 37(3), 295-308.

Bindiganavile, V., Banthia, N., and Aarup, B. (2002*). "Impact response of an ultra-high strength cement composite."* Proceedings of the Annual Conference of the Canadian Society for Civil Engineering, CSCE, Montreal.

Burrell, R. (2012). "*Performance of steel fibre reinforced concrete columns under shock tube induced shock wave loading.*" (M.A.Sc. thesis). University of Ottawa, Ottawa

Burrell, R. P., Aoude, H., and Saatcioglu, M. (2014). "*Response of SFRC columns under blast loads. Journal of Structural Engineering.*" 141(9), 04014209.

Carriere, M., Heffernan, P. J., Wight, R. G., and Braimah, A. (2007). *"Behaviour of steel reinforced polymer (SRP) strengthened RC members under blast load."* Can. J. Civ. Eng. 36: 1356-1365 (2009), doi:10.1139/L09-053.

CEB-FIP (1993). *"Model Code 90 for concrete structures." Federation international de la preconstraint*, CEB Bulletin No. 213/214, Paris.

CSA Standard A23.3. (2004). *"Design of Concrete Structures." Canadian Standards Association*, Mississauga, Ontario, Canada.

Cusson, D., and Paultre, P. (1995). "*Stress-strain model for confined high-strength concrete.*" Journal of Structural Engineering, 121(3), 468-477. doi:10.1061/(ASCE)0733-9445(1995)121:3(468).

De Carufel, S. (2016). *"Effect of high-performance steel materials on the blast behaviour of ultra-high performance concrete columns."* M.A.Sc. Thesis, University of Ottawa, Ottawa.

Fujikura, S., and Bruneau, M. (2008*). "Blast resistance of seismically designed bridge piers."* The 14th World Conference on Earthquake Engineering October 12-17, 2008, Beijing, China.

Fujikura, S., and Bruneau, M. (2011). *"Experimental Investigation of Seismically Resistant Bridge Piers under Blast Loading."* Journal of Bridge Engineering,16(1), 63-71.

Gopalaratnam, V. S., and Shah, S. P. (1986). *"Properties of steel fiber reinforced concrete subjected to impact loading."* ACI J., 83(1), 117–126.

Hognestad, E. (1951). "*Study of combined bending and axial load in reinforced concrete members. University of Illinois.*" Engineering Experiment Station. Bulletin; No. 399.

Huynh, L., Foster, S., Valipour, H., and Randall, R. (2015). *"High strength and reactive powder concrete columns subjected to impact: Experimental investigation."* Construction and Building Materials 78 (2015) 153–171.

ICC-ES Report (2014). *"ChromX 9100 Grade 100 Steel reinforcement bars." MMFX Steel Corporation of America*. California, United States.

Jacques, E. (2014). RCBLAST (Version 0.5.1). Retrieved from www.rcblast.ca

Jacques, E. (2016). "*Performance Characteristic of reinforced concrete bond at high strain-rates.*" PH. D. Thesis, University of Ottawa, Ottawa

Jacques, E., Lloyd, A., and Saatcioglu, M. (2012). "*Predicting reinforced concrete response to blast loads."* Canadian Journal of Civil Engineering, 40(5), 427-444. doi:10.1139/l2012-014

Légeron F, and Paultre P. (2003). *"Uniaxial confinement model for normal and high strength concrete columns."* ASCE Journal of Structural Engineering, 129(2), 241-252.

Li, B., Nair, A., and Kai, Q. (2012). *"Residual axial capacity of reinforced concrete columns with simulated blast damage."* J. Perform. Constr. Facil., 2012, 26(3): 287-299.

Li, J., Wu, C., Hao, H., Su, Y., and Liu, Z. (2016). *"Blast resistance of concrete slab reinforced with high performance fibre material."* Journal of Structural Integrity and Maintenance, 1:2, 51-59.

Li, Y. (2016). "*Blast performance of reinforced concrete beams constructed with high-strength concrete and high-strength reinforcement."* (M.A.Sc. thesis). University of Ottawa, Ottawa

Lloyd, A. (2010). *"Columns under Shock Tube Induced Shock Wave Loading."* M.A.Sc. Thesis, University of Ottawa, Ottawa.

Lloyd A. (2015). "*Blast retrofit of reinforced concrete columns."* Ph.D. Thesis. University of Ottawa, Ottawa.

Lloyd, A., Jacques, E., Saatcioglu, M., Palermo, D., Nistor, I., and Tikka, T. (2011). *"Capabilities and Effectiveness of using a Shock Tube to Simulate Blast Loading on Structures and Structural Components."* ACI Special Publication, SP-281 Behavior of Concrete Structures Subjected to Blast and Impact, 3.1- 3.20.

Lok, T. S., and Pei, J. S. (1998). *"Flexural behavior of steel fibre reinforced concrete."* Journal of Materials in Civil Engineering, 10(2), 86-97.

Lok, T. S., and Xiao, J. R. (1999). *"Steel-fibre-reinforced concrete panels exposed to air blast loading."* Instn. Civ. Engrs. Structs. & Bldgs, 1999, 134, Nov. 319-331, Paper 11927.

Lok, T. S., and Zhao, P. J. (2004). "*Impact response of steel fiber-reinforced concrete using a split Hopkinson pressure bar."* Journal of Materials in Civil Engineering, 2004, 16(1): 54-59.

Louw, J. M., Maritz, G., and Loedolff, M. J. (1992). *"The behaviour of RC columns under impact loading."* DIE SIYIELE INGENIEUR in Suid-Afrika.

Magnusson, J., Hallgren, M., and Ansell, A. (2010). "*Air-blast-loaded, high-strength concrete beams. Part I: Experimental investigation.*" Magazine of Concrete Research, 62(2), 127-136.

Malvar, L. J. (1998). "*Review of static and dynamic properties of steel reinforcing bars.*" ACI Materials Journal-American Concrete Institute, 95(5), 609-616.

Malvar, L. J., and Ross, C. A. (1998). "*Review of strain rate effects for concrete in tension.*" Materials Journal, 95(6), 735-739.

Mansur, M. A., Chin, M. S., and Wee, T. H. (1999). "*Stress-strain relationship of high-strength fibre concrete in compression.*" Journal of materials in civil engineering, 11(1), 21-29.

Melançon, C. (2015). *"Effect of High-Performance Concrete and Steel Materials on the Blast Performance of Reinforced Concrete One-Way Slabs."* M.A.Sc. Thesis, University of Ottawa, Ottawa.

Miyamoto, A., and King, M. E. (1989). *"Non-linear dynamic analysis and design concepts for RC beams under impulsive loads."* Bulletin of the New Zealand National Society for Earthquake Engineering, Vol. 22 No. 2 June 1989.

MMFX Steel Corporation of America. *"MMFX$_2$ Rebar - Product Guide Specification."* http://www.mmfx.com/wp-content/uploads/2012/06/1-Mechanical_Properties8.pdf

MMFX Steel Corporation of America. *"Mechanical properties MMFX$_2$ (ASTM A1035/A1035M)."* www.mmfx.com/wp-content/uploads/2013/10/Product_Guide_Specification_Sept2013.pdf

Naaman, A. E., and Gopalaratnam, V. S. (1983). *"Impact properties of steel fiber reinforced concrete in bending."* Int. J. Cem. Compos. Lightweight Concr., 5(4), 225–233.

National Earthquake Hazards Reduction Program. (2014). "*NIST GCR 14-917-30: Use of high-strength reinforcement in earthquake-resistant concrete structures.*"

Popovics, S. (1973*). "A numerical approach to the complete stress-strain curve of concrete."* Cement and concrete research, 3(5), 583-599.

Remennikov, A. and Kaewunruen, S., (2006). *"Impact resistance of reinforced concrete columns: experimental studies and design considerations."* 19th Australasian Conference on the Mechanics of Structures and Materials, Nov 29 - Dec 1, Christchurch, New Zealand, 817-824.

.Saatcioglu, M., Lloyd, A., Jacques, E., Braimah, A., and Doudak, G. (2011). “*Focused research for development of a CSA standard on design and assessment of buildings subjected to blast loads.”* Interim report submitted to Public Works and Government Services Canada, Hazard Mitigation and Disaster Management Research Centre, University of Ottawa, Ottawa, Canada.

Sheikh, S. A., and Uzumeri, S. M. (1982). *"Analytical model for concrete confinement in tied columns."* Struct, Div., ASCE, 108(12), 2703-2722.

Thiagarajan, G., and Johnson, C. F. (2014). “*Experimental behavior of reinforced concrete slabs subjected to shock loading.”* ACI Structural Journal, Title No. 111-S120.

United Facilities Criteria (UFC) 03-340-02 (2008). *"Structures to resist the effects of accidental explosions."* United States of America Department of Defense, Washington, D.C.

Wang, N., Mindess, S., and Ko, K. (1996). *“Fiber reinforced concrete beams under impact loading.”* Cem. Concr. Res., 26(3), 363–376.

Wang, Z. L., Liu, Y. S., and Shen, R. F. (2007). *“Stress-strain relationship of steel fiber-reinforced concrete under dynamic compression.”* Constr. Build. Mater., 22(5), 811–819.

Williamson, E., Bayrak, O., Davis, C., and Williams, D. (2011). *"Performance of Bridge Columns Subjected to Blast Loads. II: Results and Recommendations Experimental Program."* Journal of Bridge Engineering, 16 (6), 693-702.

Wight, J., and MacGregor, James G. (n.d.). “*Reinforced concrete: Mechanics and design (6th ed.).”* Upper Saddle River, NJ: Pearson.

Wu, K., Li, B., and Tsai, K. (2011). *“Residual axial compression capacity of localized blast-damaged RC columns.”* International Journal of Impact Engineering 38 (2011) 29e40.

Xu, H., Mindess, S., and Banthia, N. (2006). *“The impact response of normal and very high strength FRC round panels.”* RILEM Proc., PRO 49: Int. RILEM Workshop on High Performance Fiber Reinforced Cementitious Composites (HPFRCC) in Structural Applications, RILEM, France, 561–570.

Yalcin, C., and Saatcioglu, M. (2000). *“Inelastic Analysis of Reinforced Concrete Columns.”* Computers & Structures. 77(5), 539–555.

Yoo, D., Banthia, N., Kim, S., and Yoon, Y. (2015). *“Response of ultra-high-performance fiber-reinforced concrete beams with continuous steel reinforcement subjected to low-velocity impact loading.”* Composite Structures 126 (2015) 233–245.

Yusof, M. A., Norazman, Ariffin, Zain, F. M., Risby, and Ng, C. P. (2010). *“Normal strength steel fiber reinforced concrete subjected to explosive loading.”* International Journal of Sustainable Construction Engineering & Technology, Vol 1, No 2, December 2010.

Zhang, L., and Mindness, S. (2011). *"Dynamic compressive toughness of high strength fiber reinforced concrete.”* ACI (Special Publication), SP-281 Behavior of Concrete Structures Subjected to Blast and Impact, 7.1-7.21.